OPTICAL FINGERPRINTS OF UPCONVERSION NANOPARTICLES FOR SUPER-CAPACITY MULTIPLEXING

By

Jiayan Liao

Institute for Biomedical Materials & Devices

School of Mathematical and Physical Sciences, Faculty of Science

Supervisors:

Dr. Jiajia Zhou & Prof. Dayong Jin

This thesis is presented for the degree of Doctor of Philosophy

September 2020

Certificate of Original Authorship

I, Jiayan Liao declare that this thesis, submitted in fulfillment of the requirements for the award of Doctor of Philosophy, in the School of Mathematical and Physical Sciences, Faculty of Science, University of Technology Sydney.

This thesis is wholly my own work unless otherwise reference or acknowledged.

In addition, I certify that all information sources and literatures used are indicated in the thesis.

This document has not been submitted for qualifications at any other academic institution.

This research is supported by China Scholarship Council Scholarships (Jiayan Liao: No. 201508530231) and University of Technology Sydney Ph.D. Scholarship.

This research is supported by an Australian Government Research Training Program.

Signature: Production Note:
Signature removed prior to publication.

Date: 07-09-2020

Acknowledgments

After 4 years' study at the University of Technology Sydney (UTS), I have completed my Ph.D. thesis with the help of people in our group. Firstly, I would like to thank my supervisor, Prof. Dayong Jin, for the valuable opportunity of the Ph.D. study in Australia. Dr. Jin is a professor of great personal charisma, always considerate, patient and encouraging. From the beginning of my study, Prof. Jin has paid much energy and time to my research plan development. I respect very much his diligence in research and kindness in person. I learned a lot from Jin's self-motivated and optimistic attitude to life, aspiring, energetic and collaborative research style. He has insights to foresee the trend of the related research area and provided great ideas and suggestions for my research. I could not imagine how to complete my research without his guidance. Moreover, supervised by Prof. Jin, I have improved my ability on how to conduct the research project logically. I feel very lucky to have such great mentors and very grateful to them for their enormous efforts in guiding me throughout my Ph.D. study to reach the completion of this thesis.

Meanwhile, I also would like to express my heartfelt thanks to my supervisor Dr. Jiajia Zhou, for her precious supervision and guidance through all the years I studied at UTS. Although Dr. Zhou has been my principal supervisor in the last year of my Ph.D. study, she started to support my research since 2017 as my research project is closely connected to her research area. Dr. Zhou helped me a lot with my experimental design, discussion and we overcame the challenges in my research together. I learned how to undertake a research project logically, solve problems and overcome challenges. She is my idol. Her tender care and warm encouragement were of vital importance to my growth.

I acknowledge our group members and lab colleagues. I am proud that our lab is a place full of the atmosphere of sharing and support. Greatly, thanks a lot to our group members and collaborators who contributed to my research. Thanks to Dr. Fan Wang, Baolei Liu and Chaohao Chen for teaching me on the optical test systems. As my background is optical

material synthesis, I learned a lot of new knowledge on the optical instrument operation from them, and my research benefits a lot from this. Also, I would like to thank Dr. Shihui Wen, Dr. Chao Mi, Dr. Deming Liu and Dr. Helen Xu for help with upconversion nanoparticle synthesis. Thanks to Prof. Jie Lu and Dr. Yiliao Song from the Faculty of Engineering and IT, the University of Technology Sydney for providing deep learning algorithm support. Thanks for Dr. Lin Zhang from the University of New South Wales for providing the polymer used in my research, Dr. Yinghui Chen for the DNA conjugation, Dr. Mark Lockrey for STEM characterization and Dr. Hongwei Liu in the University of Sydney for his assistance on TEM characterization.

Next, I would like to acknowledge all my colleagues who have given me help over the last several years. Thanks to the optics group including Zhiguang Zhou, Yongtao Liu, Xuchen Shan, and Yuan Liu. And my office mates, Hao He, Wei Ren, Ming Guan, Dejiang Wang, Lei Ding, Xiangjun Di, Guochen Bao, Guochen Fang. I cherish interactions with Dr. Gungun Lin, Dr. Qian Peter Su, Dr. Hongxu Lu, Dr. Joris Goudsmits, Dr. Olga Shimoni. Thank you for a lot of beneficial discussions and helps in both my study and life, and I appreciate your supports and friendship very much.

I give my deep appreciation to my family. I thank my parents for their moral support to my oversea Ph.D. study, understanding and sincere company. Words can't express how much I love all of you.

Special thanks to our school manager Elizabeth Gurung Tamang, lab manager Katie McBean, scientific officer Mark Lockrey and Ronald Shimmon for their technical support.

Finally, I would like to acknowledge the China Scholarship Council Scholarships and UTS for providing me with Ph.D. scholarship and research opportunities.

Table of Contents

List of Publications

Research papers:

[1] **Jiayan Liao,** Dayong Jin, Chaohao Chen, Yiming Li, Jiajia Zhou, "Helix shape power-dependent properties of single UCNPs", The Journal of Physical Chemistry Letters, 11 (8), 2883-2890

[2] **Jiayan Liao,** Baolei Liu, Yiliao Song, Fan Wang, Chaohao Chen, Jiajia Zhou, Jie Lu, Dayong Jin, "Optical Fingerprints of Single Nanoparticles for Deep Learning Aided Super-Capacity Optical Multiplexing", revised, Nature Communications.

[3] Jiajia Zhou, Shihui Wen, **Jiayan Liao,** Christian Clarke, Sherif Abdulkader Tawfik, Wei Ren, Chao Mi, Fan Wang, Dayong Jin, "Activation of the surface dark-layer to enhance upconversion in a thermal field", Nature Photonics, 2018, 12, 154.

[4] Baolei Liu, Chaohao Chen, Xiangjun Di, **Jiayan Liao,** Shihui Wen, Qian Peter Su, Xuchen Shan, Zai-Quan Xu, Lining Arnold Ju, Fan Wang, Dayong Jin, "Upconversion nonlinear structured illumination microscopy", Nano Letters, 2020, 20, 7, 4775–4781.

[5] Chaohao Chen, Baolei Liu, Yongtao Liu, **Jiayan Liao,** Xuchen Shan, Dayong Jin, "Fourier domain heterochromatic fusion for single beam scanning super-resolution microscopy" revised, Nature Communication.

[6] Xuchen Shan, Fan Wang, Dejiang Wang, Shihui Wen, Chaohao Chen, Xiangjun Di, Peng Nie, **Jiayan Liao,** Yongtao Liu, Peter Reece, Dayong Jin, "Optical trapping beyond refractive index mismatch using ion resonance", revised, Nature Nanotechnology.

[7] Hao He, Baolei Liu, Shihui Wen, **Jiayan Liao,** Gungun Lin, Jiajia Zhou, Dayong Jin, "Quantitative Lateral Flow Strip Sensor Using Highly Doped UCNPs", Analytical Chemistry, 2018, 90, 12356-12360.

[8] Yingzhu Zhou, Yinghui Chen, Hao He, **Jiayan Liao,** Hien TT Duong, Maryam Parviz, Dayong Jin, "Activation of the surface dark-layer to enhance upconversion in a thermal field", Journal of Rare Earths, 2018, 37, 11-18.

[9] **Jiayan Liao,** Zhengwen Yang, Bo Shao, Jun Li, Jianbei Qiu, Zhiguo Song, Yong Yang, "Significant Suppression of Photoluminescence of $NaGdF_4$: Eu^{3+} Nanocrystals in the Crystalline Colloidal Arrays." Science of Advanced Materials, 2016, 8, 697-702.

([1] – [8] are closely related to my Ph.D. program)

Conference papers:

2020 Oral presentation, Institute for Biomedical Materials and Devices (IBMD), UTS Research Week (Sydney, Australia)

2020 Oral presentation, International Conference on Nanoscience and Nanotechnology, ICONN 2020, (Brisbane, Australia)

2020 Poster presentation, Three Wise Men Winter School on Luminescent Nanothermometry for Biomedical Applications (Madrid, Spain)

2019 Poster presentation, International Symposium on Luminescent Materials, Phosphor Safari 2019 (Xiamen, China)

Awards:

Vice Chancellor's Postgraduate Research Student Conference fund, 2019

CSC-UTS Ph.D. scholarship, 2016-2020

Abstract

This thesis includes six chapters.

Chapter 1 outlines the background knowledge and motivation relevant to the development of luminescence materials for optical multiplexing. The materials include fluorescence dyes, quantum dots, metal particles and upconversion nanoparticles (UCNPs). This thesis introduces different optical dimensions of UCNPs. The challenges associated with luminescence materials for multiplexing are approached. These sections detail the motivation for and the specific aims of the current study—that is, to tune the energy-transfer process in the core-shell UCNPs and to achieve the optical multiplexing of UCNPs in the spectral and lifetime orthogonal dimensions.

Chapter 2 provides detailed information on the materials, instruments and equipment, preparation and characterization methods.

Chapter 3 is the first research chapter, and it investigates the peak tuning of the excited state population of powder samples in Nd-Yb-Tm core-shell UCNPs. For the take-off of upconversion emissions, the duration can be extended from 100 μs to 900 μs after the 808 nm excitation is switched off. This strategy creates a set of time-resolved emission profiles over a large dynamic range, where they can be tuned from either the time of rising or decay.

Chapter 4 synthesizes two groups of UCNPs: Yb^{3+}-Nd^{3+}-Er^{3+} and Yb^{3+}-Tm^{3+} core-shell UCNPs. This chapter outlines the systematic analysis (via the confocal microscope system) of the emission intensity/spectra and lifetimes of single UCNPs. Strategies to control the energy migration process and to arbitrarily tune the rising and decay times and the plateau moment are presented, where it is suggested a unique time-domain optical fingerprint can be assigned to each type of nanoparticles.

Chapter 5 outlines the finding that the nanoparticles show a unique lifetime signature under wide-field systems upon 976 nm (Yb^{3+}-Tm^{3+} doped UCNPs) and 808 nm (Yb^{3+}-Nd^{3+}-Er^{3+} doped UCNPs) excitation. To achieve high-throughput multiplexing, the lifetime profiles can

be detected under a wide-field microscope system. A novel method is also introduced here (i.e., deep learning) to decode the lifetime fingerprints of 14 batches of UCNPs. Through deep learning, the large amount of optical data from different batches of UCNPs allows the classification of each single UCNPs for the untapped opportunity to decode these nanoscale lifetime barcodes. The classification capability associated with deep learning allows all 14 kinds of UCNPs to achieve accuracies of over 90%.

Finally, the research results of this thesis are summarised in Chapter 6. Potential future developments and prospects regarding the multidimensional optical properties of UCNPs are discussed.

Keywords: rare earth doped nanomaterials, upconversion, optical multiplexing, wide-field microscope, machining learning, DNA conjugation.

The relationship between these chapters is shown in the flowchart given below.

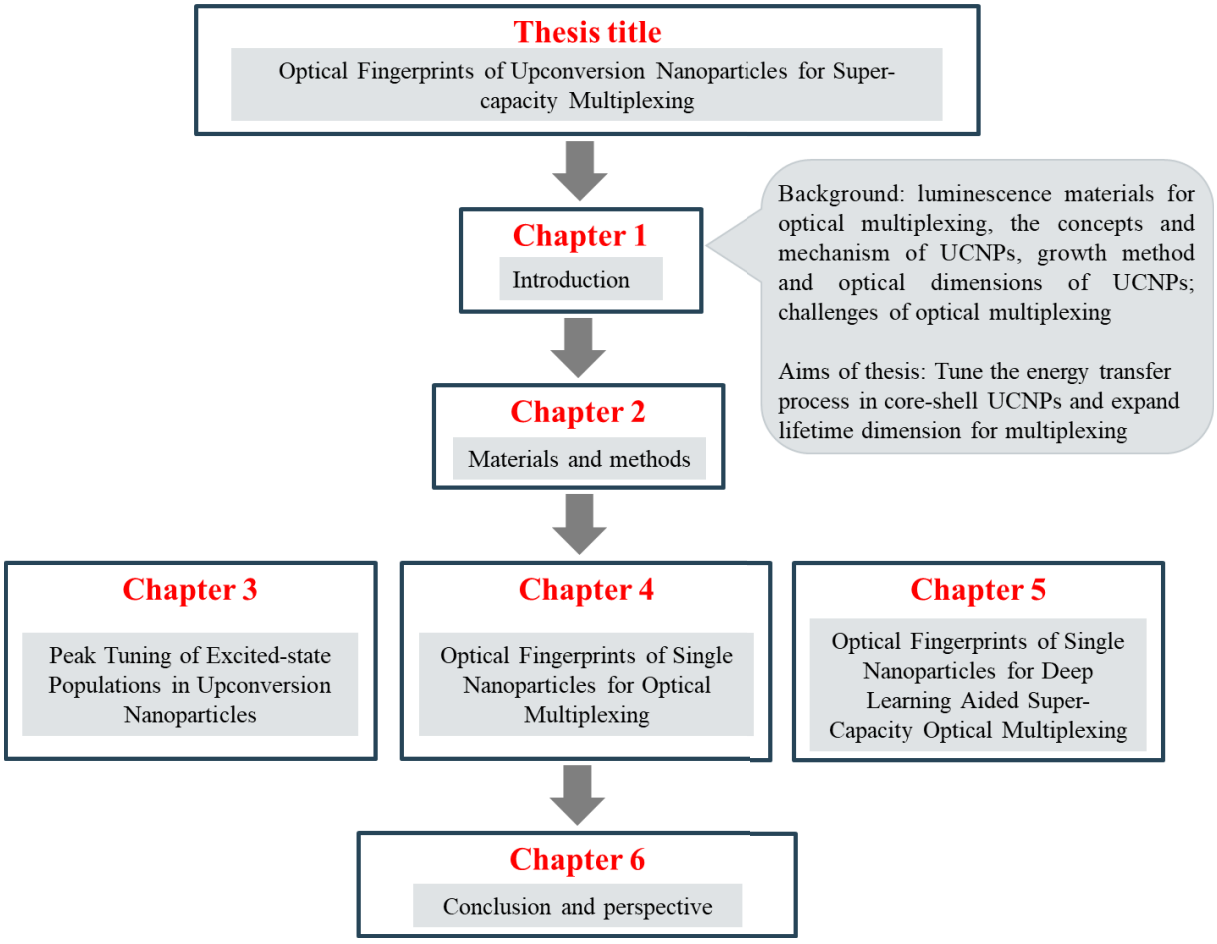

List of Acronyms (in alphabetic order)

BET	Back Energy Transfer
CR	Cross-Relaxation
DNA	Deoxyribonucleic Acid
EMCCD	Electron Multiplying Charge Coupled Device
ESA	Excited State Absorption
ETU	Energy Transfer Upconversion
ET	Energy Transfer
EDC	N-(3-Dimethylaminopropyl)-N′-ethyl carbodiimide hydrochloride
ESP	Excited-state Populations
HCl	Hydrochloric Acid
IEM	Interfacial Energy Migration
NIR	Near-Infrared
NaOH	Sodium Hydroxide
NH_4F	Ammonium Fluoride
OA	Oleic Acid
ODE	1-Octadecene
QDs	Quantum Dots
RE	Rare Rarth
SEM	Scanning Electron Microscopy

STEM	Scanning Transition Electron Microscopy
SERS	Surface-enhanced Raman Spectroscopy
SHG	Second-harmonic Generation
TEM	Transmission Electron Microscopy
TPA	Two-photon Absorption
THF	Tetrahydrofuran
UCNPs	Upconversion Nanoparticles
UV	Ultraviolet
XRD	X-ray Diffraction

Optical Fingerprints of Upconversion Nanoparticles for Super-capacity Multiplexing

Chapter 1 Introduction

1.1 Luminescence materials for optical multiplexing

In contrast to classical analytical and bioanalytical strategies that detect analytes individually, an ideal analytical tool should allow users to investigate a sample for a large number of targets. In the modern era, the development of new encoding strategies strengthens our capacity to acquire and process information, which is a driving force for multiplexed analyte detection in complex mixtures. Among the analytical techniques which contain the potential for multiplexing, spectroscopic methods are frequently used. Fabrication approaches of new luminescent materials have underpinned the development of various forms of optical information carriers. In recent years, optical multiplexing has been used to widely investigate and significantly strengthen our ability to encode information. For example, barcode labels used in packaging are based on optical intensity multiplexed in space, where unique patterns consisting of stripes of different widths and spacing to encode large amounts of information are used. Moreover, luminescent materials contain different dimensional parameters, such as wavelength, intensity, polarization, and lifetime. Through the use of different dimensions of light, it is possible to multiplex several optical signals into a single optical carrier. Significant advances have also been made toward high level next-generation optical data storage and security inks by multiple, higher-order combinations of such dimensions[1,2].

The scope of optical multiplexing is rapidly expanding into biological and biomedical fields. In areas such as disease diagnostics, drug discovery, molecular and cell dynamics, and cellular organization and function, it is extremely useful to be able to efficiently analyze enormous

amounts of information. Multiplexing applications in the fields of chemistry, biology, and security have generated a higher demand for research into new materials. Furthermore, incorporating multiple pieces of information into an individual encoding carrier is like to be of great significance in intensifying multiplexing. Multidimensional optical coding has been developed to increase the throughput of imaging, which allows simultaneous tracking of multiple targets, as well as assigns addressable molecular probes for multiplexed molecular and cellular sensing. In recent years, varied luminescent materials have been explored as encoding materials and a variety of nanoparticle-based coding techniques have also studied to advance optical multiplexing.

1.1.1 Fluorescence dyes

In recent decades, fluorescent dyes (also known as reactive dyes or fluorophores) have been investigated widely for biological applications. Compared with fluorescent proteins, fluorescent dyes do not require a maturation time and maintain higher photostability and brightness. Among different optical encoding methods, fluorescence-encoding has been most widely used in biological applications, owing to the simple encoding process[3,4]. Additionally, microspheres have a large surface area and enable fast-binding kinetics; therefore, encoded microspheres are frequently-used information carriers for analyte detection[5,6]. The fluorescence-encoded beads are prepared by entrapping fluorescent dyes into microbeads such as polystyrene, and then the swollen beads are put into an organic solvent containing defined concentrations of fluorophores[7]. Fluorescent labeled beads by incorporating different amounts of fluorescent dyes can be defined as a unique bead type. The number of possible discrete assays that can be multiplexed depends on the number of identifier codes that can be detected separately. For example, when microspheres are labeled by two fluorescent dyes emitting either green and red light. The emission intensity of each dye can be modulated individually by adjusting their concentrations, so four intensity levels and two wavelengths can result in over 10 coding-capacity types[8]. Braeckmans and coworkers employed spatial selective photo-bleaching on microparticles fixed with fluorescent dyes (Figure1.1)[9]. Fluorescence in such a homogeneously dyed microsphere was then selectively bleached using a modified confocal

scanning laser microscope to form a unique pattern. This method has the potential to create an unlimited number of unique codes.

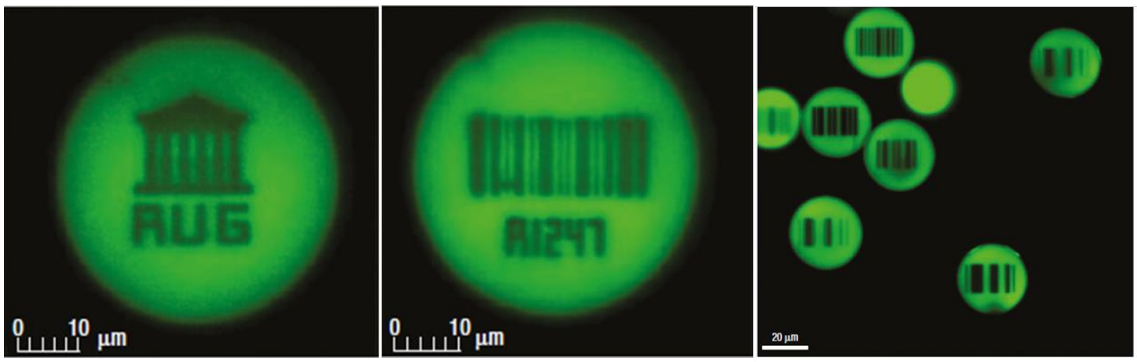

Fig. 1.1. Encoding via spatial-selective photobleaching on microparticles fixed with fluorescent dyes.[9]

Moreover, a combinatorial code can be generated using a biomolecule, (e.g., DNA) as the encoding information carrier.[10–13] The specific DNA barcode can be modified to the surface of the microspheres and then decoded by hybridizing it with different fluorophores through sequential-hybridization and de-hybridization processes. Luo and et al.[14] labeled DNA with different types of fluorescent dyes and simultaneously detected five sequences of DNA using DL-DNA-based bio-barcodes. The five kinds of nano-barcodes were then decoded based on the ratio of fluorescence intensity. The nano-barcodes possess coding capabilities and molecular sensing abilities when attached to a probe DNA. Furthermore, Lin et al. created a fluorescent barcode using a rigid DNA origami submicrometre rod with multiple fluorescent tags (Figure1.2).[15] They demonstrated that spatial control over the positioning of fluorophores on the surface of a stiff DNA nanorod is capable of producing 216 distinct barcodes. However, the broad and overlapping features of emission bands, photobleaching, complex experimental set-ups requiring multiple excitation lines, and the limited number of colour codes still restrict the broad utilization of fluorescent dyes.

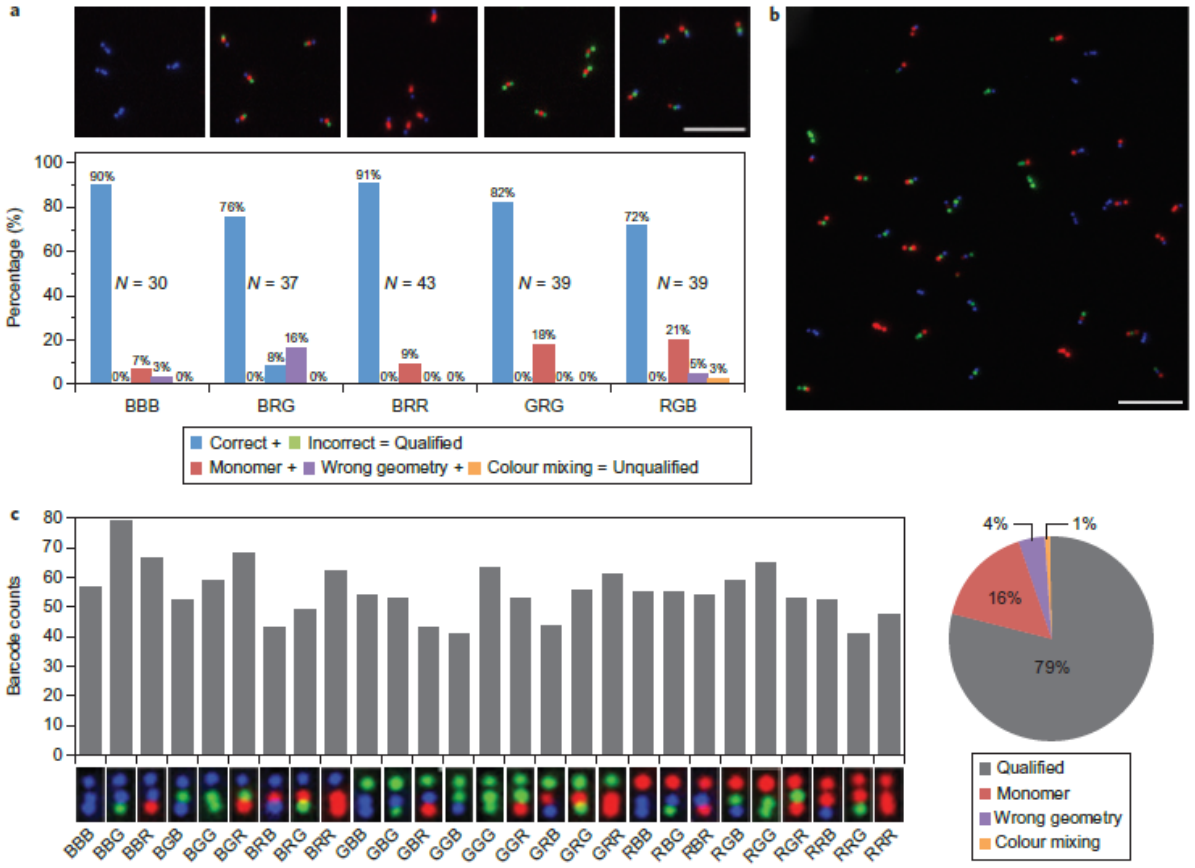

Fig. 1.2. Fluorescent barcodes using a rigid DNA origami submicrometre rod. (a) superimposed TIRF microscopy images of five barcode species and the statistics. (b) a representative image of the equimolar mixture of 27 barcode species. (c) statistics obtained by analyzing 27 of the 27-barcode mixture.[15]

1.1.2 Quantum dots

Nanoparticle-based codes have distinct advantages over conventional organic fluorophores because they are widely resistant to photobleaching and their emission spectra can be fine-tuned using the design of the nanoparticle. Constructed from elements of Group II (Zn, Cd, Hg)-VI (Se, S, Te), III-V and IV-VI of the periodic table, quantum dots (QDs) are colloidal semiconductor nanocrystals with tunable fluorescence emission which is dependent on their size and simultaneous excitation. The advantages of QDs include a broadband absorption spectrum and narrow symmetric emission spectrum (20–30 nm), as well as a high quantum yield of luminescence (approximately 70%), making QDs particularly interesting for multiplexed analysis (Figure1.3).[16] QDs can be used for spectral encoding in the same way as

organic fluorophores. By precisely controlling the ratios of composition and size, the QD-embedded beads can be used for multiplex assays.[17–21] QDs encapsulated into polystyrene beads can also diminish problems associated with the non-biocompatibility of QDs.

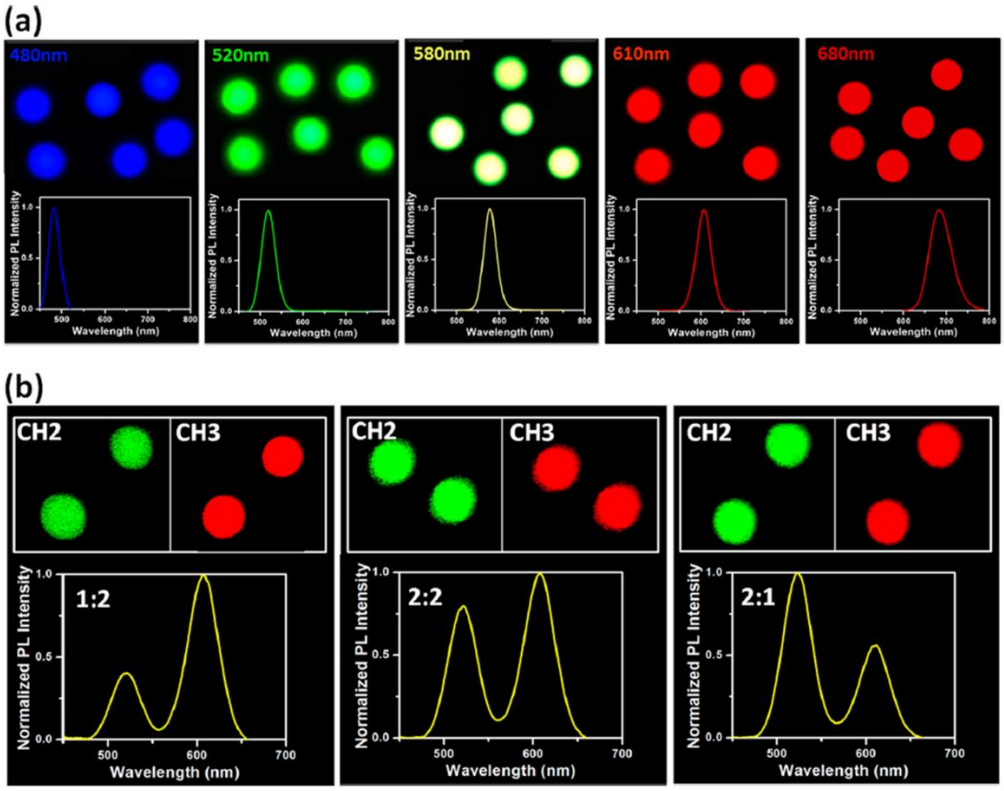

Fig. 1.3. QD barcodes (6.6 μm) were labeled with single- and dual-coloured encoding. [16]

QD-tagged microbeads for the multiplexed coding of DNAs have been reported, where single-colour encoded 1.2-mm beads are highly uniform and reproducible with 99.99% identification under favorable conditions[22]. An assay for accurate and reproducible gene expression profiling in a high-throughput and multiplexed format was reported through the use of QD nano-barcode-based microbeads[23]. Through the use of QD-nanobeads as fluorescent reporters, QD-loaded multi-colour nanobeads of 100 nm in diameter have demonstrated sensitive detection of the human prostate-specific antigen (Figure1.4).[19] However, the use of QDs for certain applications is challenging due to their cytotoxicity and photoblinking. Cd-free QDs, surface coating, and incorporating QDs into polymer or silica matrices have undergone development to overcome the issue of toxicity. The core-shell (e.g., CdSe/CdS) or core-alloyed interface shell QDs are prepared to suppress the blinking behavior.

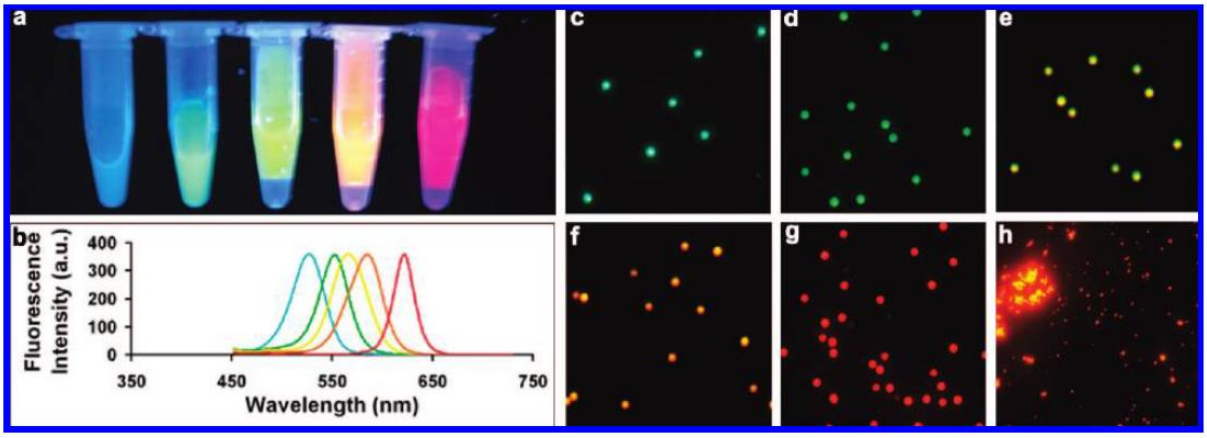

Fig. 1.4. True-colour fluorescence images of monochromatic QD-nanobeads emitting light at 525, 550, 565, 585, and 620 nm.[19]

1.1.3 Metal particles

The fluorescence-based encoding is more or less subject to limitations such as the photo-instability of single organic dyes and the fluorescence "blinking" of single QDs. Moreover, the high background noise from light scattering and the autofluorescence of samples limit the sensitivity. Therefore, nano-barcodes with non-fluorescent optical properties have been developed—that is surface-enhanced Raman spectroscopy (SERS) based encoding and segmented metallic wires and disks.[24–27] Raman scattering, the inelastic scattering, occurs as a result of the up- or down-shift of monochromatic light due to the vibration or rotation of molecules. SERS is an ultrasensitive vibrational spectroscopic technique that employs noble metal surfaces such as copper, silver, or gold layer on the detection surface. Molecules on or near the surface of plasmonic nanostructures via an electrodeposition process have been found to significantly improve the efficiency of Raman scattering. Furthermore, different Raman reporter molecules with distinct Raman spectra can be used to tag metallic nanoparticles to produce barcodes (Figure. 1.5).[28]

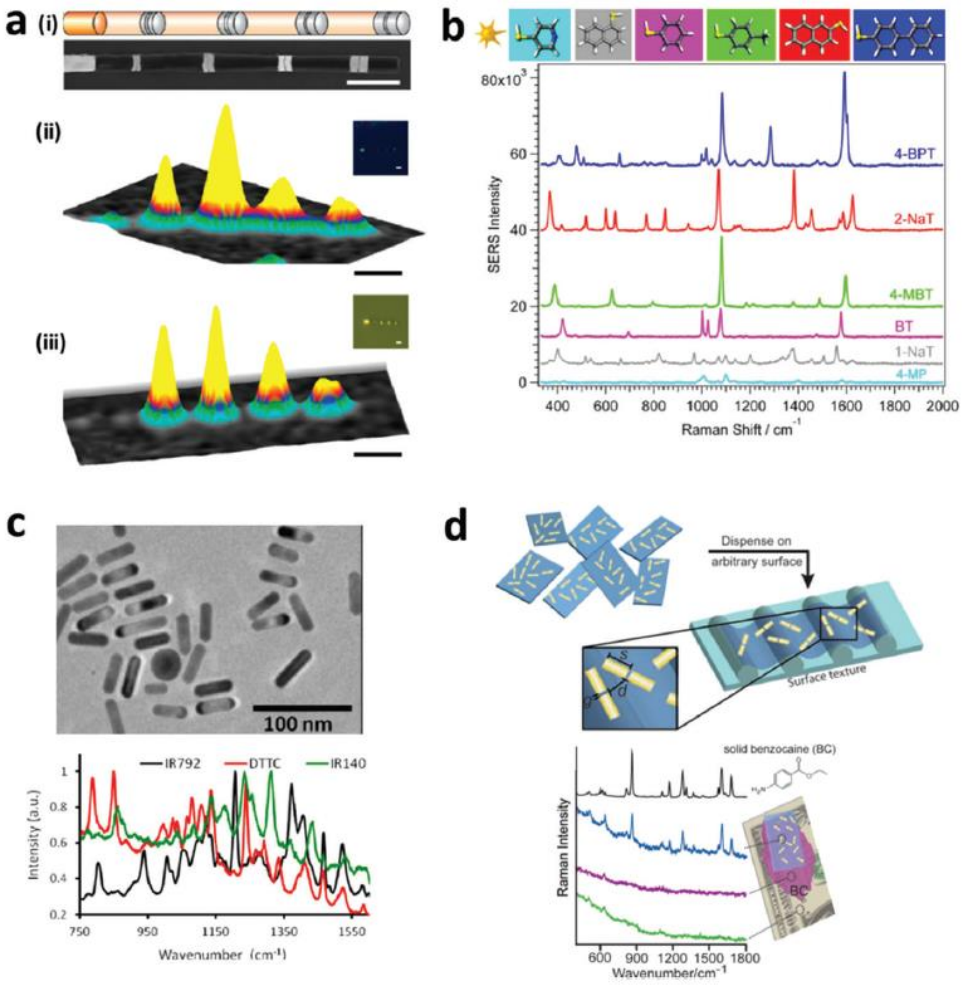

Fig. 1.5. SERS encoding: (a) Silver nanodisk barcodes with nanogaps. (b) SERS hotspots from the gold nanostars functionalized with different Raman reporters; (c) gold nanorods with different Raman reporters; and (d) SERS nanosheets based on the dispersed gold nanorod dimer on a solid surface.

Coupling molecular beacons to barcoded metal nanowires for multiplexed DNA/RNA bioassays has widely occurred through the use of a Raman microscope.[29–33] By using the signal processing methods to reduce the Raman signal from fluorescence interference, Gambhir and et al. reported 10 different SERS-based nano-barcodes for a multiplexed in-vivo imaging application.[34] The encoding method of the wavenumber-intensity-related SERS-signatures was demonstrated through the use of the core-shell structure silver nanoparticles (Fig. 1.6a).[35] through the use of three types of Raman spectra and changing their molecular ratio, 19 codes with distinguished spectral characteristics were achieved. The capacity associated with the high-throughput bioanalysis was increased by controlling the number of reporters involved in

the fabrication process. The dual-mode encoded barcodes were designed by employing both various fluorescence reporters and SERS probes to obtain a greater encoding number.[36] The Ag nanoparticles were deposited onto magnetite composite microspheres, and then the SERS probes were absorbed onto the surface of Ag-NPs to form the organic-metal-QD-hybrid barcodes with distinguished spectral codes (Figure. 1.6 b).

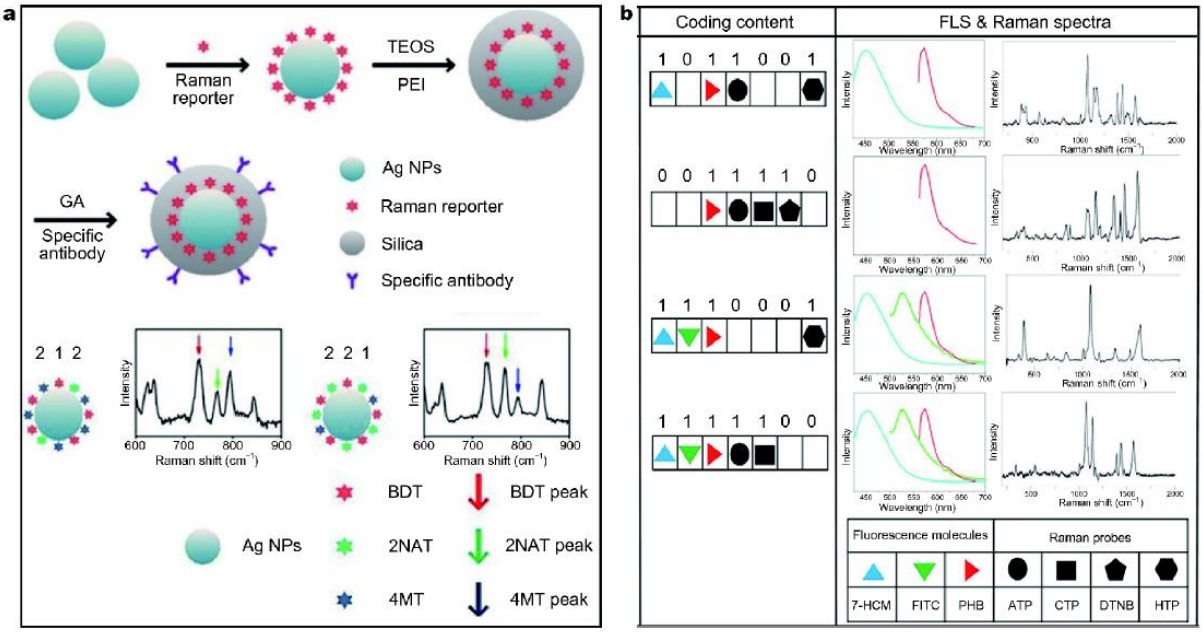

Fig. 1.6. (a) Schematic of the encoding approach, wavenumber-intensity-related SERS-signatures, and the unique SERS signatures of different associated with wavenumber and intensity ratio; (b) fluorescence spectra and Raman spectra of the dual-mode encoded barcodes.[37]

1.1.4 Rare-earth doped nanoparticles

Low background interference from biomolecules and the strong separation of emission signals to distinguish between a greater number of codes are crucial to achieving efficient spectral encoding for the multiplexed analysis of biological samples. Many biomolecules show strong autofluorescence under short-wavelength illumination, which severely limits the detection; whereas, there is almost no NIR light-induced background fluorescence, nor reporter signals. Therefore, the long-wavelength of excited materials is exploited. Lanthanide ions can achieve downconversion or upconversion based on the energy conversion process. UCNPs absorb two or multiple photons of lower energy and emit light of shorter wavelengths with large anti-

Stokes shifts and a narrow emission band. Lanthanide ions can be excited via NIR light, and various lanthanide ions are usually doped into the inorganic host materials which serve as activators or sensitizers. The energy is absorbed by sensitizers (Nd^{3+} or Yb^{3+}) and transferred to activators (Ho^{3+}, Er^{3+} or Tm^{3+}). UCNPs offer advantages and exhibit great properties with a long luminescence lifetime, photostability, single-wavelength excitation, low toxicity, sharp emission bands, and tunable emission colour through changes to the lanthanides ions. Thus, UCNPs are suitable for multicolour encoding and, accordingly, 6 different fluorescence codes have been reported by tuning the emission intensity and doped ions (Figure. 1.7 a)[38]. When components and intensities are changed simultaneously, the number of codes with a unique spectrum is capable of increasing exponentially. This kind of novel barcode material can be used in multiplexed signaling, bioassays and nuclei acid encoding (Figure. 1.7 b, c)[39,40]. The surface of the UCNPs can also be modulated with an optical-screening layer (e.g., the organic dye or gold nanoparticles) to tune the intensity ratio of the emission bands (Fig. 1.7 d)[41,42].

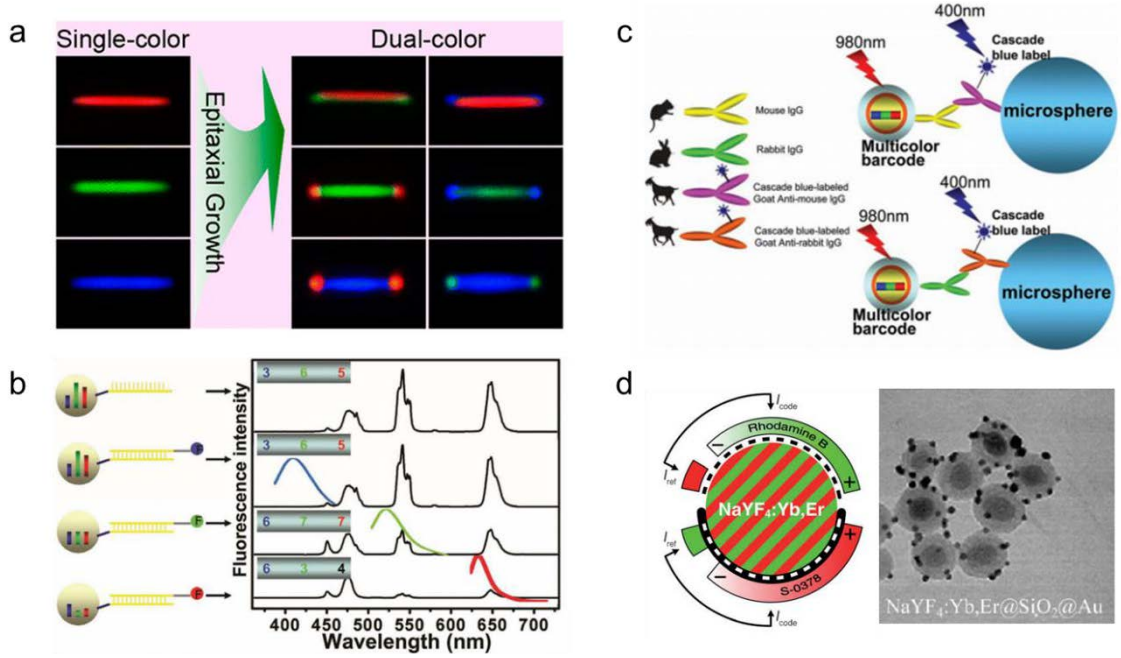

Fig. 1.7 (a) UCNPs-encoded multi-coloured nanorods achieved by combining three different primary colours. (b) Schematic illustration and test results of the multiplex bioassay by employing oligo probe-modified UCNPs-encoded barcodes. (c) Scheme for the conjugation of antibody-UPNBs with

secondary antibody microspheres. (d) Tuning the emission intensity of UCNPs differentially by organic dye and gold nanoparticles.

1.2 Fundamentals and development of UCNPs

Linear optics owns the conventional optical properties which are independent of the incident light intensity. Nonlinear optics are usually used to describe the optical phenomena for which the optical properties of the material depend on the radiant flux density of the exciting light and nonlinear power density response (Fig.1.8). Photon upconversion is one representative nonlinear optical process and is characterized by the conversion of long-wavelength radiation into short-wavelength region.[43–45] The Photon upconversion process is realized through certain ions of the d and f elements, which usually need some important requirements for such as long lifetimes of the excited states and a ladder-like arrangement of the energy levels with similar spacing. The suitable hosts doped with transition metal ions (3d, 4d, 5d) have been reported to show upconversion.[46–48] Actinide-doped materials have also been investigated for upconversion.[49–51]Two-photon absorption (TPA) in quantum dots and organic dyes and second-harmonic generation (SHG) are also realized upconversion process.[52–57] These systems require a harsh research environment, such as low temperatures, high-power density ($>10^6 W/cm^2$) photon flux or expensive ultra-short pulsed lasers.

High upconversion efficiencies have been observed for lanthanide-doped solids. Lanthanide ions are suitable elements for upconversion because their energy level spacings of 4f-valence electrons exhibit ladder-like electronic structures which correspond to NIR and visible photon energies. Accordingly, unique nonlinear processes in which two or more NIR pump photons are absorbed through real intermediate energy levels of Ln^{3+} leads to the emission of light at a wavelength shorter than incident radiation.[58] This was independently formulated in bulk crystals in the mid-1960s by Auzel, Ovsyankin and Feofilov.[59–61] Since that time, a significant research effort has been made regarding Ln^{3+}-doped upconversion luminescence owing to its remarkable optical properties (ie., massive anti-Stokes shift, excellent photostability, sharp and tunable multi-peak line emission, and the long and widely tuneable domain of the emission

lifetime).[62,63] Such intrinsic features make frequency upconversion by UCNPs appealing for photonic and biological applications.

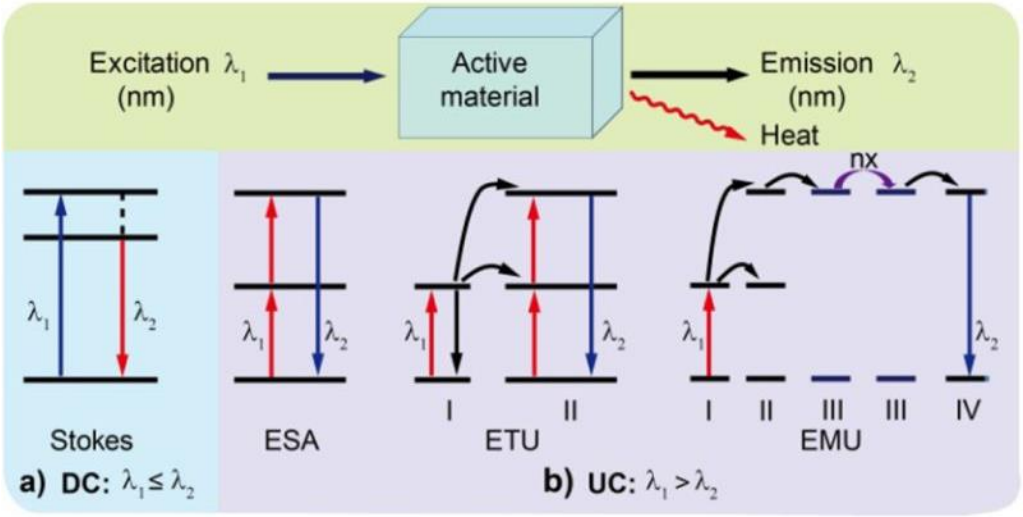

Figure 1.8 Schematic illustration of downconversion (DC) and upconversion (UC) processes.[64]

1.2.1 Lanthanides-doped UCNPs

Lanthanide-doped upconversion materials usually consist of a suitable inorganic and photostable host embedded with various trivalent lanthanide ions (Figure 1.9a).[65] A crystalline host lattice featuring a low phonon energy environment is beneficial to the photon upconversion process, where the non-radiative decay rate of lanthanides via multiphonon relaxation can effectively be suppressed. Photon upconversion in lanthanide-doped crystals relies on the physically existing intermediary energy level; Therefore, it possesses higher frequency conversion efficiency (Figure 1.9b). The lanthanide family (from La to Lu) exhibits similar physical and chemical properties due to the significant similarity present in their electron configuration, $[Xe]4f^n5d^m6s^2$.

Upconversion luminescence generally comes from electronic transitions within the $4f^N$ configuration of lanthanides. Although these electronic transitions in principle are prohibited in terms of quantum mechanical selection rules, they can occur through the intermixing of higher electronic configurations with f states. Moreover, the lanthanide's $4f^N$ electronic configuration can split into an abundance of energy sublevels as a result of strong repulsion from the Coulombic interaction of the electrons and the spin-orbit coupling among f-electrons can splits the $4f^N$ electronic configuration of lanthanides as well as weak perturbations in the

crystal field. This leads to a rich energy-level pattern from the optical transitions among these levels (Figure. 1.9b).[66,67]

Moreover, the partially filled 4f intra-configurational transitions of lanthanides are effectively shielded by outer complete 5s and 5p shells, giving rise to a weak electron-phonon coupling and, thus, sharp emission lines resulting from electronic transitions.[68] Upconversion emissions are rarely influenced by the environment due to optical transitions being localized and generally not interfered with by quantum confinement—this leads to unique optical properties such as a sharp emission band, reliable photostability and long excited-state lifetime. Such unique features make lanthanide-doped upconversion materials ideal candidates for a variety of applications, ranging from bioassay and super-resolution imaging to 3D volumetric displays and photocatalysis.[64,69–71] By properly selecting the type of lanthanide dopants in a nanoparticle, the upconversion emission wavelength can be tuned precisely to span the ultraviolet and NIR regions (Figure. 1.9c).

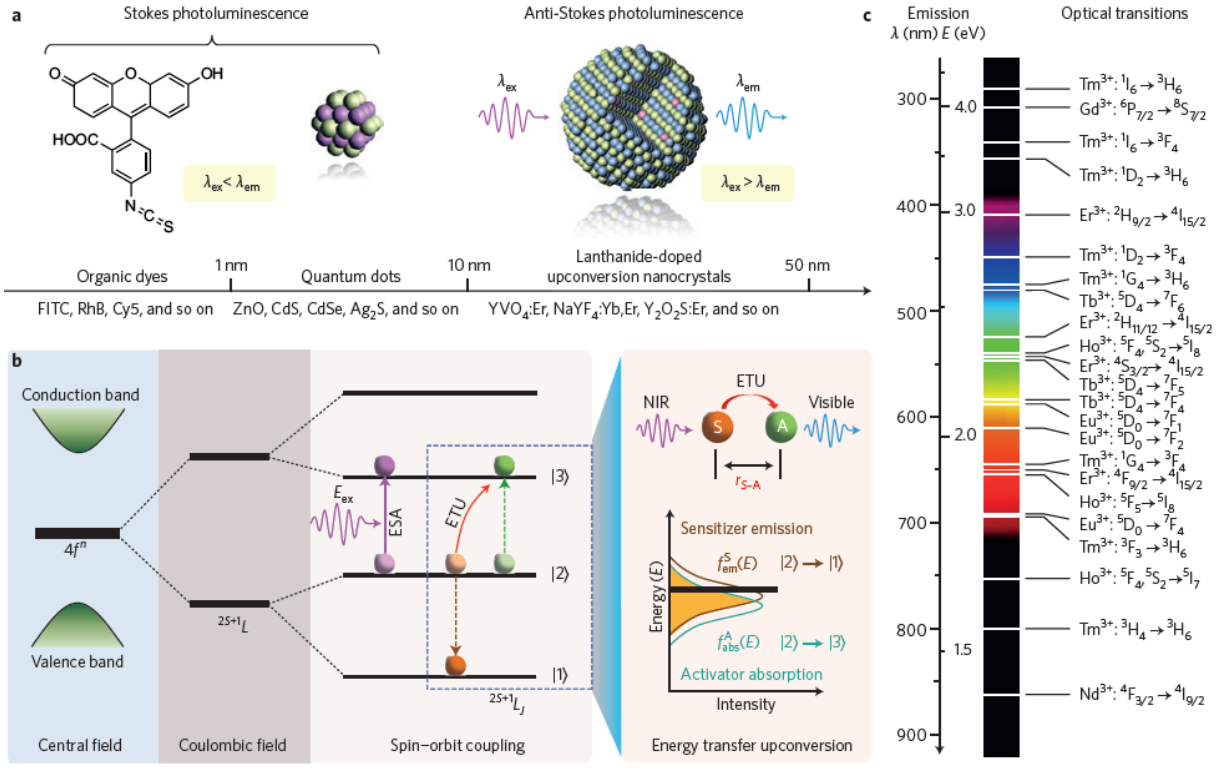

Figure 1.9 Lanthanide-doped nanoparticles and photon upconversion. (a) A comparison of three of luminescent nanomaterials: organic dyes, QDs and UCNPs. (b) Electronic energy level diagrams of

trivalent Ln^{3+} ions with upconversion processes. (c) Typical Ln^{3+}-based upconversion emission bands covering a broad range of wavelengths.[72]

It was not until the late 1990s, with the prevalent development of nanoscience and nanotechnology in the field of materials science, upconversion nanomaterials have been promoted on the nanoscale to increase their scope. The high-quality UCNPs are designed and routinely synthesized with controllable composition, crystalline phase, size, and shape through different chemical techniques (Fig. 1.10).

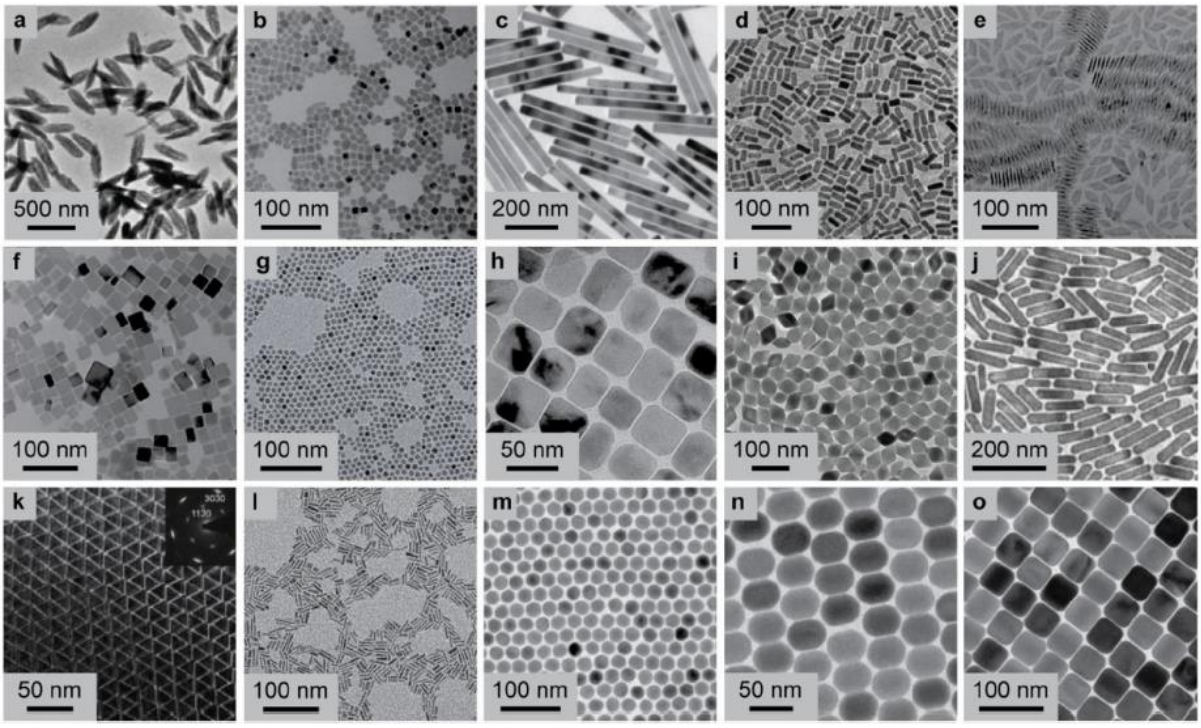

Figure. 1.10 (a) Typical TEM images of UCNPs (a) YF_3, (b, c) $NaYF_4$ and (d) $NaGdF_4$ nanocrystals synthesized by hydro/solvothermal strategy. (e) GdF_3 nanoparticles prepared through microwave irradiation. (f) $KMnF_3$, (g) CaF_2, (h) $NaScF_4$, (i)$LiYF_4$ and (j)KYb_2F_7 nanoparticles prepared by coprecipitation route. (k)LaF_3, (l)SrF_2 and (m–o)$NaYF_4$ nanoparticles synthesized by thermal decomposition method.

The upconversion process in nanomaterials involves the same mechanisms as those in bulk materials. However, due to the size confinement present in nanoparticles, ion-ion and ion-lattice interactions are modified to various degrees. The advent of these UCNPs provides a new platform that significantly expands the potential applications of nonlinear optical properties for

advanced nanophotonic and biological research.[73,74] As a result of the outstanding features of small size, low toxicity and excellent biocompatibility, and high photostability, UCNPs are particularly attractive as luminescence probes for bioimaging applications.[75–78] Furthermore, UCNPs work as spectral converters which promote the development of telecom wavelength-programmable optoelectronic devices when integrated into silicon or other semiconductor materials due to the excitation wavelength located in the telecom window (0.8-1.8μm).[64,73,74]

1.2.2 Mechanism of UC luminescence

As a nonlinear optical phenomenon, upconversion luminescence forms the sequential absorption of two or more low-energy photons followed by the luminescent emission of a high-energy photon[72,79]. Auzel first described the concept of "upconversion", summarized its mechanism and reported on upconverted visible emission based on energy transfer by using Yb^{3+} to sensitize Er^{3+} and Tm^{3+} ions.[43] After decades of development, photon UC processes involving lanthanide ions are currently predominantly categorized into five classes of mechanisms: excited-state absorption (ESA), energy-transfer upconversion (ETU), photon avalanche (PA), cooperative energy transfer (CET), and energy migration-mediated upconversion (EMU). All of these processes involve the sequential absorption of two or more photons, as shown in Figure 1.11.

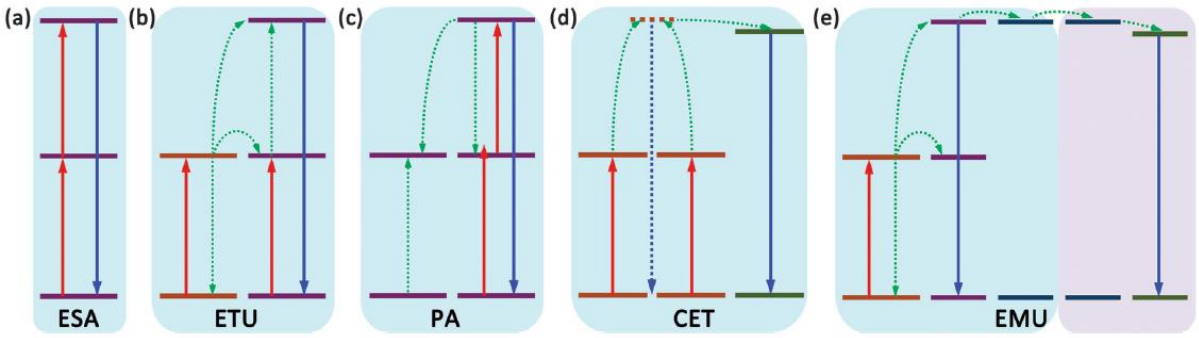

Figure. 1.11 Schematic representations of UC processes, red full arrows stand for direct excitation processes, blue full arrows stand for radiative emission processes and dashed arrows represent energy transfer processes.[80]

ESA is an appropriate pumping mechanism by the successive absorption of pumping photons for singly doped upconversion materials. In a typical ESA process, excitation takes the form of

successive absorption of pump photons by a single ion. If excitation energy is resonant with the transition from the ground state to the excited metastable intermediate state, phonon absorption occurs through the ESA process. A second pump photon that promotes the excited electrons from excited metastable level to a higher-lying state. Finally, the upconversion emission happens when the photon drops from a higher excited state back to the ground state.[81–83] Such rigorous requirements hinder the generalization of ESA processes and only a small set of lanthanides such as Ho^{3+}, $Er^{3+}$and Tm^{3+} are suitable luminescence centers for ESA process to proceed.[84–87]

ETU is similar to ESA and both of these two processes utilize sequential absorption of excitation photons to populate the intermediate levels of lanthanide dopant. However, ETU is by far the most efficient upconversion process through energy transfer, which involves the participation of two types of neighboring ions, usually called the sensitizer and activator. In a sensitizer-activator system, both the sensitizer and the activator could be pumped to their excited states upon the absorption of lower energy photons. Subsequently, a non-radiative energy transfer process promotes the sensitizer donates the energy to the activator via a dipole-dipole resonant interaction, while the activator relaxes back to the ground state. Yb^{3+} ions are commonly used as sensitizers in the ETU process.[88,89] The $^2F_{7/2} \rightarrow {}^2F_{5/2}$ transition of Yb^{3+} is conveniently resonant with many f-f transitions of Er^{3+}, Tm^{3+}, and Ho^{3+}, Yb^{3+}-Er^{3+} and Yb^{3+}-Tm^{3+}, and Yb^{3+}-Ho^{3+} doped $NaYF_4$ materials are typical and efficient dual ions activated upconversion systems Figure. 1.12.

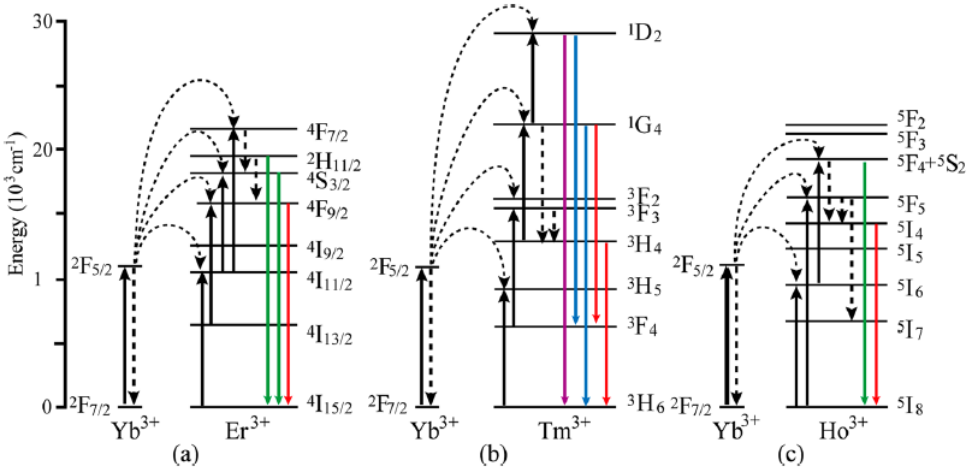

Figure. 1.12 Schematic energy level diagrams showing typical UC processes for (a)Yb^{3+} and Er^{3+}, (b)Yb^{3+} and $Tm^{3+}$and (c)Yb^{3+} and Ho^{3+}.[74]

PA is an infrequent pump mechanism that requires an excitation intensity above a certain threshold value.[90] The PA process was first discovered by Chivian and co-workers in a Pr^{3+}-doped infrared quantum counter in 1979.[91] The PA process starts with population to the intermediate excited state from the ground state by non-resonant weak ESA because of the mismatch energy. In this case, the luminescent centers may populate to the upper visible-emitting state through the resonant ESA process. After the metastable level population is finished, cross-relaxation[92] energy transfer or ion pair relaxation occurs between the excited ion and a neighboring ground-state ion, leading to the occupation of the intermediate states of both ions. The weak ground state absorption and strong feedback looping of excited state absorption followed by further initiate cross-relaxation exponentially increase exponentially intermediate states population above the excitation threshold, producing strong UC emission as an avalanche process. PA occurs when the consumption of intermediate states ions is less than that of the ground state ions, which is desirable for UC lasers. Recently, except for compact lasers application, the PA process is utilized to realize super-resolution imaging.[93,94]

Both sensitizers and activators are important for the CET process. The population of emitting levels usually arises from the cooperative energy transfer of adjacent ions. In a typical CET process, two energy donors are cooperatively activated to a virtual excited state to fulfill a simultaneous energy transfer to a neighboring acceptor.[95]UC involves two processes: cooperative sensitization (e.g., Yb^{3+}-Tb^{3+}, Yb^{3+}-Eu^{3+}, and Yb^{3+}-Pr^{3+} ion pairs.[96–99] and cooperative luminescence (e.g., Yb^{3+}-Yb^{3+} ion pair.[100]). The upconversion efficiency of CET is rather low due to the absence of a long-lived intermediate energy state of the activator, especially in nanomaterials. Most of the related studies of CET are focused on bulk materials.[97,101] A few research works demonstrated the feasibility of CET upconversion emissions in nanomaterials.[99,102]

Except for the mechanisms mentioned above, a novel UC mechanism EMU was proposed by Liu et al in 2001 (Figure. 1.13).[65,103,104] Efficient tunable upconversion emissions in $NaGdF_4$:

Tm/Yb@$NaGdF_4$: Ln core-shell nanoparticles were realized through Gd sublattice mediated energy migration. The phenomenon of EMU is essentially a type of energy transfer UC process. It brings forward a solution for enhancing the efficiency of UC emissions from activators without proper intermediate energy levels, and build a bridge between sensitized ions and the activated ions of mismatch energy states. In the process of EMU, several types of lanthanide dopants are incorporated into separate layers in the core-shell structure nanomaterials. Sensitizer ions absorb NIR excitation photons and the higher excited state of the accumulator is populated via an ETU process from sensitizer. Some of the accumulator ions at high-lying excited state do not generate radiation relaxation via their transition but migrates energy through the accumulator to the migrator. The migrator ions conduct the random energy hopping throughout the core-shell interface, resulting in a radiation transition that produces upconverted luminescence by new activators. The rational core-shell structure and arrangement are necessary to minimize luminescence quenching and facilitate the energy transfer at the core-shell interface to generate an efficient EMU process.

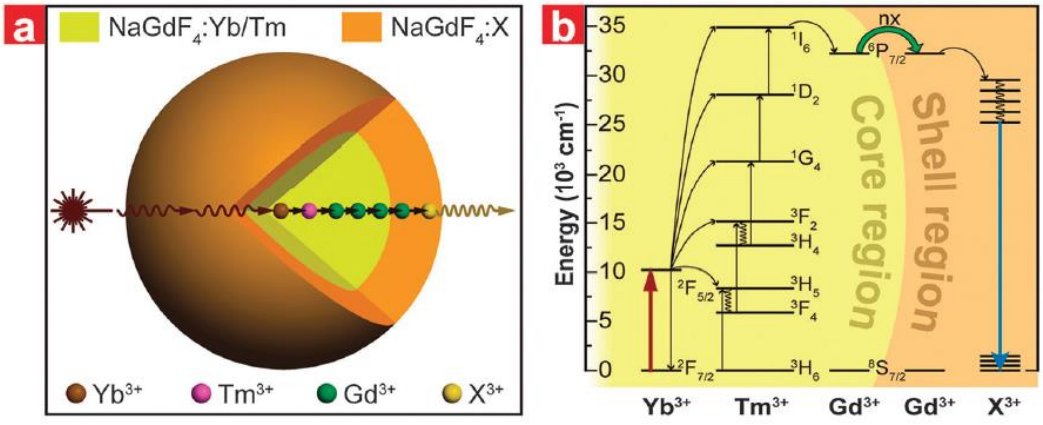

Figure. 1.13 The EMU process in core-shell-shell $NaGdF_4$ nanoparticles.[65]

In the past, great efforts were made to measure and evaluate the efficiency of energy transfer pathways.[105,106] In studies by Auzel et al., the quantum efficiency of the ETU process was found to be two or three orders of magnitude higher than those of the ESA and CET processes. ETU is a universal process in the multi-doped upconversion system. To some extent, EMU is an extension of ETU benefits from the development of the core-shell synthetic technique. The

lanthanide ions with distinctive energy levels were introduced into separate layers. Photon upconversion in core-shell nanoparticles opens up a new door for regulating dopant interactions. Furthermore, in core-shell nanoparticles, incompatible dopant ions can be spatially confined in separate layers to eliminate the quenching effect caused by short-range cross-relaxation between ions. Moreover, a long-range energy migration process from the outside layer to the inner core could be further harnessed to manipulate the photon dynamic route.

1.2.3 Core-shell structure strategy of UCNPs

The development and optimization of facile synthesis strategies for lanthanides-doped luminescent UCNPs with narrow size distribution and controlled crystalline phases, shapes and sizes are crucial to tailoring their physicochemical properties and exploring their potential bioapplications in diverse fields. Hitherto, a large variety of chemical synthetic techniques, including hydro(solve)thermal synthesis, high-temperature coprecipitation, thermal decomposition, sol-gel procedure, ionic liquid-based synthesis, and microwave-assisted synthesis have been demonstrated to synthesize high-quality UCNPs with controllable structures, sizes, and shapes (Table 1).[107–111] This is the precondition for the synthesis of high-quality and multifunctional core-shell UCNPs of various compositions.

Table 1 Typical synthetic strategies to lanthanide-doped upconversion nanocrystals.

Synthesis strategy	Host	Advantages & Disadvantages
Hydro(solvo)thermal synthesis	Na(Y, Gd, Yb, Lu)F_4, $LiYF_4$, $La_2(MoO_4)_3$, (La, Y)$_2O_3$, (La, Y, Gd, Lu)F_3, Ba(Y, Gd)F_5, BaY_2F_5, Ba_2GdF_7, (Ca, Sr)F_2, Sr_2ScF_7, (Y, Yb)PO_4, $Y_3Al_5O_{12}$, MnF_2, $KMnF_3$, $GdVO_4$, $PbTiO_3$, $KNbO_3$, Gd_2O_2S, *etc.*	Formation of highly crystalline phases at much lower temperature. Excellent control over particle size and shape. Specialized autoclaves required. Impossibility of observing the crystal as it grows.
Coprecipitation	Na(La, Y, Gd, Yb, Lu, Sc, Tb)F_4, (La, Y, Gd, Lu)F_3, Li(Y, Gd, Yb, Lu)F_4, (Ca, Sr)F_2, $BaYF_5$, GdOF, (La, Y, Yb, Lu)PO_4, ZrO_2, Y_2O_2S, ZnO, $Gd_4O_3F_6$, $CaMoO_4$, $Y_3Al_5O_{12}$, Y_4MoO_9, $Y_2(MoO_4)_3$, $Gd_2(WO_4)_3$, $Gd_3Ga_5O_{12}$, $BaTiO_3$, Y_2SiO_5, *etc.*	Simple and rapid preparation. Fast growth rate. Easy control of particle size and composition. Low product yield. Particle aggregation. Post-heat treatment typically need.
Thermal decomposition	LaF_3, Na(Y, Gd, Yb, Lu)F_4, Li(Y, Lu)F_4, (La, Y, Tb, Ho, Er, Tm, Yb, Lu)$_2O_3$, Ba(Y, Gd, Lu)F_5, CaF_2, $BaTiO_3$, YOF, (La, Gd)OL, *etc.*	High quality, monodisperse nanocrystals. Rigorous and harsh synthesis condition. Hydrophobic resultants. Toxic by-products.
Sol-gel	(La, Y)F_3, CaF_2, LaOF, (Y, Gd)$_2O_3$, TiO_2, ZnO, Ta_2O_5, GeO_2, Al_2O_3, $BaTiO_3$, LaPO4, (Gd, Lu)$_3Ga_5O_{12}$, YVO_4, ZrO_2, Y_2SiO_5, $Y_2Ti_2O_7$, $BaGd_2(MoO_4)_4$, $CaGd_2(WO_4)_4$, *etc.*	Simple and cost-effective accessories. Versatile. Better homogeneity. Less energy consumption. Cost of precursors. High-temperature post-heat treatment required.
Ionic liquid-based synthesis	Na(Y, Gd, Yb)F_4, (La, Y)F_3, CaF_2, $BaMgF_4$, *etc.*	Easy processing. Low solvent toxicity. Ratively expensive. Poorly biodegradable.
Microwave-assisted synthesis	(La, Gd)F_3, Na(Y, Gd)F_4, CaF_2, $BaYF_5$, $LaPO_4$, (Ca, Sr, Ba)MoO_4, Ca(La, Gd)$_2(MoO_4)_4$, $NaLa(MoO_4)_2$, $NaY(WO_4)_2$, $SrY_2(MoO_4)_4$, *etc.*	Uniform heating. Rapid synthesis. Higher product yields. Specialized microwave reactor required.

When lanthanide ions are embedded in the lattice of a crystalline solid, a series of electronic transition processes within complex energy levels of lanthanide ions occur successively. The UC efficiency of nanoparticles is usually lower than that of the corresponding bulk materials. Lanthanide dopants are exposed to surface quenching due to the large surface-to-volume ratio. In conventional core-only UCNPs, the dopant ions are homogeneously distributed in the host lattice, which is accessible to surface quenchers. The presence of surface impurities, solvents and surface ligands with high-energy vibrational modes such as OH or NH_2 groups can quench the energy of the excited states through multi-photon relaxation processes.[112,113] Therefore, more recent studies on UCNPs are focused predominantly on core-shell nanoparticles comprising spatially-confined lanthanide dopants. This is similar to the bandgap engineering of semiconducting core-shell quantum dots, in which the excitons stay away from quenching surface traps by coating a high-bandgap shell.[114,115] Epitaxial shells can be grown using a similar chemical procedure for core nanoparticle synthesis, excluding the notion that precursors grow directly on the surface of preformed seed nanoparticles without the nucleation process.[116] The universal core-shell synthesis approaches can be classified as the heat-up and hot-injection method.

In a typical heat-up procedure, the core and shell layers are prepared separately using a sequence of independent syntheses. The notion of the heat-up method to produce core-shell nanocrystals was first reported in 2007 by Yan et al.[117] In 2008, the heat-up method was then refined by Qian and Zhang through the use of synthesized uniform $NaYF_4$: Yb/Tm@$NaYF_4$: Yb/Er core-shell UCNPs with tunable UC emissions.[118] The as-synthesized core nanoparticles were first synthesized and extracted, and then transferred to a fresh reaction pot to mediate the growth of the shell layer following an identical protocol for the core synthesis (Figure. 1.14). In a study by Zhang et al., it was found precise control over the thin shell thickness in heat-up synthesis was readily achieved by adjusting the mass ratio of the shell precursor to the core in the nanoparticles.[119,120] This method was further extended to produce diverse shell material combinations, such as $NaGdF_4$ and KYF_4.[103,121–123] However, for multi-shell nanostructure synthesis, the core and shell layers have to successively be grown by a sequence of independent

syntheses. Precisely repeating the synthetic protocol is potentially laborious, along with the complicated separation and washing steps associated with multiple reactions. This approach also contains several limitations such as independent nucleation and anisotropic shell growth.

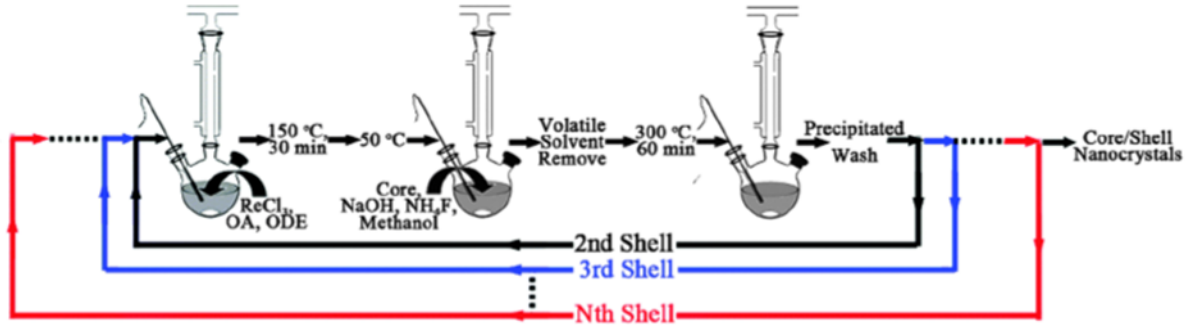

Figure. 1.14 Schematic depiction of heating-up method.[116]

The hot-injection procedure was originally developed to fabricate semiconductor core-shell quantum dots. In a study by Yi and Chow in 2007, the notion of separating the core and shell growth processes to synthesize $NaYF_4$:Yb/Er@$NaYF_4$ core-shell nanoparticles was first reported.[124] In their thermal decomposition synthesis, the core of $NaYF_4$:Yb/Er was first prepared by heating it in OM at 340 °C for 30 minutes. Subsequently, an OM solution comprising shell precursors was injected into the reaction for the epitaxial deposition of the inert $NaYF_4$ shell layer. Next, the monodisperse $NaYF_4$:Yb/Tm@$NaYF_4$ core-shell UCNPs with an average diameter of 11.1 nm were prepared. They also investigated the effect of inactive $NaYF_4$ shell coating, which shows a significant approximate 30-fold enhancement in upconversion luminescence with the addition of the shell. In follow-up studies, this method was further extended in studies by van Veggel, Capobianco, and Prasad et al. to produce diverse core-shell material combinations, including $NaYbF_4$@CaF_2 and $NaGdF_4$@$NaGdF_4$ et al.[125–127]

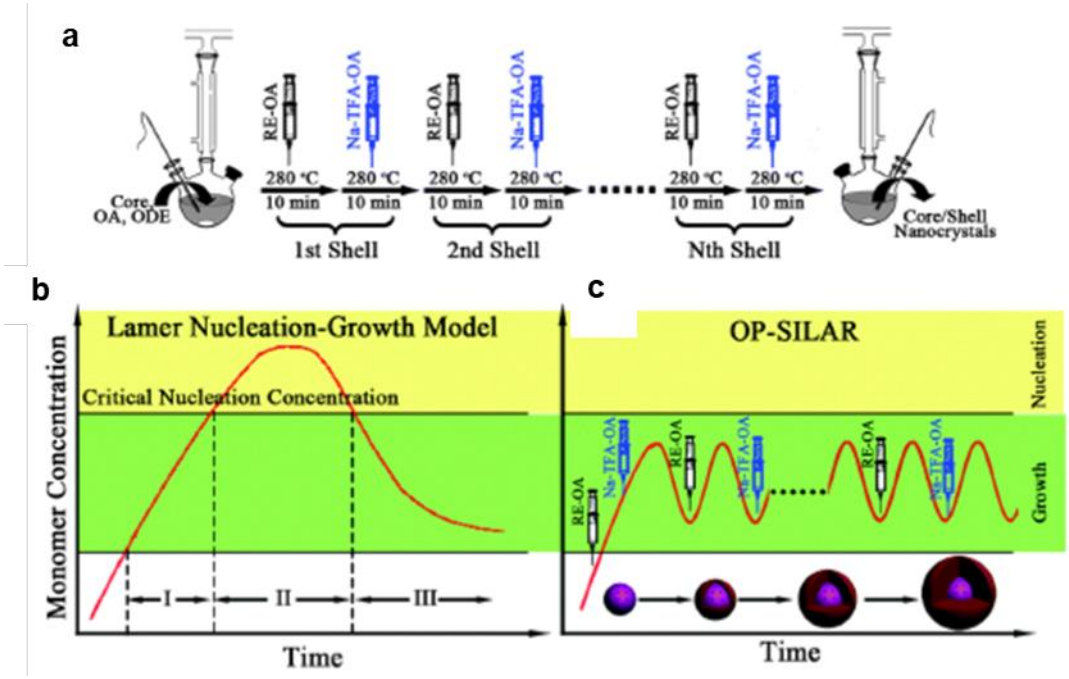

Figure 1.15 (a) Schematic depictions of the successive layer-by-layer method. (b,c) Schematic illustration of the LaMer plot and the successive layer-by-layer method for core@shell synthesis.[128]

Compared with the heat-up strategy, a distinct advantage of the hot-injection strategy is that the one-pot synthesis of multi-shell nanostructures is achieved through the successive injection of a sequence of shell precursors at high temperature (Figure 1.15a). The shell thickness can also precisely be controlled by manipulating the injection dosage of the shell precursors. In one remarkable development, a one-pot method for the successive layer-by-layer growth method was reported by Zhang et al. in 2013 (Figure. 1.15b).[128] In this method, the relatively low monomer concentration was maintained through control of the inject dosage without spontaneous nucleation, which tends to form uniform coating layers through a successive ion layer adsorption reaction. The layer-by-layer deposition is capable of generating higher emission intensity and a longer lifetime in core-shell nanocrystals compared with the one-step shell coating method. Van Veggel et al. proposed injecting small sacrificial nanoparticles as shell precursors based on the common physical phenomenon of Ostwald ripening (i.e. self-focusing by Ostwald ripening) to perform layer-by-layer shell growth on the surface of core nanoparticles.[129] The multi-shell nanoparticles were superficially synthesized through the standard oleate route (Figure. 1.16).

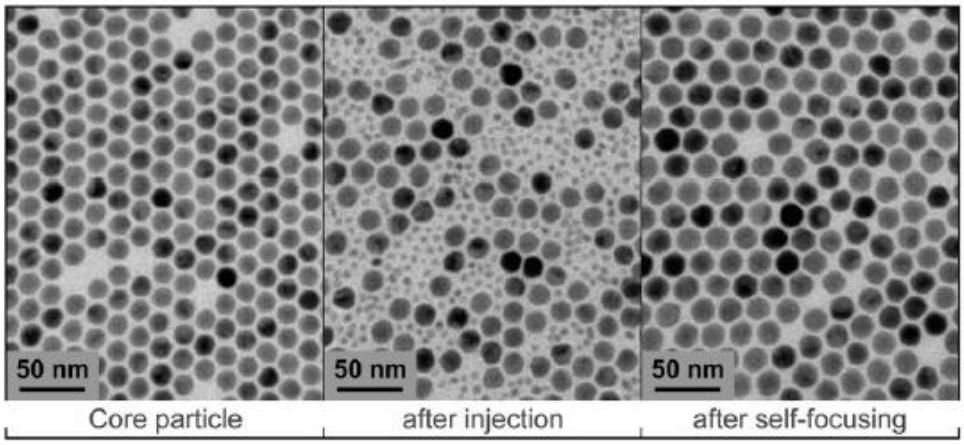

Figure. 1.16 Schematic TEM images of $NaYF_4$:Yb/Er core nanoparticles and the corresponding $NaYF_4$:Yb/Er@$NaYF_4$ core-shell nanoparticles obtained via injection of small sacrificial nanoparticles.[111]

Several factors affect the hot-injection process to proceed: the shell precursor solution must be highly compatible with the host reaction, avoiding the homogeneous nucleation of the shell precursor and homogeneous multilayer growth of the precursor onto the core nanocrystals to yield uniform shell coatings. Moreover, lifetimes and quantum yields can be continuously tuned by shell thickness which can be exploited for lifetime multiplexing and encoding.[113]

Currently, several core-shell strategies (Figure. 1.17) have proven effective in suppressing the surface-induced quenching of excitation energy and efficient in enhancing upconversion luminescence (i.e., amorphous shell coating, inert shell coating, active shell coating, and heterogenous core-shell structures).[130–134] Typically, simple core-inert shell heterostructures exhibit substantially enhance luminescence intensities. Moreover, the optical active-shell structure is also frequently employed to impart multiple functionalities to UCNPs. For example, it allows for the flexible control of the local doping concentration and distribution of dopant ions in UCNPs, minimizing deleterious cross-relaxation and concentration quenching. Furthermore, it allows for the construction of novel UCNPs by precisely tailoring the upconversion dynamics of energy migration in core-shell nanostructures.

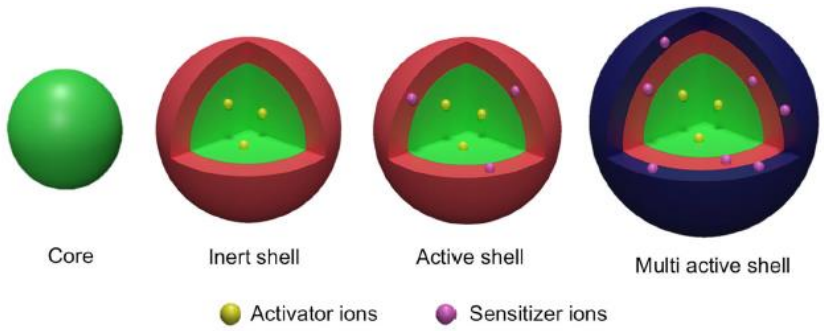

Figure. 1.17 Schematic illustration of various core-shell structures to amplify upconverting efficiency.[110]

1.2.4 Excitation wavelength design in core-shell UCNPs

The dually doped or multi-doped system (especially in core-shell structure) exhibits noticeable advantages in the achievement of high upconversion efficiency through energy transfer upconversion. It enables the fine tailoring of various upconversion properties, including the emission wavelength, intensity, power-dependent intensity and lifetime. The core-shell structure also establishes an effective separation of function between dopants. The excitation absorption can not only be sensitized by Yb^{3+} at 980 nm but also sensitized by other lanthanides such as Nd^{3+}, with high absorption cross-sections at 800 nm excitation wavelengths. This breaks the restriction and increases the flexibility toward manipulating the excitation wavelength.

The conventional UCNPs system is sensitized by trivalent Yb^{3+} ions, which exhibit an extremely simple $^2F_{7/2}$ - $^2F_{5/2}$ transition at the 4f-energy level and narrowband absorption band located at 980 nm.[135–140] Additionally, Yb^{3+} ions reveals the large absorption cross-section (ca. 1.3×10^{-20} cm^2 at 980 nm)[141]. In the Yb^{3+} sensitized core-inert shell system, the concentration of the Yb^{3+} ions can be dramatically increased to boost UCNP brightness as Yb^{3+} ions have simple energy levels and small concentration-dependent quenching.[142–144] The high efficiency of upconversion emission was achieved via high Yb^{3+} doping concentration in $NaGdF_4$ core-inert shell nanoparticles.[145] Furthermore, by varying the NIR excitation power density, the reversible dynamic red, green and blue reflections in a single thin film were demonstrated. Through confined energy migration, Wang and coworkers[146] illustrated the efficiency

associated with a five-photon upconverted UV emission of Tm^{3+} in core-shell nanoparticles without concentration quenching (Figure. 1.18). Notably, when the Yb^{3+} concentration was increased to 99 mol%, a 45-fold luminescent increment at ~290 nm was observed. The spontaneous upconversion emission provides sufficient gain in a micron-sized cavity, where nanoparticles as gain media are capable of generating stimulated lasing emissions in a deep-ultraviolet (approximately 311 nm) wavelength.

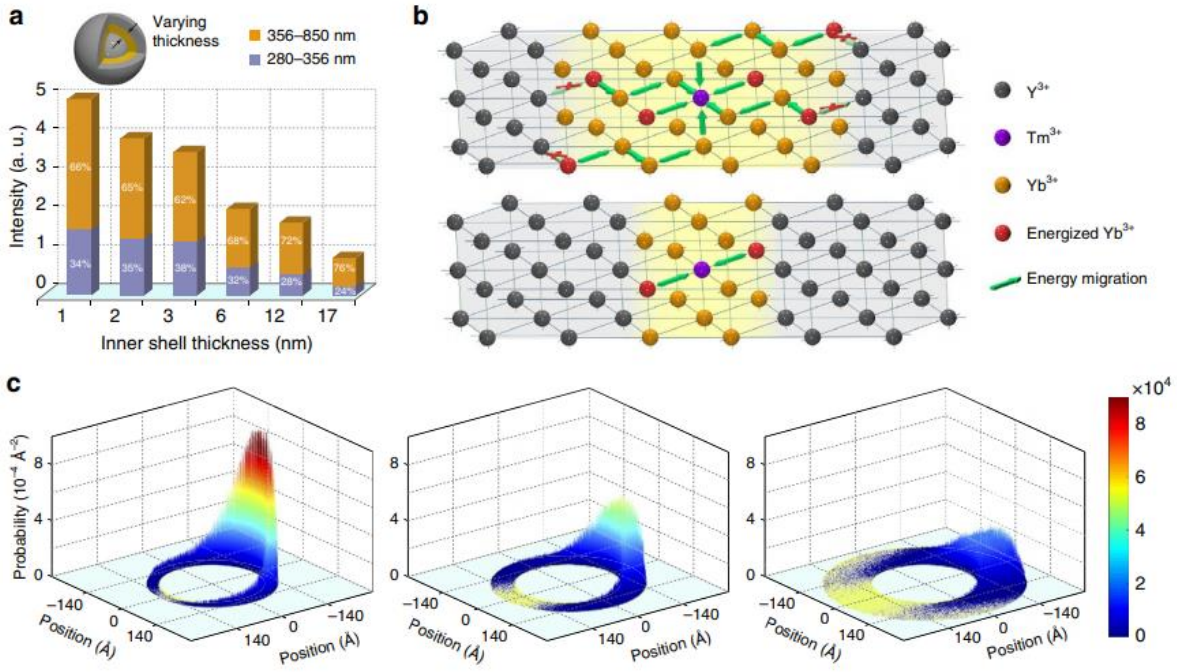

Figure. 1.18 Effect of inner shell thickness on upconversion.[146]

The concentration of activators has also been improved. For example, Almutairi et al. prepared a series of $NaYF_4$:x%Er^{3+}@$NaLuF_4$ nanocrystals after epitaxial shell growth, clearly showing a high brightness at high-doping concentrations of Er^{3+} (Figure. 1.19). When the concentrations of Er^{3+} were increased to 100 mol% in $NaErF_4$/$NaLuF_4$ core/shell nanocrystals, the emission intensities of both upconversion and downshifted luminescence were found to be the highest with negligible concentration quenching effects.[147] Furthermore, various core-inert shell materials have been constructed based on a similar strategy and these have shown success in terms of enhancing emission intensity.[148–151]

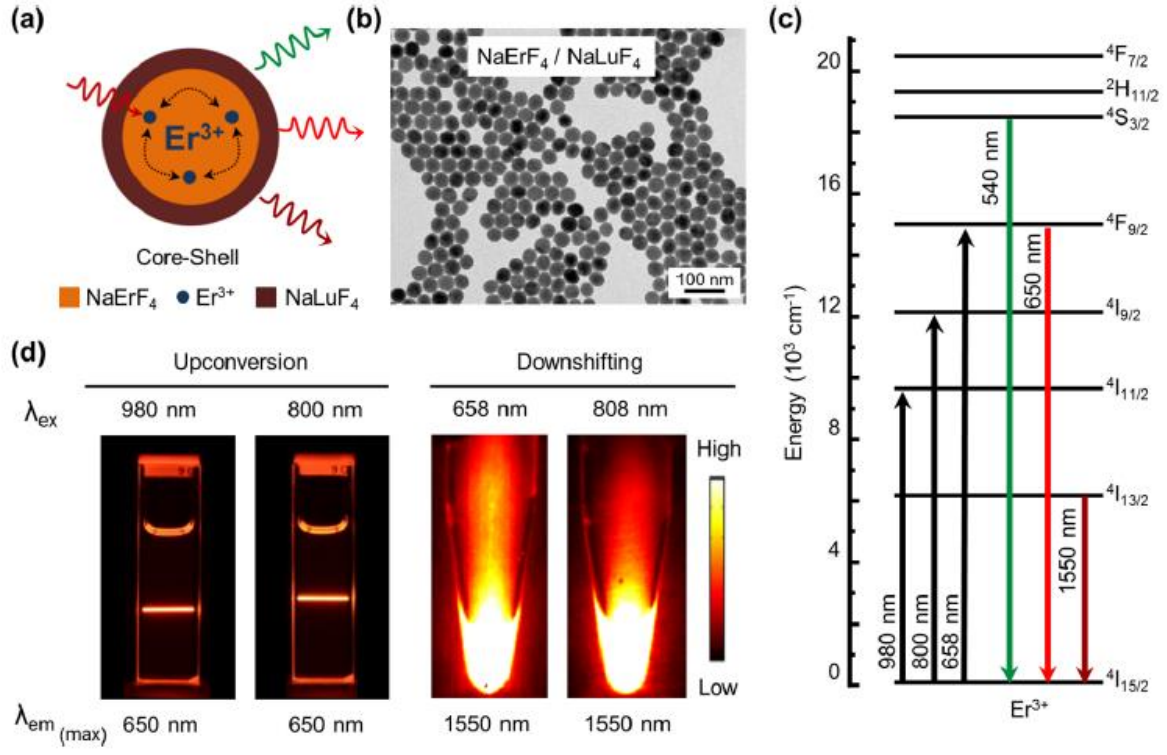

Figure. 1.19 Schematic illustration of the $NaYF_4$:x%Er^{3+}@$NaLuF_4$ core-shell nanocrystals structural composition.[147]

Coating an active shell over nanoparticles has recently been designed to enhance upconversion efficiency. Compared with inert-shell coating, the difference in this strategy is that such shell coating can be incorporated with sensitizer Yb^{3+} ions to increase the possibility that excitation photons can be absorbed and energy transfer facilitated to the core. However, the amount of Yb^{3+} in active shell needs to be optimized because the Yb^{3+} can also provide a route to transfer the absorbed excitation energy to the surface quenching centers, in turn weakening upconversion emission. Additionally, various core-active shell materials were constructed, and these were found to significantly enhance emission intensity.[118,152–159]

Despite the progress is gratifying in Yb^{3+} sensitized UC nanoparticles, the disadvantages bring certain limitations for UC nanoparticles under NIR excitation at 980 nm. The excitation wavelength of Yb^{3+}-sensitized UC nanoparticles overlaps with the strong absorption band of water molecules. The consequence is that the excitation of colloidal UCNPs in biosystems can cause severe damage due to overheating and the excitation photons suffer serious attenuation

when passing through bio-tissues. This is unsuitable for in vitro tissue culture as well as in vivo bioanalytical and biomedical applications.[160] In theory, the excitation wavelength can randomly be engineered by varying the dopants due to the abundant energy level structure of lanthanide. In recent years, the light mechanism and biological applications of different optical excitation wavelengths have been studied.[161–163] Strategies have been developed in the last five years to shift the 980 nm excitation wavelength to approximately 800 nm, where the laser light source encompasses the optical window (Figure 1.20) and the laser-induced tissue heating effect is minimized.[123,164–166]

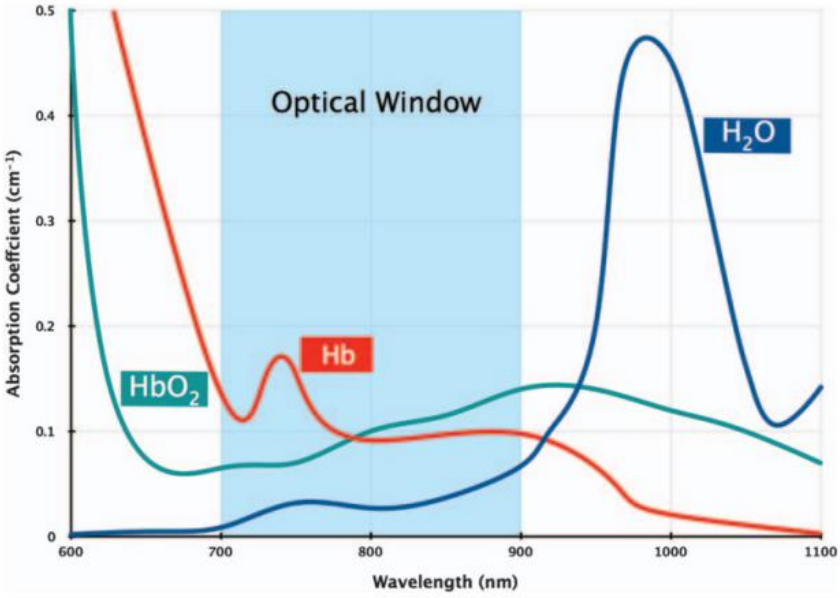

Figure. 1.20 Absorption spectra of major light absorbers in biological tissue.[167]

Thanks to the development of synthetic technique, Nd^{3+}-sensitized nanoparticles demonstrated the efficient UC emission intensity using core-shell nanostructures, which can spatially separate Nd^{3+} ions and emitter ions. In the core-shell structure, Nd^{3+}-doped UCNPs can co-doped with other lanthanide elements such as Yb^{3+} to convert the energy to activators under 808 nm excitation. The high quantum efficiency (up to 70%) between Nd^{3+} and Yb^{3+} ions also promises a comparable or stronger UC emission intensity compared with Yb^{3+}-sensitized UCNPs.[168,169]

The above mentioned facilitates energy transfer between Nd^{3+} and emitters in different types of matrices, and the energy transfer pathways of Nd^{3+}-Yb^{3+}-emitters together with minimizations in the quenching effect have been established. Li et al.[170] reported Yb-Er@Nd-Yb UCNPs with similar emission intensities under the same power density of a 980- and 808-nm laser, and dual-band visible and NIR emissions under single 808-nm excitation were obtained. Guo et al. spatially separated dopants and optimized Yb^{3+} /Nd^{3+} content to demonstrate enhanced UC emission under 808-nm excitation compared with 980-nm excitation.[171] Optimizing the doped concentration of ions is a key point in Nd^{3+}-sensitized UCNPs with variations in the configuration of nanoparticles. Tri-doped core-inert shell Nd^{3+}-sensitized UCNPs at 29 nm were first introduced by Han et al., while the doping ratio of Nd^{3+} ions was controlled below 1%.[172] High doped Nd^{3+} in core-shell Nd^{3+}-sensitized UCNPs were achieved by Liu et al. through co-doping Nd^{3+} (1%), Yb^{3+} and Tm^{3+}-Er^{3+}-Ho^{3+} in the core and then coating the active shell with 20% Nd^{3+} concentration (Figure 1.21).[173] Furthermore, Yan et al. designed a core-shell structure by adding a Yb^{3+}/Nd^{3+} co-doped shell onto the conventional Yb^{3+}-Er^{3+} doped core to separate Nd^{3+} ions and emitters, in turn demonstrating in-vivo imaging.[162] Yao et al. reported the design of a transition layer into the above core-shell structure to fabricate a quenching-shield sandwich structure. This sandwich structure was found to block quenching interactions between the Nd^{3+} ions and the activator on the core-shell interface, while also boosting UC emission to achieve a high doping concentration of up to 90% of Nd^{3+} ions in the outer layer (Figure 1.21).[174] Core-multi-shell structured $NaGdF_4$:Nd @ $NaYF_4$ @ $NaGdF_4$:Nd,Yb,Er @ $NaYF_4$ nanocrystals have also been well designed and synthesized to achieve dual-mode up/down-conversion luminescence upon the low heat effect of 800-nm excitation.[175]

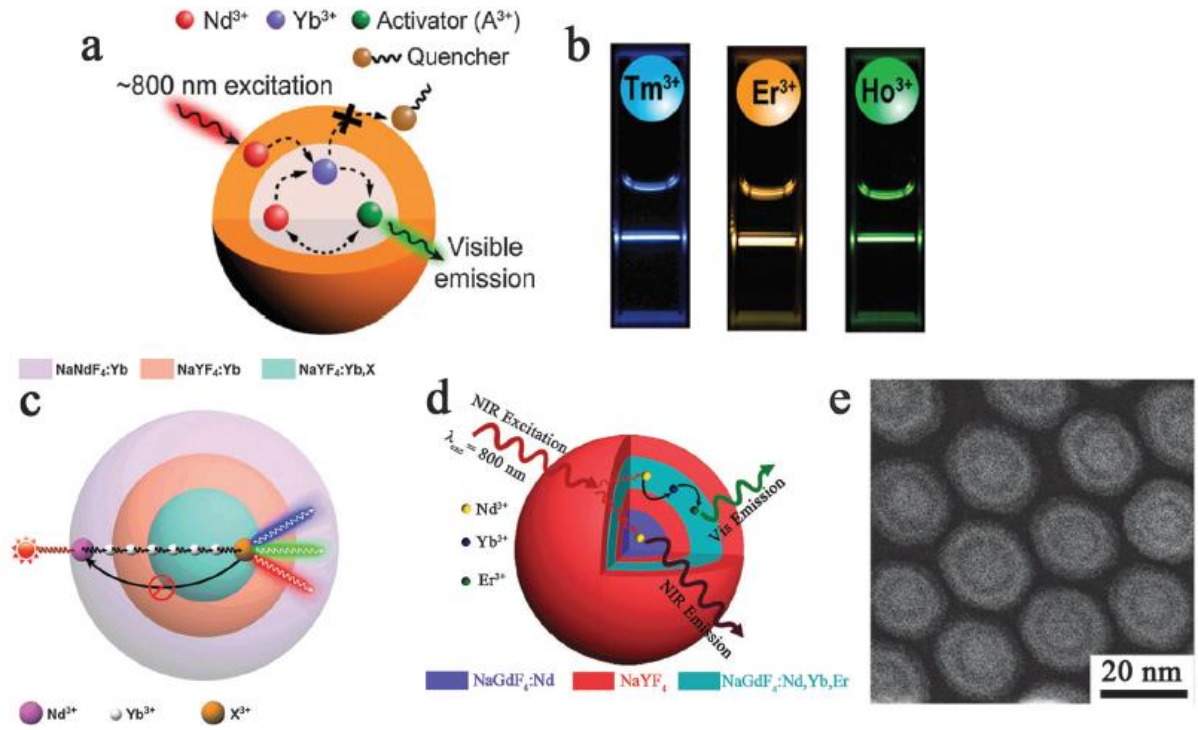

Figure. 1.21 (a, b) Schematic design and luminescence photographs of the $NaYF_4$:Yb,Nd, X@$NaYF_4$:Nd (X = Tm, Er, Ho) core-shell nanoparticles under 800 nm excitation.[173] (c) Schematic illustration of the proposed energy transfer mechanisms in the sandwich-structured UCNPs.[174] (d, e) General strategy to achieve the upconversion and downconversion dual-mode luminescence with multi-layer nanoparticles.[175]

An increasingly used concept to boost the molar absorption cross-section is combination with NIR organic dyes, which allow also increasing light absorption ability and tuning of the excitation wavelength. In general, surface bounded dye acting as antennas could harvest NIR light strongly and transfer their excitation energy to the activator to produce a bright luminescence through intermediate lanthanide sensitizers (Nd^{3+} or Yb^{3+}). Hummelen and co-workers first reported the broadband dye-sensitized upconversion luminescence via the sensitization from an IR-806 dye, which achieves a remarkable increase in luminescence intensity.[176] Some groups[177–179] introduced hybrid inorganic-organic systems consisting of epitaxial core-shell UCNPs and NIR dyes anchored shell nanocrystal surface, as shown in Figure 1.22. More importantly, in addition to the tailorable excitation bands of dye sensitizers through the rational design of their molecular structures can realize excitation-wavelength-

selective imaging and further expanded the sensitization region[179–182]. Despite implicit promising merits, current dye-sensitized upconversion systems still have some drawbacks. Photobleach with light exposure, the low photostability of dye antennas on the surface of the UCNPs is a challenge to practical applications of dye-sensitized upconversion nanosystems[183].

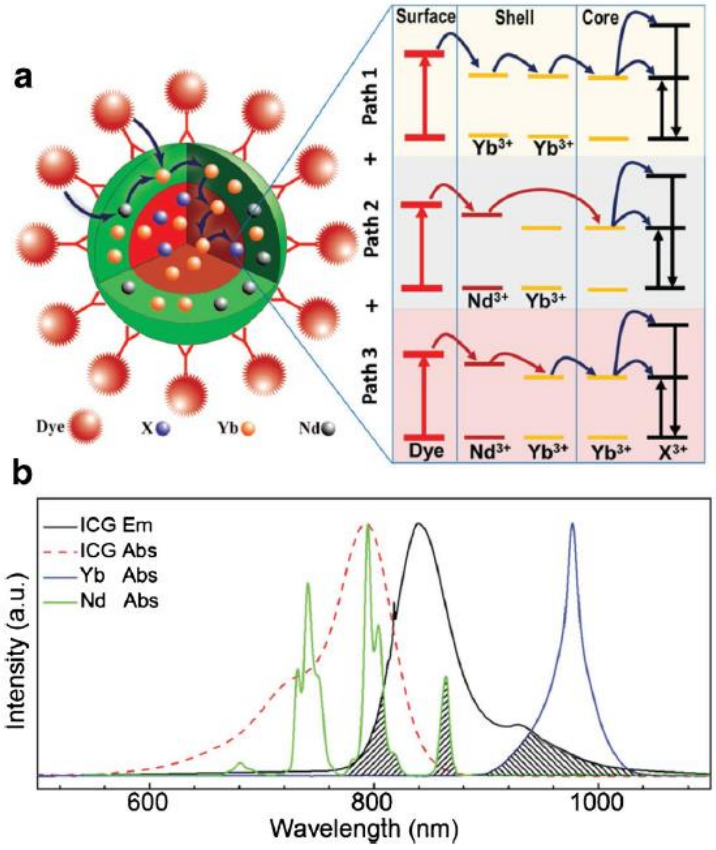

Figure 1.22 Multidimensional energy cascaded upconversion in dye-sensitized core-active-shell $NaYF_4:Yb^{3+}/X^{3+})@NaYF_4:Nd^{3+}/ Yb^{3+}$ nanocrystals.[184]

1.3 Optical parameters of UCNPs

The light-wave feature can be described using different dimensional parameters such as wavelength, intensity, polarization, and lifetime. When the incident light interacts with an object or material, one or more of these optical parameters can be altered. The variation of optical parameters can be used to reflect and record specific information in the materials, which can help with a thorough investigation of the optical mechanism, as well as turning the materials as 'information carriers'. Lanthanide-doped UCNPs, owning unique $[Xe]4f^N$

electronic configuration and ladder-like energy states, are a type of specific information carrier which enables anti-Stokes emission via the unique nonlinear optical process. Stepwise optical excitation, energy transfer, and various nonlinear and collective light-matter interaction processes act together to convert low-energy excitation photons into visible or ultraviolet regions.

1.3.1 Wavelength characteristics of UCNPs

Selective absorption or emission of light of a particular wavelength is a characteristic feature of luminescent materials. In UCNPs, when utilizing the abundant metastable-excited states with long lifetimes as the intermediate state (when the energy of the incident photons matches the gap between the two electronic states), electrons at the ground state can be excited into the higher electronic state, followed by a series of nonlinear upconversion processes. Hence, the wavelength of upconversion luminescence emission is characteristic of involved energy states and is therefore intrinsic to the materials. The most commonly used emitters are Er^{3+}, Tm^{3+} and Ho^{3+}, all of which have main upconversion emission bands ranging from the NIR region to the visible and UV regions[130,185–187] (as shown in Figure 1.23). In 2014, Liu et al. reported UC multicolour tuning in a single Er^{3+}, Tm^{3+} doped $NaYF_4$ microrod as an optical barcode through end-on growth, as well as dopant control for anticounterfeiting and multiplexed labeling applications (Figure 1.23b).[38] Liu et al. used Yb^{3+}-Er^{3+} and Yb^{3+}-Tm^{3+} doped UCNPs with different emission wavelengths to label mouth epidermal carcinoma cells, where they used the UCNPs for multicolour cancer cell labeling and achieved in-vivo cell tracking through UCL imaging.[188]

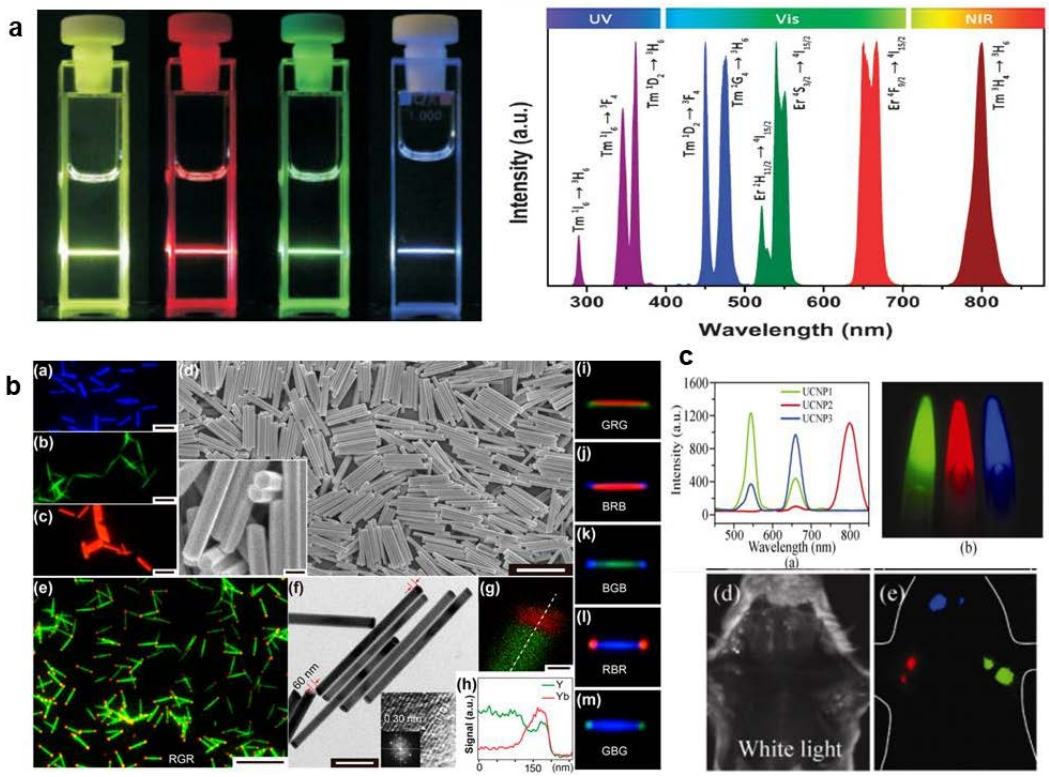

Figure 1.23 (a) Typical UC emissions from Yb^{3+}-$Er^{3+}$and Yb^{3+}-Tm^{3+}co-doped UCNPs under 980 nm excitation.[130] (b) UC multicolour tuning in a single $NaYF_4$ microrod through end-on growth and dopant control.[38] (c) In vivo multiplexed lymphangiography with three UCNPs[188]

1.3.2 Emission ratio characteristics of UCNPs

Fine-tuning the colour output and emission ratio of UCNPs is desirable for their applications in multicolour labeling and multiplexed bio-detection.[38,39,189] The structure, size, morphology, crystallinity, reaction time and temperature of UCNPs have a complex effect on UC emissions, which are fundamental strategies for tuning their intensity ratio.[190–195] Compared with the control over these strategies, the tuning of dopant combinations and core-shell structure design is a more effective and general strategy to manipulate the colour output of UC emissions.[196–202] Liu and Wang obtained multicolour UC emissions ranging from the visible to NIR regions in Yb/Er and/or Yb/Tm co-doped $NaYF_4$ UCNPs through precise control over dopant combinations as well as their concentrations (Figure 1.24a).[203] Chan combined rate constants with experimental syntheses of hundreds of lanthanide dopant combinations to demonstrate the spectral purity and emission intensity of doubly and triply doped $NaYF_4$ nanoparticles.[204,205]

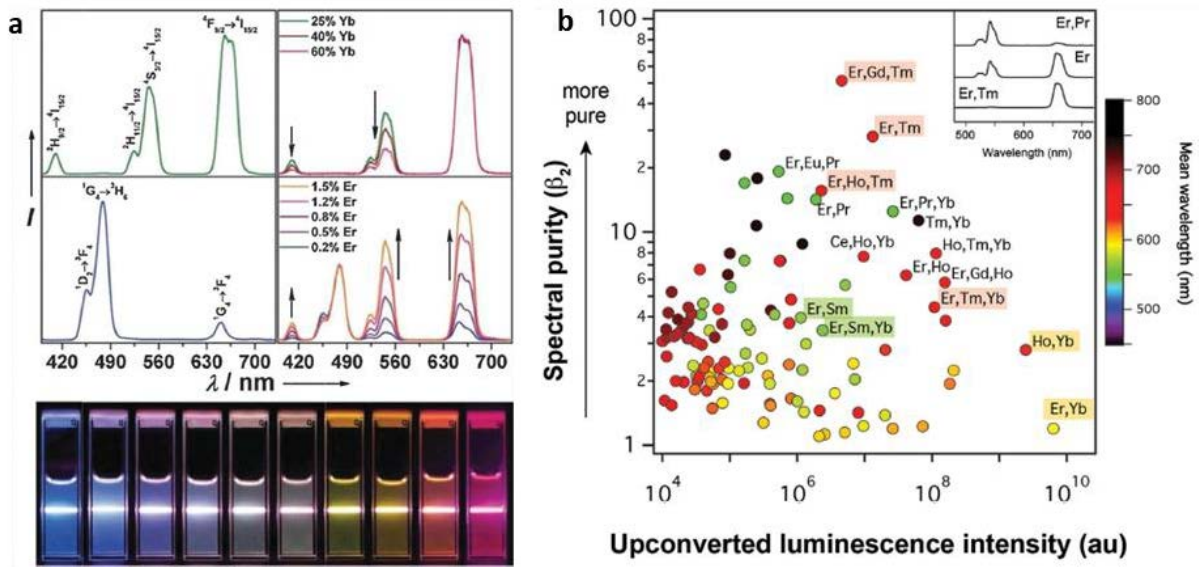

Figure 1.24 (a) UC multicolour tuning through the control over dopant concentrations in $NaYF_4$:Yb/Er/Tm UCNPs.[203] (b) Tuning energy transfer, emission intensity, and spectral purity via combinatorial screening of triply doped UCNPs.[204]

Additionally, Zhang et al. designed the sandwich core-shell structure by adjusting Er^{3+} and Tm^{3+} concentrations in different shells and shell thicknesses to fine-tune the intensity ratio of UC emission wavelengths (Figure 1.25 a).[206] Liu et al. designed the binary upconversion colours with the long-lived Mn^{2+} upconversion emission and the relatively short-living lanthanide upconversion emission in a particulate platform, which allows the generation of binary temporal codes for efficient data encoding under 980 and 808 nm irradiation. The as-prepared Mn^{2+}-doped nanoparticles have been found to be useful for multilevel anti-counterfeiting with high-throughput rate of authentication (Figure 1.25 b).[207]

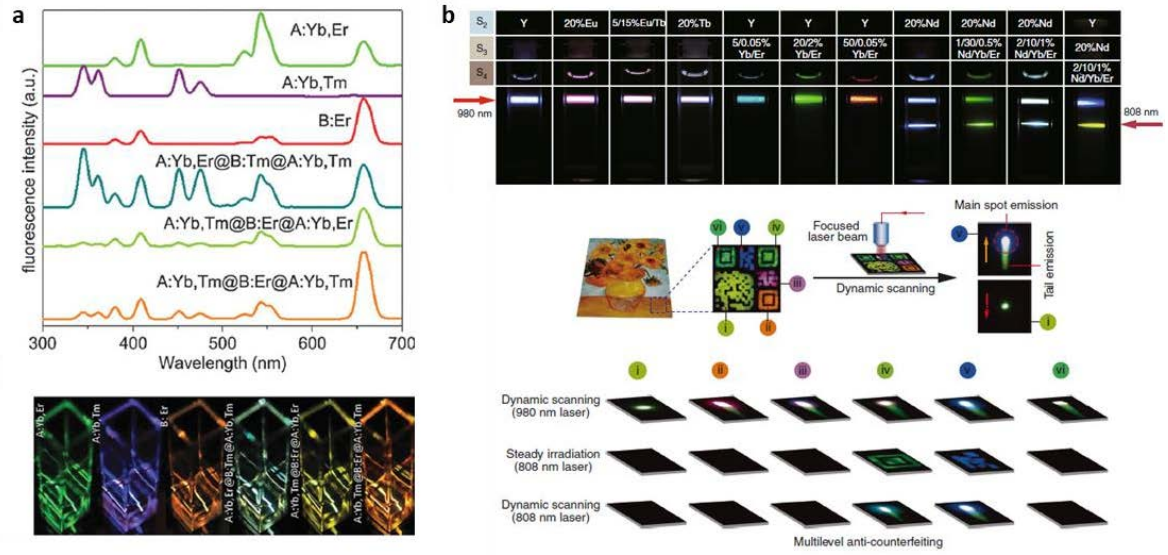

Figure 1.25 (a) Upconversion spectra and optical images of multicolour UCNPs based on doping different emitters (Er^{3+} and Tm^{3+}) into each of the shell layers.[206] (b) Luminescence photographs showing the multicolour tuning of the steady upconversion of nanoparticles under excitation at 980/808 nm. Multilevel anti-counterfeiting application with Mn^{2+}-activated core-shell nanoparticles.[207]

In 2015, Deng et al. demonstrated a strategy for dynamically fine-tuning upconversion emission in the full-colour range by manipulating the energy transfer upconversion at the non-steady-state (Figure 1.26a).[71] The blue emission band appeared from Tm^{3+} ions when a 808-nm CW laser was used. In the case of 980-nm pulsed laser excitation, adjusted from 200 μs to 6 ms, the emission colour was dynamically modulated as a result of the changing intensity ratio of the red-to-green emission from a Yb^{3+}-Ho^{3+}-Ce^{3+} triply doped system. These findings provide a new opportunity for precisely controlling upconversion emission in a wide range of applications such as volumetric display, multiplexed sensing, and anti-counterfeiting. Zhang et al. reported UC emission with a wide range of colours in the core-shell nanostructure under different excitation power densities (Figure 1.26b).[208] Accordingly, the emission colours can be tuned by changing the excitation power density, which manipulates the photon transfer pathways within the lanthanide ions.

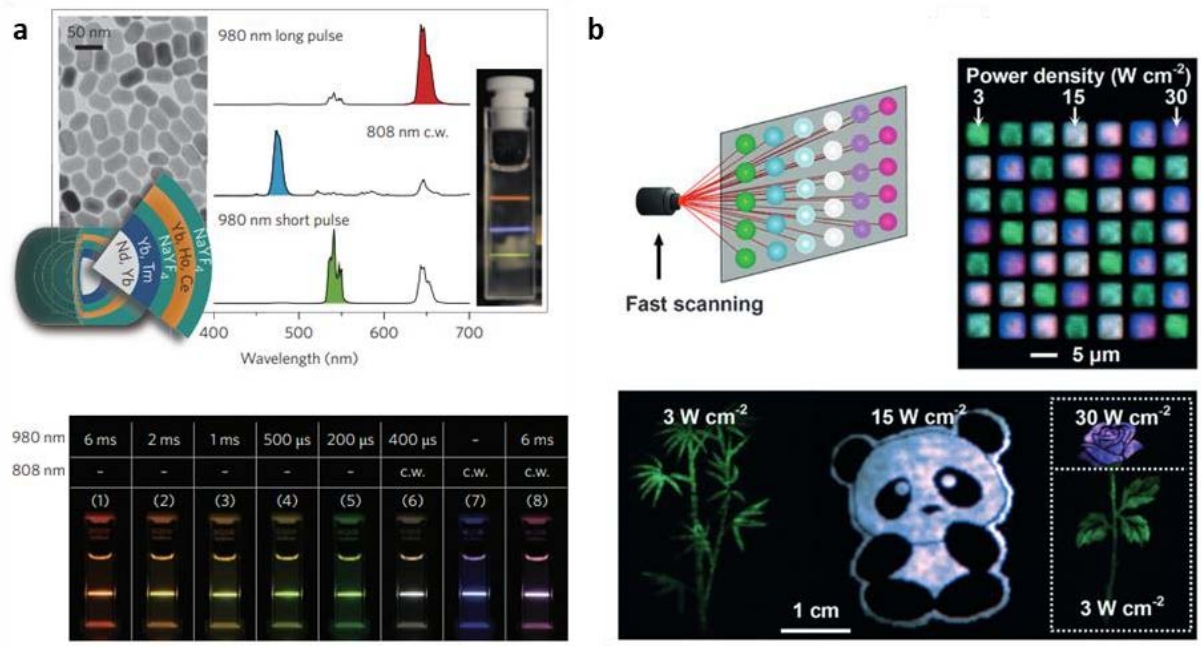

Figure 1.26 (a) Design of $NaYF_4$-based core-shell nanocrystals capable of emitting tunable colours when irradiated with NIR lasers.[71] (b) Emission with a wide range of colours under different excitation power density.[208]

1.3.3 Polarization characteristics of UCNPs

The polarized spectroscopy of a single crystalline material has often been changed with different crystallographic orientations. The polarization behavior of luminescence from anisotropic crystals has attracted substantial attention in the semiconductor system and lanthanide-doped inorganic dielectric UCNPs.[209–215] In 2013, Qiu et al demonstrated this polarized upconversion behavior along with a sharp energy-level split as well as singlet-to-triplet transitions from a single Tm^{3+}-Yb^{3+} ion couple-activated hexagonal-phase $NaYF_4$ microrod.[216] The multiple, discrete fluorescence-intensity periodic variations were polarized, and different transitions exhibited the same polarization dependence (Figure 1.27a). The surrounding environment of lanthanides can be affected by polarization, lowering the symmetry of the lattice and affecting the transition orientation of the intra-ions, which can enhance 4f-4f transition probabilities. To explore the origin of polarization anisotropy, similar observations have been reported in $NaYF_4$: Yb^{3+}, Er^{3+} nanodisks after considering the interplay between the azimuth of laser polarization and the crystallography axis (Figure 1.27b).[217] The

researchers discovered the luminescence intensity changed periodically with a sinusoidal shape when a linearly polarized laser beam was focused onto nanodisks side-up, while the emission intensity was independent of the polarization angle in the case of the face-up form. Based on the strong polarization-dependent upconverted luminescence of UCNPs, Daniel et al. demonstrated the three-dimensional orientation of optically manipulated $NaYF_4:Er^{3+},Yb^{3+}$ upconverting nanorods at a 140-nm of diameter and 1100-nm of length (Figure 1.27c).[218] Accordingly, it is possible to determine a three-dimensional orientation of UCNPs in real-time as well as full spatial control over UCNR orientation when using the beam optical tweezers.

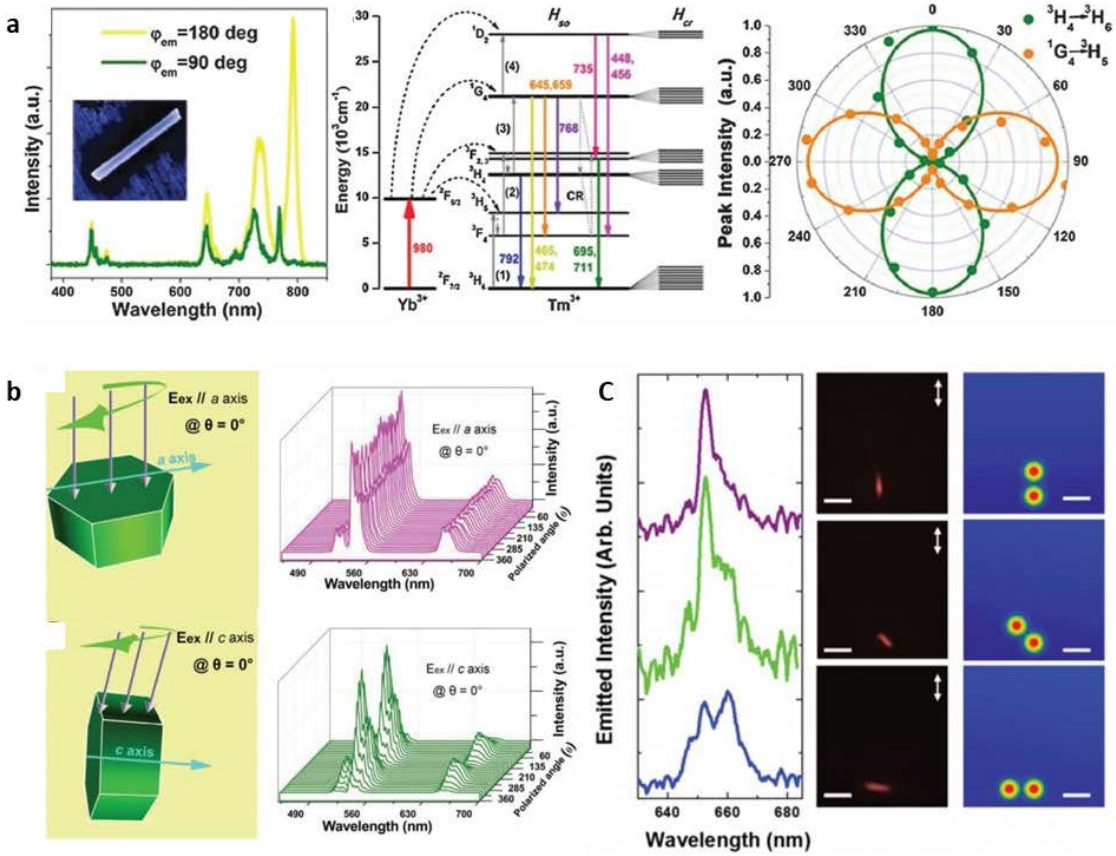

Figure 1.27 (a) Polarized upconversion emission of a single $NaYF_4:Yb^{3+}/Tm^{3+}$ microrod.[216] (b) Polarized upconversion emission of the $NaYF_4$: Yb^{3+}/Tm^{3+} nanodisk with its a-axis or c-axis parallel to the horizontal plane.[217] (c) Evolution of the emitted spectra when rotating the longitudinal axis of the $NaYF_4$: Er^{3+}, Yb^{3+} UCNPs.[218]

1.3.4 Lifetime characteristics of UCNPs

Because $4f^N$ - $4f^N$ electric dipole transitions are Laporte (parity) and prohibited in terms of by quantum mechanical selection rules and the filled shells of the larger 5s and 5p orbitals shield the 4f orbitals from external interactions, the excited states of upconverting lanthanide ions relax slowly to achieve long radiative lifetimes. Due to their long luminescence lifetimes, lanthanide-doped nanoparticles are widely used for high-sensitive biosensing and high-contrast bioimaging via time-resolved luminescence methodology to enhance the detection sensitivity and imaging resolution of fluorescence analysis.[219] The time-gated luminescence technique can be used to detect the luminescence intensity variation in the time domain. It consists of a pulsed excitation source to excite the long-lived UCNPs, a rotating mechanical chopper to block the excitation signals, and a detector to collect the long-lived signal from nanoparticles.[220,221] For biological applications, to avoid false results and improve the reliability of bio-detection, the simultaneous identification of multiple distinctive species is significant. The time-domain luminescence lifetime of UCNPs provides a new distinguishable dimension for the simultaneous detection of multiple species. Some groups have reported the ability to tune the lifetimes of UCNPs using different strategies, such as varied doped concentrations of lanthanides,[222] epitaxial growth of inert shells[223,224] and mediated energy migration in the core-shell structure.[207,225–228]

This concept was first proposed by Jin et al. to precisely tune the luminescence lifetimes in $NaYF_4$: Yb, Tm UCNPs (as shown in Figure 1.28 a, b).[222] By adjusting the doping concentration of Tm^{3+} (0.2-4%), varied luminescent lifetimes in the microsecond region were explored to code individual nanocrystals (named ‘‘τ-dots’’) based on the time-resolved confocal scanning system. The luminescence lifetimes observed in the blue emission band of Tm^{3+} generated more than ten nanocrystal populations with distinct lifetimes ranging from 25.6 μs to 662.4 μs. The long-lived lifetimes of nanoparticles are suitable for autofluorescence-free bioapplications, high-throughput cytometry quantification, high-density data storage, as well as security codes to combat counterfeiting through time-resolved measurements. Yan and co-workers designed core-shell structure nanoparticles consisting of two non-interfering regions

separated by an optically inert layer to simultaneously achieve emission colour and lifetime multiplexing in UCNPs (Figure 1.28 c, d).[228] The blue emission of Tm^{3+} in the core was excited under 980-nm laser excitation, and the green emission of Er^{3+} in the outer region was triggered by stimulation with both 808- and 980-nm lasers, which endowed the nanoparticles with different colours and luminescence lifetimes under different excitations. This will greatly expand the application of luminescent nanomaterials for optical multiplexing. Liu et al. fabricated the core-shell structure with long-lived Mn^{2+}-doped $NaGdF_4$, which served as the core, and short-lived Yb/Tm-doped $NaGdF_4$, which served as the first shell layer (Figure 1.28 e, f).[207] The luminescence lifetimes of UCNPs were adjusted by mediating the energy migration along the $Yb^{3+}\rightarrow Tm^{3+}\rightarrow Gd^{3+}\rightarrow Mn^{3+}$ pathway. The lifetime of Mn^{2+} at a broad emission (490–625 nm) was 39 ms, which was much longer than the lifetime of the blue emission of Tm^{3+} centered at 475 nm (0.6 ms).

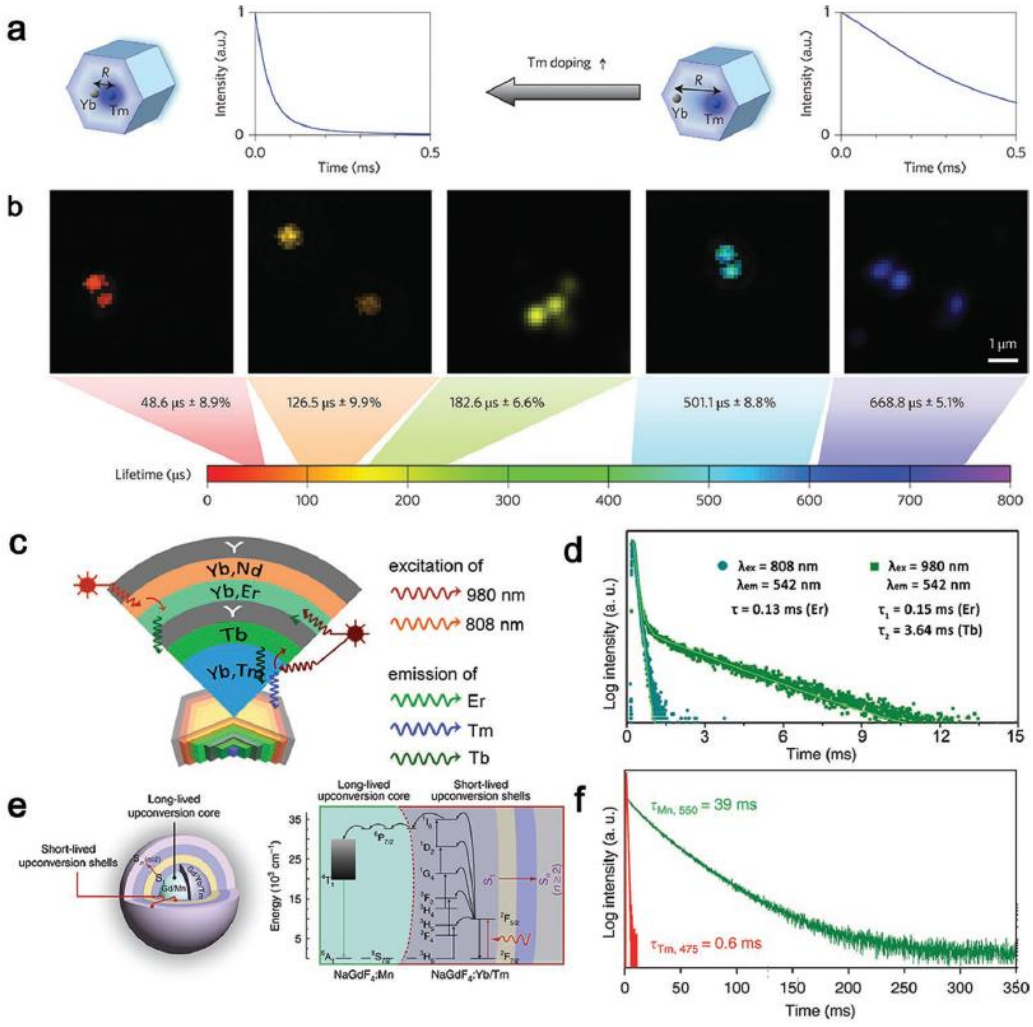

Figure 1.28 (a) (b) Time-resolved confocal images of $NaYF_4$: Yb, Tm nanocrystals doped with different concentrations of Tm^{3+}.[222] (c)(d) Decay curves of the multicompartment core/shell UCNPs under 808 and 980 nm excitation.[228] (e) (f) Energy transfer pathway and luminescence decay curves of multilayer UCNPs with long-lived Mn^{2+} luminescence.[207]

1.4 Challenges of luminescence materials for super-capacity optical multiplexing

1.4.1 Limitations for spectral multiplexing

Detecting a large number of molecules simultaneously has become increasingly important in a variety of fields. Wide varieties of luminescent materials as encoding materials have been developed in luminescence-based applications thus far (e.g., QDs). Furthermore, UCNPs can sequentially absorb two or more low-energy photons to give out visible luminescent emission, and plasmonic particles are attracting growing interest because of their unique properties. These materials have been employed for many applications such as the detection of biomolecules (e.g., nucleic acid, proteins), pathogen sensing, gene profiling, imaging, security, drug delivery, theranostics and environmental analysis.

Despite the progress that has been made to date, each type of luminescent material has certain limitations to encoding. Fluorescence is the most widely used dimension in the biotechnology and biomedical fields. However, there are still some challenges to be addressed for conventional fluorescent colour coding in biomedical applications, such as autofluorescence and spectral overlap. In many cases, fluorescent nano-barcodes have a limited number of barcodes, where about four different fluorescent colours can be detected simultaneously due to the spectral overlap of fluorescent encoding elements. Such a crosstalking problem can create challenges for the detection of spectral signals and create inaccuracies regarding quantifying different analytes in spectral multiplexing. Despite the outstanding strengths of UCNPs toward new-level biomedical applications, they are still hampered in terms of being ideal fluorescence bio-probes due to limited spectral multiplexing. Orthogonal encoding signals combining

multicolour emission and other optical dimensions, such as lifetime dimension, provide a good strategy for increased coding capacity.

1.4.2 Micro-sized information carriers

Various luminescence-based applications of luminescent materials are mostly based on micro-sized information carriers (e.g., dye/quantum dots/UCNPs-tagged or -loaded micro-beads), which display efficient binding and are easy to handle and detect. Generally, capture molecules which specifically bind to target analytes are immobilized in terms of corresponding unique micro-sized beads for decoding. Beads can have larger surface areas, which means more capture biomolecules can be immobilized on the bead.

However, the size of macroscopic carriers becomes a limiting factor for certain applications such as quantitative labeling and detection of biomolecules (e.g. DNA sequences, antibodies). Moreover, it difficult to achieve high-throughput optical multiplexing using micro-sized beads. In this regard, nanoscopic carriers are being utilized for various applications due to their advantages pertaining to the nanoscale dimension, including a large surface area to volume ratio, and unique physical and optical properties. The smaller size of nanoscopic carriers allows them to identify and quantitatively analyze smaller sized targets for use in imaging applications. However, unlike microbeads, the use of nanoscopic carriers for applications is challenging due to their smaller size, weak signal and complex decoding.

1.5 Thesis aims and outline

Luminescent nanomaterials have attracted considerable attention in luminescence-based applications—particularly for optical multiplexing due to their tunable wavelength properties. Despite researchers have developed various strategies for fine-tuning the multicolour luminescence of UCNPs over the past few years, there are still several challenges regarding the conventional fluorescent colour-coding in biomedical applications, such as limited encoding ability and false decoding because of spectral overlap. Moreover, the spectrum encoding in macroscopic carriers is unable to meet with bioanalysis in the nanoscale and

efficiently analyze the increase in information in the complicated analytes. For example, Cow's milk increasingly causes food allergies in childhood (~3%) because of the proteins and their mutation forms in the cow's milk that cause allergic reactions. These allergic symptoms and their potential links with milk proteins require a comprehensive understandings of the ingredients of milk and dairy products, as well as high-throughput monitoring of their variations for the quality controls of Australian dairy products. However, the complexity, analogy, and variability of the protein ingredients challenge our ability in accurate and rapid measurements of the trace amount of protein complex in milk. For these reasons, methods that allow high-throughput profiling and quantification of milk proteins are crucially needed for the quality controls of dairy products. Optical multiplexing brings the new capacity for multiplexed bioassays, as luminescent materials can carry information from multiple dimensions, such as colours, intensities, polarizations, and flash-rates (lifetimes). Through the use of different dimensions of light, it is possible to multiplex more optical signals into a single optical carrier. It allows simultaneous tracking of multiple targets, as well as assigns addressable molecular probes for multiplexed molecular and cellular sensing.

It is necessary to find additional optical coding dimensions in nanosized carriers to accurately decode new identities to realize super-capacity optical multiplexing. In this thesis, I utilize spectral and lifetime orthogonal multiplexing in single UCNPs to increase encoding capacity. Furthermore, I systematically investigate the nonlinear optical properties of Nd^{3+}-Yb^{3+}-Er^{3+}/Tm^{3+}-doped core-multi-shell nanoparticles under 808-nm excitation and Yb^{3+}-Tm^{3+}-doped core-shell nanoparticles under 976-nm excitation. After the pulse laser excitation, the duration for upconversion emissions can be extended significantly following the switching off of NIR excitation. This lifetime strategy creates a set of time-resolved emission profiles over a large dynamic range, which opens up new opportunities regarding nanoparticle carriers in the time domain as a new dimension for display, data storage, anti-counterfeiting, and high-throughput optical multiplexing.

Two groups of UCNPs, Yb^{3+}, Nd^{3+}, Er^{3+} core three-layer shell UCNPs and Yb^{3+}-Tm^{3+} core-inert shell UCNPs were prepared for this study, which can form a spectral and lifetime

orthogonal multiplexing under 808-nm and 976-nm excitation at the single nanoparticle level, respectively. I demonstrate a library of 16 kinds of single UCNPs with unique and tailored lifetime profiles that show significant potential for super-capacity multiplexing. By using the confocal microscope system to detect the optical fingerprints of single nanoparticles, it is possible to encode information carriers from the macroscopic level to the nanoscale. After the high-dimensional spectroscopy analysis of single nanoparticles, including the power-dependent lifetimes, emission spectra and lifetime, I further reveal the underpinning mechanism for a helix-shaped power-dependent evolution process under 976-nm and 808-nm excitation.

To achieve high-throughput multiplexing, the lifetime profiles are detected under a wide-field microscope system. Except for investigating the lifetime properties of single nanoparticles, I further implement deep-learning to decode the lifetime fingerprints of nanoparticles. By training the machine with ten batches of nanoparticle types, deep learning can intelligently define a territory for each type of nanoparticle, where an average accuracy of more than 90% was achieved. The implementation of the optical super-resolution microscopy technique through the use of time-resolved SIM allows the high-throughput decoding of these nanoscale super-multiplexed dots to be decodable beyond the diffraction limit. I also demonstrate the potential of single nanoparticles for DNA assay. The current study further suggests the future synthesis of other types of uniform nanoparticles with diverse and tunable optical signatures in multiple optical dimensions (e.g., spectrum, lifetime, and intensity) to expand super-capacity optical multiplexing. Assignments of these highly uniform and bright luminescent carriers with unique and distinguishable optical signatures will enable high-throughput biomolecular discoveries and data storage.

Upconversion nanoparticles (UCNPs) can sequentially absorb two or more low-energy photons to produce visible luminescent emissions. These unique emissions have tunable long luminescence lifetimes, are photostable, spectrally sharp, and can be fine-tuned by the controlled synthesis, which provides additional optical coding dimensions in nanosized

carriers. Key advantages of high dimensional fingerprints based multiplexed digital assay technologies include:

- Orthogonal encoding luminescent signals of UCNPs by combining excitation wavelength, emission colour, and lifetime profiles provide a good strategy for increased coding capacity.
- Unlocks the multiplexed digital assays of a number of analytes meets the needs of a wide variety of applications— a new solution for high throughput screening the multiple DNA/RNA strands from cancer and virus, as well as multiple proteins and other biomolecular biomarkers.
- Provide a new solution for screening/identifying multiple species of cellular biomolecules and pathogenic viruses.
- The machine learning approach can be implemented to extract the high dimensional signatures of single UCNPs and decode these fingerprints.
- The smaller size of nanoscopic UCNPs as carriers allows them to identify and quantitatively analyze single biomolecules and imaging applications.
- The super-capacity multiplexing of single biomolecules becomes possible.

1.6 Reference

(1) Wang, M.; Duong, B.; Fenniri, H.; Su, M. Nanomaterial-Based Barcodes. *Nanoscale* **2015**, *7* (26), 11240–11247.

(2) Gu, M.; Zhang, Q.; Lamon, S. Nanomaterials for Optical Data Storage. *Nature Reviews Materials*. 2016, p 16070.

(3) Pickering, J. W.; Martins, T. B.; Schroder, M. C.; Hill, H. R. Comparison of a Multiplex Flow Cytometric Assay with Enzyme-Linked Immunosorbent Assay for Quantitation of Antibodies to Tetanus, Diphtheria, and Haemophilus Influenzae Type B. *Clin. Diagn. Lab. Immunol.* **2002**, *9* (4), 872–876.

(4) Martins, T. B.; Burlingame, R.; Von Mühlen, C. A.; Jaskowski, T. D.; Litwin, C. M.; Hill, H. R. Evaluation of Multiplexed Fluorescent Microsphere Immunoassay for Detection of Autoantibodies to Nuclear Antigens. *Clin. Diagn. Lab. Immunol.* **2004**, *11* (6), 1054–1059.

(5) Wang, Y.; Jin, M.; Chen, G.; Cui, X.; Zhang, Y.; Li, M.; Liao, Y.; Zhang, X.; Qin, G.; Yan, F.; et al. Bio-Barcode Detection Technology and Its Research Applications: A Review. *J. Adv. Res.* **2019**, *20*, 23–32.

(6) Gorris, H. H.; Walt, D. R. Analytische Chemie Im Femtoliter. *Angew. Chemie* **2010**, *122* (23), 3970–3986.

(7) Jun, B. H.; Kang, H.; Lee, Y. S.; Jeong, D. H. Fluorescence-Based Multiplex Protein Detection Using Optically Encoded Microbeads. *Molecules* **2012**, *17* (3), 2474–2490.

(8) Wang, L.; Tan, W. Multicolour FRET Silica Nanoparticles by Single Wavelength Excitation. *Nano Lett.* **2006**, *6* (1), 84–88.

(9) Braeckmans, K.; De Smedt, S. C.; Roelant, C.; Leblans, M.; Pauwels, R.; Demeester, J. Encoding Microcarriers by Spatial Selective Photobleaching. *Nat. Mater.* **2003**, *2* (3), 169–174.

(10) Li, X.; Wang, T.; Zhang, J.; Zhu, D.; Zhang, X.; Ning, Y.; Zhang, H.; Yang, B. Controlled Fabrication of Fluorescent Barcode Nanorods. *ACS Nano* **2010**, *4* (8), 4350–4360.

(11) Zhou, W.; Li, D.; Xiong, C.; Yuan, R.; Xiang, Y. Multicolour-Encoded Reconfigurable DNA Nanostructures Enable Multiplexed Sensing of Intracellular MicroRNAs in Living Cells. *ACS Appl. Mater. Interfaces* **2016**, *8* (21), 13303–13308.

(12) Um, S. H.; Lee, J. B.; Kwon, S. Y.; Li, Y.; Luo, D. Dendrimer-like DNA-Based Fluorescence Nanobarcodes. *Nat. Protoc.* **2006**, *1* (2), 995–1000.

(13) Li, L.; Shen, L.; Zhang, X.; Shui, L.; Sui, B.; Zhang, X.; Zhao, X.; Jin, W. Multiplexed Optical Coding Nanobeads and Their Application in Single-Molecule Counting Analysis for Multiple Gene Expression Analysis. *Anal. Chim. Acta* **2015**, *886*, 123–132.

(14) Li, Y.; Cu, Y. T. H.; Luo, D. Multiplexed Detection of Pathogen DNA with DNA-Based Fluorescence Nanobarcodes. *Nat. Biotechnol.* **2005**, *23* (7), 885–889.

(15) Lin, C.; Jungmann, R.; Leifer, A. M.; Li, C.; Levner, D.; Church, G. M.; Shih, W. M.; Yin, P. Submicrometre Geometrically Encoded Fluorescent Barcodes Self-Assembled from DNA. *Nat. Chem.* **2012**, *4* (10), 832–839.

(16) Wang, G.; Leng, Y.; Dou, H.; Wang, L.; Li, W.; Wang, X.; Sun, K.; Shen, L.; Yuan, X.; Li, J.; et al. Highly Efficient Preparation of Multiscaled Quantum Dot Barcodes for Multiplexed Hepatitis b Detection. *ACS Nano* **2013**, *7* (1), 471–481.

(17) Smith, A. M.; Gao, X.; Nie, S. Quantum Dot Nanocrystals for In Vivo Molecular and Cellular Imaging. *Photochem. Photobiol.* **2004**, *80* (3), 377.

(18) Wilson, R.; Spiller, D. G.; Prior, I. A.; Bhatt, R.; Hutchinson, A. Magnetic Microspheres Encoded with Photoluminescent Quantum Dots for Multiplexed Detection. *J. Mater. Chem.* **2007**, *17* (41), 4400–4406.

(19) Yang, J.; Dave, S. R.; Gao, X. Quantum Dot Nanobarcodes: Epitaxial Assembly of Nanoparticle-Polymer Complexes in Homogeneous Solution. *J. Am. Chem. Soc.* **2008**, *130* (15), 5286–5292.

(20) Zhao, Y.; Shum, H. C.; Chen, H.; Adams, L. L. A.; Gu, Z.; Weitz, D. A. Microfluidic Generation of Multifunctional Quantum Dot Barcode Particles. *J. Am. Chem. Soc.* **2011**, *133* (23), 8790–8793.

(21) Chan, W. C. W.; Maxwell, D. J.; Gao, X.; Bailey, R. E.; Han, M.; Nie, S. Luminescent Quantum Dots for Multiplexed Biological Detection and Imaging. *Curr. Opin. Biotechnol.* **2002**, *13* (1), 40–46.

(22) Han, M.; Gao, X.; Su, J. Z.; Nie, S. Quantum-Dot-Tagged Microbeads for Multiplexed Optical Coding of Biomolecules. *Nat. Biotechnol.* **2001**, *19* (7), 631–635.

(23) Eastman, P. S.; Ruan, W.; Doctolero, M.; Nuttall, R.; De Feo, G.; Park, J. S.; Chu, J. S. F.; Cooke, P.; Gray, J. W.; Li, S.; et al. Qdot Nanobarcodes for Multiplexed Gene Expression Analysis. *Nano Lett.* **2006**, *6* (5), 1059–1064.

(24) Wang, Y.; Yan, B.; Chen, L. SERS Tags: Novel Optical Nanoprobes for Bioanalysis. *Chem. Rev.* **2013**, *113* (3), 1391–1428.

(25) Banholzer, M. J.; Osberg, K. D.; Li, S.; Mangelson, B. F.; Schatz, G. C.; Mirkin, C. A. Silver-Based Nanodisk Codes. *ACS Nano* **2010**, *4* (9), 5446–5452.

(26) Nicewarner-Peña, S. R.; Freeman, R. G.; Reiss, B. D.; He, L.; Peña, D. J.; Walton, I. D.; Cromer, R.; Keating, C. D.; Natan, M. J. Submicrometer Metallic Barcodes. *Science.* **2001**, *294* (5540), 137–141.

(27) Park, B. C.; Kim, Y. K. Synthesis, Microstructure, and Physical Properties of Metallic Barcode Nanowires. *Met. Mater. Int.* **2017**, *23* (3), 413–425.

(28) Shikha, S.; Salafi, T.; Cheng, J.; Zhang, Y. Versatile Design and Synthesis of Nano-Barcodes. *Chem. Soc. Rev.* **2017**, *46* (22), 7054–7093.

(29) Zeng, Y.; Koo, K. M.; Trau, M.; Shen, A. G.; Hu, J. M. Watching SERS Glow for

Multiplex Biomolecular Analysis in the Clinic: A Review. *Appl. Mater. Today* **2019**, *15*, 431–444.

(30) Stoermer, R. L.; Cederquist, K. B.; McFarland, S. K.; Sha, M. Y.; Penn, S. G.; Keating, C. D. Coupling Molecular Beacons to Barcoded Metal Nanowires for Multiplexed, Sealed Chamber DNA Bioassays. *J. Am. Chem. Soc.* **2006**, *128* (51), 16892–16903.

(31) Tok, J. B. H.; Chuang, F. Y. S.; Kao, M. C.; Rose, K. A.; Pannu, S. S.; Sha, M. Y.; Chakarova, G.; Penn, S. G.; Dougherty, G. M. Metallic Striped Nanowires as Multiplexed Immunoassay Platforms for Pathogen Detection. *Angew. Chemie - Int. Ed.* **2006**, *45* (41), 6900–6904.

(32) Rodriguez-Lorenzo, L.; Fabris, L.; Alvarez-Puebla, R. A. Multiplex Optical Sensing with Surface-Enhanced Raman Scattering: A Critical Review. *Anal. Chim. Acta* **2012**, *745*, 10–23.

(33) Lu, N. C.; Cheng, Y. H.; Wang, Y. T.; Cheng, J. Dynamic Propagation Problems on Mode III Asymmetrical Interface Crack. *Nanobiotechno.* **2007**, *39* (11), 1710–1714.

(34) Zavaleta, C. L.; Smith, B. R.; Walton, I.; Doering, W.; Davis, G.; Shojaei, B.; Natan, M. J.; Gambhir, S. S. Multiplexed Imaging of Surface Enhanced Raman Scattering Nanotags in Living Mice Using Noninvasive Raman Spectroscopy. *Proc. Natl. Acad. Sci.* **2009**, *106* (32), 13511–13516.

(35) Zhu, D.; Wang, Z.; Zong, S.; Chen, H.; Chen, P.; Cui, Y. Wavenumber-Intensity Joint SERS Encoding Using Silver Nanoparticles for Tumor Cell Targeting. *RSC Adv.* **2014**, *4* (105), 60936–60942.

(36) Li, R.; Zhang, Y.; Tan, J.; Wan, J.; Guo, J.; Wang, C. Dual-Mode Encoded Magnetic Composite Microsphere Based on Fluorescence Reporters and Raman Probes as Covert Tag for Anticounterfeiting Applications. *ACS Appl. Mater. Interfaces* **2016**, *8* (14), 9384–9394.

(37) Xu, Y.; Wang, H.; Chen, B.; Liu, H.; Zhao, Y. Emerging Barcode Particles for Multiplex Bioassays. *Sci. China Mater.* **2019**, *62* (3), 289–324.

(38) Zhang, Y.; Zhang, L.; Deng, R.; Tian, J.; Zong, Y.; Jin, D.; Liu, X. Multicolour Barcoding in a Single Upconversion Crystal. *J. Am. Chem. Soc.* **2014**, *136* (13), 4893–4896.

(39) Zhang, F.; Shi, Q.; Zhang, Y.; Shi, Y.; Ding, K.; Zhao, D.; Stucky, G. D. Fluorescence Upconversion Microbarcodes for Multiplexed Biological Detection: Nucleic Acid

Encoding. *Adv. Mater.* **2011**, *23* (33), 3775–3779.

(40) Zhang, F.; Haushalter, R. C.; Haushalter, R. W.; Shi, Y.; Zhang, Y.; Ding, K.; Zhao, D.; Stucky, G. D. Rare-Earth Upconverting Nanobarcodes for Multiplexed Biological Detection. *Small* **2011**, *7* (14), 1972–1976.

(41) Li, Z.; Wang, L.; Wang, Z.; Liu, X.; Xiong, Y. Modification of $NaYF_4$:Yb,Er@SiO_2 Nanoparticles with Gold Nanocrystals for Tunable Green-to-Red Upconversion Emissions. *J. Phys. Chem. C* **2011**, *115* (8), 3291–3296.

(42) Gorris, H. H.; Ali, R.; Saleh, S. M.; Wolfbeis, O. S. Tuning the Dual Emission of Photon-upconverting Nanoparticles for Ratiometric Multiplexed Encoding. *Adv. Mater.* **2011**, *23* (14), 1652–1655.

(43) Auzel, F. Upconversion and Anti-Stokes Processes with f and d Ions in Solids. *Chem. Rev.* **2004**, *104* (1), 139–174.

(44) Liu, X.; Yan, C. H.; Capobianco, J. A. Photon Upconversion Nanomaterials. *Chem. Soc. Rev.* **2015**, *44* (6), 1299–1301.

(45) Haase, M.; Schäfer, H. Upconverting Nanoparticles. *Angew. Chemie Int. Ed.* **2011**, *50* (26), 5808–5829.

(46) Wenger, O. S.; Wermuth, M.; Güdel, H. U. Chemical Tuning of Transition Metal Upconversion Properties. *J. Alloys Compd.* **2002**, *341* (1–2), 342–348.

(47) Wermuth, M.; Güdel, H. U. Upconversion Luminescence in a 5d Transition-Metal Ion System: Cs_2ZrCl_6:Os^{4+}. *Chem. Phys. Lett.* **1997**, *281* (1–3), 81–85.

(48) Song, E. H.; Ding, S.; Wu, M.; Ye, S.; Xiao, F.; Dong, G. P.; Zhang, Q. Y. Temperature-Tunable Upconversion Luminescence of Perovskite Nanocrystals $KZnF_3$:Yb^{3+},Mn^{2+}. *J. Mater. Chem. C* **2013**, *1* (27), 4209–4215.

(49) Yin, M.; Joubert, M. F.; Krupa, J. C. Infrared to Green Up-Conversion in $LaCl_3$:U^{3+}. *J. Lumin.* **1997**, *75* (3), 221–227.

(50) Barandiaran, Z.; Seijo, L. Structure and Spectroscopy of U^{4+} Defects in Cs_2ZrCl_6: Ab Initio Theoretical Studies on the 5f2 and 5f16d1 Manifolds. *J. Chem. Phys.* **2003**, *118* (16), 7439–7456.

(51) Dereń, P. J.; Strek, W.; Zych, E.; Drozdzyński, J. Up-Conversion in Elpasolite Crystals Doped with U^{3+}. *Chem. Phys. Lett.* **2000**, *332* (3–4), 308–312.

(52) Xu, L.; Xu, C.; Sun, H.; Zeng, T.; Zhang, J.; Zhao, H. Self-Induced Second-Harmonic

and Sum-Frequency Generation from Interfacial Engineered Er^{3+}/Fe^{3+} Doped $LiNbO_3$ Single Crystal via Femtosecond Laser Ablation. *ACS Photonics* **2018**, *5* (11), 4463–4468.

(53) Zhan, Q.; Zhang, X.; Wang, B.; Li, N.; He, S. Two-Photon Luminescence and Second Harmonic Generation of Single Layer Molybdenum Disulphide Nanoprobe for Nonbleaching and Nonblinking Optical Bioimaging. *Prog. Electromagn. Res.* **2019**, *166*, 107–117.

(54) Vega, M.; Martin, I. R.; Llanos, J. Near-Infrared to Visible Upconversion and Second Harmonic Generation in $BaTiO_3:Ho^{3+}$ and $BaTiO_3:Ho^{3+}/Yb^{3+}$ Phosphors. *J. Alloys Compd.* **2019**, *806*, 1146–1152.

(55) Qi, Z. De; Li, D. W.; Jiang, P.; Jiang, F. L.; Li, Y. S.; Liu, Y.; Wong, W. K.; Cheah, K. W. Biocompatible CdSe Quantum Dot-Based Photosensitizer under Two-Photon Excitation for Photodynamic Therapy. *J. Mater. Chem.* **2011**, *21* (8), 2455–2458.

(56) He, T.; Ren, C.; Li, Z.; Xiao, S.; Li, J.; Lin, X.; Ye, C.; Zhang, J.; Guo, L.; Hu, W.; et al. Thermally Activated Delayed Fluorescence Organic Dots for Two-Photon Fluorescence Lifetime Imaging. *Appl. Phys. Lett.* **2018**, *112* (21), 211102.

(57) Zhang, X.; Wang, H.; Wang, H.; Zhang, Q.; Xie, J.; Tian, Y.; Wang, J.; Xie, Y. Single-Layered Graphitic-C_3N_4 Quantum Dots for Two-Photon Fluorescence Imaging of Cellular Nucleus. *Adv. Mater.* **2014**, *26* (26), 4438–4443.

(58) Bloembergen, N. Solid State Infrared Quantum Counters. *Phys. Rev. Lett.* **1959**, *2* (3), 84–85.

(59) Auzel, F. E. Materials and Devices Using Double-Pumped Phosphors with Energy Transfer. *Proc. IEEE* **1973**, *61* (6), 758–786.

(60) Auzel, F. Multiphonon-Assisted Anti-Stokes and Stokes Fluorescence of Triply Ionized Rare-Earth Ions. *Phys. Rev. B* **1976**, *13* (7), 2809–2817.

(61) Ovsyakin, V. V; Feofilov, P. P. Cooperative Sensitization of Luminescence in Crystals Activated with Rare Earth Ions. *Sov. J. Exp. Theor. Phys. Lett.* **1966**, *4*, 317.

(62) Wang, F.; Banerjee, D.; Liu, Y.; Chen, X.; Liu, X. Upconversion Nanoparticles in Biological Labeling, Imaging, and Therapy. *Analyst*. 2010, pp 1839–1854.

(63) Liu, G. Advances in the Theoretical Understanding of Photon Upconversion in Rare-Earth Activated Nanophosphors. *Chem. Soc. Rev.* **2015**, *44* (6), 1635–1652.

(64) Yang, W.; Li, X.; Chi, D.; Zhang, H.; Liu, X. Lanthanide-Doped Upconversion Materials: Emerging Applications for Photovoltaics and Photocatalysis. *Nanotechnology* **2014**, *25* (48), 482001.

(65) Wang, F.; Deng, R.; Wang, J.; Wang, Q.; Han, Y.; Zhu, H.; Chen, X.; Liu, X. Tuning Upconversion through Energy Migration in Core-Shell Nanoparticles. *Nat. Mater.* **2011**, *10* (12), 968–973.

(66) Dieke, G. H.; Crosswhite, H. M.; Dunn, B. Emission Spectra of the Doubly and Triply Ionized Rare Earths. *JOSA* **1961**, *51* (8), 820–827.

(67) Huang, B. 4f Fine-structure Levels as the Dominant Error in the Electronic Structures of Binary Lanthanide Oxides. *J. Comput. Chem.* **2016**, *37* (9), 825–835.

(68) Binnemans, K. Lanthanide-Based Luminescent Hybrid Materials. *Chem. Rev.* **2009**, *109* (9), 4283–4374.

(69) He, H.; Liu, B.; Wen, S.; Liao, J.; Lin, G.; Zhou, J.; Jin, D. Quantitative Lateral Flow Strip Sensor Using Highly Doped Upconversion Nanoparticles. *Anal. Chem.* **2018**, *90* (21), 12356–12360.

(70) Liu, Y.; Lu, Y.; Yang, X.; Zheng, X.; Wen, S.; Wang, F.; Vidal, X.; Zhao, J.; Liu, D.; Zhou, Z.; et al. Amplified Stimulated Emission in Upconversion Nanoparticles for Super-Resolution Nanoscopy. *Nature* **2017**, *543* (7644), 229–233.

(71) Deng, R.; Qin, F.; Chen, R.; Huang, W.; Hong, M.; Liu, X. Temporal Full-Colour Tuning through Non-Steady-State Upconversion. *Nat. Nanotechnol.* **2015**, *10* (3), 237–242.

(72) Zhou, B.; Shi, B.; Jin, D.; Liu, X. Controlling Upconversion Nanocrystals for Emerging Applications. *Nat. Nanotechnol.* **2015**, *10* (11), 924.

(73) Huang, X.; Han, S.; Huang, W.; Liu, X. Enhancing Solar Cell Efficiency: The Search for Luminescent Materials as Spectral Converters. *Chem. Soc. Rev.* **2013**, *42* (1), 173–201.

(74) Zhou, J.; Liu, Q.; Feng, W.; Sun, Y.; Li, F. Upconversion Luminescent Materials: Advances and Applications. *Chem. Rev.* **2015**, *115* (1), 395–465.

(75) Dong, H.; Du, S. R.; Zheng, X. Y.; Lyu, G. M.; Sun, L. D.; Li, L. D.; Zhang, P. Z.; Zhang, C.; Yan, C. H. Lanthanide Nanoparticles: From Design toward Bioimaging and Therapy. *Chem. Rev.* **2015**, *115* (19), 10725–10815.

(76) Ai, X.; Ho, C. J. H.; Aw, J.; Attia, A. B. E.; Mu, J.; Wang, Y.; Wang, X.; Wang, Y.; Liu, X.; Chen, H.; et al. In Vivo Covalent Cross-Linking of Photon-Converted Rare-Earth Nanostructures for Tumour Localization and Theranostics. *Nat. Commun.* **2016**, *7*, 10432–10440.

(77) Zhao, J.; Gao, J.; Xue, W.; Di, Z.; Xing, H.; Lu, Y.; Li, L. Upconversion Luminescence-Activated DNA Nanodevice for ATP Sensing in Living Cells. *J. Am. Chem. Soc.* **2018**, *140* (2), 578–581.

(78) Chatterjee, D. K.; Rufaihah, A. J.; Zhang, Y. Upconversion Fluorescence Imaging of Cells and Small Animals Using Lanthanide Doped Nanocrystals. *Biomaterials* **2008**, *29* (7), 937–943.

(79) Wang, F.; Liu, X. Upconversion Multicolour Fine-Tuning: Visible to near-Infrared Emission from Lanthanide-Doped $NaYF_4$ Nanoparticles. *J. Am. Chem. Soc.* **2008**, *130* (17), 5642–5643.

(80) Dong, H.; Sun, L. D.; Yan, C. H. Energy Transfer in Lanthanide Upconversion Studies for Extended Optical Applications. *Chem. Soc. Rev.* **2015**, *44* (6), 1608–1634.

(81) Sun, L.; Gao, R.; Pan, T.; Ai, X. C.; Fu, L.; Zhang, J. P. Concentration-Regulated Photon Upconversion and Quenching in $NaYF_4$:Yb^{3+},Er^{3+} Nanocrystals: Nonexponentiality Revisited. *Nanoscale* **2019**, *11* (39), 18150–18158.

(82) Zheng, X.; Shikha, S.; Zhang, Y. Elimination of Concentration Dependent Luminescence Quenching in Surface Protected Upconversion Nanoparticles. *Nanoscale* **2018**, *10* (35), 16447–16454.

(83) Zhang, X.; Chen, Z.; Qiu, J. Mechanistic Investigation of Upconversion Luminescence in Er^{3+}-Doped $BaCl_2$, BaF_2 and $NaYF_4$ Phosphors. *Mater. Chem. Phys.* **2015**, *162*, 76–81.

(84) Sun, T.; Li, Y.; Ho, W. L.; Zhu, Q.; Chen, X.; Jin, L.; Zhu, H.; Huang, B.; Lin, J.; Little, B. E. Integrating Temporal and Spatial Control of Electronic Transitions for Bright Multiphoton Upconversion. *Nat. Commun.* **2019**, *10* (1), 1–7.

(85) Lin, H.; Xu, D.; Li, Y.; Yao, L.; Xu, L.; Ma, Y.; Yang, S.; Zhang, Y. Intense Red Upconversion Luminescence in Er^{3+}-Sensitized Particles through Confining the 1532 nm Excitation Energy. *J. Lumin.* **2019**, *216*, 116731.

(86) Liu, L.; Wang, S.; Zhao, B.; Pei, P.; Fan, Y.; Li, X.; Zhang, F. Er^{3+} Sensitized 1530 nm to 1180 nm Second Near-Infrared Window Upconversion Nanocrystals for In Vivo

Biosensing. *Angew. Chemie - Int. Ed.* **2018**, *57* (25), 7518–7522.

(87) Martín-Rodríguez, R.; Fischer, S.; Ivaturi, A.; Froehlich, B.; Krämer, K. W.; Goldschmidt, J. C.; Richards, B. S.; Meijerink, A. Highly Efficient IR to NIR Upconversion in Gd_2O_2S: Er^{3+} for Photovoltaic Applications. *Chem. Mater.* **2013**, *25* (9), 1912–1921.

(88) De La Rosa, E.; Salas, P.; Desirena, H.; Angeles, C.; Rodríguez, R. A. Strong Green Upconversion Emission in ZrO_2: Yb^{3+}- Ho^{3+} Nanocrystals. *Appl. Phys. Lett.* **2005**, *87* (24), 1–3.

(89) Krämer, K. W.; Biner, D.; Frei, G.; Güdel, H. U.; Hehlen, M. P.; Lüthi, S. R. Hexagonal Sodium Yttrium Fluoride Based Green and Blue Emitting Upconversion Phosphors. *Chem. Mater.* **2004**, *16* (7), 1244–1251.

(90) Deng, H.; Yang, S.; Xiao, S.; Gong, H. M.; Wang, Q. Q. Controlled Synthesis and Upconverted Avalanche Luminescence of Cerium(III) and Neodymium(III) Orthovanadate Nanocrystals with High Uniformity of Size and Shape. *J. Am. Chem. Soc.* **2008**, *130* (6), 2032–2040.

(91) Chivian, J. S.; Case, W. E.; Eden, D. D. The Photon Avalanche: A New Phenomenon in Pr3+-based Infrared Quantum Counters. *Appl. Phys. Lett.* **1979**, *35* (2), 124–125.

(92) Chan, E. M.; Chan, E. M. Combinatorial Approaches for Developing Upconverting Nanomaterials: High-Throughput Screening, Modeling, and Applications. *Chem Soc Rev* **2015**, *44*, 1653–1679.

(93) Liu, Y.; Lu, Y.; Yang, X.; Zheng, X.; Wen, S.; Wang, F.; Vidal, X.; Zhao, J.; Liu, D.; Zhou, Z.; et al. Amplified Stimulated Emission in Upconversion Nanoparticles for Super-Resolution Nanoscopy. *Nature* **2017**, *543* (7644), 229–233.

(94) Zhan, Q.; Liu, H.; Wang, B.; Wu, Q.; Pu, R.; Zhou, C.; Huang, B.; Peng, X.; Ågren, H.; He, S. Achieving High-Efficiency Emission Depletion Nanoscopy by Employing Cross Relaxation in Upconversion Nanoparticles. *Nat. Commun.* **2017**, *8* (1), 1–11.

(95) Strek, W.; Deren, P.; Bednarkiewicz, A. Cooperative Processes in $KYb(WO4)_2$ Crystal Doped with Eu^{3+} and Tb^{3+} Ions. *J. Lumin.* **2000**, *87*, 999–1001.

(96) Liang, H.; Chen, G.; Li, L.; Liu, Y.; Qin, F.; Zhang, Z. Upconversion Luminescence in Yb^{3+}/Tb^{3+}-Codoped Monodisperse $NaYF_4$ Nanocrystals. *Opt. Commun.* **2009**, *282* (14), 3028–3031.

(97) Hernández, I.; Pathumakanthar, N.; Wyatt, P. B.; Gillin, W. P. Cooperative Infrared to

Visible up Conversion in Tb^{3+}, Eu^{3+}, and Yb^{3+} Containing Polymers. *Adv. Mater.* **2010**, *22* (47), 5356–5360.

(98) Hao, S.; Shao, W.; Qiu, H.; Shang, Y.; Fan, R.; Guo, X.; Zhao, L.; Chen, G.; Yang, C. Tuning the Size and Upconversion Emission of $NaYF_4$:Yb^{3+}/Pr^{3+} Nanoparticles through Yb^{3+} Doping. *RSC Adv.* **2014**, *4* (99), 56302–56306.

(99) Dong, H.; Sun, L. D.; Wang, Y. F.; Xiao, J. W.; Tu, D.; Chen, X.; Yan, C. H. Photon Upconversion in Yb^{3+}-Tb^{3+} and Yb^{3+}-Eu^{3+} Activated Core/Shell Nanoparticles with Dual-Band Excitation. *J. Mater. Chem. C* **2016**, *4* (19), 4186–4192.

(100) Qin, W. P.; Liu, Z. Y.; Sin, C. N.; Wu, C. F.; Qin, G. S.; Chen, Z.; Zheng, K. Z. Multi-Ion Cooperative Processes in Yb^{3+} Clusters. *Light Sci. Appl.* **2014**, *3*, 1–6.

(101) Arai, Y.; Yamashidta, T.; Suzuki, T.; Ohishi, Y. Upconversion Properties of Tb^{3+}-Yb^{3+} Codoped Fluorophosphate Glasses. *J. Appl. Phys.* **2009**, *105* (8), 083105.

(102) Prorok, K.; Gnach, A.; Bednarkiewicz, A.; Stręk, W. Energy Up-Conversion in Tb^{3+}/Yb^{3+} Co-Doped Colloidal α-$NaYF_4$ Nanocrystals. *J. Lumin.* **2013**, *140*, 103–109.

(103) Su, Q.; Han, S.; Xie, X.; Zhu, H.; Chen, H.; Chen, C. K.; Liu, R. S.; Chen, X.; Wang, F.; Liu, X. The Effect of Surface Coating on Energy Migration-Mediated Upconversion. *J. Am. Chem. Soc.* **2012**, *134* (51), 20849–20857.

(104) Wen, H.; Zhu, H.; Chen, X.; Hung, T. F.; Wang, B.; Zhu, G.; Yu, S. F.; Wang, F. Upconverting Near-Infrared Light through Energy Management in Core-Shell-Shell Nanoparticles. *Angew. Chemie - Int. Ed.* **2013**, *52* (50), 13419–13423.

(105) Auzel, F.; Pecile, D. Absolute Efficiency for IR to Blue Conversion Materials and Theoretical Prediction for Optimized Matrices. *J. Lumin.* **1976**, *11* (5–6), 321–330.

(106) Auzel, F.; Pecile, D. Comparison and Efficiency of Materials for Summation of Photons Assisted by Energy Transfer. *J. Lumin.* **1973**, *8* (1), 32–43.

(107) Johnson, N. J. J.; van Veggel, F. C. J. M. Sodium Lanthanide Fluoride Core-Shell Nanocrystals: A General Perspective on Epitaxial Shell Growth. *Nano Res.* **2013**, *6* (8), 547–561.

(108) Liu, Y.; Tu, D.; Zhu, H.; Chen, X. Lanthanide-Doped Luminescent Nanoprobes: Controlled Synthesis, Optical Spectroscopy, and Bioapplications. *Chem. Soc. Rev.* **2013**, *42* (16), 6924–6958.

(109) Gainer, C. F.; Romanowski, M. A Review of Synthetic Methods for the Production of

Upconverting Lanthanide Nanoparticles. *J. Innov. Opt. Health Sci.* **2014**, *7* (2), 1330007.

(110) Lyu, L.; Cheong, H.; Ai, X.; Lin, J.; Xing, B. Nanocrystals : Recent Advances in Improving Photon Conversion and Alleviating the Thermal Effect. *NPG Asia Mater.* **2018**, 685–702.

(111) Chen, X.; Peng, D.; Ju, Q.; Wang, F. Photon Upconversion in Core-Shell Nanoparticles. *Chem. Soc. Rev.* **2015**, *44* (6), 1318–1330.

(112) Wang, F.; Wang, J.; Liu, X. Direct Evidence of a Surface Quenching Effect on Size-dependent Luminescence of Upconversion Nanoparticles. *Angew. Chemie Int. Ed.* **2010**, *49* (41), 7456–7460.

(113) Würth, C.; Fischer, S.; Grauel, B.; Alivisatos, A. P.; Resch-Genger, U. Quantum Yields, Surface Quenching, and Passivation Efficiency for Ultrasmall Core/Shell Upconverting Nanoparticles. *J. Am. Chem. Soc.* **2018**, *140* (14), 4922–4928.

(114) Peng, X.; Schlamp, M. C.; Kadavanich, A. V; Alivisatos, A. P. Epitaxial Growth of Highly Luminescent CdSe/CdS Core/Shell Nanocrystals with Photostability and Electronic Accessibility. *J. Am. Chem. Soc.* **1997**, *119* (30), 7019–7029.

(115) Peng, X.; Schlamp, M. C.; Kadavanich, A. V.; Alivisatos, A. P. Epitaxial Growth of Highly Luminescent CdSe/CdS Core/Shell Nanocrystals with Photostability and Electronic Accessibility. *J. Am. Chem. Soc.* **1997**, *119* (30), 7019–7029.

(116) Li, X.; Zhang, F.; Zhao, D. Lab on Upconversion Nanoparticles: Optical Properties and Applications Engineering via Designed Nanostructure. *Chem. Soc. Rev.* **2015**, *44* (6), 1346–1378.

(117) Mai, H. X.; Zhang, Y. W.; Sun, L. D.; Yan, C. H. Highly Efficient Multicolour Up-Conversion Emissions and Their Mechanisms of Monodisperse $NaYF_4$:Yb,Er Core and Core/Shell-Structured Nanocrystals. *J. Phys. Chem. C* **2007**, *111* (37), 13721–13729.

(118) Qian, H.-S.; Zhang, Y. Synthesis of Hexagonal-Phase Core−Shell $NaYF_4$ Nanocrystals with Tunable Upconversion Fluorescence. *Langmuir* **2008**, *24* (21), 12123–12125.

(119) Wang, F.; Deng, R.; Liu, X. Preparation of Core-Shell $NaGdF_4$ Nanoparticles Doped with Luminescent Lanthanide Ions to Be Used as Upconversion-Based Probes. *Nat. Protoc.* **2014**, *9* (7), 1634.

(120) Zhang, F.; Che, R.; Li, X.; Yao, C.; Yang, J.; Shen, D.; Hu, P.; Li, W.; Zhao, D. Direct

Imaging the Upconversion Nanocrystal Core/Shell Structure at the Subnanometer Level: Shell Thickness Dependence in Upconverting Optical Properties. *Nano Lett.* **2012**, *12* (6), 2852–2858.

(121) Abel, K. A.; Boyer, J. C.; Van Veggel, F. C. J. M. Hard Proof of the $NaYF_4$/$NaGdF_4$ Nanocrystal Core/Shell Structure. *J. Am. Chem. Soc.* **2009**, *131* (41), 14644–14645.

(122) Abel, K. A.; Boyer, J. C.; Andrei, C. M.; Van Veggel, F. C. J. M. Analysis of the Shell Thickness Distribution on $NaYF_4$/$NaGdF_4$ Core/Shell Nanocrystals by EELS and EDS. *J. Phys. Chem. Lett.* **2011**, *2* (3), 185–189.

(123) Chen, G.; Ohulchanskyy, T. Y.; Liu, S.; Law, W. C.; Wu, F.; Swihart, M. T.; Ågren, H.; Prasad, P. N. Core/Shell $NaGdF_4$:Nd^{3+}/$NaGdF_4$ Nanocrystals with Efficient near-Infrared to near-Infrared Downconversion Photoluminescence for Bioimaging Applications. *ACS Nano* **2012**, *6* (4), 2969–2977.

(124) Yi, G. S.; Chow, G. M. Water-Soluble $NaYF_4$:Yb,Er(Tm)/$NaYF_4$/Polymer Core/Shell/Shell Nanoparticles with Significant Enhancement of Upconversion Fluorescence. *Chem. Mater.* **2007**, *19* (3), 341–343.

(125) Capobianco, J. A.; Morgan, C. G.; Vetrone, F.; Naccache, R.; Mahalingam, V. The Active-Core/Active-Shell Approach: A Strategy to Enhance the Upconversion Luminescence in Lanthanide-Doped Nanoparticles. *Adv. Funct. Mater.* **2009**, *19* (18), 2924–2929.

(126) Huang, P.; Zheng, W.; Zhou, S.; Tu, D.; Chen, Z.; Zhu, H.; Li, R.; Ma, E.; Huang, M.; Chen, X. Lanthanide-Doped $LiLuF_4$ Upconversion Nanoprobes for the Detection of Disease Biomarkers. *Angew. Chemie - Int. Ed.* **2014**, *53* (5), 1252–1257.

(127) Chen, G.; Shen, J.; Ohulchanskyy, T. Y.; Patel, N. J.; Kutikov, A.; Li, Z.; Song, J.; Pandey, R. K.; Ågren, H.; Prasad, P. N. (α-$NaYbF_4$: Tm^{3+})/CaF_2 Core/Shell Nanoparticles with Efficient near-Infrared to near-Infrared Upconversion for High-Contrast Deep Tissue Bioimaging. *ACS Nano* **2012**, *6* (9), 8280–8287.

(128) Li, X.; Shen, D.; Yang, J.; Yao, C.; Che, R.; Zhang, F.; Zhao, D. Successive Layer-by-Layer Strategy for Multi-Shell Epitaxial Growth: Shell Thickness and Doping Position Dependence in Upconverting Optical Properties. *Chem. Mater.* **2012**, *25* (1), 106–112.

(129) Johnson, N. J. J.; Korinek, A.; Dong, C.; Van Veggel, F. C. J. M. Self-Focusing by Ostwald Ripening: A Strategy for Layer-by-Layer Epitaxial Growth on Upconverting Nanocrystals. *J. Am. Chem. Soc.* **2012**, *134* (27), 11068–11071.

(130) Heer, S.; Kömpe, K.; Güdel, H. U.; Haase, M. Highly Efficient Multicolour Upconversion Emission in Transparent Colloids of Lanthanide-Doped $NaYF_4$ Nanocrystals. *Adv. Mater.* **2004**, *16* (23–24), 2102–2105.

(131) Ågren, H.; Chen, G.; Valiev, R. R.; Shao, W.; Ohulchanskyy, T. Y.; He, G. S.; Prasad, P. N. Efficient Broadband Upconversion of Near-Infrared Light in Dye-Sensitized Core/Shell Nanocrystals. *Adv. Opt. Mater.* **2016**, *4* (11), 1760–1766.

(132) Liu, Q.; Zhang, Y.; Peng, C. S.; Yang, T.; Joubert, L. M.; Chu, S. Single Upconversion Nanoparticle Imaging at Sub-10 W cm^{-2} Irradiance. *Nat. Photonics* **2018**, *12* (9), 548–553.

(133) Li, X.; Wang, R.; Zhang, F.; Zhao, D. Engineering Homogeneous Doping in Single Nanoparticle to Enhance Upconversion Efficiency. *Nano Lett.* **2014**, *14* (6), 3634–3639.

(134) Lü, Q.; Guo, F.; Sun, L.; Li, A.; Zhao, L. Silica-/Titania-Coated Y_2O_3: Tm^{3+}, Yb^{3+} Nanoparticles with Improvement in Upconversion Luminescence Induced by Different Thickness Shells. *J. Appl. Phys.* **2008**, *103* (12), 123533.

(135) Yang, Z.; Wu, H.; Liao, J.; Li, W.; Song, Z.; Yang, Y.; Zhou, D.; Wang, R.; Qiu, J. Infrared to Visible Upconversion Luminescence in Er^{3+}/Yb^{3+} Co-Doped CeO_2 Inverse Opal. *Mater. Sci. Eng. B* **2013**, *178* (15), 977–981.

(136) Lai, S.; Yang, Z.; Liao, J.; Li, J.; Shao, B.; Qiu, J.; Song, Z. Investigation on Existing States and Photoluminescence Property of Silver in the SiO_2 Three-Dimensionally Ordered Macroporous Materials. *RSC Adv.* **2014**, *4* (63), 33607–33613.

(137) Wu, H.; Yang, Z.; Liao, J.; Lai, S.; Qiu, J.; Song, Z.; Yang, Y.; Zhou, D.; Yin, Z. Investigation of Upconversion and near Infrared Emission Properties in CeO_2: Er^{3+}, Yb^{3+} Inverse Opals. *Opt. Express* **2013**, *21* (19), 22186.

(138) Wang, F.; Liu, X. Recent Advances in the Chemistry of Lanthanide-Doped Upconversion Nanocrystals. *Chem. Soc. Rev.* **2009**, *38* (4), 976–989.

(139) Yang, Y.; Liao, J.; Yang, Z.; Lai, S.; Shao, B.; Li, J.; Qiu, J.; Song, Z. Upconversion Emission Enhancement of $NaYF_4$:Yb,Er Nanoparticles by Coupling Silver Nanoparticle Plasmons and Photonic Crystal Effects. *J. Phys. Chem. C* **2014**, *118* (31), 17992–17999.

(140) Yang, Z. W.; Wang, Y. D.; Liao, J. Y.; Yang, J. Z.; Qiu, J. B.; Song, Z. G. Upconversion Emission Modification and White Light Generation in $NaYF_4$: Yb^{3+}, Er^{3+}, Tm^{3+}

Nanocrystals Opal Photonic Crystal Composites. *IEEE Photonics J.* **2015**, *7* (6), 1–8.

(141) Wiesholler, L. M.; Frenzel, F.; Grauel, B.; Würth, C.; Resch-Genger, U.; Hirsch, T. Yb,Nd,Er-Doped Upconversion Nanoparticles: 980 nm: Versus 808 nm Excitation. *Nanoscale* **2019**, *11* (28), 13440–13449.

(142) Liao, J.; Yang, Z.; Wu, H.; Lai, S.; Qiu, J.; Song, Z.; Yang, Y.; Zhou, D.; Yin, Z. Upconversion Luminescence Enhancement of $NaYF_4$: Yb^{3+}, Er^{3+} Nanoparticles on Inverse Opal Surface. *Surf. Rev. Lett.* **2014**, *21* (01), 1450017.

(143) Zhou, J.; Wen, S.; Liao, J.; Clarke, C.; Tawfik, S. A.; Ren, W.; Mi, C.; Wang, F.; Jin, D. Activation of the Surface Dark-Layer to Enhance Upconversion in a Thermal Field. *Nat. Photonics* **2018**, *12* (3), 154–158.

(144) Gu, Y.; Guo, Z.; Yuan, W.; Kong, M.; Liu, Y.; Liu, Y.; Gao, Y.; Feng, W.; Wang, F.; Zhou, J.; et al. High-Sensitivity Imaging of Time-Domain near-Infrared Light Transducer. *Nat. Photonics* **2019**, *13* (8), 525–531.

(145) Wang, L.; Dong, H.; Li, Y.; Xue, C.; Sun, L. D.; Yan, C. H.; Li, Q. Reversible Near-Infrared Light Directed Reflection in a Self-Organized Helical Superstructure Loaded with Upconversion Nanoparticles. *J. Am. Chem. Soc.* **2014**, *136* (12), 4480–4483.

(146) Jin, L.; Chen, X.; Liu, X.; Sun, T.; Yu, S. F.; Wang, F.; Kong, W.; Zhang, W.; Fan, J. Confining Energy Migration in Upconversion Nanoparticles towards Deep Ultraviolet Lasing. *Nat. Commun.* **2016**, *7* (1), 1–6.

(147) Johnson, N. J. J.; He, S.; Diao, S.; Chan, E. M.; Dai, H.; Almutairi, A. Direct Evidence for Coupled Surface and Concentration Quenching Dynamics in Lanthanide-Doped Nanocrystals. *J. Am. Chem. Soc.* **2017**, *139* (8), 3275–3282.

(148) Hu, Y.; Dong, Y.; Zhang, G.; Jiang, J.; Ouyang, L.; Shao, Q. Emission Colour Tuning of Core/Shell Upconversion Nanoparticles through Modulation of Laser Power or Temperature. *Nanoscale* **2017**, *9* (33), 12132–12141.

(149) Chen, D.; Lei, L.; Yang, A.; Wang, Z.; Wang, Y. Ultra-Broadband near-Infrared Excitable Upconversion Core/Shell Nanocrystals. *Chem. Commun.* **2012**, *48* (47), 5898–5900.

(150) Chen, G.; Ågren, H.; Ohulchanskyy, T. Y.; Prasad, P. N. Light Upconverting Core-Shell Nanostructures: Nanophotonic Control for Emerging Applications. *Chem. Soc. Rev.* **2015**, *44* (6), 1680–1713.

(151) Wang, M.; Tian, Y.; Zhao, F.; Li, R.; You, W.; Fang, Z.; Chen, X.; Huang, W.; Ju, Q.

Alleviating the Emitter Concentration Effect on Upconversion Nanoparticles via an Inert Shell. *J. Mater. Chem. C* **2017**, *5* (6), 1537–1543.

(152) Liu, Y.; Tu, D.; Zhu, H.; Li, R.; Luo, W.; Chen, X. A Strategy to Achieve Efficient Dual-mode Luminescence of Eu^{3+} in Lanthanides Doped Multifunctional $NaGdF_4$ Nanocrystals. *Adv. Mater.* **2010**, *22* (30), 3266–3271.

(153) Zhang, H.; Liu, X.; Zeng, Q.; Zhang, Y.; Wang, Y.; Kong, X.; Tu, L.; Shi, Z.; Li, C. Breakthrough in Concentration Quenching Threshold of Upconversion Luminescence via Spatial Separation of the Emitter Doping Area for Bio-Applications. *Chem. Commun.* **2011**, *47* (43), 11957.

(154) Yang, D.; Li, C.; Li, G.; Shang, M.; Kang, X.; Lin, J. Colloidal Synthesis and Remarkable Enhancement of the Upconversion Luminescence of $BaGdF_5:Yb^{3+}/Er^{3+}$ Nanoparticles by Active-Shell Modification. *J. Mater. Chem.* **2011**, *21* (16), 5923–5927.

(155) Zhang, C.; Lee, J. Y. Prevalence of Anisotropic Shell Growth in Rare Earth Core-Shell Upconversion Nanocrystals. *ACS Nano* **2013**, *7* (5), 4393–4402.

(156) Zhang, Y.; Wang, F.; Lang, Y.; Yin, J.; Zhang, M.; Liu, X.; Zhang, D.; Zhao, D.; Qin, G.; Qin, W. $KMnF_3:Yb^{3+},Er^{3+}@KMnF_3:Yb^{3+}$ Active-Core-Active-Shell Nanoparticles with Enhanced Red up-Conversion Fluorescence for Polymer-Based Waveguide Amplifiers Operating at 650 nm. *J. Mater. Chem. C* **2015**, *3* (38), 9827–9832.

(157) Zhang, Y.; Liu, X.; Lang, Y.; Yuan, Z.; Zhao, D.; Qin, G.; Qin, W. Synthesis of Ultra-Small $BaLuF_5:Yb^{3+},Er^{3+}$ at $BaLuF_5:Yb^{3+}$ Active-Core-Active-Shell Nanoparticles with Enhanced up-Conversion and down-Conversion Luminescence by a Layer-by-Layer Strategy. *J. Mater. Chem. C* **2015**, *3* (9), 2045–2053.

(158) Ghosh, P.; Oliva, J.; Rosa, E. De; Haldar, K. K.; Solis, D.; Patra, A. Enhancement of Upconversion Emission of $LaPO_4$: Er@Yb Core-Shell Nanoparticles / Nanorods. *J. Phys. Chem. C* **2008**, *112*, 9650–9658.

(159) Chen, D.; Yu, Y.; Huang, F.; Lin, H.; Huang, P.; Yang, A.; Wang, Z.; Wang, Y. Lanthanide Dopant-Induced Formation of Uniform Sub-10 nm Active-Core/Active-Shell Nanocrystals with near-Infrared to near-Infrared Dual-Modal Luminescence. *J. Mater. Chem.* **2012**, *22* (6), 2632–2640.

(160) Zhan, Q.; Qian, J.; Liang, H.; Somesfalean, G.; Wang, D.; He, S.; Zhang, Z.; Andersson-Engels, S. Using 915 nm Laser Excited $Tm^{3+}/Er^{3+}/Ho^{3+}$-Doped $NaYbF_4$

Upconversion Nanoparticles for in Vitro and Deeper in Vivo Bioimaging without Overheating Irradiation. *ACS Nano* **2011**, *5* (5), 3744–3757.

(161) Kobayashi, H.; Ogawa, M.; Alford, R.; Choyke, P. L.; Urano, Y. New Strategies for Fluorescent Probe Design in Medical Diagnostic Imaging. *Chem. Rev.* **2010**, *110* (5), 2620–2640.

(162) Wang, Y. F.; Liu, G. Y.; Sun, L. D.; Xiao, J. W.; Zhou, J. C.; Yan, C. H. Nd^{3+}-Sensitized Upconversion Nanophosphors: Efficient in Vivo Bioimaging Probes with Minimized Heating Effect. *ACS Nano* **2013**, *7* (8), 7200–7206.

(163) Song, K.; Kong, X.; Liu, X.; Zhang, Y.; Zeng, Q.; Tu, L.; Shi, Z.; Zhang, H. Aptamer Optical Biosensor without Bio-Breakage Using Upconversion Nanoparticles as Donors. *Chem. Commun.* **2012**, *48* (8), 1156–1158.

(164) Skripka, A.; Marin, R.; Benayas, A.; Canton, P.; Hemmer, E.; Vetrone, F. Covering the Optical Spectrum through Collective Rare-Earth Doping of $NaGdF_4$ Nanoparticles: 806 and 980 nm Excitation Routes. *Phys. Chem. Chem. Phys.* **2017**, *19* (19), 11825–11834.

(165) Wang, R.; Li, X.; Zhou, L.; Zhang, F. Epitaxial Seeded Growth of Rare-Earth Nanocrystals with Efficient 800 nm Near-Infrared to 1525 nm Short-Wavelength Infrared Downconversion Photoluminescence for in Vivo Bioimaging. *Angew. Chemie - Int. Ed.* **2014**, *53* (45), 12086–12090.

(166) Zeng, L.; Pan, Y.; Zou, R.; Zhang, J.; Tian, Y.; Teng, Z.; Wang, S.; Ren, W.; Xiao, X.; Zhang, J.; et al. 808 nm-Excited Upconversion Nanoprobes with Low Heating Effect for Targeted Magnetic Resonance Imaging and High-Efficacy Photodynamic Therapy in HER_2-Overexpressed Breast Cancer. *Biomaterials* **2016**, *103*, 116–127.

(167) Phan, T. G.; Bullen, A. Practical Intravital Two-Photon Microscopy for Immunological Research: Faster, Brighter, Deeper. *Immunol. Cell Biol.* **2010**, *88* (4), 438–444.

(168) Lu, F.; Yang, L.; Ding, Y.; Zhu, J. J. Highly Emissive Nd^{3+}-Sensitized Multilayered Upconversion Nanoparticles for Efficient 795 Nm Operated Photodynamic Therapy. *Adv. Funct. Mater.* **2016**, *26* (26), 4778–4785.

(169) Zhang, Y.; Yu, Z.; Li, J.; Ao, Y.; Xue, J.; Zeng, Z.; Yang, X.; Tan, T. T. Y. Ultrasmall-Superbright Neodymium-Upconversion Nanoparticles via Energy Migration Manipulation and Lattice Modification: 808 Nm-Activated Drug Release. *ACS Nano* **2017**, *11* (3), 2846–2857.

(170) Shi, S.; Wang, Y.-F.; Chen, C.; Sun, L.-D.; Yan, C.-H.; Pan, D.-X.; Liu, Y.; Li, Y.; Tang, J. A Versatile Imaging and Therapeutic Platform Based on Dual-Band Luminescent Lanthanide Nanoparticles toward Tumor Metastasis Inhibition. *ACS Nano* **2016**, *10* (2), 2766–2773.

(171) Guo, S.; Tsang, M. K.; Lo, W. S.; Hao, J.; Wong, W. T. 808 Nm Excited Energy Migration Upconversion Nanoparticles Driven by a Nd^{3+}-Trinity System with Colour-Tunability and Superior Luminescence Properties. *Nanoscale* **2018**, *10* (6), 2790–2803.

(172) Shen, J.; Chen, G.; Vu, A. M.; Fan, W.; Bilsel, O. S.; Chang, C. C.; Han, G. Engineering the Upconversion Nanoparticle Excitation Wavelength: Cascade Sensitization of Tri-Doped Upconversion Colloidal Nanoparticles at 800 nm. *Adv. Opt. Mater.* **2013**, *1* (9), 644–650.

(173) Xie, X.; Gao, N.; Deng, R.; Sun, Q.; Xu, Q. H.; Liu, X. Mechanistic Investigation of Photon Upconversion in Nd^{3+}- Sensitized Core-Shell Nanoparticles. *J. Am. Chem. Soc.* **2013**, *135* (34), 12608–12611.

(174) Zhong, Y.; Tian, G.; Gu, Z.; Yang, Y.; Gu, L.; Zhao, Y.; Ma, Y.; Yao, J. Elimination of Photon Quenching by a Transition Layer to Fabricate a Quenching-shield Sandwich Structure for 800 nm Excited Upconversion Luminescence of Nd^{3+}-sensitized Nanoparticles. *Adv. Mater.* **2014**, *26* (18), 2831–2837.

(175) Wu, H.; Yang, Z.; Liao, J.; Lai, S.; Qiu, J.; Song, Z.; Yang, Y.; Zhou, D.; Yin, Z. Upconversion Luminescence Properties of Three-Dimensional Ordered Macroporous CeO_2: Er^{3+}, Yb^{3+}. *J. Alloys Compd.* **2014**, *586* (3), 485–487.

(176) Zou, W.; Visser, C.; Maduro, J. A.; Pshenichnikov, M. S.; Hummelen, J. C. Broadband Dye-Sensitized Upconversion of near-Infrared Light. *Nat. Photonics* **2012**, *6* (8), 560–564.

(177) Wu, X.; Zhang, Y.; Takle, K.; Bilsel, O.; Li, Z.; Lee, H.; Zhang, Z.; Li, D.; Fan, W.; Duan, C. Dye-Sensitized Core/Active Shell Upconversion Nanoparticles for Optogenetics and Bioimaging Applications. *ACS Nano* **2016**, *10* (1), 1060–1066.

(178) Lee, J.; Yoo, B.; Lee, H.; Cha, G. D.; Lee, H.; Cho, Y.; Kim, S. Y.; Seo, H.; Lee, W.; Son, D. Ultra-wideband Multi-Dye-sensitized Upconverting Nanoparticles for Information Security Application. *Adv. Mater.* **2017**, *29* (1), 1603169.

(179) Wu, X.; Lee, H.; Bilsel, O.; Zhang, Y.; Li, Z.; Chen, T.; Liu, Y.; Duan, C.; Shen, J.;

Punjabi, A. Tailoring Dye-Sensitized Upconversion Nanoparticle Excitation Bands towards Excitation Wavelength Selective Imaging. *Nanoscale* **2015**, *7* (44), 18424–18428.

(180) Zou, X.; Xu, M.; Yuan, W.; Wang, Q.; Shi, Y.; Feng, W.; Li, F. A Water-Dispersible Dye-Sensitized Upconversion Nanocomposite Modified with Phosphatidylcholine for Lymphatic Imaging. *Chem. Commun.* **2016**, *52* (91), 13389–13392.

(181) Muhr, V.; Würth, C.; Kraft, M.; Buchner, M.; Baeumner, A. J.; Resch-Genger, U.; Hirsch, T. Particle-Size-Dependent Forster Resonance Energy Transfer from Upconversion Nanoparticles to Organic Dyes. *Anal. Chem.* **2017**, *89* (9), 4868–4874.

(182) Chen, G.; Damasco, J.; Qiu, H.; Shao, W.; Ohulchanskyy, T. Y.; Valiev, R. R.; Wu, X.; Han, G.; Wang, Y.; Yang, C.; et al. Energy-Cascaded Upconversion in an Organic Dye-Sensitized Core/Shell Fluoride Nanocrystal. *Nano Lett.* **2015**, *15* (11), 7400–7407.

(183) Shao, W.; Chen, G.; Kuzmin, A.; Kutscher, H. L.; Pliss, A.; Ohulchanskyy, T. Y.; Prasad, P. N. Tunable Narrow Band Emissions from Dye-Sensitized Core/Shell/Shell Nanocrystals in the Second near-Infrared Biological Window. *J. Am. Chem. Soc.* **2016**, *138* (50), 16192–16195.

(184) Chen, G.; Shao, W.; Valiev, R. R.; Ohulchanskyy, T. Y.; He, G. S.; Ågren, H.; Prasad, P. N. Efficient Broadband Upconversion of Near-Infrared Light in Dye-Sensitized Core/Shell Nanocrystals. *Adv. Opt. Mater.* **2016**, *4* (11), 1760–1766.

(185) Dong, H.; Sun, L.-D.; Yan, C.-H. Energy Transfer in Lanthanide Upconversion Studies for Extended Optical Applications. *Chem. Soc. Rev.* **2015**, *44* (6), 1608–1634.

(186) Ehlert, O.; Thomann, R.; Darbandi, M.; Nann, T. A Four-Colour Colloidal Multiplexing Nanoparticle System. *ACS Nano* **2008**, *2* (1), 120–124.

(187) Boyer, J. C.; Vetrone, F.; Cuccia, L. A.; Capobianco, J. A. Synthesis of Colloidal Upconverting NaYF4 Nanocrystals Doped with Er^{3+}, Yb^{3+} and Tm^{3+}, Yb^{3+} via Thermal Decomposition of Lanthanide Trifluoroacetate Precursors. *J. Am. Chem. Soc.* **2006**, *128* (23), 7444–7445.

(188) Cheng, L.; Yang, K.; Zhang, S.; Shao, M.; Lee, S.; Liu, Z. Highly-Sensitive Multiplexed in Vivo Imaging Using Pegylated Upconversion Nanoparticles. *Nano Res.* **2010**, *3* (10), 722–732.

(189) Wilson, R.; Cossins, A. R.; Spiller, D. G. Encoded Microcarriers for High-Throughput Multiplexed Detection. *Angew. Chemie - Int. Ed.* **2006**, *45* (37), 6104–6117.

(190) Niu, W.; Wu, S.; Zhang, S. A Facile and General Approach for the Multicolour Tuning of Lanthanide-Ion Doped $NaYF_4$ Upconversion Nanoparticles within a Fixed Composition. *J. Mater. Chem.* **2010**, *20* (41), 9113–9117.

(191) Yin, A.; Zhang, Y.; Sun, L.; Yan, C. Colloidal Synthesis and Blue Based Multicolour Upconversion Emissions of Size and Composition Controlled Monodisperse Hexagonal $NaYF_4$:Yb,Tm Nanocrystals. *Nanoscale* **2010**, *2* (6), 953–959.

(192) Mai, H. X.; Zhang, Y. W.; Si, R.; Yan, Z. G.; Sun, L. D.; You, L. P.; Yan, C. H. High-Quality Sodium Rare-Earth Fluoride Nanocrystals: Controlled Synthesis and Optical Properties. *J. Am. Chem. Soc.* **2006**, *128* (19), 6426–6436.

(193) Teng, X.; Zhu, Y.; Wei, W.; Wang, S.; Huang, J.; Naccache, R.; Hu, W.; Tok, A. I. Y.; Han, Y.; Zhang, Q.; et al. Lanthanide-Doped $NaxScF_{3+x}$ Nanocrystals: Crystal Structure Evolution and Multicolour Tuning. *J. Am. Chem. Soc.* **2012**, *134* (20), 8340–8343.

(194) Niu, W.; Wu, S.; Zhang, S. Utilizing the Amidation Reaction to Address the "Cooperative Effect" of Carboxylic Acid/Amine on the Size, Shape, and Multicolour Output of Fluoride Upconversion Nanoparticles. *J. Mater. Chem.* **2011**, *21* (29), 10894–10902.

(195) Niu, W.; Wu, S.; Zhang, S.; Li, J.; Li, L. Multicolour Output and Shape Controlled Synthesis of Lanthanide-Ion Doped Fluorides Upconversion Nanoparticles. *Dalt. Trans.* **2011**, *40* (13), 3305–3314.

(196) Liao, J.; Yang, Z.; Wu, H.; Lai, S.; Qiu, J.; Song, Z.; Yang, Y.; Zhou, D.; Yin, Z. Upconversion Luminescence Enhancement of $NaYF_4$: Yb^{3+}, Er^{3+} Nanoparticles on Inverse Opal Surface. *Surf. Rev. Lett.* **2014**, *21* (1), 1450017.

(197) Yan, D.; Yang, Z.; Liao, J.; Wu, H.; Qiu, J.; Song, Z.; Zhou, D.; Yang, Y.; Ying, Z. Investigation of the Mechanism of Upconversion Luminescence in Er^{3+}/Yb^{3+} Co-Doped $Bi_2Ti_2O_7$ Inverse Opal. *Chinese Opt. Lett.* **2013**, *11* (4), 41602.

(198) Yin, W.; Zhou, L.; Gu, Z.; Tian, G.; Jin, S.; Yan, L.; Liu, X.; Xing, G.; Ren, W.; Liu, F.; et al. Lanthanide-Doped $GdVO_4$ Upconversion Nanophosphors with Tunable Emissions and Their Applications for Biomedical Imaging. *J. Mater. Chem.* **2012**, *22* (14), 6974–6981.

(199) Chen, G.; Qiu, H.; Fan, R.; Hao, S.; Tan, S.; Yang, C.; Han, G. Lanthanide-Doped Ultrasmall Yttrium Fluoride Nanoparticles with Enhanced Multicolour Upconversion

Photoluminescence. *J. Mater. Chem.* **2012**, *22* (38), 20190–20196.

(200) Mahalingam, V.; Naccache, R.; Vetrone, F.; Capobianco, J. A. Preferential Suppression of High-Energy Upconverted Emissions of Tm^{3+} by Dy^{3+} Ions in $Tm^{3+}/Dy^{3+}/Yb^{3+}$-Doped $LiYF_4$ Colloidal Nanocrystals. *Chem. Commun.* **2011**, *47* (12), 3481–3483.

(201) Qian, H. S.; Zhang, Y. Synthesis of Hexagonal-Phase Core-Shell $NaYF_4$ Nanocrystals with Tunable Upconversion Fluorescence. *Langmuir* **2008**, *24* (21), 12123–12125.

(202) Yang, Z. W.; Wang, Y. D.; Liao, J. Y.; Yang, J. Z.; Qiu, J. B.; Song, Z. G. Upconversion Emission Modification and White Light Generation in $NaYF_4$: Yb^{3+}, Er^{3+}, Tm^{3+} Nanocrystals/Opal Photonic Crystal Composites. *IEEE Photonics J.* **2015**, *7* (6), 1–8.

(203) Wang, F.; Liu, X. Upconversion Multicolour Fine-Tuning: Visible to near-Infrared Emission from Lanthanide-Doped $NaYF_4$ Nanoparticles. *J. Am. Chem. Soc.* **2008**, *130* (17), 5642–5643.

(204) Chan, E. M.; Han, G.; Goldberg, J. D.; Gargas, D. J.; Ostrowski, A. D.; Schuck, P. J.; Cohen, B. E.; Milliron, D. J. Combinatorial Discovery of Lanthanide-Doped Nanocrystals with Spectrally Pure Upconverted Emission. *Nano Lett.* **2012**, *12* (7), 3839–3845.

(205) Chan, E. M.; Gargas, D. J.; Schuck, P. J.; Milliron, D. J. Concentrating and Recycling Energy in Lanthanide Codopants for Efficient and Spectrally Pure Emission: The Case of $NaYF_4$:Er^{3+}/Tm^{3+} Upconverting Nanocrystals. *J. Phys. Chem. B* **2012**, *116* (35), 10561–10570.

(206) Dou, Q.; Idris, N. M.; Zhang, Y. Sandwich-Structured Upconversion Nanoparticles with Tunable Colour for Multiplexed Cell Labeling. *Biomaterials* **2013**, *34* (6), 1722–1731.

(207) Liu, X.; Wang, Y.; Li, X.; Yi, Z.; Deng, R.; Liang, L.; Xie, X.; Loong, D. T. B.; Song, S.; Fan, D.; et al. Binary Temporal Upconversion Codes of Mn^{2+}-Activated Nanoparticles for Multilevel Anti-Counterfeiting. *Nat. Commun.* **2017**, *8* (1), 1–7.

(208) Zhang, C.; Yang, L.; Zhao, J.; Liu, B.; Han, M. Y.; Zhang, Z. White-Light Emission from an Integrated Upconversion Nanostructure: Toward Multicolour Displays Modulated by Laser Power. *Angew. Chemie - Int. Ed.* **2015**, *54* (39), 11531–11535.

(209) Gong, S.; Ren, Z.; Jiang, S.; Li, M.; Li, X.; Wei, X.; Xu, G.; Shen, G.; Han, G. Phase-Modified Up-Conversion Luminescence in Er-Doped Single-Crystal $PbTiO_3$ Nanofibers. *J. Phys. Chem. C* **2014**, *118* (10), 5486–5493.

(210) Chen, L.; Rong, Y.; Ren, M.; Wu, W.; Qin, M.; Pan, C.; Ma, Q.; Liu, S.; Wu, B.; Wu, E.; et al. Selective Polarization Modification of Upconversion Luminescence of $NaYF_4:Yb^{3+},Er^{3+}$ Nanoparticles by Plasmonic Nanoantenna Arrays. *J. Phys. Chem. C* **2018**, *122* (27), 15666–15672.

(211) Chaudan, E.; Kim, J.; Tusseau-Nenez, S.; Goldner, P.; Malta, O. L.; Peretti, J.; Gacoin, T. Polarized Luminescence of Anisotropic $LaPO_4$:Eu Nanocrystal Polymorphs. *J. Am. Chem. Soc.* **2018**, *140* (30), 9512–9517.

(212) Shi, S.; Sun, L. D.; Xue, Y. X.; Dong, H.; Wu, K.; Guo, S. C.; Wu, B. T.; Yan, C. H. Scalable Direct Writing of Lanthanide-Doped $KMnF_3$ Perovskite Nanowires into Aligned Arrays with Polarized Up-Conversion Emission. *Nano Lett.* **2018**, *18* (5), 2964–2969.

(213) Liu, H.; Huang, K.; Valiev, R. R.; Zhan, Q.; Zhang, Y.; Ågren, H. Photon Upconversion Kinetic Nanosystems and Their Optical Response. *Laser Photonics Rev.* **2018**, *12* (1), 1700144.

(214) Yang, D.; Peng, Z.; Zhan, Q.; Huang, X.; Peng, X.; Guo, X.; Dong, G.; Qiu, J. Anisotropic Excitation Polarization Response from a Single White Light-Emitting β-$NaYF_4:Yb^{3+},Pr^{3+}$ Microcrystal. *Small* **2019**, *15* (43), 1–9.

(215) Kim, J.; Michelin, S.; Hilbers, M.; Martinelli, L.; Chaudan, E.; Amselem, G.; Fradet, E.; Boilot, J. P.; Brouwer, A. M.; Baroud, C. N.; et al. Monitoring the Orientation of Rare-Earth-Doped Nanorods for Flow Shear Tomography. *Nat. Nanotechnol.* **2017**, *12* (9), 914–919.

(216) Zhou, J.; Chen, G.; Wu, E.; Bi, G.; Wu, B.; Teng, Y.; Zhou, S.; Qiu, J. Ultrasensitive Polarized Up-Conversion of Tm^{3+}-Yb^{3+} Doped β-$NaYF_4$ Single Nanorod. *Nano Lett.* **2013**, *13* (5), 2241–2246.

(217) Chen, P.; Song, M.; Wu, E.; Wu, B.; Zhou, J.; Zeng, H.; Liu, X.; Qiu, J. Polarization Modulated Upconversion Luminescence: Single Particle vs. Few-Particle Aggregates. *Nanoscale* **2015**, *7* (15), 6462–6466.

(218) Rodríguez-Sevilla, P.; Labrador-Páez, L.; Wawrzyńczyk, D.; Nyk, M.; Samoć, M.; Kar, A. K.; Mackenzie, M. D.; Paterson, L.; Jaque, D.; Haro-González, P. Determining the 3D Orientation of Optically Trapped Upconverting Nanorods by in Situ Single-Particle Polarized Spectroscopy. *Nanoscale* **2016**, *8* (1), 300–308.

(219) Bergstrand, J.; Liu, Q.; Huang, B.; Peng, X.; Würth, C.; Resch-Genger, U.; Zhan, Q.;

Widengren, J.; Ågren, H.; Liu, H. On the Decay Time of Upconversion Luminescence. *Nanoscale* **2019**, *11* (11), 4959–4969.

(220) Zhang, H.; Jiang, J.; Gao, P.; Yang, T.; Zhang, K. Y.; Chen, Z.; Liu, S.; Huang, W.; Zhao, Q. Dual-Emissive Phosphorescent Polymer Probe for Accurate Temperature Sensing in Living Cells and Zebrafish Using Ratiometric and Phosphorescence Lifetime Imaging Microscopy. *ACS Appl. Mater. Interfaces* **2018**, *10* (21), 17542–17550.

(221) Liao, Z.; Tropiano, M.; Mantulnikovs, K.; Faulkner, S.; Vosch, T.; Just Sørensen, T. Spectrally Resolved Confocal Microscopy Using Lanthanide Centred Near-IR Emission. *Chem. Commun.* **2015**, *51* (12), 2372–2375.

(222) Lu, Y.; Zhao, J.; Zhang, R.; Liu, Y.; Liu, D.; Goldys, E. M.; Yang, X.; Xi, P.; Sunna, A.; Lu, J.; et al. Tunable Lifetime Multiplexing Using Luminescent Nanocrystals. *Nat. Photonics* **2014**, *8* (1), 32–36.

(223) Dong, H.; Sun, L. D.; Li, L. D.; Si, R.; Liu, R.; Yan, C. H. Selective Cation Exchange Enabled Growth of Lanthanide Core/Shell Nanoparticles with Dissimilar Structure. *J. Am. Chem. Soc.* **2017**, *139* (51), 18492–18495.

(224) Fischer, S.; Bronstein, N. D.; Swabeck, J. K.; Chan, E. M.; Alivisatos, A. P. Precise Tuning of Surface Quenching for Luminescence Enhancement in Core-Shell Lanthanide-Doped Nanocrystals. *Nano Lett.* **2016**, *16* (11), 7241–7247.

(225) Liu, Y.; Zhou, S.; Tu, D.; Chen, Z.; Huang, M.; Zhu, H.; Ma, E.; Chen, X. Amine-Functionalized Lanthanide-Doped Zirconia Nanoparticles: Optical Spectroscopy, Time-Resolved Fluorescence Resonance Energy Transfer Biodetection, and Targeted Imaging. *J. Am. Chem. Soc.* **2012**, *134* (36), 15083–15090.

(226) Chen, X.; Jin, L.; Sun, T.; Kong, W.; Yu, S. F.; Wang, F. Energy Migration Upconversion in Ce (III)-Doped Heterogeneous Core−Shell−Shell Nanoparticles. *Small* **2017**, *13* (43), 1701479.

(227) Zhou, L.; Fan, Y.; Wang, R.; Li, X.; Fan, L.; Zhang, F. High-Capacity Upconversion Wavelength and Lifetime Binary Encoding for Multiplexed Biodetection. *Angew. Chemie* **2018**, *130* (39), 13006–13011.

(228) Dong, H.; Sun, L. D.; Feng, W.; Gu, Y.; Li, F.; Yan, C. H. Versatile Spectral and Lifetime Multiplexing Nanoplatform with Excitation Orthogonalized Upconversion Luminescence. *ACS Nano* **2017**, *11* (3), 3289–3297.

Chapter 2 Materials and methods

In this chapter, the synthetic strategies of the RE doped luminescent nanocrystals and the characterization methods used in this thesis are introduced. The structures for different morphologies including core nanoparticles, core-shell nanoparticles, and core-multi shell nanoparticles. The characterization methods including XRD, SEM, TEM, STEM, absorbance spectrum, photoluminescence spectroscopy, time-resolved photoluminescence lifetime, power-dependent intensity curves, and single nanoparticle microscopy imaging are described together with the commercial instruments and home-built optical systems used.

2.1 Chemicals and reagents

The chemicals and reagents described in this thesis are listed below. These were used as received without further purification or modification unless described in the methods given in the result chapters.

Table 2.1 Manufacturer details for used chemicals and reagents

Chemicals and Reagents	Purity	CAS number	Manufacturer
Yttrium(III) chloride hexahydrate ($YCl_3 \cdot 6H_2O$)	99.99% trace metals basis	10025-94-2	Sigma-Aldrich (Australia)
Ytterbium(III) chloride hexahydrate ($YbCl_3 \cdot 6H_2O$)	99.998% trace metals basis	10035-01-5	Sigma-Aldrich (Australia)
Neodymium(III) chloride hexahydrate ($NdCl_3 \cdot 6H_2O$)	99.998% trace metals basis	13477-89-9	Sigma-Aldrich (Australia)
Thulium(III) chloride hexahydrate ($TmCl_3 \cdot 6H_2O$)	99.99% trace metals basis	1331-74-4	Sigma-Aldrich (Australia)

Erbium(III) chloride hexahydrate ($ErCl_3 \cdot 6H_2O$)	99.995% trace metals basis	10025-75-9	Sigma-Aldrich (Australia)
Sodium hydroxide (NaOH)	semiconductor grade, 99.99% trace metals basis	1310-73-2	Sigma-Aldrich (Australia)
Ammonium fluoride (NH_4F)	⩾ 99.99% trace metals basis	12125-01-8	Sigma-Aldrich (Australia)
Oleic Acid (OA)	Technical grade, 90%	112-80-1	Sigma-Aldrich (Australia)
1-Octadecene (ODE)	Technical grade, 90%	112-88-9	Sigma-Aldrich (Australia)
Ethanol	Undenatured 100%	64-17-5	Chem-Supply (Australia)
Methanol	for HPLC, ⩾ 99.9%	67-56-1	Sigma-Aldrich (Australia)
Cyclohexane	for HPLC, ⩾ 99.9%	110-82-7	Chem-Supply (Australia)
2,2′-Azobis(2-methylpropionitrile)	98%	78-67-1	Sigma-Aldrich (Australia)
Poly(ethylene glycol) methyl ether methacrylate	average Mn 300, contains 100 ppm MEHQ as inhibitor	26915-72-0	Sigma-Aldrich (Australia)
Phosphoric acid 2-hydroxyethyl methacrylate ester	Premium Grade	52628-03-2	Sigma-Aldrich (Australia)

4-Cyano-4-(phenylcarbonothioylthio) pentanoic acid	Premium Grade	201611-92-9	Sigma-Aldrich (Australia)
Chloroform-d	99.8 atom % D	865-49-6	Sigma-Aldrich (Australia)
Toluene	anhydrous, 99.8%	108-88-3	Chem-supply
Tetrahydrofuran (THF)	anhydrous, ⩾ 99.9%, inhibitor-free	109-99-9	Sigma-Aldrich (Australia)
N-(3-Dimethylaminopropyl)-N′-ethylcarbodiimide hydrochloride (EDC)	Premium Grade	N/A	Life Technologies Australia Pty Ltd.
Tris buffer	Ultrapure, powder format	N/A	Life Technologies Australia Pty Ltd.
HEPES buffer	Ultrapure	N/A	Life Technologies Australia Pty Ltd.
PBS buffer	10×concentrated, pH 7.2	N/A	Life Technologies Australia Pty Ltd.
DNA (Deoxyribonucleic Acid)	HIV Target/C1/C2 EV Target/C1/C2 HBV Target/C1/C2 HPV Target/C1/C2 HCV Target/C1/C2	N/A	Integrated DNA technologies

2.2 Instruments and equipment

The commercial instruments and equipment described in this thesis are listed in the following table. The commercial components that made up the in house-constructed microscopy instruments are not included in this list.

Table 2.2 Instruments with specifications used for material synthesis.

Instrument/Equipment	**Property**	**Manufacturer**
Magnetic stirrer	0-1800 rpm	Labquip (Australia)
Heating mantle	Range 20 to 400 ºC	Labquip (Australia)
Temperature controller	Range 20 to 400 ºC	Labquip (Australia)
Three-neck round-bottom flask	50 mL, 100 mL	Synthware (China)
Thermometer	Range: -10 to 330 ºC	RS Components PTY Ltd.
Flow control adapter	19/22	Synthware (China)
Teflon-coated, Elliptical rare earth extra power stir bars	15 × 10 mm	Sigma-Aldrich (Australia)
Micropipettes	ranges: 10–100 µL, 100–1,000 µL and 500–5,000 µL;	Eppendorf (Germany)
Centrifuge	Centrifuge 5424 Centrifuge 5804	Eppendorf (Germany)
Vortex mixer	LSE	Corning (Australia)
Ultrasonic cleaner	Commercial Benchtop Cleaners (FXP) 2.7 Liter	Unisonics (Australia)

Laboratory balance	SJF2104 (0.1 mg)	ProSciTech (Australia)
TEM	Model: Tecnai T20 JEM-ARM200F/ JEOL TEM-2200FS	FEI JEOL
TEM copper grids	300 mesh with carbon film	Pacific Grid-Tech (USA)
UV-Vis spectrophotometer	Agilent Cary 60	Agilent Technologies (USA)
Tweezers	Style: N5	Dumont
Dialysis tubing cellulose membrane	3500 Dalton 600-8000 Dalton	Thermo Fisher
Glass slide	25×57 mm	Hurst Scientific Pty. Ltd.
Cover slip	22×22 mm	Muraban Laboratories
Pipettes	Eppendorf Reference® 2, whole set	Eppendorf (Germany)
Pipette tips	epT.I.P.S.® Motion, full range	Eppendorf (Germany)
Tubes	SSUbio 1260-00 (1.5 mL) and 1310-00 (2.0 mL)	Scientific Specialties, Inc.

2.3 Characterisation methods and home-built optical instruments

2.3.1 Characterisation methods

The morphology characterization of the nanoparticles was performed by transmission electron microscope (TEM), JEOL TEM-1400 at an acceleration voltage of 120 kV and JEOL TEM-2200FS with the 200 kV voltage. High-angle annular dark-field imaging in the scanning TEM (HAADF-STEM) observations were performed on The Helios G4 PFIB series Dual Beam

systems with an accelerating voltage of 30 kV. The cyclohexane dispersed UCNPs were imaged by dropping them onto carbon-coated copper grids.

The surface morphology and structure of the beads and single nanoparticle correlation were investigated using a Zeiss Supra 55VP Scanning Electron Microscope (SEM) operated at 20.00 kV.

The phase composition of the core sample was detected by X-ray powder diffraction (XRD) with a Bruker D8 Discover diffractometer with a slit of 0.02° at a scanning speed of 2° min-1 using CuKα1 radiation, λ=0.154 nm.

The absorption spectrum was measured with the Agilent Cary 60 UV-Vis spectrophotometer in the wavelength range of 700 to 1100 nm in a step of 1 nm.

The UCNPs' optical properties were measured at the single-particle scale using the house built laser scanning confocal microscope. To achieve the best imaging quality, the sample slides carrying individual-distributed UCNPs were carefully prepared. A coverslip was washed with pure ethanol by ultrasonication, and then the coverslip was air-dried. The poly-L-lysine solution (at 0.1% w/v concentration in water) was added to the coverslip, the polylysine was washed off with water after 30 minutes and left to dry at room temperature. 20 μL of the nanoparticles (diluted to 0.01 mg/mL in cyclohexane) was dropped onto the surface of the coverslip and the coverslip flushed by cyclohexane carefully and then left to dry. After being air-dried, the coverslip was put over a clean glass slide before measurement.

20 μL of the UCNPs (diluted to 0.01 mg/mL in cyclohexane) was dropped onto the treated surface, which was immediately washed with 500 μL cyclohexane twice. After being air-dried, the coverslip was put over a clean glass slide spread with 10 μL as-prepared embedding medium, and any air bubbles were squeezed out by gentle force. The sample was kept at room temperature for another 24 h to ensure complete dryness before measurement.

2.3.2 Spectra measurement system

The spectral properties of UCNPs in solution were measured with a home-built system. Fig. 2.1 shows the schematic drawing of the experimental setup, a fiber-coupled 980 nm (BL976-PAG500, controller CLD1015, Thorlabs) an 808 nm (LE-LS-808-300TFCS) diode laser works as the excitation source. The emission spectra of the sample were measured by a commercial spectrometer (Shamrock 193i, Andor) with an EMCCD (Electron Multiplying Charge Coupled Device, iXon Ultra 888, Andor) as the detector. Additionally, the emission signal was filtered by a 750 short pass filter (SPF, FF01-750/SP-25, Semrock).

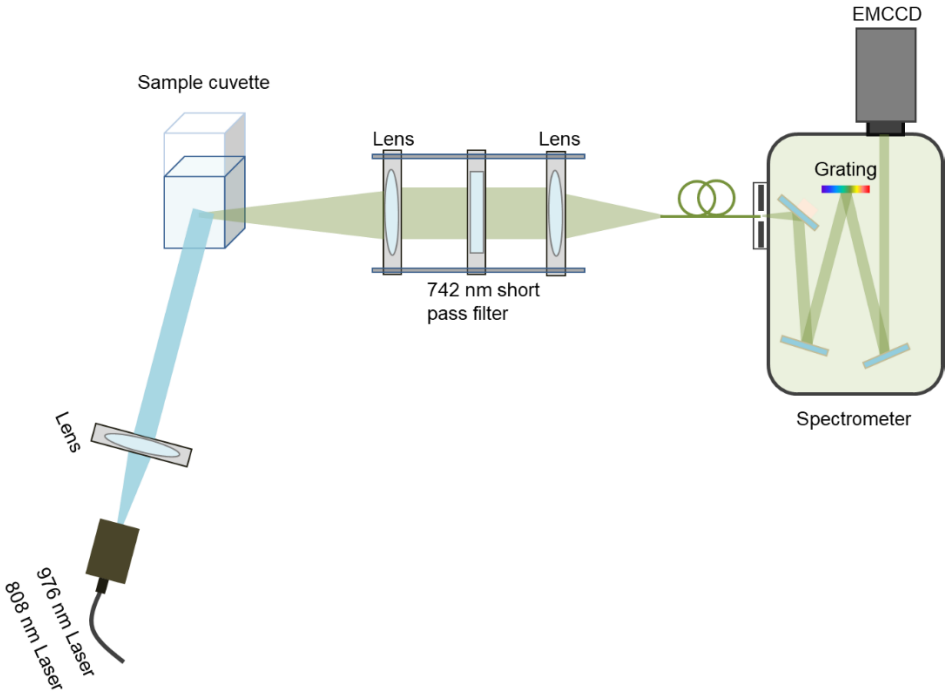

Figure 2.1 Spectra measurement setup for UCNPs in cyclohexene solution in the quartz cuvette.

2.3.3 Confocal microscope for single nanoparticles

We built a stage-scan confocal microscope for power-dependent intensity and lifetime measurements of single nanoparticles, as shown in Figure. 2.2. The excitation source is an 808 nm single mode polarized laser, which is focused onto the sample through a 100x objective lens (UPLanSApo100X, oil immersion, NA = 1.40, Olympus Inc., JPN). The emission from the sample is collected by the same objective lens and refocused into an optical fiber which has

a core size matching with system first Airy disk. The fluorescence signals can be filtered from the laser by a short-pass dichroic mirror (DM, ZT785spxxr-UF1, Chroma Inc., USA) and a short pass filter (SPF, ET750sp-2p8, Chroma Inc., USA). A single-photon counting avalanche photodiode (APD, SPCM-AQR-14-FC, Excelitas Inc., USA) is connected to the collection of multi-mode fiber (MMF, M42L02, Thorlabs Inc., USA) to detect the emission intensity. The scanning is achieved by moving the 3D piezo stage. During the point by the point scanning process, when the excitation laser beam moves closer to a single nanoparticle, the system will detect a brighter emission intensity. Therefore each single nanoparticle will show a Gaussian spot in the confocal scanning microscopic image. The maximum brightness value (photon counts) of each Gaussian spot can be used to represent the brightness of that single particle. For each confocal image, we record all of the single nanoparticles' brightness values (photon counts). We evaluate more than 30 single nanoparticles' values to calculate the mean brightness.

For the lifetime measurement here, we modulate the diode laser to produce 200 μs excitation pulses. The photon-counting SPAD is continuously switched on to capture the long-lifetime luminescence. For each time point, the gate-width is 2 μs with an accumulation of 10000 times. The pulsed excitation, time-gated data collection, and the confocal scanning are controlled and synchronized using a multifunction data acquisition device (USB-6343, National Instruments) and a purpose-built LabVIEW program.

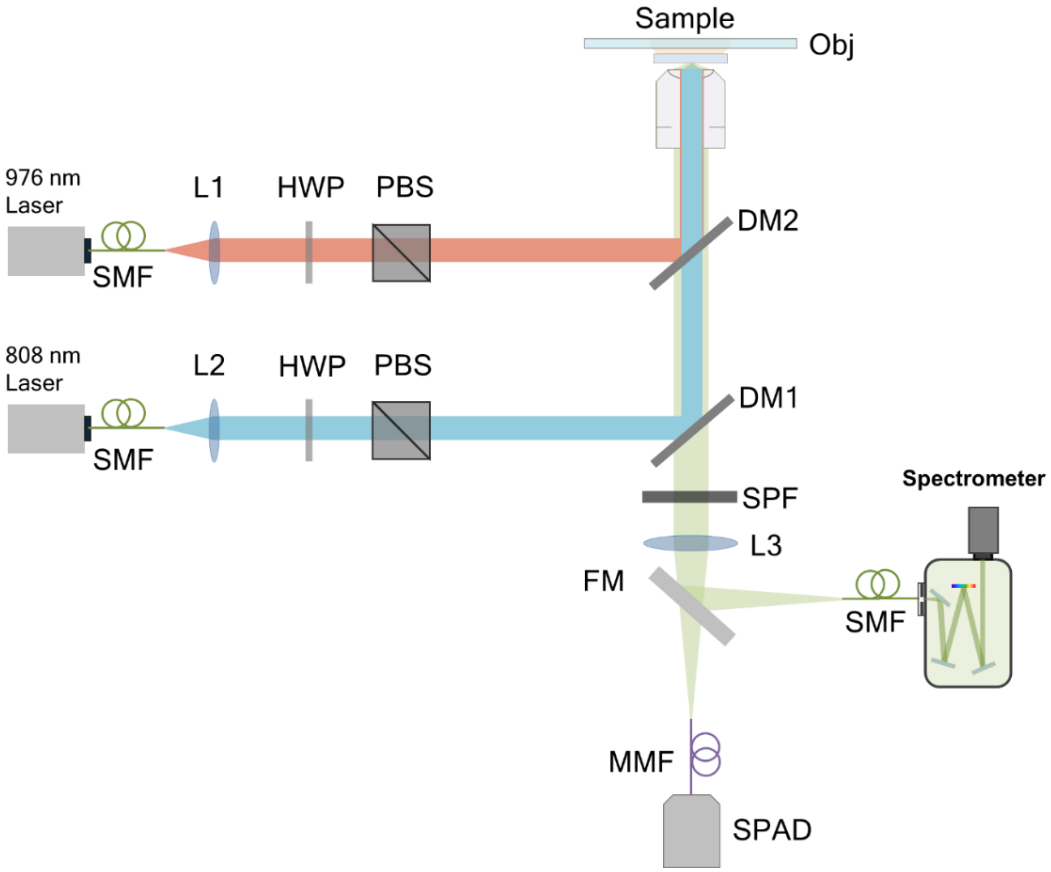

Figure 2.2. Schematic view of confocal microscopy. (SMF, single-mode fiber; MMF, multi-mode fiber; L1, L2 collimation lens; L3, collection lens; HWP, half-wave plate; PBS, polarized beam splitter; FM, flexible mirror; DM, dichroic mirror; Obj, objective lens; SPF, short pass filter; SPAD, single-photon avalanche diode; Spectrometer (Shamrock 193i, Andor).

2.3.4 Wide-field microscope for spectra and lifetime measurement

We built a widefield fluorescence microscope to acquire the fluorescence lifetime imaging sequences of Yb^{3+}-Nd^{3+}-Er^{3+} core-multi shell single nanoparticles as shown in Figure.2.3. A single mode diode-pumped solid-state laser (LU0808M250, Lumics Inc., GER, 808 nm, the excitation power density of 5.46 kW/cm^2) is used to excite the nanoparticles after expanding the laser beam 3 times. The emission of τ^2-dots is collected by a high NA objective lens (UPLanSApo100X, oil immersion, NA = 1.40, Olympus Inc., JPN) and separated from the laser reflection by a short-pass dichroic mirror (DM1, ZT785spxxr-UF1, Chroma Inc., USA) and a short pass filter (SPF, ET750sp-2p8, Chroma Inc., USA), then focused by a tube lens to

the time-resolved sCMOS camera (iStar sCMOS, Andor Inc., UK). The camera also functions as a pulse modulator of an exciting laser beam via a BNC cable. By applying the Kinetics Mode of the camera and Integrate-On-Chip (IOC) at 250Hz, we acquired the lifetime imaging sequences of 75 frames from 0 μs to 3750 μs with a time gate of 50 μs, under the laser excitation pulse of 0-200 μs. The IOC mode here we used enables the accumulation of fluorescence signal to greatly improve the signal-to-noise ratio. To measure the fluorescence lifetime imaging sequences of τ^2-dots under 976 nm excitation, a single-mode 976 nm laser (BL976-PAG900, Thorlabs Inc., USA, the excitation power density of 8.7 kW/cm^2) is also added in the setup as the excitation light. After collimation, the excitation beam is expanded 2.5 times and then reflected by the short-pass dichroic mirror (DM2, T875spxrxt-UF1, Chroma Inc., USA), and focused through the objective lens to the sample slide.

The fluorescence signals can also be coupled into a multi-mode fiber (MMF, M24L02, Thorlabs Inc., USA) by switching a flip mirror and then detected by a miniature monochromator (iHR550, Horiba Inc., JPN) for measuring upconversion emission spectra. The detected spectra region ranges from 400 to 740 nm.

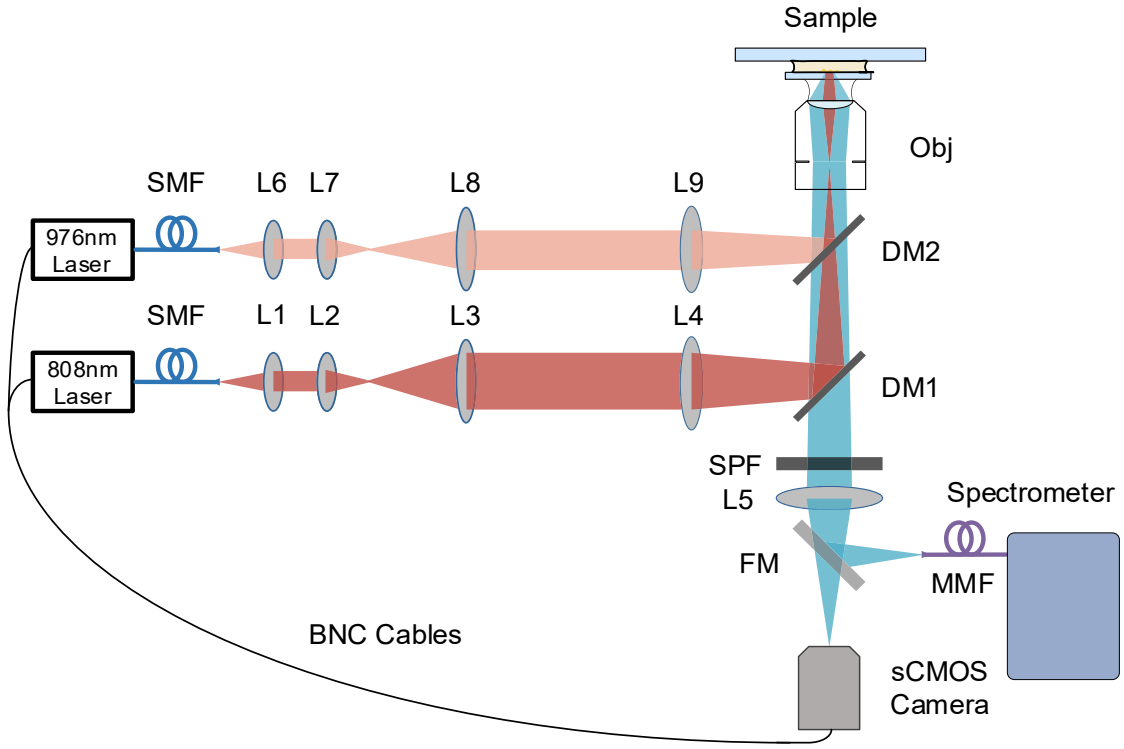

Fig. 2.3. Schematic view of widefield fluorescence imaging setup. (SMF, single-mode fiber; MMF, multi-mode fiber; L1&L6: collimation lens; L2 and L3 & L7 and L8: lenses for beam expanding; L4 & L9: tube lenses; DM1&DM2: dichroic mirrors; Obj: objective lens; L5: collection lens; SPF: short pass filter; FM, flexible mirror).

Structured illumination microscopy (SIM), as a wide-field super-resolution technique, was based on the spatial modulation of the excitation patterns on the sample plane. In this work, a digital micro-mirror device (DMD, DLP 4100, Texas Instruments Inc., USA) was used as the spatial light modulator to generate excitation patterns. DMD contained an array of 1024×768 micro-mirrors on the chip. The size of each micromirror was 13.68×13.68 μm^2. Each micro-mirror can be tilted to two positions along its diagonal: ±12° tilt to deflect the incident light beam away from the optical path. These micro-mirrors can be controlled independently to modulate the amplitude of incoming light to generate arbitrary illumination patterns. As shown in Fig.2.4, the optical system for the time-resolved SIM was built based on conventional widefield fluorescence microscopy (Fig. 2.3) with proper modification. Then we acquired the nine groups of lifetime image series with nine illuminating patterns, corresponding to three different angular orientations ($\theta1 = 0°$, $\theta2 = 60°$ and $\theta3 = 120°$) and three different phase shifts ($\varphi1 = 0°$, $\varphi2 = 120°$ and $\varphi3 = 240°$). The other test parameters were the same as the conventional widefield microscopy. In the reconstruction of the super-resolution image series, these nine images are processed in the Fourier domain to reconstruct the final super-resolution image.

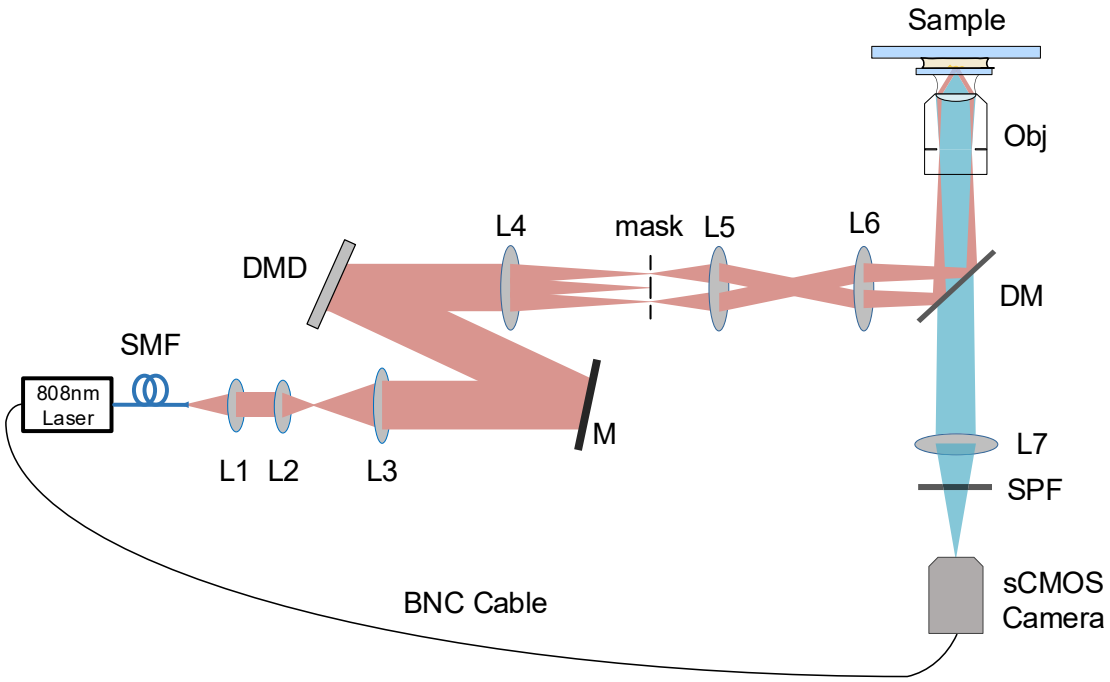

Fig. 2.4. Time-resolved structured illumination microscopy for sub-diffraction imaging. SMF, single-mode fibre; L1: collimation lens; L2 and L3: lenses for beam expanding; M: silver mirror; DMD: digital micromirror device; L4-L6: relay lens; DM: dichroic mirror; Obj: objective lens; L7: collection lens; SPF: short pass filter)

2.4 General $NaREF_4$ nanocrystals and polymer synthesis

2.4.1 General $NaREF_4$ nanocrystals synthesis methods

In this thesis, the uniform RE doped core nanoparticles were synthesized by the co-precipitation method[1–3] and the hot-injection method[4–8] was utilized for core-shell and core-multi shell nanoparticles synthesis. The lanthanide-oleate complexes, sodium hydroxide reagents, and ammonium fluoride were reacted in the three-neck flask. Temporally discrete Nucleation followed by phase growth of the UCNPs were performing in solution by heating it to 300 °C.[9] Due to the low energy barrier between the nucleation and growth process, the reaction conditions such as solvent composition, temperature, reaction time, etc. were very important to produce uniform phase and size UCNPs. High boiling point solvents long-chain hydrocarbons (1-octadecene) and unsaturated fatty acids (oleic acid) were used as solvents for

the reaction. OA also acted as the surfactant ligand molecules of the UCNPs to control their growth and the subsequent stabilization to avoid agglomeration. Because of the tiny lattice mismatch between different types of $NaREF_4$,[10] different lanthanide ions can be incorporated into one nanocrystal particle by varying the composition of the lanthanide-oleate precursor through the hot-injection method, which enables the co-doping of the sensitizer and activator ions in different layers to obtain high efficient upconversion emission (Fig. 2.5).

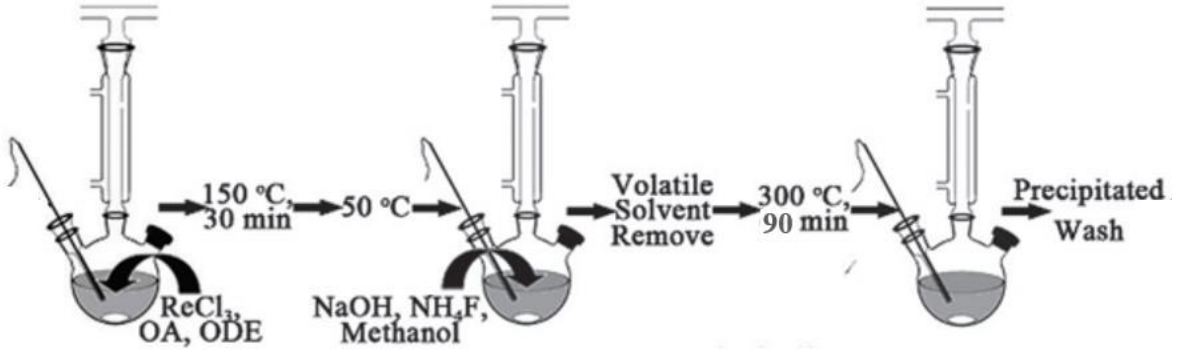

Figure 2.5 Schematic illustration of the co-precipitation synthesis of $NaREF_4$ nanocrystals.

2.4.2 Synthesis protocols of UCNPs

2.4.2.1 Lanthanide solution preparation and equipment set up

The stock solution of lanthanide chloride solution was prepared by dissolving $RECl_3.6H_2O$ in methanol. The lanthanide chloride was prepared with different concentrations in the range of 0.1 to 0.4 M and then stored in plastic tubes at -20 ℃ until needed. In this way, the lanthanide solutions can be stored for 12 months without noticeable precipitation. NaOH and NH_4F stock solutions were prepared by dissolving the appropriate amount of solid NaOH or NH_4F in methanol of 0.5 M concentrations. The stock solution could be stored in the fridge similar to the lanthanide solution for up to two months without noticeable precipitation.

Figure 2.6 shows the reaction equipment set up for the UCNP synthesis. A 50-mL three-neck flask with the round bottom (a) was used as the reaction container. It was equipped with a condenser (b) for inert gas flow, a stir bar for mixing the reaction solution, and a thermometer

(c) for monitoring the temperature of the reaction mix. The heat for the reaction was provided by a heating mantle (d) that was integrated with a temperature controller (e). A magnetic mixer (f) was employed to drive the stir bar inside the flask. The temperature of the reaction mix was adjusted using the heating mantle based on the temperature values observed with the thermometer. (g) An injection syringe was used to inject the precursor's solution to the reaction container.

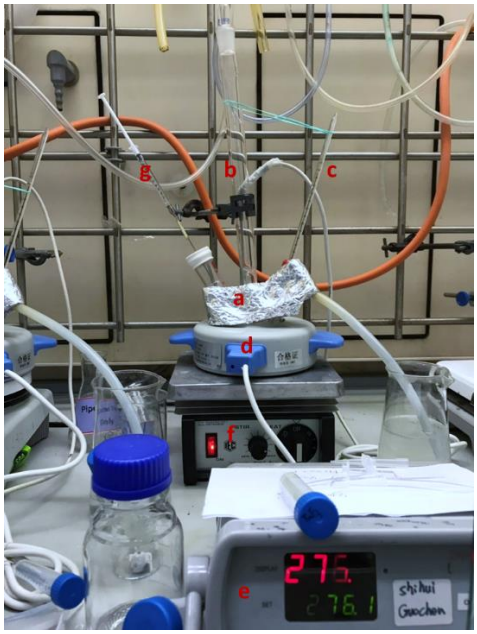

Figure 2.6 Reaction equipment set up for UCNPs synthesis. (a) Three-neck flask; (b) Glass condenser; (c) Thermometer; (d) Heating mantle; (e) Temperature controller; (f) Magnetic mixer; (g) Injection syringe.

2.4.2.2 One-pot synthesis of $NaYF_4$ core UCNPs

The $NaYF_4$:30%Yb, 2%Er core nanoparticles were synthesized using a coprecipitation method. In a typical procedure, 1 mmol $RECl_3$ (RE=Y, Yb, Er) with $YCl_3 \cdot 6H_2O$ (0.68 mmol), $YbCl_3 \cdot 6H_2O$ (0.3 mmol) and $ErCl_3 \cdot 6H_2O$ (0.02 mmol) together with oleic acid (OA, 6 mL) and 1-octadecene (ODE, 15 mL) were added to a 50 mL three-neck round-bottom flask under vigorous stirring. The resulting mixture was heated at 150 ^oC for 30 mins to form lanthanide oleate complexes. The solution was then cooled to room temperature. Subsequently, a methanol solution (6 mL) containing NaOH (2.5 mmol, 0.1g) and NH_4F (4 mmol, 0.14g) was added and

stirred at 50 °C for 30 mins, and then the mixture was slowly heated to 150 °C and kept for 20 mins under argon flow to remove the methanol and residual water. Next, the solution was quickly heated at 300 °C under argon flow for 1.5 h before cooling to room temperature (Figure 2.7).

For the purification, the resulting core nanoparticles were transferred into two 15-ml centrifuge tubes and precipitated by the addition of ethanol to precipitate the nanocrystals. The nanoparticles were precipitated in the bottom and the supernatant was discarded after centrifugation at 9000 rpm for 5 min. The final $NaYF_4$: Yb, Er nanocrystals were redispersed in 10 ml cyclohexane after washing with cyclohexane/ethanol/methanol several times.

The studied $NaYF_4$: Yb^{3+}, Tm^{3+}, $NaYF_4$: Yb^{3+}, Er^{3+} with a different doped concentration in this thesis were all synthesized the same method.

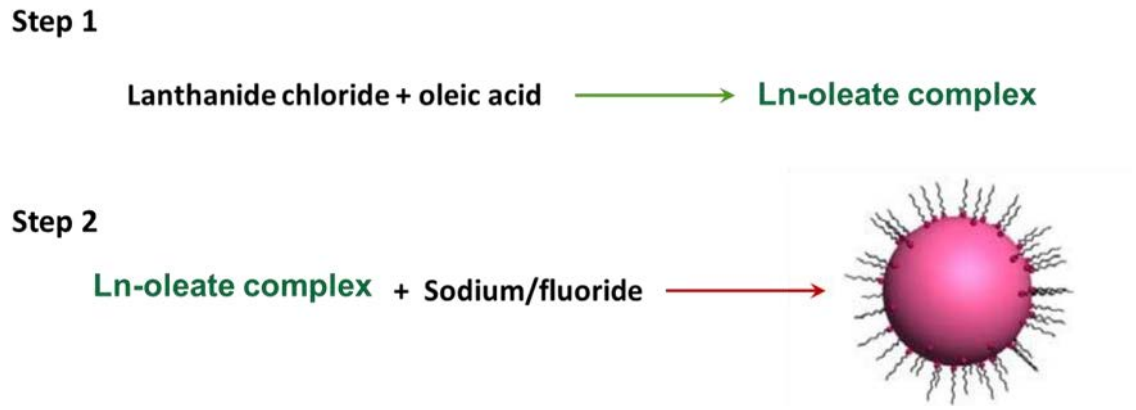

Figure 2.7 Schematic illustration of the co-precipitation strategy for the synthesis of lanthanide-doped $NaREF_4$ nanocrystals. Lanthanide-oleate precursors are prepared by the reaction of lanthanide chloride and oleic acid at 150 °C. The precipitation of the lanthanide-oleate precursors by sodium and fluoride at low temperature and subsequent annealing in high boiling solvent affords monodisperse $NaREF_4$ nanocrystals[2].

2.4.2.3 Epitaxial growth to form core-shell/core-multi-shell nanoparticles

The shell precursor solution was needed to prepare before the epitaxial growth of the nanocrystals by using the hot-injection method. A similar synthesized procedure for seed nanocrystals can be employed for the shell precursor growth, and then the precursors were used

to grow on the surface of preformed seed nanocrystals directly at a high temperature with a precision-controlled speed without the self-nucleation process (Figure 2.8). In this experiment, $NaYF_4$ shell precursors were prepared as an example, 1.0 mmol $YCl_3 \cdot 6H_2O$ containing 6 mL OA and 15 mL ODE was added to a 50 mL flask. The mixture was heated to 150 °C under argon for 30 min to obtain a clear solution and then cooled to room temperature. 5 mL methanol solution of NH_4F (4.0 mmol) and NaOH (2.5 mmol) was added into the flask. After stirring at room temperature for 30 min, the temperature was set at 100 °C and the solution was heated under argon for 30 min to remove methanol, and then the solution was further heated to 150 °C for 20 min to remove the get rid of residual water in the flask. Finally, the reaction solution was cooled to room temperature to obtain the $NaYF_4$ shell precursors. The $NaYF_4$: 5%Yb, $NaYF_4$: x%Yb, y%Nd (x= 5, 15, 30; y=20, 40, 60) shell precursors used in this thesis were prepared with the similar method.

Because of the merits and wide applications of multifunctional core-shell UCNPs, the synthesis technology to obtain core-shell nanostructure was significantly improved in recent years. The shell thickness and homogeneous multilayer growth can also be fine-tuning by manipulating the injection dosage and times of the precursors to yield uniform shell coating. The epitaxial growth of $NaYF_4$, $NaYF_4$: 5%Yb^{3+} and NaYF4: x%Yb, y%Nd (x= 5, 15, 30; y=20, 40, 60) nanocrystals to form $NaYF_4$: Yb^{3+}, Tm^{3+}@$NaYF_4$, $NaYF_4$: Yb^{3+}, Er^{3+}@ $NaYF_4$: 5%Yb^{3+} and @ $NaYF_4$: Yb^{3+}, Er^{3+}@ $NaYF_4$: x%Yb, y%Nd core-shell nanoparticles was realised by the hot-injection method. A total of 0.2 mmol core particles in cyclohexane were added to a 50 mL flask containing 3.6 mL OA and 9.2 mL ODE. The mixture was heated to 150 °C under argon for 20 min to remove cyclohexene, and then the solution was further heated to 300 °C.[11–13] Subsequently, an appropriate amount of shell precursors were injected into the reaction mixture step-by-step with an injection rate of 0.15 mL every 2 min. After finishing the injection of the shell precursors, the reaction solution was ripened at 300 °C for 10 min. Finally, the reaction solution was cooled to room temperature and core-shell nanocrystals were precipitated by ethanol and washed with cyclohexane, ethanol, and methanol.

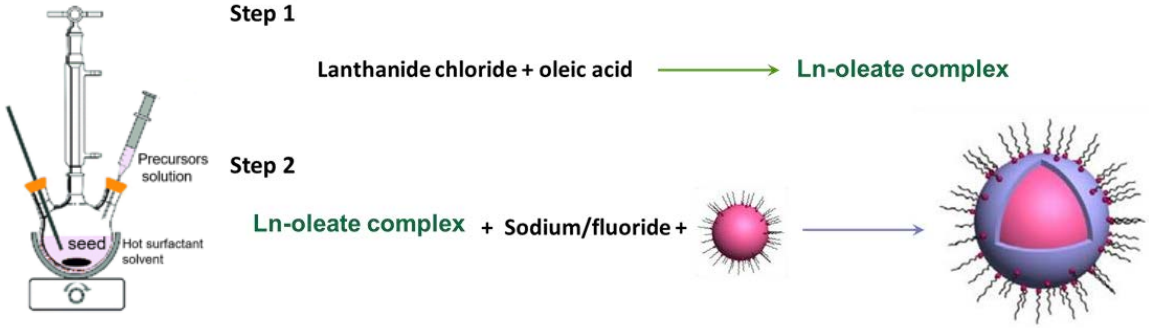

Figure 2.8 Schematic illustration of the hot-injection reaction equipment to prepare nanoparticles and the co-precipitation strategy for the synthesis of lanthanide-doped $NaREF_4$ core-shell nanocrystals. Lanthanide-oleate precursors are prepared by the reaction of lanthanide chloride and oleic acid at 150 °C. The precipitation of the lanthanide-oleate precursors by sodium and fluoride at low temperature as shell precursor and subsequent annealing in the high boiling solvent with core nanocrystals afford monodisperse $NaREF_4$ core-shell nanocrystals[2,14].

The core-multi shell nanoparticles were also prepared by the epitaxial growth method described above and the core-shell samples were used as the seeds. It should be noted that core-multi-shell nanocrystals could be easily synthesized using this protocol (Figure 2.9).

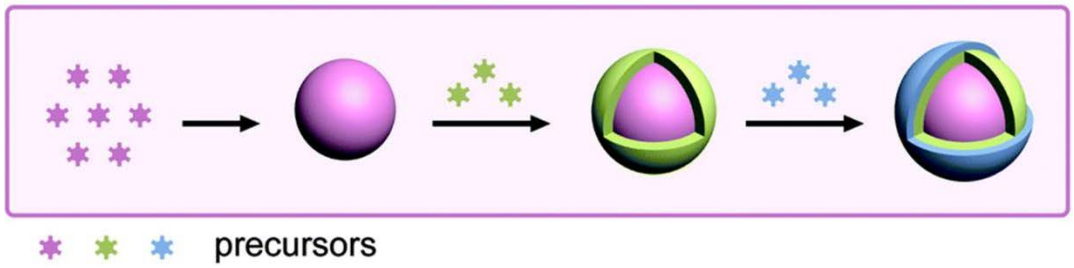

Figure 2.9 Schematic illustration of the epitaxial growth of $NaREF_4$ nanocrystals using the hot-injection process[5].

2.4.3 Synthesis protocols of PEGMEMA-b-EGMP polymer

The author acknowledges Dr. Lin Zhang for providing the polymer (Figure 2.10).

PEGMEMA (8g, 2.67×10^{-2} mol), CPADB (36.4 mg, 1.3×10^{-4}mol) and AIBN (2.13mg, 1.3×10^{-5} mol) was dissolved in toluene (10 mL), the solution was put in a round-bottom flask equipped with a magnetic stirrer bar. The flask was then sealed with a rubber septum and purged with

nitrogen gas for 45 min. The reaction mixtures were then placed in a preheated oil bath at 70 ℃. After different time at 2.5 h, the polymerization was terminated by quenching the samples in an ice bath for 15 min. The PEGMEMA polymer was then purified several times by precipitation with excess n-hexane followed by centrifugation (7000 rpm for 10 min) and the polymer was dried under vacuum at 40℃ overnight.[15] The samples were stored at 4 ℃ until required for further chain extension to form diblock copolymers. The conversion of monomer was determined using ^{1}H NMR. The molecular weight of the PEGMEMA macro-RAFT agent was measured by DMF SEC.

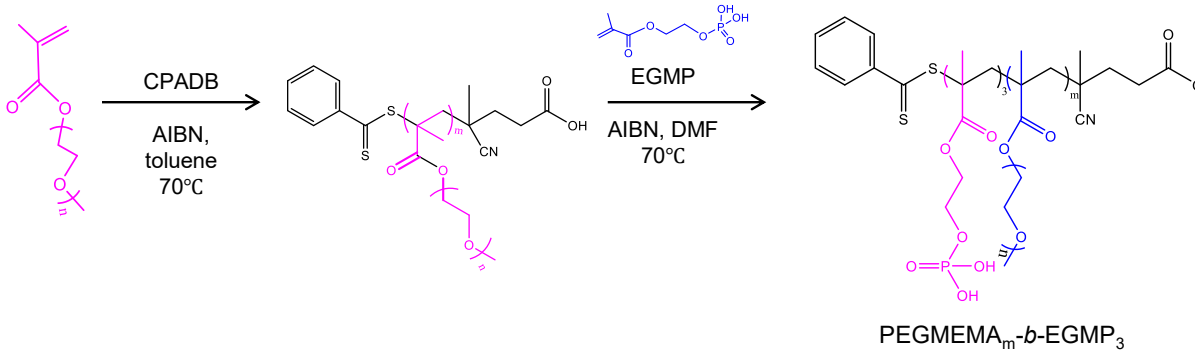

Figure 2.10. The synthesis scheme of different chain length PEGMEMA-b-EGMP block copolymers via RAFT polymerization.

PEGMEMA was used as a macro-RAFT agent for chain extension with EGMP to introduce the functional phosphonic acid group that allows the conjugation to UCNP. PEGMEMA (5×10^{-5} mol), EGMP (3×10^{-4} mol) and AIBN (5×10^{-6} mol) were dissolved in DMF (1 mL) in a round bottom flask equipped with a magnetic stirrer bar. The reaction mixture was degassed with N_2 gas for 45 min in an ice bath. The polymerization was carried out in a preheated oil bath at 70 °C. The reaction was terminated by placing the sample in an ice bath for 15 min when the conversion is around 90%. The copolymer was purified by dialysis against methanol for 48 h to remove unreacted EGMP, and the purified polymer was then dried in a vacuum oven overnight to remove the remaining solvent. The purified copolymer PEGMEMA-b-

EGMP was characterized by ^{1}H NMR, ^{31}P NMR, and GPC, before being stored at 4°C until required for further use (Figure 2.11).

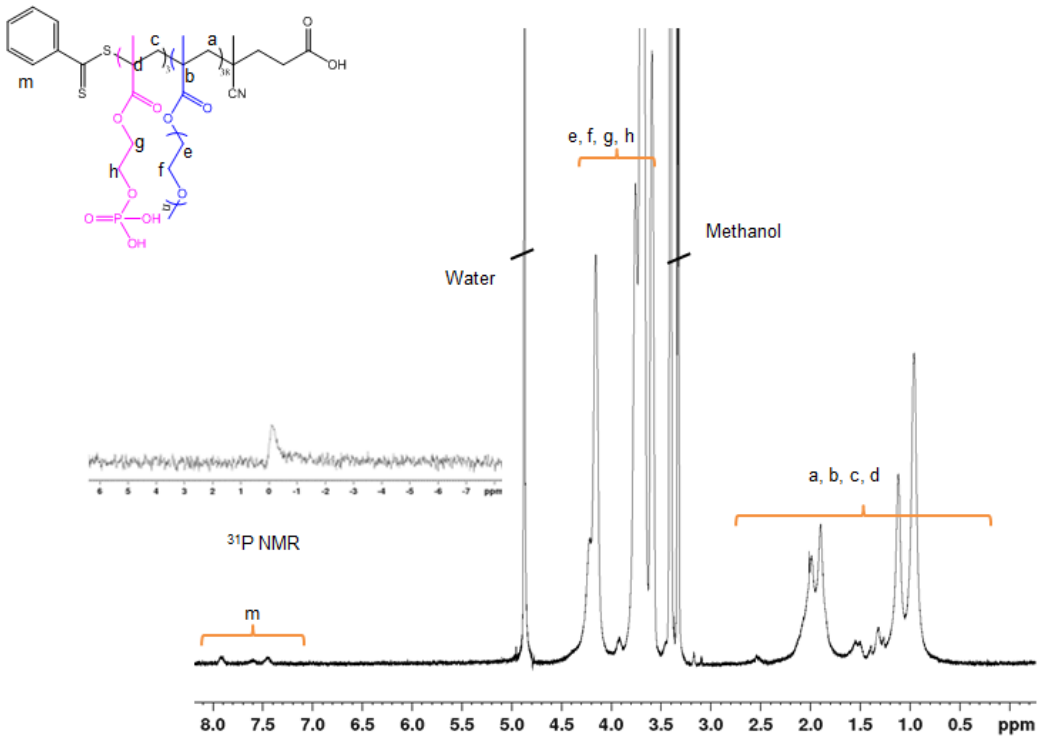

Figure 2.11. ^{1}H NMR and ^{31}P spectra of purified $PEGMEMA_{38}$-b-$EGMP_3$

2.5 PEGMEMA-b-EGMP polymer-modified UCNPs

Due to the ability to absorb multiple low energy photons from near-infrared (NIR) light and convert them into a high energy visible luminescence, UCNPs have emerged as a promising new class of nanomaterials. Since the monodisperse UCNPs with uniform size are synthesized in high boiling organic solvents (e.g. oleic acid of long-chain hydrophobic molecules) and the oleic acid used as a surfactant can prevent nanoparticles' aggregation. These UCNPs are coated with a hydrophobic layer and require to overcome a critical challenge of surface functionalization that will transform UCNPs to be stable in the physiological environment and specific to recognize the target biomolecules. Therefore, it is necessary to transfer UCNPs to hydrophilic and biocompatible through post-synthesis surface modification. Moreover, functional groups on the surface of UCNPs are also needed for further bioconjugation with

antibodies, DNA, etc. For further applications such as bioimaging, labeling, and bioassays[16–19]. Surface modification methods to yield well-dispersed nanoparticles in aqueous media are introduced systematically in some review papers (Figure 2.12), including silica coating, inorganic shell, bilayer coating, ligand oxidation, ligand exchange, and layer-by-layer coating[20–24].

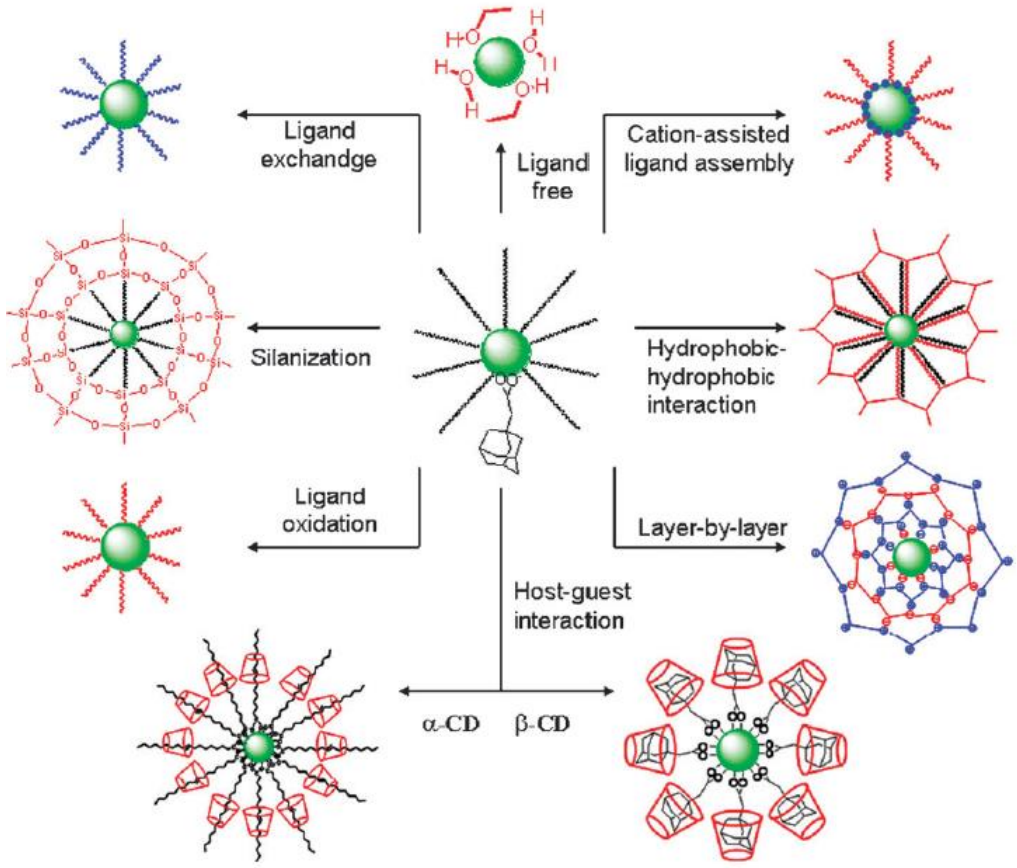

Figure. 2.12 The synthesis mechanism of two-step conversion synthesis of water-soluble UCNPs. ligand exchange, ligand exchange, organic ligand-free, cation-assisted ligand assembly, ligand oxidation reaction, silanization, layer-by-layer method, hydrophobic–hydrophobic interaction, and host-guest interaction[20].

Post-synthesis surface modification was adopted to transfer the UCNPs into hydrophilic and biocompatible before bioconjugation with DNA oligonucleotides. Here, surface modification of UCNPs was performed via ligand exchange with polymers containing multiple anchoring ligands, multiple anchoring points, which can lead to the higher coating density on the surface

of the UCNPs[15]. PEG-like block on the polymer serves as the outer shell on the coated UCNPs that greatly assists with colloidal stability in water, and to be the benefit of biological applications with high biocompatibility, low toxicity. Generally, there are two necessary groups including in the ligand, reacting groups, and the functional groups. The binding strength of the reacting groups is the key element for the replacement of the OA molecules on the surface of UCNPs, and also affect the stability of the nanoparticles in biological reagents containing various molecules.

In terms of surface modification of the nanocrystals with polymers, 500 μL of OA-coated UCNPs (20 mg/mL) kept in cyclohexane were centrifuged and redispersed in tetrahydrofuran (THF). A solution of the copolymer (5 mg) in 2 mL THF was individually added to UCNP dispersion. The resulting dispersion was sonicated for one min following by incubation in a shaker overnight at room temperature. The polymer-coated UCNPs were purified four times by washing/centrifugation at 14860 rpm for 20 min to obtain carboxyl group modified UCNPs. The supernatant was removed and the nanoparticles were redispersed in water for further conjugation with DNA.

2.6 Detection of DNA based on UCNPs assay

2.6.1 Conjugation of carboxyl-UCNPs with NH_2-DNA

We have five couples of DNA molecules. Conjugation of five kinds of probe NH_2-DNAs onto the surface of five batches of carboxyl-UCNPs was performed according to the protocol of carbodiimide chemistry. The carboxyl-UCNPs were re-activated by the EDC (100-folder molar ratio to carboxyl-UCNPs) in HEPES buffer (0.2mM, pH 7.02) with slightly shaking at room temperature for 30 mins. The NH_2-DNA (100μM) was added into the above solution with 600rpm shaking 3 hours at room temperature. The activated carboxyl-UCNPs were washing/centrifuged at 14680 rpm cycle two times to remove EDC and resuspended in HEPES buffer to obtain DNA-polymer-UCNPs.

2.6.2 Detection of DNA target based on UCNPs assay

We selected five couples of pathogen-related genetic sequences in the short length of 24 bases (HBV, HCV, HIV, HPV-16, EV), the sequences of these oligonucleotides used in this work were listed in Table 2.3. The protocol of carbodiimide chemistry was adopted to conjugate the carboxyl group on the polymer with the amine groups of probe DNA molecules. Preparing 5 pairs of plate wells, coating plate wells with 200 µL of the appropriate Streptavidin, at a concentration of about 0.5 µg/mL in PBS buffer. Cover the plate and incubate 4 h at RT. Wash the plate 3 times in PBS washing buffer. The 200 µL Biotin-DNA was added into the plate, cover the plate and incubate overnight at 4°C. Then wash the plate 3 times with PBS buffer. Adding 200 µL of blocking casein solution to each well. Incubate at RT for 1 H. Wash 3 times in PBS washing buffer. The Target DNA in 200uL Tris buffer was added to five of the relevant wells. The no Target DNA Tris buffer was added into another five corresponding wells as the control experiment. Then incubate at RT for 2 h. Wash 3 times in Tris buffer. Add 100 µL of DNA-polymer-UCNPs in blocking buffer (use Tris to prepare this blocking buffer) to each well. Incubate at RT for 1 h and then wash 3 times in washing buffer (Figure 2.13).

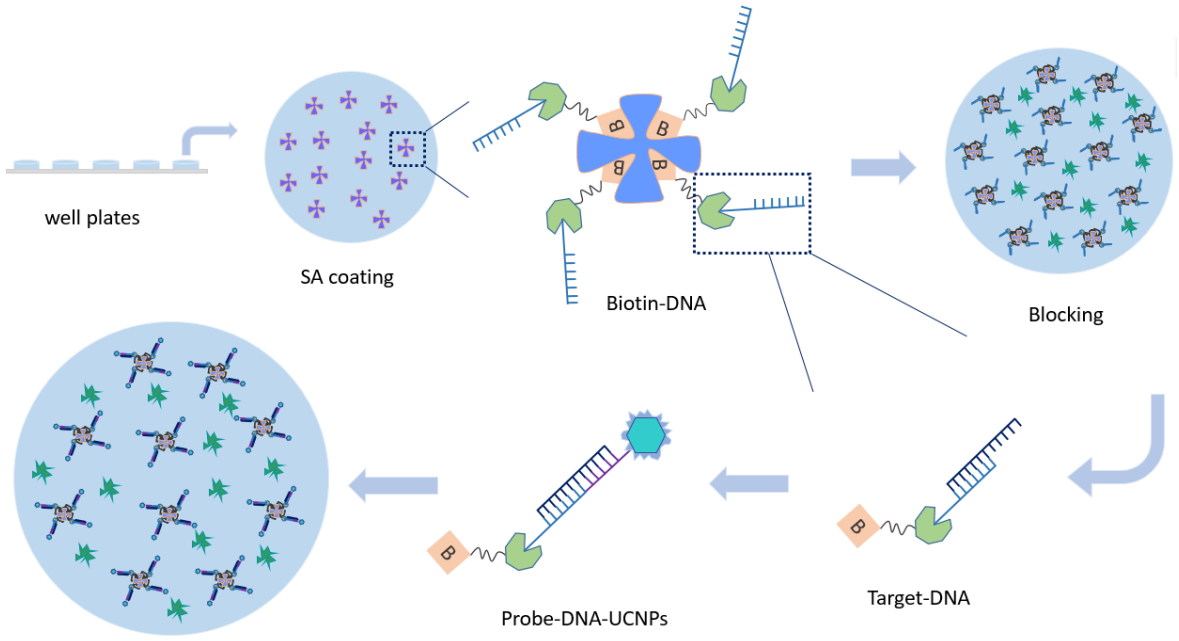

Figure 2.13. Illustration of the single UCNPs-assisted DNA molecules assay.

Table 2.3. Five kinds of pathogenetic DNA sequences conjugated with 5 batches of UCNPs.

Virus	Probe DNA	Target DNA	Capture DNA
Hepatitis B virus (HBV)	5'- /5AmMC12/ATC ATC CAT ATA -3'	5'- TTG GCT TTC AGT TAT ATG GAT GAT -3'	5'- ACT GAA AGC CAA /iSpC12//3Bio/ -3'
Hepatitis C virus (HCV)	5'- /5AmMC12/CGT GTA AGT GAC -3'	5'- GGC GTT GAC GGG GTC ACT TAC ACG -3'	5'- CCC GTC AAC GCC /iSpC12//3Bio/ -3'
Human immunodeficiency virus (HIV)	5'- /5AmMC12/GTC ATG TTA TTC -3'	5'- AGA AGA TAT TTG GAA TAA CAT GAC -3'	5'- CAA ATA TCT TCT /iSpC12//3Bio/ -3'
Human papillomavirus type-16 (HPV-16)	5'- /5AmMC12/AAT GCT AGT GCT -3'	5'- ATT TGC TGC ATA AGC ACT AGC ATT -3'	5'- TAT GCA GCA AAT /iSpC12//3Bio/ -3'
Ebola virus (EV)	5'- /5AmMC12/ATA CTG TTC TCC -3'	5'- GGA GTA AAT GTT GGT GAA CAG TAT -3'	5'- AAC ATT TAC TCC /iSpC12//3Bio/ -3'

2.7 Data processing and networks for deep learning

In recent years, artificial intelligence has been applied to various fields and rapidly altered many aspects of modern society. Machine learning, the part of artificial intelligence, is becoming an essential part of multiple fields including medical diagnosis, life sciences, materials design, and computer development. Machine learning has an unprecedented ability to rapidly classify and predict species within data and quickly discern the unforeseen relationships. This powerful tool has brought convenience to most scientific fields, from prediction to the generation of data/parameter estimation. The deep learning algorithm is becoming increasingly popular. It has a strong capability of finding latent data structures and classifying highly nonlinear datasets in dealing with light-matter interaction in the fields of materials discovery and photonics technologies. Combining with the algorithms of realistic theoretical calculations, deep learning can accelerate the screening efficiency of different materials. Because of the engagement of deep learning, materials photonic technologies relevant to the light-matter interaction have been promoted to a new stage.

High-throughput multiplexing assay and automation of data analysis are desirable for the implementation of single-particle studies into routine sample analysis. The ensemble and speedy method can be used as a prescreening tool for single-particle analysis. A widefield

imaging strategy used in this thesis can drastically enhance the detection throughput and speed. Machine (deep) learning can go beyond the limits of conventional data analysis, which has been recently used in analyzing single-molecule patterns. Once the computational model was built, machine learning also can reconstruct a widefield image into a super-resolution image without substantive implementation. It shows high recognition accuracies at high throughput by using deep learning to identify and record the optical signatures (e.g. lifetime curves) of single nanoparticles. The time-resolved wide-field imaging and deep-learning techniques were implemented to decode the lifetime fingerprints. These high-dimensional optical fingerprints provide a new horizon for applications spanning from sub-diffraction-limit data storage, security inks, to high-throughput single-molecule digital assays and super-resolution imaging.

2.7.1 Data processing to select single nanoparticles

The optical fingerprints of particles are originally presented in the fluorescence lifetime imaging sequences, which are collected by the sCMOS camera. The nanoparticles dispersed on a coverslip are randomly separated or aggregated. To perform single nanoparticle-based machine learning, we first performed data processing to select the single nanoparticles in the collected images.

For each sample, 75 frame images are recorded in the time domain within 3.75 ms (50 μs detector gate). We first select the brightest frame (maximum mean brightness) from the 75 frame images. Then we find peak positions of each bright spot. For each peak, we crop a 40 pixel by 40-pixel region of interest (ROI) centered on the peak. In each ROI, we segment the image with the OTSU threshold and get a binary mask. Considering that two adjacent peaks might be connected in the binary mask, we employ watershed segmentation on the binary mask to get the boundaries of each peak. Finally, we sort all the spots by its peak intensity. We divide all spots into four groups (Q1 to Q4) according to their peak intensities. The Q1-Q4 represents 4 intensity thresholds to classify the groups. We count the spots as the single nanoparticles when the peak intensities within the statistical range of single nanoparticle intensity. After filtering out all the aggregation-induced spots. We obtain the image that only involves single

nanoparticles. After that, the imaging sequence is transformed into multiple single nanoparticle sequences. For example, if 100 particles are identified as single nanoparticles in an imaging sequence, this imaging sequence is decomposed into 100 particle sequences. Each particle sequence has 75 frames in the time domain.

2.7.2 Determining the network architecture

The artificial neural networks (ANN) are implemented in python using the PyTorch package. (https://pytorch.org/). After selecting single nanoparticles in imaging sequences, we normalize the intensities of all 75 frames. We use the normalized time-domain fluorescence intensity sequences of single nanoparticles as the input to deep learning.

We perform the aforementioned data processing for all the ten kinds of samples. We randomly pick out ~500 single nanoparticles for each sample as the training sets, where their lifetime features and types are known. ~ 100 single nanoparticles are used as the validation sets. There are five key aspects during determining the networking architecture: 1) the number of layers in the convolutional network; 2) the number of filters in each 1D convolutional layer; 3) whether to use activation function; 4) the number of neurons in each fully connected (FC) layer; 5) the keep probability for the dropout regularization scheme. We start with the network structure of one convolutional layer with 10 filters and two fully connected layers with 10 neurons for each of them.

We first determine the number of neurons in each fully connected layer ranging from 10 to 1000. Given one convolutional layer with 10 filters, the network obtains satisfactory results when the number of neurons in each FC layer is around 500. Given the above two FC layers, we start to determine the number of convolutional layers and the number of filters for each layer. The network obtains satisfactory results when using two convolutional layers with 50 filters in the first layer and 20 filters in the second layer. Then, given the above convolutional layers, we further adjusted the number of neurons for each FC layer, and found 100-200 neurons in each layer can obtain satisfactory results. With the above conductions, the network structure is temporarily determined as two convolutional layers with 50 filters in the first layer

and 20 filters in the second layer followed by two FC layers with 100 neurons for each layer. With this network structure, we validate the network performance when activation functions or/and dropout scheme is/are introduced. Three activation functions have been validated during this procedure, which is ReLU, ReLU6, and RReLU. The keep probability of the dropout scheme is determined in the range from 0.5 to 0.9. After the above adjustment of the network, we go back to adjust the number of neurons in FC layers and obtain the final network architecture as below (Figure 2.14).

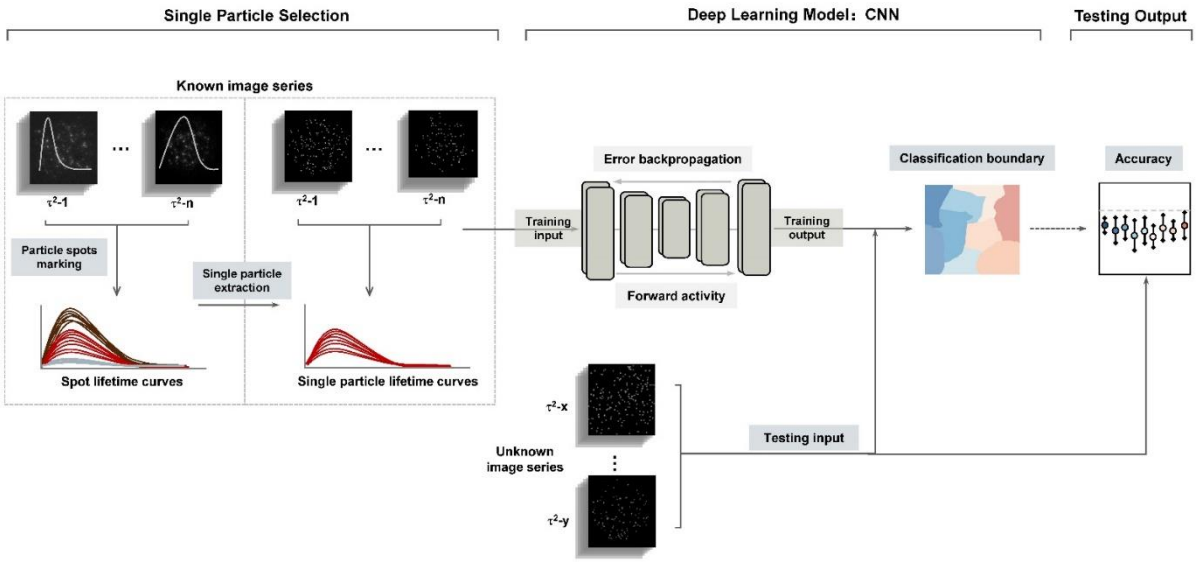

Figure 2.14. The workflow of the deep learning process to classify the single UCNPs.

2.7.3 Network architecture

The fingerprint retrieval network contains two convolutional networks and two fully connected networks. The two 1D convolutional layers use the element-wise function $ReLU6(x) = \min(\max(0, x), 6)$. There are 50 filters in the first 1D convolutional layer using a kernel of size 3 and the stride size is 2. The second 1D convolutional layer has 20 filters with a kernel of size 2 and the stride size is 1. The two fully connected networks contain two layers with 150 (FC1) neurons in the first layer and 100 (FC1) neurons in the second layer and also employs the element-wise function for each layer. We apply a dropout regularization scheme with 80% keep probability for the fully connected part. During training, the output layer neuron whose

index corresponds to the input binary number is set to “1” while the other neuron activations are kept at “0”. A variant of the stochastic gradient descent (SGD) algorithm (“Adam”) is applied to train the parameters in the network through a randomly shuffled batch of size 200. We use the categorical cross-entropy loss, a learning rate of 0.005 and train the network for 50 epochs.

We have 7 sets of imaging sequences of each sample and run 50 experiments of training and testing to compute the average error and deviation. In each experiment, we firstly randomly select one set of imaging sequences for particles. For 10 particles, we select 10 image sequences. The data of single nanoparticles in the rest image sequences are used as the training set, and the data of single nanoparticles in these 10 selected image sequences are used as the testing set, where their lifetime features are available, but the label is unknown until computing the model error. After one training-and-testing process, the testing error for 10 image sequences is obtained. The mean and deviation of errors are computed through 50 random selections.

2.8 Reference

(1) Chen, X.; Peng, D.; Ju, Q.; Wang, F. Photon Upconversion in Core-Shell Nanoparticles. *Chem. Soc. Rev.* **2015**, *44* (6), 1318–1330.

(2) Wang, F.; Deng, R.; Liu, X. Preparation of Core-Shell $NaGdF_4$ Nanoparticles Doped with Luminescent Lanthanide Ions to Be Used as Upconversion-Based Probes. *Nat. Protoc.* **2014**, *9* (7), 1634–1644.

(3) Li, X.; Zhang, F.; Zhao, D. Lab on Upconversion Nanoparticles: Optical Properties and Applications Engineering via Designed Nanostructure. *Chem. Soc. Rev.* **2015**, *44* (6), 1346–1378.

(4) Fischer, S.; Swabeck, J. K.; Alivisatos, A. P. Controlled Isotropic and Anisotropic Shell Growth in β-$NaLnF_4$ Nanocrystals Induced by Precursor Injection Rate. *J. Am. Chem. Soc.* **2017**, *139* (35), 12325–12332.

(5) Chen, X.; Peng, D.; Ju, Q.; Wang, F. Photon Upconversion in Core-Shell Nanoparticles. *Chem. Soc. Rev.* **2015**, *44* (6), 1318–1330.

(6) Wang, F.; Deng, R.; Wang, J.; Wang, Q.; Han, Y.; Zhu, H.; Chen, X.; Liu, X. Tuning Upconversion through Energy Migration in Core-Shell Nanoparticles. *Nat. Mater.* **2011**, *10* (12), 968–973.

(7) Yi, G.-S.; Chow, G.-M. Water-Soluble $NaYF_4$: Yb, Er (Tm)/$NaYF_4$/Polymer Core/Shell/Shell Nanoparticles with Significant Enhancement of Upconversion Fluorescence.

Chem. Mater. **2007**, *19* (3), 341–343.

(8) Li, X.; Shen, D.; Yang, J.; Yao, C.; Che, R.; Zhang, F.; Zhao, D. Successive Layer-by-Layer Strategy for Multi-Shell Epitaxial Growth: Shell Thickness and Doping Position Dependence in Upconverting Optical Properties. *Chemistry of Materials*. 2013, 2 (5), 106–112.

(9) Johnson, N. J. J.; van Veggel, F. C. J. M. Sodium Lanthanide Fluoride Core-Shell Nanocrystals: A General Perspective on Epitaxial Shell Growth. *Nano Res.* **2013**, *6* (8), 547–561.

(10) Liu, D.; Xu, X.; Du, Y.; Qin, X.; Zhang, Y.; Ma, C.; Wen, S.; Ren, W.; Goldys, E. M.; Piper, J. A.; et al. Three-Dimensional Controlled Growth of Monodisperse Sub-50 nm Heterogeneous Nanocrystals. *Nat. Commun.* **2016**, *7*, 1–8.

(11) Mai, H. X.; Zhang, Y. W.; Sun, L. D.; Yan, C. H. Highly Efficient Multicolour Up-Conversion Emissions and Their Mechanisms of Monodisperse $NaYF_4$:Yb,Er Core and Core/Shell-Structured Nanocrystals. *J. Phys. Chem. C* **2007**, *111* (37), 13721–13729.

(12) Li, Z.; Zhang, Y.; Jiang, S. Multicolour Core/Shell-Structured Upconversion Fluorescent Nanoparticles. *Adv. Mater.* **2008**, *20* (24), 4765–4769.

(13) Qian, H. S.; Zhang, Y. Synthesis of Hexagonal-Phase Core-Shell $NaYF_4$ Nanocrystals with Tunable Upconversion Fluorescence. *Langmuir* **2008**, *24* (21), 12123–12125.

(14) Hao, S.; Chen, G.; Yang, C. Sensing Using Rare-Earth-Doped Upconversion Nanoparticles. *Theranostics* **2013**, *3* (5), 331–345.

(15) Duong, H. T. T.; Chen, Y.; Tawfik, S. A.; Wen, S.; Parviz, M.; Shimoni, O.; Jin, D. Systematic Investigation of Functional Ligands for Colloidal Stable Upconversion Nanoparticles. *RSC Adv.* **2018**, *8* (9), 4842–4849.

(16) Zhang, Z.; Shikha, S.; Liu, J.; Zhang, J.; Mei, Q.; Zhang, Y. Upconversion Nanoprobes: Recent Advances in Sensing Applications. *Anal. Chem.* **2019**, *91* (1), 548–568.

(17) Wang, M.; Abbineni, G.; Clevenger, A.; Mao, C.; Xu, S. Upconversion Nanoparticles: Synthesis, Surface Modification and Biological Applications. *Nanomedicine Nanotechnology, Biol. Med.* **2011**, *7* (6), 710–729.

(18) He, H.; Liu, B.; Wen, S.; Liao, J.; Lin, G.; Zhou, J.; Jin, D. Quantitative Lateral Flow Strip Sensor Using Highly Doped Upconversion Nanoparticles. *Anal. Chem.* **2018**, *90* (21), 12356–12360.

(19) Sedlmeier, A.; Gorris, H. H. Surface Modification and Characterization of Photon-Upconverting Nanoparticles for Bioanalytical Applications. *Chem. Soc. Rev.* **2015**, *44* (6), 1526–1560.

(20) Zhou, J.; Liu, Z.; Li, F. Upconversion Nanophosphors for Small-Animal Imaging. *Chem. Soc. Rev.* **2012**, *41* (3), 1323–1349.

(21) Muhr, V.; Wilhelm, S.; Hirsch, T.; Wolfbeis, O. S. Upconversion Nanoparticles:

From Hydrophobic to Hydrophilic Surfaces. *Acc. Chem. Res.* **2014**, *47* (12), 3481–3493.

(22) Ren, W.; Zhou, Y.; Wen, S.; He, H.; Lin, G.; Liu, D.; Jin, D. DNA-Mediated Anisotropic Silica Coating of Upconversion Nanoparticles. *Chem. Commun.* **2018**, *54* (52), 7183–7186.

(23) Lu, J.; Chen, Y.; Liu, D.; Ren, W.; Lu, Y.; Shi, Y.; Piper, J.; Paulsen, I.; Jin, D. One-Step Protein Conjugation to Upconversion Nanoparticles. *Anal. Chem.* **2015**, *87* (20), 10406–10413.

(24) Johnson, N. J. J.; Sangeetha, N. M.; Boyer, J. C.; Van Veggel, F. C. J. M. Facile Ligand-Exchange with Polyvinylpyrrolidone and Subsequent Silica Coating of Hydrophobic Upconverting β-$NaYF_4$:Yb^{3+}/Er^{3+} Nanoparticles. *Nanoscale* **2010**, *2* (5), 771–777.

Chapter 3 Peak Tuning of Excited-state Populations in Upconversion Nanoparticles

3.1 Preamble

In this result chapter, coding optical information has moved from the macroscopic level to the nanoscale carriers[1], which enables many recent breakthroughs in data storage[2], anti-counterfeiting[3–5], and high throughput sensing and imaging of multiple target[6,7]. The key is to develop optical multiplexing into the multiple orthogonal dimensions, e.g., emission intensity, colour, polarization and decay time. Here, we report a yet uncapped dimension by tuning the peak time of excited-state populations in lanthanide-doped UCNPs. Through the use of an Nd^{3+}-Yb^{3+}-Tm^{3+} doped core-shell-shell design of nanoparticles, the cascade energy transfer network from primary sensitizers (Nd^{3+}), secondary sensitizers (Yb^{3+}) and to emission activators (Tm^{3+}) can be engineered. We demonstrate the duration for blue upconversion emissions can be significantly extended from 100 μs to 900 μs after switching off the NIR excitation. This strategy creates a set of time-resolved emission profiles over a large dynamic range, where they can be arbitrarily tuned from either the rise time or decay time. When assigning these codes to a new library of nanoparticle carriers, each batch of UCNPs can take the turn to shine in the time domain which acts as a new dimension for optical multiplexing application.

3.2 Introduction

As discussed in Chapter 1, a light wave can be described by many parameters such as wavelength, intensity, polarisation and lifetime. Each of the parameters could be viewed as a ‘dimension’. Recording light information in nanoparticles will turn a range of inorganic nanomaterials into ‘information carriers’. Nanoscale optical multiplexing underpins many recent developments of exciting nanophotonics and biophotonics applications.[8–10] A general strategy for optical multiplexing is to explore many optical dimensions to encode as much information as possible in a single nanoscale carrier, e.g., doping different elements in the

hybrid nanocomposites or combinatorial assemblies of multiple building blocks in encoding nanostructures.

Fine-tuning of the emission decay lifetimes has been demonstrated as a powerful approach for high-throughput screening of multiple biomolecules, multiplexing imaging, anti-counterfeiting, and new dimensional data storage applications. The decay lifetime of lanthanide-doped UCNPs can be tuned in a large dynamic range from tens of microseconds to hundreds of microseconds. The long decay lifetime is attributed to several metastable emitting states, such as the lower-energy states $^3F_4$, $^3H_5$ of Tm^{3+} to emit infrared emissions, higher-energy states $^3F_{2,3}$, $^3H_4$, $^3G_4$ and $^1G_2$ of Tm^{3+} responsible for upconversion emissions in the visible range, and multi-step energy transfer process among ions.[11–14] To generate an array of tunable decay codes for multiplexing applications, approaches, including the introduction of external quenchers from the surface or more internal cross relaxations between dopants, are used to shorten the decay lifetimes.[15–17]

In 2013, with the development of advanced approaches for core-shell nanostructures nanoparticle synthesis, some groups independently demonstrated efficient Nd^{3+} sensitized $NaYF_4$ UCNPs.[18–22] The excitation of UCNPs can be moved from 980 to 800 nm to minimize the overheating problem through core@shell design. Wang et al. reported Nd^{3+} doped $NaYF_4$ nanoparticles using a core@shell nanoparticles with improved efficiency, in which different types of lanthanide dopants were doped into various domains (Fig. 3.1).[23] Nd^{3+} ions transfer the excitation energy to nearby Yb^{3+} ions under 800 nm laser excitation. To result in upconversion emission, the excited Yb^{3+} ions then serve as energy migrators to transfer the energy to emitting ions. Here we report another optical feature in a similar core-shell-shell structure nanoparticles, the tunable time-resolved upconversion luminescence. That is, the duration from photon sensitizers to activators builds up the electron populations at higher-energy excited state. This forms a new time-resolved emission profile by balancing the dynamics of the rise time and decay time of excited-state populations. It offers a set of the different optimized time windows for upconversion to take turns to shine which provides a significant opportunity with respect to optical multiplexing.

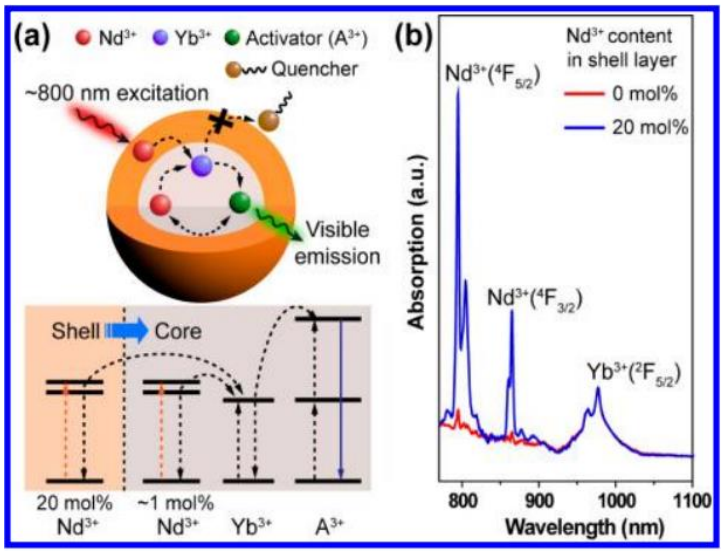

Figure 3.1 (**a**) Schematic design and simplified energy level diagram of a core@shell nanoparticle for photon upconversion under 800 nm excitation. (**b**) Near-IR absorption spectra of $NaYF_4$: Yb/Nd(30/1%)@$NaYF_4$ and NaYF4: Yb/Nd(30/1%)@ $NaYF_4$: Nd(20%) nanoparticles.

3.3 Experimental section

3.3.1 Synthesis of $NaYF_4$:18%Yb, 0.5%Nd, 0.2%Tm core nanoparticles

The $NaYF_4$:18%Yb, 0.5%Nd, 0.2%Tm core nanoparticles were synthesized using a coprecipitation method. In a typical procedure, an methanol solution (2 mmol) of YCl_3•$6H_2O$ (493.26 mg; 1.626 mmol), $YbCl_3$•$6H_2O$ (139.2 mg; 0.36 mmol), $NdCl_3$•$6H_2O$ (3.58 mg; 0.01 mmol) and $TmCl_3$•$6H_2O$ (1.54 mg; 0.004 mmol) together with oleic acid (12 mL) and 1-octadecene (30 mL) were added to a 100 ml three-neck round-bottom flask under vigorous stirring. The resulting mixture was heated at 150 ºC for 40 mins to form lanthanide oleate complexes. The solution was cooled down to room temperature. Subsequently, a methanol solution (6 mL) containing NaOH (5 mmol, 0.32g) and NH_4F (8 mmol, 0.20g) was added and stirred at 50 ºC for 40 mins, and then the mixture was slowly heated to 150 °C and kept for 40 mins under argon flow to remove methanol and residual water. Next, the solution was quickly heated at 300 ºC under argon flow for 1.5 h before cooling down to room temperature. The resulting core nanoparticles were precipitated by the addition of ethanol, collected by centrifugation at 9000 rpm for 5 min, the final $NaYF_4$: Yb, Tm, Nd nanocrystals were

redispersed in cyclohexane with 5 mg/mL concentration after washing with cyclohexane/ethanol/methanol several times.

The $NaYF_4$: x%Yb,20%Nd and $NaYF_4$ precursors were prepared as above procedure until the step where the reaction solution was slowly heated to 150 °C after adding $NaOH/NH_4F$ solution and kept for 40 min. Instead of further heating to 300 °C to trigger nanocrystal growth, the solution was cooled down to room temperature to yield the shell precursors.

3.3.2 Synthesis of core-shell nanoparticles

The of $NaYF_4$:18%Yb, 0.2%Tm, 0.5%Nd@ $NaYF_4$:x%Yb, 20%Nd (x=0, 5, 15, 15, 20, 30, 45) core-shell nanoparticles were prepared by layer by layer epitaxial growth method. The pre-synthesized $NaYF_4$: Yb, Tm, Nd core nanoparticles were used as seeds for shell modification. 0.2 mmol as-prepared core nanocrystals were added to a 50 ml flask containing 3 ml OA and 8 ml ODE. The mixture was heated to 160 °C under argon for 30 min, and then further heated to 300 °C. Next, 0.2 ml as-prepared shell precursors were injected into the reaction mixture and ripened at 300 °C for 2 min, followed by the same injection and ripening cycles for approximately several times to get around 5 nm thickness shell. Finally, the slurry was cooled down to room temperature and the formed nanocrystals.

The $NaYF_4$:18%Yb, 0.2%Tm, 0.5%Nd@ $NaYF_4$:x%Yb, 20%Nd (x=0, 5, 15, 30, 45) @ $NaYF_4$ core-shell-shell nanoparticles were also prepared by the epitaxial growth method described above and the core-shell samples were used as the seeds.

3.4 Results and discussion

3.4.1 Materials characterization and the lifetime peak tailoring in core-shell ensemble nanoparticles.

As a proof of concept, we demonstrate the controlling of duration time to populate electrons in a typical upconversion nanoparticle system, i.e., Nd^{3+}-Yb^{3+}-Tm^{3+} co-doped β-$NaYF_4$ nanoparticles, to create a library of UCNPs taking turns to shine with diverse temporal lifetime peak. Firstly, we synthesized the β-$NaYF_4$:18% Yb^{3+}, 0.2% Tm^{3+}, 0.5% Nd^{3+} core nanoparticles (Figure. 3.2). TEM images and the histogram of the size distribution of the

nanocrystals in Fig. 3.2a showed that the nanocrystals were nanospheres in shape with a uniform size of 23 nm in diameter. The peak positions and intensities in figure3.2 b agree well with those calculated for the hexagonal β-$NaYF_4$ phase (PDF card No. 16-0334), the XRD results indicated the good crystalline of β-$NaYF_4$ and no impurity was produced.

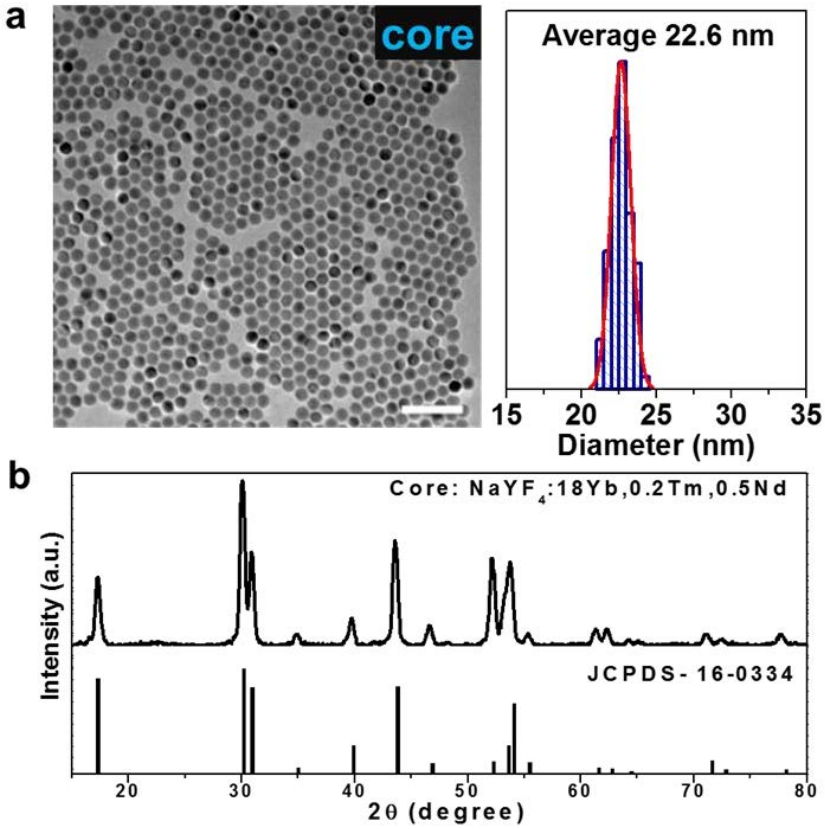

Figure 3.2 (a) Transmission electron microscopy characterization and the corresponding size distribution of $NaYF_4$: 18%Yb^{3+},0.5%Nd^{3+},0.2% Tm^{3+} core nanoparticles. The size of core nanoparticles is nearly spherical in shape and monodisperse, with an average diameter of 22.6 nm. (b) XRD pattern as a pure hexagonal phase $NaYF_4$ (JCPDS: 00-016-0334) of the core nanoparticles. Scale bars are 100 nm

Then a series of core-shell nanoparticles with active $NaYF_4$: x% Yb^{3+}, 20%Nd^{3+} (x = 0, 5, 15, 20, 30 and 45% mol) at same shell thickness were synthesized to investigate the dynamics of the rise time and decay time of excited-state populations (Figure. 3.3). The diameter of these six batches of core@shell nanoparticles is about 35 nm after the growth of around 5 nm active layer within Nd^{3+} and Yb^{3+} codoped.

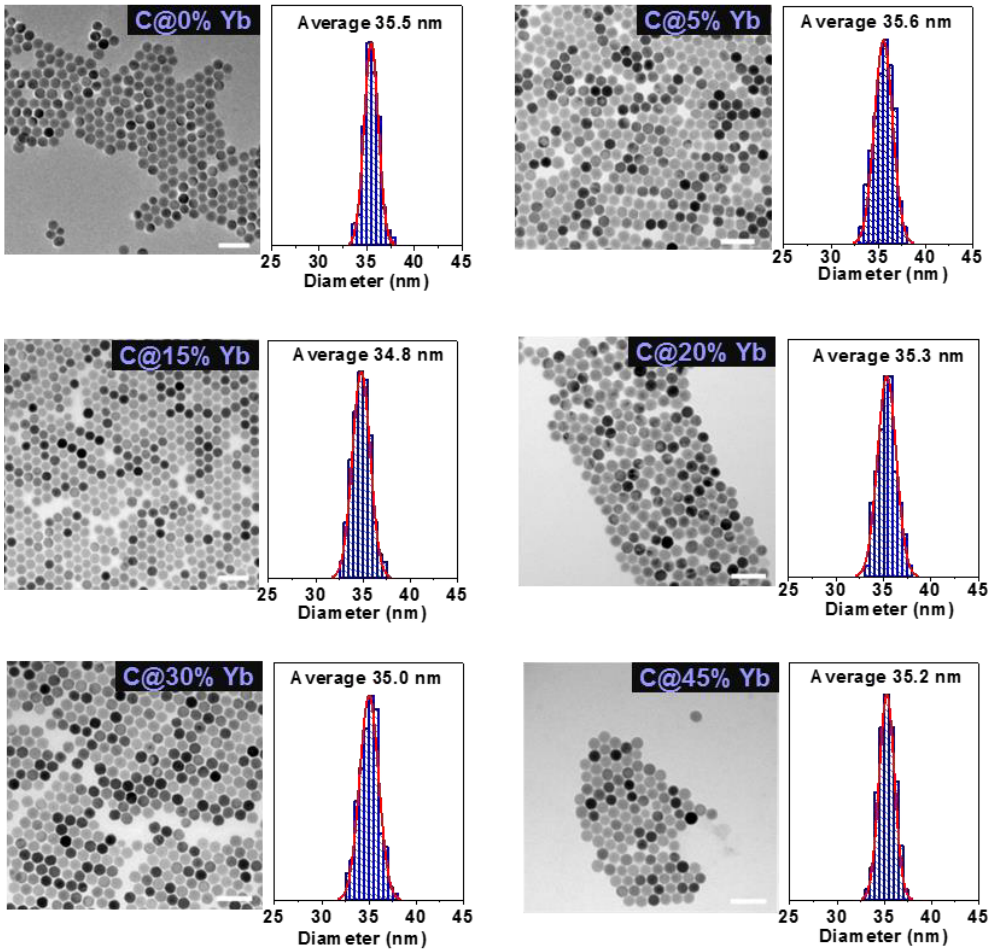

Figure 3.3 TEM images and histograms of the size distribution of core@ $NaYF_4$: x% Yb^{3+}, 20%Nd^{3+} (x = 0, 5, 15, 20, 30 and 45) core/active-shell nanoparticles. The diameter of the core@shell nanoparticle is about 35 nm after the growth of around 5 nm active layer. Scale bars are 100 nm

As illustrated in Figure 3.4a, the electron populations of activator Tm^{3+} in core-shell nanoparticles experience interfacial energy migration (IEM) from primary sensitizer Nd^{3+} to the secondary sensitizer Yb^{3+} under the excitation of 808 nm, which is suitable for deep-tissue bio-imaging applications. This IEM shows stronger manipulability in the time domain to pump Tm^{3+} compared to that of the direct excitation of Yb^{3+} using 976 nm. Figure 3.4b gives the characteristic upconversion emissions of Tm^{3+} ions, in which the blue emission bands covering $^1D_2 \rightarrow {}^3F_4$ and $^1G_4 \rightarrow {}^3H_6$ transitions are monitored for the evolution of peak time of excited-state populations (ESP) (Figure 3.5).[24,25] We believe that postpone of temporal lifetime peak dominated by IEM can be confirmed by excitation of Yb^{3+} using 976 nm laser and of Nd^{3+}

using 808 nm laser (see Fig. 3.4c). The 808 nm diode laser is modulated to produce 200 μs excitation pulses with a period of 5 ms on a home-built microscopy system. The photon counting is switched on to capture the long-lifetime luminescence for another 4.8 ms. The pulsed excitation and time-gated data collection are controlled and synchronized using a multifunction data acquisition camera (iStar-Scmos-18U-64). Figure 3.4c clearly shows that the peak time of ESP of Tm^{3+} blue emission from the core@5%Yb^{3+},20%Nd^{3+} nanoparticles has been extended from 350 μs to 650 μs when shifting the excitation wavelength from 976 nm to 808 nm. Figure 3.4d further proves that IEM consistently prolongs the temporal lifetime peak in a series of samples with different Yb^{3+} concentrations by comparing the peak times of 808 nm and 976 nm excitation cases. The temporal lifetime peak moments of $NaYF_4$:Nd^{3+},Yb^{3+},Tm^{3+}@$NaYF_4$:Nd^{3+},Yb^{3+} with varied Yb^{3+} concentration in the active shell layer are all prolonged under 808 nm and the temporal lifetime peak ranges from 150 μs (45% Yb^{3+}) to 650 μs (5% Yb^{3+}). Moreover, the time gap becomes the largest value of 300 μs when Yb^{3+} concentration is 5 %, while further increasing the Yb^{3+} amount in the active-shell, the peak times and gaps in between gradually reduce.

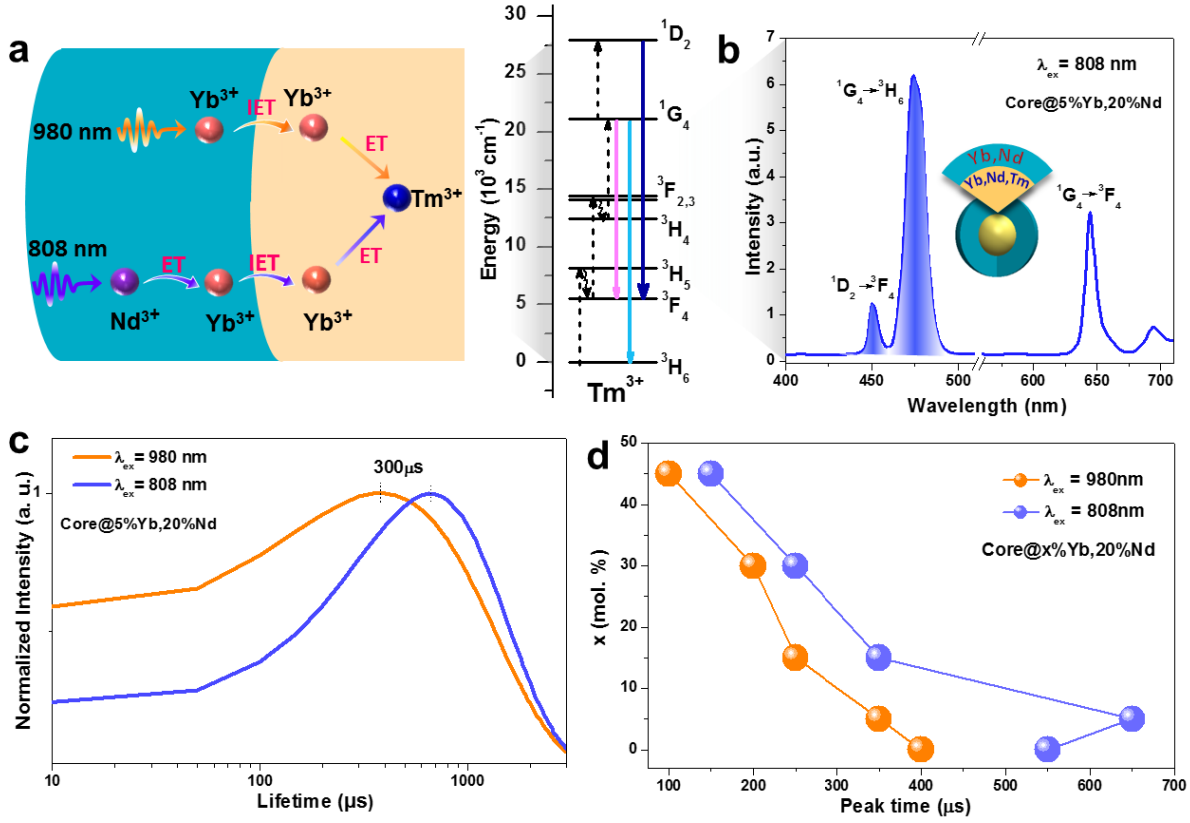

Figure 3.4 Interfacial energy migration prolongs the peak moment of the maximum excited state population. (a) Schematic illustration of photon upconversion through Yb sensitized under 976 nm and Nd-mediated interfacial energy migration under 808 nm in the core-shell system. (b) Upconversion emission spectrum under 808 nm excitation. (c) Temporal evolution Tm^{3+} excited state populations by monitoring the emissions from $^1D_2$ and $^1G_4$ states after pulse excitation at 808 nm and 976 nm excitation of Core@ $NaYF_4$:5%Yb, 20%Nd samples with 200 μs pulse. (d) Temporal lifetime peak moment of $NaYF_4$ core-shell nanocrystals with varied Yb concentrations under 808 nm and 976 nm excitation: core@ x%Yb, 20%Nd (x = 0, 5, 15, 20, 30 and 45% mol.)

From the upconversion emission spectra and the measurements of lifetime curves, the upconversion mechanism of the Nd^{3+}–Yb^{3+}–Tm^{3+} system under 808 and 976 nm excitation has been proposed and is shown in Figure 3.5. Under 808 nm excitation, Nd^{3+} ions in the ground state are excited by the 808 nm laser and reach their excited state $^4F_{5/2}$ corresponding to the transition $^4I_{9/2} \rightarrow {}^4F_{5/2}$. Then the Nd^{3+} ions relax to the $^4F_{3/2}$ state through a multi-phonon non-radiative relaxation. The energy transfer to the core by the IEM from primary sensitizer Nd^{3+} to Yb^{3+} in the shell and energy transfer (ET) between Nd^{3+} ions and Yb^{3+} ions in the core , $^2F_{7/2}$ (Yb^{3+}) + $^4F_{3/2}$ (Nd^{3+}) $\rightarrow$ $^2F_{5/2}$ (Yb^{3+}) + $^4I_{11/2}$ (Nd^{3+}). As a result, the $^2F_{5/2}$ state of Yb^{3+} ions is populated. Several subsequent successive energy transfers from excited Yb^{3+} ions to the excited state of Tm^{3+} ions and give the blue (455 nm, 475 nm) and red (655 nm) emissions.

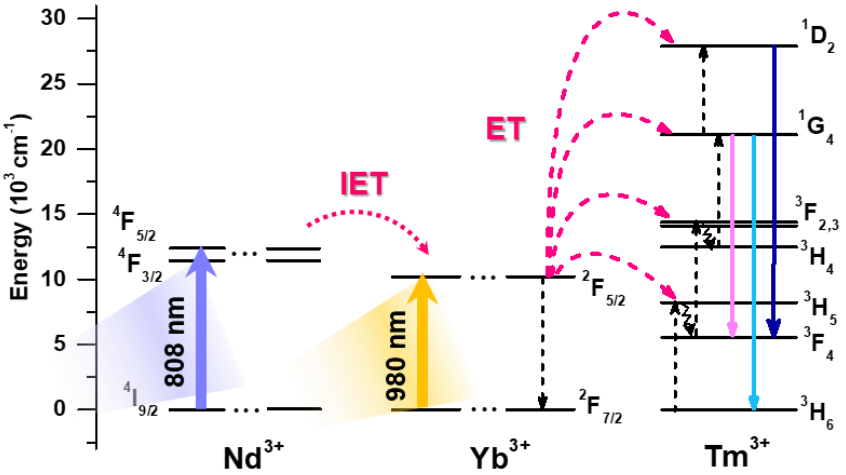

Figure 3.5 The schematic illustration of the UC emission mechanism under 976 nm and 808 nm excitation.

3.4.2 Lifetime peak tailoring in core-shell-shell ensemble nanoparticles.

Surface quenching typically happens when Yb^{3+} concentration is high[26–28], which offer an unblocked channel to evacuate excitation energy to the quenching centers, such as surface ligands and crystal defects.[29–33] Inert shell growth as thick as 5 nm breaks the quenching channel, leading to the prolonging of temporal lifetime peak. To further extend the peak time of ESP and improve the brightness of UC emissions, we employ inert shell growth (Figure 3.6) to isolate the surface quenchers. The TEM images of the core@ $NaYF_4$:x% Yb^{3+}, 20% Nd @ $NaYF_4$ (x = 0, 5, 15, 30 and 45%) samples are shown in Figure 3.6. The calculated average particle size for different amounts of Yb^{3+} ions doped samples are also shown in Figure 3.6, all of the Nd^{3+}-Yb^{3+}-Tm^{3+} doped core-active shell-inert shell UCNPs have a uniform morphology with an average diameter of about 46 nm.

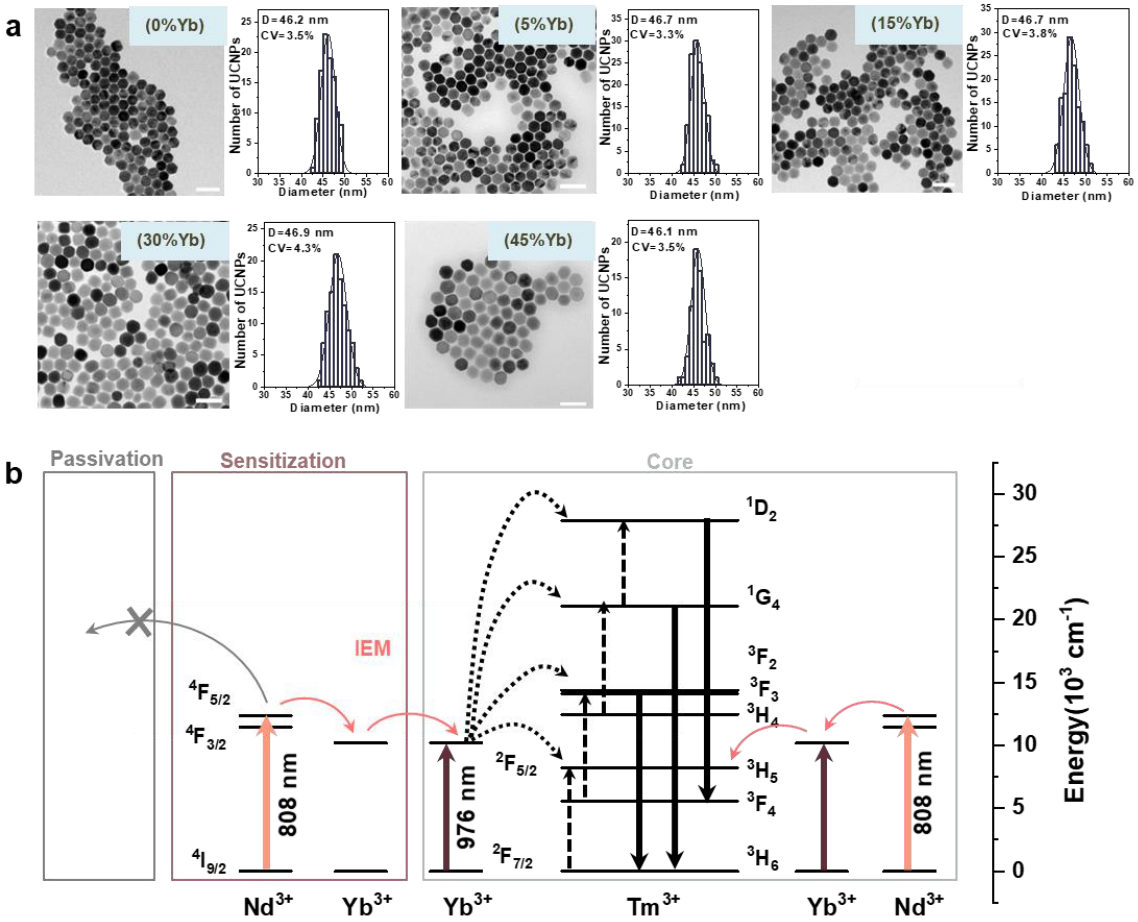

Figure 3.6 (a) TEM morphology and histograms of core@ $NaYF_4$: x% Yb^{3+}, 20%Nd^{3+} (x = 0, 5, 15, 30 and 45)@$NaYF_4$ core/active-shell/inert-shell nanoparticles. The diameter of the nanoparticles increased

up to about 46 nm with 5 nm thickness after growth of the pure $NaYF_4$ shell layer, the uniformity of size and shape remained almost unchanged. Scale bars are 100 nm. (b) Energy level diagram of Nd^{3+}, Yb^{3+}, Tm^{3+} in the core-multi-shell β-$NaYF_4$ nanoparticles showing the energy transfer upconversion mechanism under 808 nm and 976 nm excitations.

As illustrated in Figure 3.7, the core-shell-shell samples with the inert shell as thick as 5 nm passivates UCNPs evacuating excitation energy through Yb^{3+} or Nd^{3+} to the surface quenchers. we can see from Figure 3.7b, all the lifetime peaks of core-shell-shell samples are prolonged compared with relevant core-shell samples. For example, the peak was shifted from 650 μs to 900 μs for core@$NaYF_4$:20% Nd , 5% Yb^{3+} and from 100 μs to 450 μs for core@$NaYF_4$: 20% Nd^{3+}, 45% Yb^{3+} samples, respectively (Figure 3.7c). Because of the protection of an inert shell, the brightness of core-shell-shell samples is obviously enhanced (Figure 3.7d). The 15% Yb^{3+} concentration of core-active shell and core-active shell-inert shell yields the maximum lifetime prolong. Figure 3.7c clearly shows that the Yb^{3+} concentration of 5% yields the longest delayed peak time of ESP, and more importantly with the brightest UC emissions (Figure 3.7d). The detailed temporal lifetime peaks are summarized in Table 3.1.

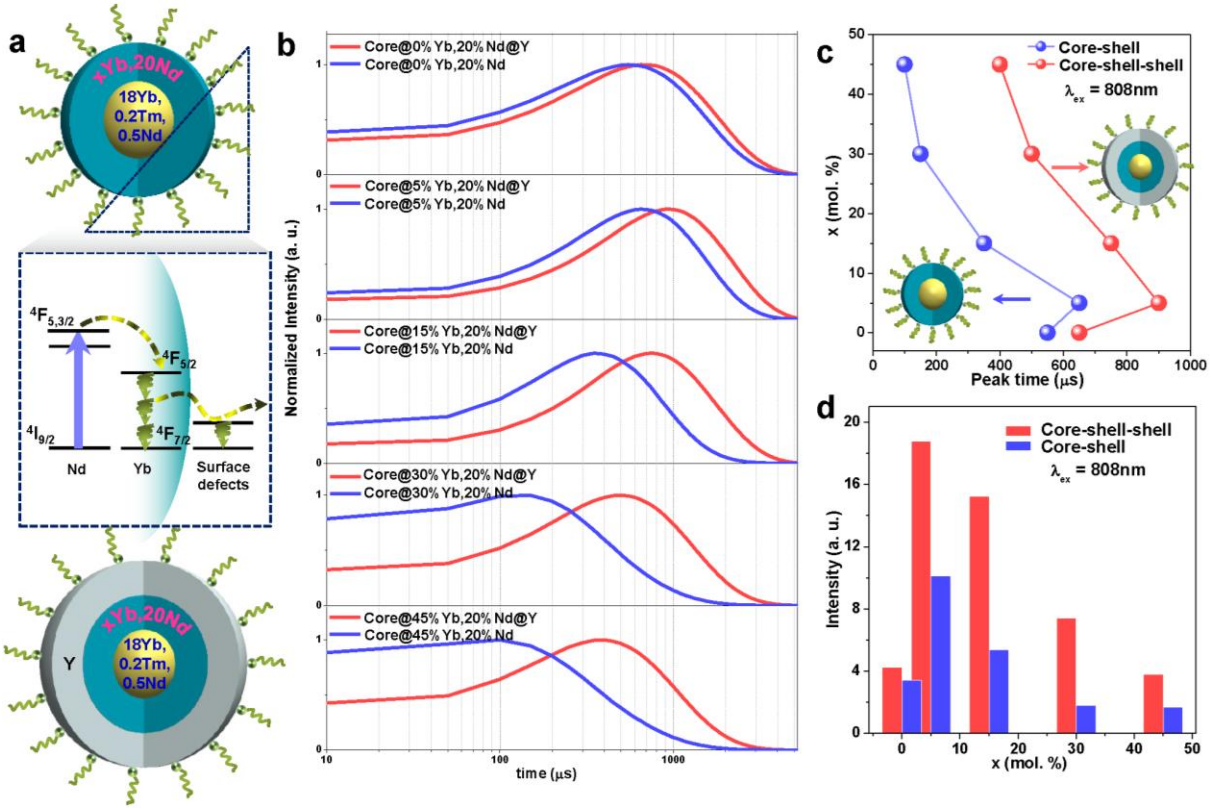

Figure 3.7 Isolation of surface quenchers prolongs the peak moment of the maximum excited state population. (a) Schematic design and surface environment of the active-core/active-shell and the active-core/active-shell/inert shell nanoparticle architecture for photon upconversion. (b) Temporal evolution of UC luminescence of Tm^{3+} blue emission (435-485 nm) after 808 nm pulse excitation of core@$NaYF_4$:x% Yb^{3+}, 20% Nd and core@$NaYF_4$:x% Yb^{3+}, 20% Nd@ $NaYF_4$ samples with 200 μs pulse width (x = 0, 5, 15, 20, 30 and 45% mol). (c) The shift of rising time peak by varying the Yb^{3+} concentration. (d) The upconversion emission intensity of blue (435-485 nm) and red (625-675 nm) emission of Tm^{3+} in core-shell and core-shell-shell samples, which are ascribed to the $^1D_2 \rightarrow {}^3F_4$, $^1G_4 \rightarrow {}^3H_6$, $^1G_4 \rightarrow {}^3F_4$ transitions, respectively.

Table 3.1. The summary lifetime and lifetime peak of $NaYF_4$: 18%Yb^{3+}, 0.2%Tm^{3+}, 0.5%Nd^{3+} series nanoparticles by adjusting the Yb^{3+} concentration in the active shell, which can obtain the ranging lifetime from 392 μs to1083 μs in the Tm^{3+} blue-emission band.

	Core lifetime	**Core-shell Decay lifetime**	**Peak Moment**
core	451.3 μs		100μs
core@20%Nd		864.6 μs	550μs
core@20%Nd,5%Yb		768.9 μs	650μs
core@20%Nd,15%Yb		497.3 μs	350μs
core@20%Nd,20%Yb		461.2 μs	250μs
core@20%Nd,30%Yb		400.6 μs	150μs
core@20%Nd,45%Yb		392.5 μs	100μs
		Core-shell-shell Decay lifetime	Peak Moment
core@20%Nd@Y		1049.3 μs	650μs
core@20%Nd,5%Yb@Y		1083.3 μs	900μs
core@20%Nd,15%Yb@Y		981.4 μs	750μs
core@20%Nd,30%Yb@Y		772.6 μs	500μs
core@20%Nd,45%Yb@Y		656.2 μs	400μs

Compare with under 976 nm laser excitation, the temporal lifetime peaks in core-shell-shell samples are more prolonged under 808 nm excitation, as shown in Figure 3.8. As the size and size-distributions are almost the same for the as-prepared core-shell-shell nanoparticles, so the size difference upon the change in the rising time peak position can be ruled out. Therefore, the prolonger activator temporal lifetime peak moment can be attributed to the multi-step interfacial energy transfer process from Nd^{3+} to the core UCNPs through Yb^{3+} and the assistance of the active-shell design.

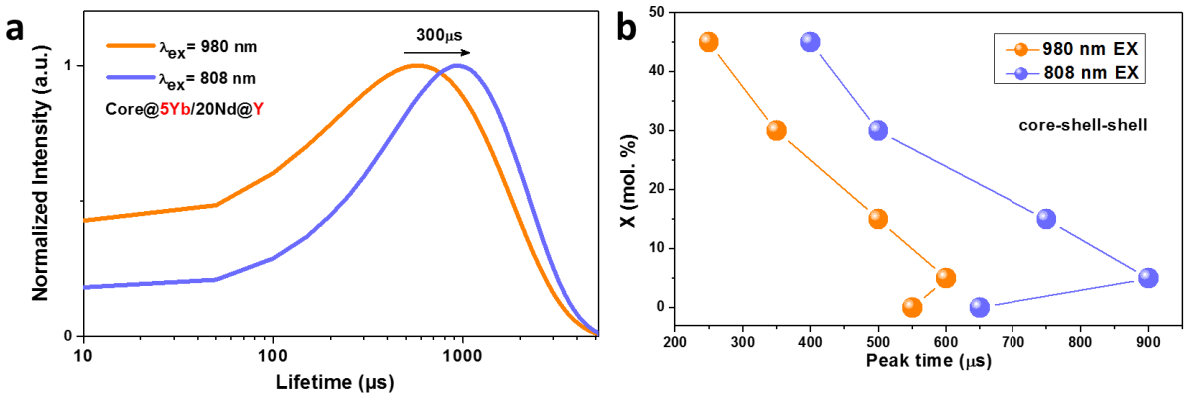

Figure 3.8. Temporal evolution UC luminescence decays curves of Tm^{3+} at blue emission band of (a) core@ $NaYF_4$:5% Yb^{3+}, 20% Nd@$NaYF_4$, (b) lifetime peak moment of core@ $NaYF_4$:x% Yb^{3+}, 20% Nd@$NaYF_4$ samples (x = 0, 5, 15, 30 and 45% mol) after 808 nm and 976 nm pulse excitation with 200μs pulse width.

3.4.3 Cross-relaxation in core-shell-shell ensemble nanoparticles.

To deeply investigated the possible cross-relaxation (CR) process in the core-shell-shell samples, we perform a detailed spectroscopic study of the core-shell-shell nanoparticles with an increasing concentration of Yb^{3+} in the active shell. Generally, CR happens with the spectroscopic feature of trade-off intensities between the associated peaks from the ion pair.[34,35] It is confirmed in our system that with the increasing of Yb^{3+} concentration from 5 % to 45 %, all the visible emission bands of Tm^{3+} decrease, but simultaneously the emission bands according to Nd^{3+}: $^4G_{7/2} \rightarrow {}^4I_{13/2}/{}^4I_{11/2}$ transitions increase (Fig. 3.9a and 3.9c). It's worth mention here the weakening of Tm^{3+} emissions inner core is a responsive visualization of the energy consumption of Yb^{3+} in the active shell. This means CR between Yb^{3+} and Nd^{3+} in the

active shell dominates the appearance of Nd^{3+}' visible emission through depleting the majority of the excited Yb^{3+} ions, resulting in the quenching of Tm^{3+} upconversion luminescence(Fig. 3.9b). This is further confirmed by a verification experiment, in which the $NaYF_4$: x%Yb, 20%Nd@Y (x=0, 5, 45) nanoparticles are designed (TEM images in Fig.3.10). As shown in Figure 3.9d, the similar phenomenon of the Nd^{3+} emission enhancement with higher Yb^{3+} concentration is observed under 808 nm laser, though Tm^{3+} is absent in the core. Detailed CR between Nd^{3+} and Yb^{3+}, as well as the resulting upconverting emission of Nd^{3+}, as shown in Figure 3.9b. The two or three photons involved upconversion of Nd^{3+} are proved by the double-log diagram with the slope of ~2.2 in both core@45%Yb, 20%Nd@$NaYF_4$ and $NaYF_4$:45%Yb, 20%Nd@$NaYF_4$ samples.

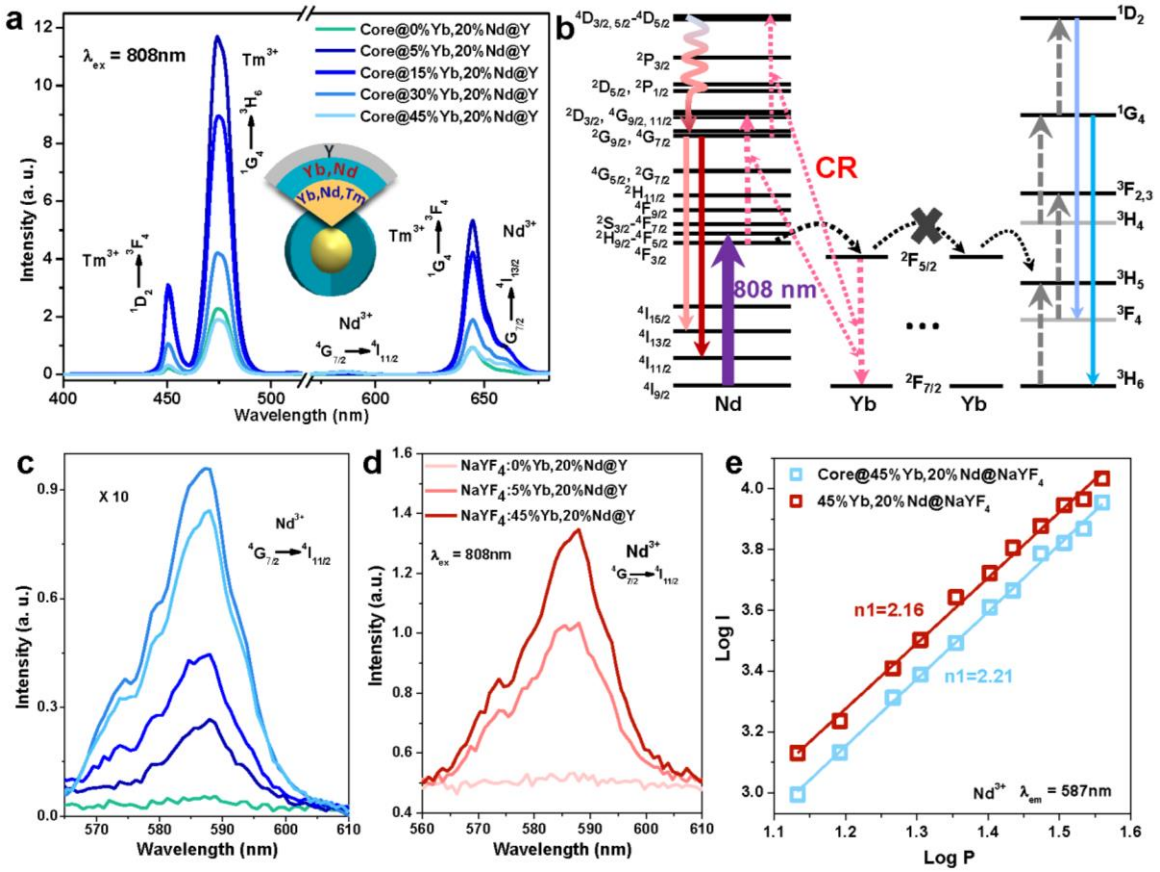

Figure 3.9 Cross relaxation between Nd and Yb shortens the arrival time of the peak moment of the excited state population. (a) Up-conversion emission spectra of core-active shell-inert shell nanoparticles with different Yb^{3+} concentration in the active shell under 808 nm excitation. (b) Energy levels of Nd^{3+} and sensitizer Yb^{3+} upon 808 nm excitation. Increasing the Yb^{3+} concentration, CR happens, the sensitized photon energy of Yb^{3+}, instead of being transferred to the Tm^{3+} ions, will be

back transferred to the Nd^{3+} ions to emit upconversion emissions. (c) amplified (x10) upconversion emission spectra between 565 nm and 610 nm in panel (a). (d) Upconversion emission spectra of $NaYF_4$:x%Yb, 20%Nd @ $NaYF_4$ (x=0,5,45) samples under excitation of 808 nm. (e)Power dependent intensity plots of core@ $NaYF_4$:45%Yb, 20%Nd @ $NaYF_4$ sample and 45%Yb, 20%Nd @ $NaYF_4$ sample.

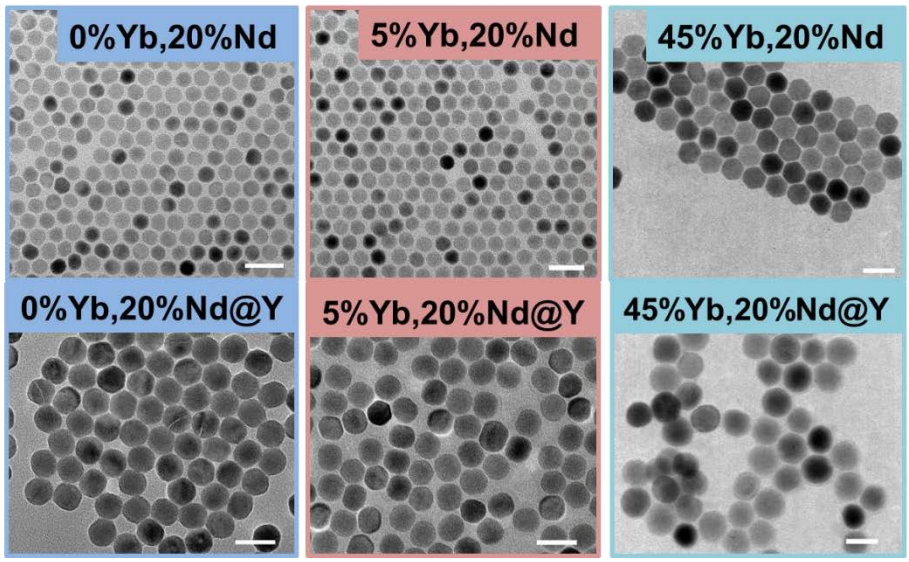

Figure 3.10 TEM morphology and histograms of $NaYF_4$: x% Yb^{3+}, 20%Nd^{3+} and $NaYF_4$: x% Yb^{3+}, 20%Nd^{3+}@ $NaYF_4$ (x = 0, 5 and 45) nanoparticles. Scale bars are 50 nm

3.4.4 The library of time-resolved profiles in core-shell-shell ensemble nanoparticles.

Combinational control of IEM, surface quenching and CR effects can create a library of time-resolved profiles to code UCNPs so that the new set of nanoparticles take turns to shine with diverse ESP peak moments. We conducted controlled synthesis of a series of β-$NaYF_4$:18% Yb^{3+}, 0.2% Tm^{3+}, 0.5% Nd^{3+} core nanoparticles, core-shell nanoparticles with active $NaYF_4$: x% Yb^{3+}, 20%Nd^{3+} (x = 0, 5, 15, 20, 30 and 45) at same shell thickness, as well as the corresponding core-shell-shell nanoparticles with further inert $NaYF_4$ shell epitaxial growth. As illustrated in Figure 3.11a, when invoking the IEM through Yb^{3+} concentration optimization and an inert shell epitaxial growth, the ESP moment of Tm^{3+} ions is positively prolonged. While surface quenching effect (Figure 3.11b) and CR (Figure 3.11c) result in the emergence of short ESP moment of Tm^{3+} ions. Through comprehensive controlling surface quenching

effect and interionic CR act as the resistance while the IEM process as the positive force to pin each other, we successfully achieve the whole sub-millisecond scale ESP tuning, ranging from 100 μs to 900 μs (Figure 3.11e). Simultaneously, the decay time shows the same tendency of prolonging from 392 μs to1083 μs. Their lifetime profiles display very differently in the time domain. Values in Figure 3.11f further quantitatively map the large dynamic ranges of rising time, peak moment, and decay time distributions in identifying each batch of UCNPs samples.

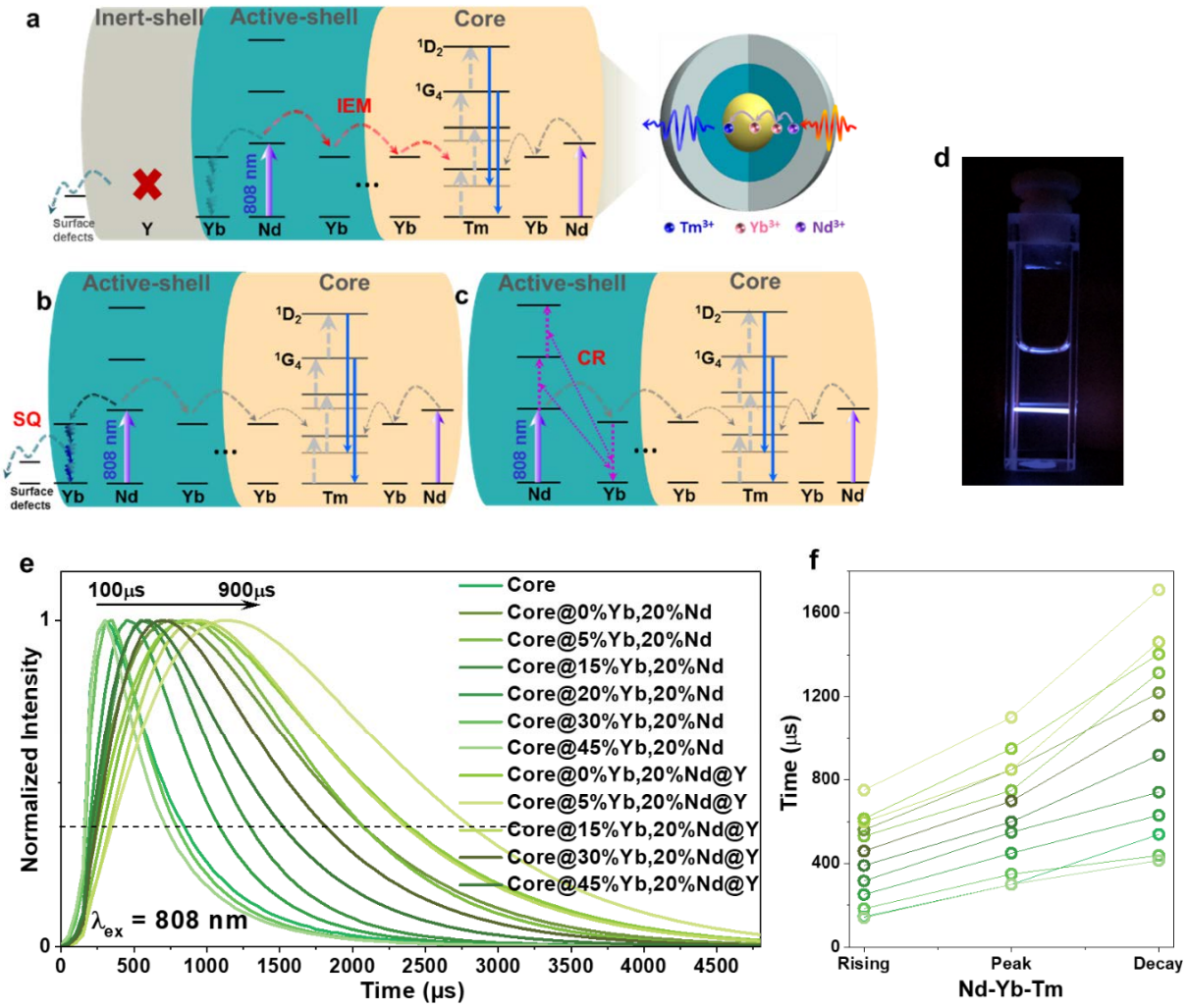

Figure 3.11 Principle of tailoring the excited state populations of Tm^{3+} blue emission to create a library of nanoparticles with continuous tenability of the excited state population. Nd^{3+} ions act as the new NIR absorbers and sensitizers in the traditional Yb^{3+} sensitized UCNPs in the core-shell structure under 808 nm excitation. The core-shell structure not only can increase the UC emission by transfer absorbed NIR laser from shell to the activators in the core but also has the ability to modulate

the rising time and decay time by regulating the interfacial energy migration process ($Nd^{3+}\rightarrow Yb^{3+}\rightarrow Tm^{3+}$) (a) and surface quenching effect (b). The interionic cross-relaxation can shorter the peak time and decay time (c). (d) Photo of representative UCNPs in Yb-Tm series showing their upconversion colour under 808 nm NIR excitation. (e) The time of the balanced population reflects in the temporal maximum excited state population moment. (f) Calculated rising time (τ_{I_1}-$\tau_{I_{1/e-rising}}$), peak moment (τ_{I_1}), and decay time ($\tau_{I_{1/e-decay}} - \tau_{I_1}$) according to the curves in panels (e) for Nd-Yb-Tm series.

The time-domain anti-counterfeiting by using four types of Yb-Nd-Tm series of UCNPs was based on the spatial modulation of the excitation patterns on the sample plane. A digital micro-mirror device (DMD) was added in the wide-field optical system as the spatial light modulator to generate excitation patterns of the ABC alphabet. The laser beam illuminated the DMD after beam collimation and expansion. Then the illuminated alphabet patterns were imaged on the sample plane. Then we acquired the lifetime image sequences of these four batches of UCNPs under 808 nm pulse laser illumination of ABC alphabetical patterns.This large scale time-domain tunability enables us to demonstrate a time-resolved display upon pulse excitation. Figure 3.12 shows the gating time to display the dynamic patterns that appeared at the surface of four selected powder pallets.

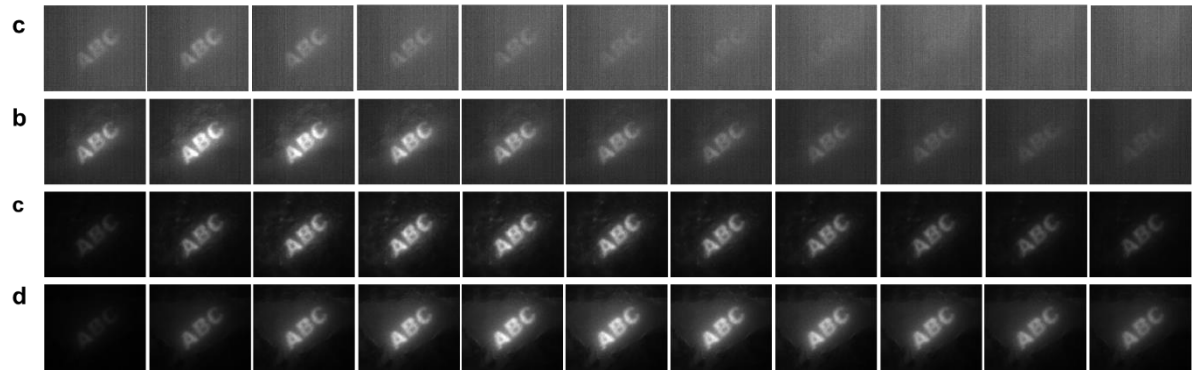

Figure 3.12 Time-resolved scanning of Tm^{3+} blue emission band after 808 nm with 200 μs pulse excitation of core@ $NaYF_4$:45%Yb, 20%Nd(a), core@ $NaYF_4$:20%Yb, 20%Nd(b), core@ $NaYF_4$:5%Yb, 20%Nd(c) and core@ $NaYF_4$:5%Yb, 20%Nd @ $NaYF_4$(d) samples.

3.5 Conclusion

In summary, we have uncapped a dimension by tuning the peak time of excited-state populations of upconversion luminescence following the pulsed excitation. We decode the underpinning physics and realize the full control of IEM, surface quenching effect, and interionic CR processes. We master the full control of the peak time of the balanced excited states from both the rise time and decay time profile. The duration can be extended from 100 μs to 900 μs after the 808 nm excitation is switched off. These components intricately intertwined in the nanoparticles, while a key found to effectively manage the energy transfers was the core-shell-shell design with rational doping of the ions and isolation of surface molecules/defects. By using the temporal dimension of luminescent lifetime signals, this approach opens a new opportunity of nanoparticles in the display, data storage, anti-counterfeiting, and life science.

3.6 Reference

(1) Lin, G.; Baker, M. A. B.; Hong, M.; Jin, D. The Quest for Optical Multiplexing in Bio-Discoveries. *Chem.* **2018**, *4* (5), 997–1021.

(2) Gu, M.; Zhang, Q.; Lamon, S. Nanomaterials for Optical Data Storage. *Nat. Rev. Mater.* **2016**, *1* (12), 16070.

(3) Xu, L.; Chen, J.; Song, J.; Li, J.; Xue, J.; Dong, Y.; Cai, B.; Shan, Q.; Han, B.; Zeng, H. Double-Protected All-Inorganic Perovskite Nanocrystals by Crystalline Matrix and Silica for Triple-Modal Anti-Counterfeiting Codes. *ACS Appl. Mater. Interfaces* **2017**, *9* (31), 26556–26564.

(4) Lei, L.; Chen, D.; Li, C.; Huang, F.; Zhang, J.; Xu, S. Inverse Thermal Quenching Effect in Lanthanide-Doped Upconversion Nanocrystals for Anti-Counterfeiting. *J. Mater. Chem. C* **2018**, *6* (20), 5427–5433.

(5) Lu, Y.; Zhao, J.; Zhang, R.; Liu, Y.; Liu, D.; Goldys, E. M.; Yang, X.; Xi, P.; Sunna, A.; Lu, J.; et al. Tunable Lifetime Multiplexing Using Luminescent Nanocrystals. *Nat. Photonics* **2014**, *8* (1), 32–36.

(6) Chan, E. M. Combinatorial Approaches for Developing Upconverting Nanomaterials: High-Throughput Screening, Modeling, and Applications. *Chem. Soc. Rev.* **2015**, *44* (6), 1653–1679.

(7) Lu, Y.; Lu, J.; Zhao, J.; Cusido, J.; Raymo, F. M.; Yuan, J.; Yang, S.; Leif, R. C.; Huo, Y.; Piper, J. A.; et al. On-the-Fly Decoding Luminescence Lifetimes in the Microsecond Region for Lanthanide-Encoded Suspension Arrays. *Nat. Commun.* **2014**, *5* (1), 3741.

(8) Cheng, L.; Wang, C.; Liu, Z. Upconversion Nanoparticles and Their Composite Nanostructures for Biomedical Imaging and Cancer Therapy. *Nanoscale* **2013**, *5* (1), 23–37.

(9) Zhang, Y.; Huang, L.; Liu, X. Unraveling Epitaxial Habits in the $NaLnF_4$ System for Colour Multiplexing at the Single-Particle Level. *Angew. Chemie - Int. Ed.* **2016**, *55* (19), 5718–5722.

(10) Dong, H.; Sun, L.-D.; Yan, C.-H. Energy Transfer in Lanthanide Upconversion Studies for Extended Optical Applications. *Chem. Soc. Rev.* **2015**, *44* (6), 1608–1634.

(11) Alyatkin, S.; Asharchuk, I.; Khaydukov, K.; Nechaev, A.; Lebedev, O.; Vainer, Y.; Semchishen, V.; Khaydukov, E. The Influence of Energy Migration on Luminescence Kinetics Parameters in Upconversion Nanoparticles. *Nanotechnology* **2016**, *28* (3), 35401.

(12) Tu, L.; Liu, X.; Wu, F.; Zhang, H. Excitation Energy Migration Dynamics in Upconversion Nanomaterials. *Chem. Soc. Rev.* **2015**, *44* (6), 1331–1345.

(13) Güdel, H. U.; Pollnau, M. Near-Infrared to Visible Photon Upconversion Processes in Lanthanide Doped Chloride, Bromide and Iodide Lattices. *J. Alloys Compd.* **2000**, *303*, 307–315.

(14) Haase, M.; Schäfer, H. Upconverting Nanoparticles. *Angew. Chemie Int. Ed.* **2011**, *50* (26), 5808–5829.

(15) Chen, X.; Peng, D.; Ju, Q.; Wang, F. Photon Upconversion in Core-Shell Nanoparticles. *Chem. Soc. Rev.* **2015**, *44* (6), 1318–1330.

(16) Zhao, J.; Lu, Z.; Yin, Y.; McRae, C.; Piper, J. A.; Dawes, J. M.; Jin, D.; Goldys, E. M. Upconversion Luminescence with Tunable Lifetime in $NaYF_4$: Yb, Er Nanocrystals: Role of Nanocrystal Size. *Nanoscale* **2013**, *5* (3), 944–952.

(17) Wang, Y.; Deng, R.; Xie, X.; Huang, L.; Liu, X. Nonlinear Spectral and Lifetime Management in Upconversion Nanoparticles by Controlling Energy Distribution. *Nanoscale* **2016**, *8* (12), 6666–6673.

(18) Yu, Z.; Chan, W. K.; Tan, T. T. Y. Neodymium-Sensitized Nanoconstructs for Near-Infrared Enabled Photomedicine. *Small* **2019**, *1905265*, 1–21.

(19) Guo, S.; Tsang, M. K.; Lo, W. S.; Hao, J.; Wong, W. T. 808 Nm Excited Energy Migration Upconversion Nanoparticles Driven by a Nd^{3+}-Trinity System with Colour-Tunability and Superior Luminescence Properties. *Nanoscale* **2018**, *10* (6), 2790–2803.

(20) Wiesholler, L. M.; Frenzel, F.; Grauel, B.; Würth, C.; Resch-Genger, U.; Hirsch, T. Yb,Nd,Er-Doped Upconversion Nanoparticles: 980 nm: Versus 808 nm Excitation. *Nanoscale* **2019**, *11* (28), 13440–13449.

(21) Zhang, Y.; Yu, Z.; Li, J.; Ao, Y.; Xue, J.; Zeng, Z.; Yang, X.; Tan, T. T. Y. Ultrasmall-Superbright Neodymium-Upconversion Nanoparticles via Energy Migration Manipulation and Lattice Modification: 808 Nm-Activated Drug Release. *ACS Nano* **2017**, *11* (3), 2846–2857.

(22) Zeng, L.; Pan, Y.; Zou, R.; Zhang, J.; Tian, Y.; Teng, Z.; Wang, S.; Ren, W.; Xiao, X.; Zhang, J.; et al. 808 nm-Excited Upconversion Nanoprobes with Low Heating Effect for Targeted Magnetic Resonance Imaging and High-Efficacy Photodynamic Therapy in HER_2-Overexpressed Breast Cancer. *Biomaterials* **2016**, *103*, 116–127.

(23) Xie, X.; Gao, N.; Deng, R.; Sun, Q.; Xu, Q.; Liu, X. Mechanistic Investigation of Photon Upconversion in Nd^{3+} sensitized Core−shell Nanoparticles. *J. Am. Chem. Soc* **2013**, *135* (34), 12608–12611.

(24) Shan, J.; Uddi, M.; Yao, N.; Ju, Y. Anomalous Raman Scattering of Colloidal Yb^{3+},Er^{3+} Codoped $NaYF_4$ Nanophosphors and Dynamic Probing of the Upconversion Luminescence. *Adv. Funct. Mater.* **2010**, *20* (20), 3530–3537.

(25) Suyver, J. F.; Aebischer, A.; Biner, D.; Gerner, P.; Grimm, J.; Heer, S.; Krämer, K. W.; Reinhard, C.; Güdel, H. U. Novel Materials Doped with Trivalent Lanthanides and Transition Metal Ions Showing Near-Infrared to Visible Photon Upconversion. *Opt. Mater. (Amst).* **2005**, *27* (6), 1111–1130.

(26) Huang, X.; Lin, J. Active-Core/Active-Shell Nanostructured Design: An Effective Strategy to Enhance Nd^{3+}/Yb^{3+} Cascade Sensitized Upconversion Luminescence in Lanthanide-Doped Nanoparticles. *J. Mater. Chem. C* **2015**, *3* (29), 7652–7657.

(27) Xu, D.; Liu, C.; Yan, J.; Yang, S.; Zhang, Y. Understanding Energy Transfer Mechanisms for Tunable Emission of Yb^{3+}-Er^{3+} Codoped GdF_3 Nanoparticles: Concentration-Dependent Luminescence by near-Infrared and Violet Excitation. *J. Phys. Chem. C* **2015**, *119* (12), 6852–6860.

(28) Zhang, Y.; Liu, X.; Lang, Y.; Yuan, Z.; Zhao, D.; Qin, G.; Qin, W. Synthesis of Ultra-Small $BaLuF_5$: Yb^{3+}, Er^{3+}@ $BaLuF_5$: Yb^{3+} Active-Core–active-Shell Nanoparticles with Enhanced up-Conversion and down-Conversion Luminescence by a Layer-by-Layer Strategy. *J. Mater. Chem. C* **2015**, *3* (9), 2045–2053.

(29) Wilhelm, S.; Kaiser, M.; Würth, C.; Heiland, J.; Carrillo-Carrion, C.; Muhr, V.; Wolfbeis, O. S.; Parak, W. J.; Resch-Genger, U.; Hirsch, T. Water Dispersible Upconverting Nanoparticles: Effects of Surface Modification on Their Luminescence and Colloidal Stability. *Nanoscale* **2015**, *7* (4), 1403–1410.

(30) Sun, T.; Ma, R.; Qiao, X.; Fan, X.; Wang, F. Shielding Upconversion by Surface Coating: A Study of the Emission Enhancement Factor. *ChemPhysChem* **2016**, *17* (5), 766–770.

(31) Boyer, J.-C.; Manseau, M.-P.; Murray, J. I.; Van Veggel, F. C. J. M. Surface Modification of Upconverting $NaYF_4$ Nanoparticles with PEG−phosphate Ligands for NIR (800nm) Biolabeling within the Biological Window. *Langmuir* **2010**, *26* (2), 1157–1164.

(32) Fischer, S.; Bronstein, N. D.; Swabeck, J. K.; Chan, E. M.; Alivisatos, A. P. Precise Tuning of Surface Quenching for Luminescence Enhancement in Core–shell Lanthanide-Doped Nanocrystals. *Nano Lett.* **2016**, *16* (11), 7241–7247.

(33) Scatena, L. F.; Brown, M. G.; Richmond, G. L. Water at Hydrophobic Surfaces: Weak Hydrogen Bonding and Strong Orientation Effects. *Science.* **2001**, *292* (5518), 908–

912.

(34) Hölsä, J.; Laamanen, T.; Laihinen, T.; Lastusaari, M.; Pihlgren, L.; Rodrigues, L. C. V. White Up-Conversion Luminescence of $NaYF_4:Yb^{3+},Pr^{3+},Er^{3+}$. *Opt. Mater.* **2014**, *36* (10), 1627–1630.

(35) Miazato, K.; De Sousa, D. F.; Delben, A.; Delben, J. R.; De Oliveira, S. L.; Nunes, L. A. O. Upconversion Mechanisms in Tm^{3+} Doped Lead Fluoroindogallate Glasses. *J. Non. Cryst. Solids* **2000**, *273* (1–3), 246–251.

Chapter 4 Optical Fingerprints of Single Nanoparticles for Optical Multiplexing

4.1 Preamble

Despite their remarkable potential utility, the practical use of UCNPs in recent decades has primarily focused on bulk materials or ensemble nanoparticles, which extremely limits their applications. These limitations are largely attributed to the difficulties in preparing small nanocrystals sub to 50 nm that exhibit high dispersibility and strong UC emission at a single nanoparticle level.[1–3] It was not until the last ten years, because of the rapid developments in nano synthesis technology, the UCNPs became more prominent in the different fields, particularly in terms of biological applications. The development of materials science makes it possible to encode information carriers from the macroscopic level to the nanoscale. As high-quality UC nanocrystals can be arbitrarily prepared, the study of UC processes and potential applications has evolved into a highly interdisciplinary field, which has rapidly expanded at the frontiers of photochemistry, biophysics and biomedical science.[4–10]

Non-blinking, non-bleaching, multidimensional and super-bright single upconversion nanoparticles can be excited under different NIR excitation lights, which is ideal for super-capacity multiplexing, single-molecule tracking, and digital assays. Optical multiplexing challenges our abilities in creating multiplexed codes in orthogonal dimensions and assigning them to the macroscopic and nanoscale carriers[11]. In the current study, two groups of UCNPs, Yb^{3+}, Nd^{3+}, Er^{3+} core three-layer shell and Yb^{3+}-Tm^{3+} core-inert shell UCNPs were prepared, which can form spectral and lifetime orthogonal multiplexing under 808-nm and 976-nm excitation at the single nanoparticle level, respectively. We systematically investigated the upconversion optical properties, particularly the lifetime curves of single nanoparticles using 976-nm and 808-nm excitations under the confocal microscope system. This work suggests that optical uniformity and diversity create high-dimensional optical signatures that will enable high throughput applications in biomolecular screening, imaging analysis, and data storage and security.

4.2 Introduction

Multiplexed encoding in information technologies, high-throughput clinical diagnostics, multichannel bioimaging, and security applications require code-intensive materials to achieve high data-storage capacity and simultaneous identification. Incorporating multiple pieces of information into an individual encoding unit should be of great significance toward intensifying multiplexing. Trivalent lanthanide ion (Ln^{3+})-doped UCNPs can convert multiple NIR photons into shorter wavelength ultraviolet (UV), visible or NIR luminescence by utilizing the real long-lived, ladder-like energy levels of Ln^{3+} ions. UCNPs are made of rigid crystal hosts and can be doped by multiple Ln^{3+} ions, allowing excellent photostability and a significant tunability in emission colours, lifetimes and brightness, all of which are highly dependent on excitation power density following the sophisticated non-linear process.[12–17] Single nanoparticle characterization has played an important role in the discoveries of the many unique properties of UCNPs, including their photostability, optical uniformity, and switchability under different wavelength excitations, which have led to a range of recent advances being developed using single UCNPs for applications, such as super-resolution imaging[18,19], single-molecule tracking[20,21], digital assay[22–24] and optical multiplexing.

Optical multiplexing with increased capacity will advance the ongoing development of next-generation enabling technologies, which range from high-capacity data storage[25,26], anti-counterfeiting[3,27], and large-volume information communication[28,29] to high-throughput screening and imaging of multiple molecules and cells in a single test[30–32]. Super-capacity optical multiplexing challenges our ability to create multiplexed codes in orthogonal dimensions, (e.g., intensity, colour, polarization and decay time) and to assign them to the macroscopic and nanoscale carriers. Spectrum encoding based on the luminescent emission wavelength and relative intensity in microsized beads is still the most frequently used technique. However, spectrum-encoding approaches and macroscopic carriers alone are limited due to the requirement of challenging spectral deconvolution and nanoscale biological applications. On the other hand, the limited coding density of the emission spectra is unable to meet increases in information in complicated analytes. Therefore, it is critical to increasing

encoding capacity by using orthogonal encoding dimensions in nanomaterials. The control inherent in optical uniformity and tuning the diversity of single nanoparticles, nanoparticle to nanoparticle, holds the key. Though desirably the size of material that carries the optical barcodes can be pushed from microscopic to the nanoscopic range, it sacrifices the number of detectable codes, e.g. typically three to four colour channels or brightness levels[33,34]. This is because the amount of signal from a nanoscale object drops exponentially and the size of them is well below the optical diffraction limit for imaging, which prevents the conventional optics and detection process.

In this work, we controlled the synthesis of eight batches of Yb^{3+}, Nd^{3+}, Er^{3+}-doped β-$NaYF_4$ UCNPs with the core three-layer shell design and eight batches of Yb^{3+}-Tm^{3+} core-inert shell UCNPs. The former can emit green and red emission under an 808-nm laser, and the emission band of the latter is located in the blue region at approximately 470 nm through the use of the 976-nm laser. We systematically investigated the upconversion intensity, spectrum and lifetime properties at a single nanoparticle level under the confocal microscope system. We demonstrated a library of these 16 kinds of single UCNPs with unique and tailored lifetime profiles show great potential for super-capacity multiplexing. This enables the nanoparticles to generate versatile orthogonalized upconversion optical properties in both emission colours and lifetime dimensions, which could greatly increase coding density.

4.3 Experimental section

4.3.1 Synthesis of $NaYF_4$: Yb, Er/Tm core nanoparticles

The $NaYF_4$:20%Yb, 2%Er core nanoparticles were synthesized using a coprecipitation method. In a typical procedure, 1 mmol $RECl_3$ (RE=Y, Yb, Er) with $YCl_3 \cdot 6H_2O$ (0.78 mmol), $YbCl_3 \cdot 6H_2O$ (0.2 mmol) and $ErCl_3 \cdot 6H_2O$ (0.02 mmol) together with oleic acid (OA, 6 mL) and 1-octadecene (ODE, 15 mL) were added to a 50 ml three-neck round-bottom flask under vigorous stirring. The resulting mixture was heated at 150 ºC for 40 mins to form lanthanide oleate complexes. The solution was cooled down to room temperature. Subsequently, a methanol solution (6 mL) containing NaOH (2.5 mmol, 0.1g) and NH_4F (4 mmol, 0.14g) was added and stirred at 50 ºC for 40 mins, and then the mixture was slowly heated to 150 °C and

kept for 40 mins under argon flow to remove methanol and residual water. Next, the solution was quickly heated at 300 ºC under argon flow for 1.5 h before cooling down to room temperature. The resulting core nanoparticles were precipitated by the addition of ethanol, collected by centrifugation at 9000 rpm for 5 min, the final $NaYF_4$:Yb,Er nanocrystals were redispersed in cyclohexane with 5 mg/mL concentration after washing with cyclohexane/ethanol/methanol several times.

We synthesized another four kinds of Er^{3+} doped core nanoparticles for similar size with different doping concentrations ($NaYF_4$:20%Yb, 1.5%Er, $NaYF_4$:20%Yb, 1%Er, $NaYF_4$:30%Yb, 2%Er, $NaYF_4$:30%Yb, 8%Er) using the same above method.

We also synthesized another eight kinds of Tm^{3+} doped core nanoparticles for similar size with different doping concentrations ($NaYF_4$:40%Yb, 0.2%Tm, $NaYF_4$:40%Yb, 0.5%Tm, $NaYF_4$:40%Yb, 0.8%Tm, $NaYF_4$:40%Yb, 1%Tm, $NaYF_4$:40%Yb, 2%Tm, $NaYF_4$:40%Yb, 4%Tm, $NaYF_4$:40%Yb, 6%Tm, $NaYF_4$:40%Yb, 8%Tm) using the same above method.

The precursors were prepared as the above procedure until the step where the reaction solution was slowly heated to 150 °C after adding NaOH/NH_4F solution and kept for 40 min. Instead of further heating to 300 °C to trigger nanocrystal growth, the solution was cooled down to room temperature to yield the shell precursors.

4.3.2 Synthesis of core-shell nanoparticles

The core@ $NaYF_4$:5%Yb and core@ $NaYF_4$ core-shell nanoparticles was prepared by layer by layer epitaxial growth method. The pre-synthesized $NaYF_4$: Yb, Er core nanoparticles were used as seeds for shell modification. 0.2 mmol as-prepared core nanocrystals were added to a 50 ml flask containing 3 ml OA and 8 ml ODE. The mixture was heated to 160 °C under argon for 30 min, and then further heated to 300 °C. Next, a certain amount of as-prepared shell precursors were injected into the reaction mixture and ripened at 300 °C for 2 min, followed by the same injection and ripening cycles for approximately several times to get around 3 nm thickness shell. Finally, the slurry was cooled down to room temperature and the formed core-shell nanocrystals were washed dispersed in cyclohexane for next step epitaxial growth.

The core@$NaYF_4$:5%Yb@$NaYF_4$:x%Yb, 20%Nd (x=5, 15, 30) core-shell-shell nanoparticles were also prepared by epitaxial growth method described above and the core-shell samples were used as the seeds.

The core@$NaYF_4$:5%Yb@$NaYF_4$:x%Yb,20%Nd@$NaYF_4$ (x=5, 15, 30) core-shell-shell-shell nanoparticles were also prepared by epitaxial growth method described above and the core-shell-shell samples were used as the seeds.

To systemically investigate the optical fingerprints of single nanoparticles in Yb^{3+}, Nd^{3+}, Er^{3+} core three-layer shell and Yb^{3+}-Tm^{3+} core-inert shell UCNPs, we synthesized 16 arbitrary types of core multi-shell nanoparticles, the summary of the composition of these core-multi shell UCNPs are shown in Table. 4.1 and Table. 4.2, respectively.

Table 4.1. Summary of the composition of Nd^{3+}-Yb^{3+}-Er^{3+} tri-doped core-multi shell UCNPs.

	Sample	core	Migration Layer	Sensitization Layer	Inert Layer
Er^{3+} in core	1	$30Yb^{3+}/2Er^{3+}$	$5Yb^{3+}$	$15Yb^{3+}/20Nd^{3+}$	Y^{3+}
	2	$30Yb^{3+}/8Er^{3+}$	$5Yb^{3+}$	$15Yb^{3+}/20Nd^{3+}$	Y^{3+}
Yb^{3+} in core	3	$20Yb^{3+}/2Er^{3+}$	$5Yb^{3+}$	$15Yb^{3+}/20Nd^{3+}$	Y^{3+}
	4	$40Yb^{3+}/2Er^{3+}$	$5Yb^{3+}$	$15Yb^{3+}/20Nd^{3+}$	Y^{3+}
Yb^{3+} in Sensitization Layer	5	$30Yb^{3+}/2Er^{3+}$	$5Yb^{3+}$	$5Yb^{3+}/20Nd^{3+}$	Y^{3+}
	6	$30Yb^{3+}/2Er^{3+}$	$5Yb^{3+}$	$30Yb^{3+}/20Nd^{3+}$	Y^{3+}
Nd^{3+} in Sensitization Layer	7	$30Yb^{3+}/2Er^{3+}$	$5Yb^{3+}$	$15Yb^{3+}/40Nd^{3+}$	Y^{3+}
	8	$30Yb^{3+}/2Er^{3+}$	$5Yb^{3+}$	$15Yb^{3+}/60Nd^{3+}$	Y^{3+}

Table 4.2. Summary of composition and size of eight kinds of Yb^{3+}-Tm^{3+} doped $NaYF_4$ core-shell samples.

Core	Passivation layer (6 nm)	Sample
$40Yb^{3+}/0.2Tm^{3+}$ (45 nm)	Y^{3+} (6 nm)	I
$40Yb^{3+}/0.5Tm^{3+}$ (44nm)	Y^{3+} (6 nm)	II
$40Yb^{3+}/0.8Tm^{3+}$ (42 nm)	Y^{3+} (6 nm)	III
$40Yb^{3+}/1Tm^{3+}$ (42 nm)	Y^{3+} (6 nm)	IV
$40Yb^{3+}/2\ Tm^{3+}$ (48 nm)	Y^{3+} (6 nm)	V
$40Yb^{3+}/4\ Tm^{3+}$ (53 nm)	Y^{3+} (6 nm)	VI
$40Yb^{3+}/6\ Tm^{3+}$ (51 nm)	Y^{3+} (6 nm)	VII
$40Yb^{3+}/8\ Tm^{3+}$ (53 nm)	Y^{3+} (6 nm)	VIII

4.4 Results and discussion

4.4.1 Materials characterization of two groups of nanoparticles

Compared to the conventional micron-sized information carriers by tagging the nanoparticles onto microbeads (Figure. 4.1a), optical codes created on nanoscopic sized nanoparticles can significantly increase the capacity of coding information. In this chapter, we built a stage-scan confocal microscope (Figure. 4.1b) for spectra, power-dependent intensity and lifetime measurements of single nanoparticles. When use the confocal scanning microscopy to test the optical fingerprints of single nanoparticles, the emission from the sample is collected by the same objective lens and refocused into an optical fiber. During the point by point scanning across each pixel, when the excitation laser beam moves closer to a single nanoparticle, the system will detect a brighter emission intensity. Therefore each single nanoparticle will show a Gaussian spot in the confocal scanning microscopic image (Figure. 4.1c). The diode laser was modulated to produce 200 μs excitation pulses for the lifetime measurement. The photon-counting SPAD is continuously switched on to capture the long-lifetime luminescence.

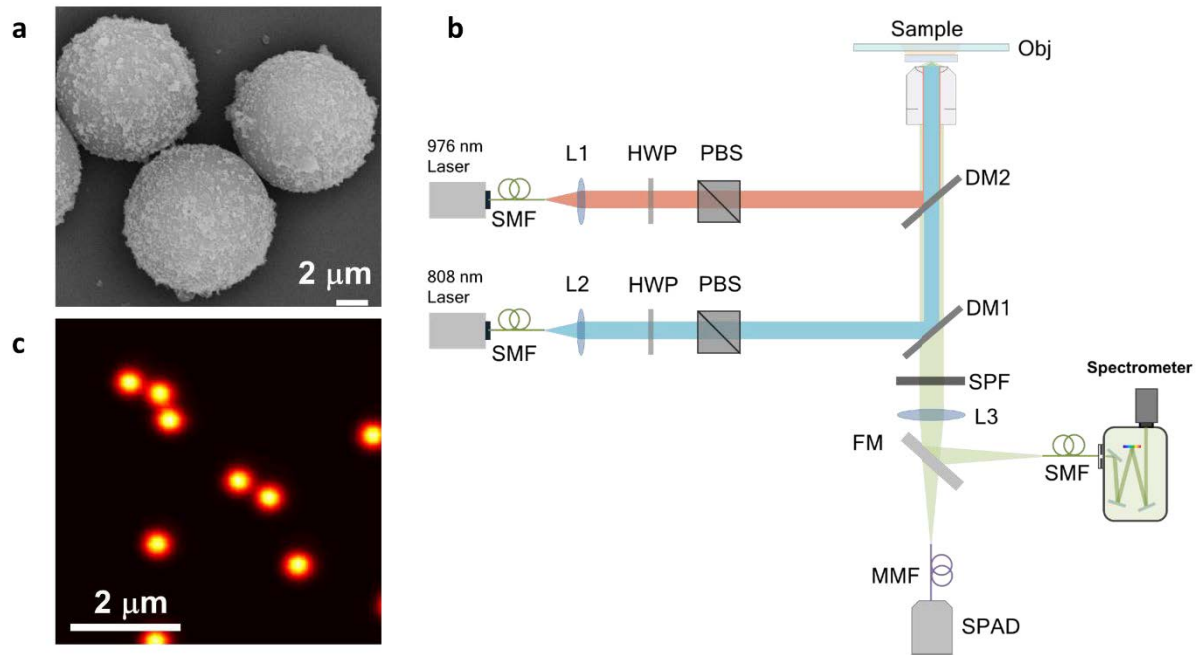

Figure 4.1 (a) SEM photos of 5 μm polystyrene microbeads after tagged with UCNPs nanoparticles. Scale bar: 1 μm. (b) Schematic view of confocal microscopy. (c) One typical confocal scanning microscopic image.

The design structure of Yb^{3+}, Nd^{3+}, Er^{3+} core three-layer shell UCNPs is consisting of a β-$NaYF_4$: Yb, Er core (~ 30 nm in diameter), migration layer doped with Yb^{3+} (~ 2.5 nm), sensitization layer doped with Nd^{3+} and Yb^{3+} (~ 6 nm), and inert layer (~5 nm). Simplified energy levels and cascade photon energy sensitization, transfer, and conversion process were shown in Figure. 4.2b. The morphology and size distribution of the core-multi shell upconversion nanoparticles $NaYF_4$: 30%Yb, 2%Er@ $NaYF_4$: 5%Yb@ $NaYF_4$:15%Yb, 20%Nd@$NaYF_4$ named as the sample 1 as shown in Figure. 4.2a. The TEM image in Figure 4.2c shows a typical Yb^{3+}-Tm^{3+} core-inert shell structure $NaYF_4$ UCNPs with morphology uniformity, the average size of about 50 nm in diameter ($NaYF_4$: 20%Yb, 0.2%Tm@ $NaYF_4$ named sample I). The illustration in figure 4.2d shows the design of the Yb^{3+}-Tm^{3+} doped nanoparticles, including a core-shell structure through layer-by-layer epitaxial growth, and doping strategies to achieve lifetime tunability in plateau moment, rising time, and decay time. It shows the simplified energy levels and cascade photon energy sensitization, transfer and

conversion process, Yb^{3+}-sensitization at 976 nm, and upconversion of near-infrared photons into higher-energy visible emissions in a typical Yb^{3+}/Tm^{3+} system.

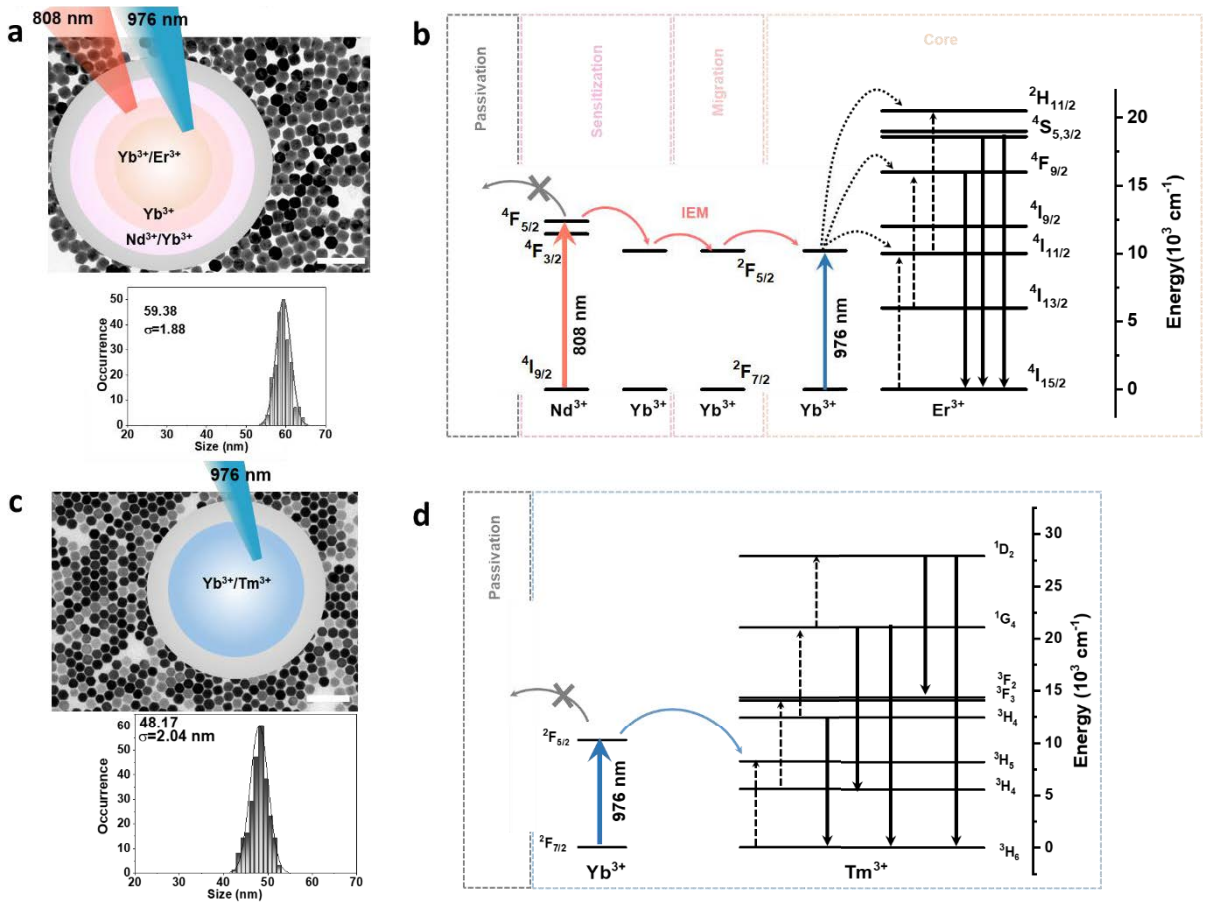

Figure 4.2 Materials characterization of Nd^{3+} and Yb^{3+} sensitized UCNPs. (a) TEM characterization of a kind of typical morphology uniform nanocrystals of Yb^{3+}, Nd^{3+}, Er^{3+} core three-layer shell UCNPs. An arbitrary batch used here was chosen from a library of core-shell nanoparticles we synthesized in this work. **(b)** Schematic illustration of the above core-multi-shell nanoparticles under the excitations at 976 nm and 808 nm. The design structure of Nd^{3+} sensitized UCNPs used in this chapter is consisting of a β-$NaYF_4$: Yb, Er core, migration layer doped with Yb^{3+}, sensitization layer doped with Nd^{3+} and Yb^{3+}, and inert layer. **(c)** TEM characterization of a kind of typical morphology uniform Yb^{3+}-Tm^{3+} core-inert shell nanocrystals. **(d)** Schematic illustration of Yb^{3+}-Tm^{3+} core-shell UCNPs.

The morphology and size distributions of a set of typical core, core-shell, and core-shell-shell were shown in Figure. 4.3, and the relevant core-three layer shell upconversion nanoparticles $NaYF_4$: 30%Yb, 2%Er@ $NaYF_4$: 5%Yb@ $NaYF_4$:15%Yb, 20%Nd@$NaYF_4$ named 1 was

shown in Figure. 4.4c. Simplified energy levels and cascade photon energy sensitization, transfer and conversion process: Nd^{3+} sensitization at 808 nm, Yb^{3+}-mediated interfacial energy migration at 976 nm, and upconversion of near-infrared photons into higher-energy visible emissions in a typical Yb^{3+}/Er^{3+} system.

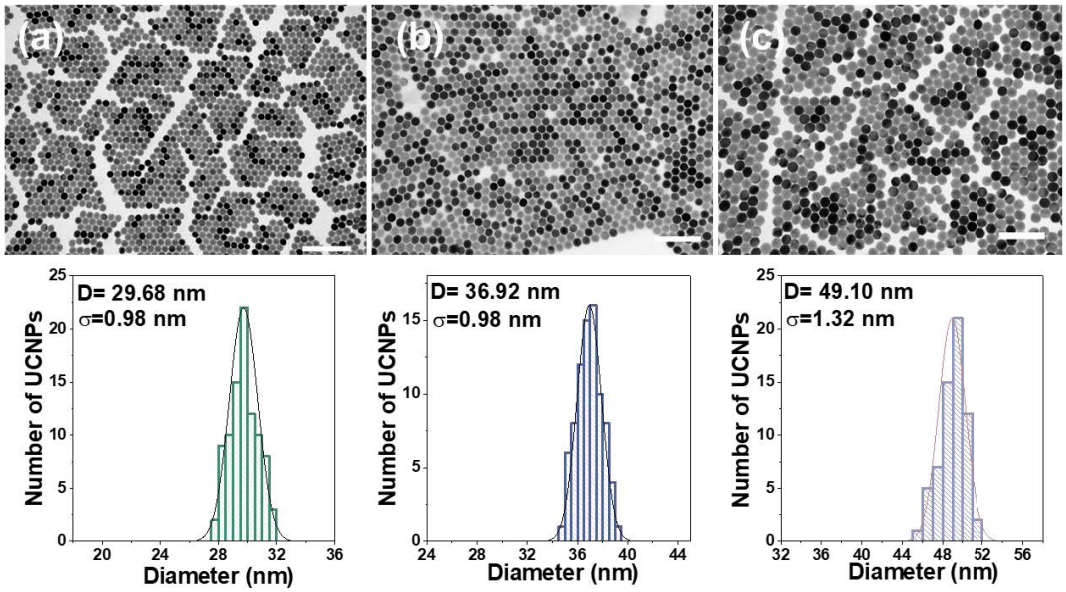

Figure 4.3 TEM photos and size distributions of a set of core, core-shell and core-shell-shell samples. (a) $NaYF_4$:30%Yb^{3+},2% Er^{3+} core nanoparticles. (b) $NaYF_4$: 30%Yb^{3+},2% Er^{3+}@ $NaYF_4$: 5%Yb^{3+} core-shell nanoparticles. (c) $NaYF_4$: 30%Yb^{3+},2% Er^{3+}@ $NaYF_4$: 5%Yb^{3+}@$NaYF_4$:15%Yb^{3+},20% Nd^{3+} core-shell-shell nanoparticles. Scale bar: 200 nm

The Nd^{3+} ions serve as the sensitizer to harvest 808 nm excitation energy, which results in the population of the $^4F_{5/2}$ excited state. The Yb^{3+} ion is used as the secondary sensitizer by passing on the energy from Nd^{3+} to β-$NaYF_4$: Yb, Er core or as the primary sensitizer to directly absorb 976 nm laser excitation (Figure 4.4a). The energy migrated or sensitized via Yb^{3+} will eventually reach the β-$NaYF_4$: Yb, Er core for upconversion emission by the activator Er^{3+} ions embedded in the inner core. The luminescence photograph and upconversion emission spectra for ensemble colloidal nanoparticles (Figure 4.4b) show nearly identical intensity profiles under 808 nm and 976 nm excitation at a power density of 0.5 W/cm^2. The upconversion emission phenomenon of ensemble colloidal nanoparticles is consistent with the previous report. The predominantly green and red emission of Er^{3+} is obtained at 976 and 808 nm

excitation light (Figure 4.4c) and the emission intensity of the dispersed oleate-capped nanoparticles under the 808 nm-excited is roughly equivalent to that 976 nm-excited at a low excitation power density at 0.5 W/cm^{-2}. As exhibited in Figure. 4.4c, the distinct contrast of the shell layers and the core for all the core-multi-shell nanoparticles is detected because of different doped concentration of lanthanide ions with different atomic number. This result evidences the formation of core-multi-shell nanoarchitecture where the three shell layers successfully grow on the β-$NaYF_4$: Yb, Er core. A high-resolution TEM micrograph of an individual sample I nanoparticle confirms its single-crystalline characteristic with high-crystallinity. The (100) plane of the β-$NaYF_4$ phase with an interplanar spacing of 5.3 Å is resolved in Figure. 4.4d.

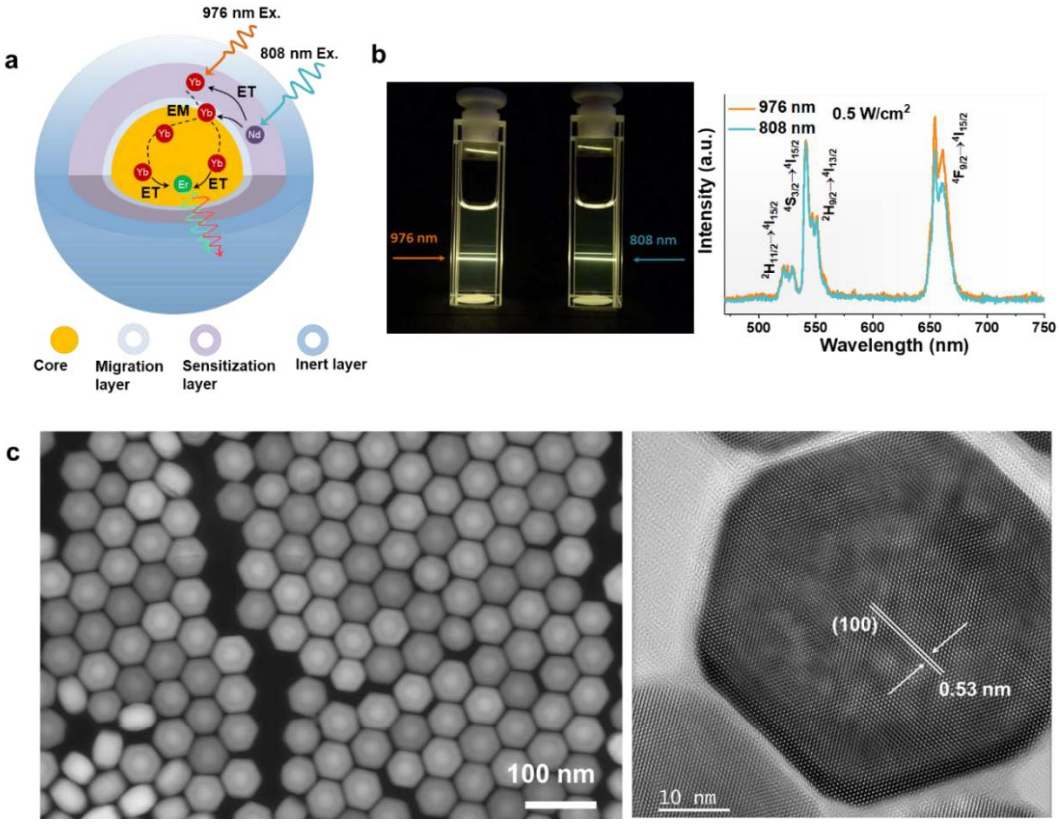

Figure 4.4 Structure design and optical property of the colloidal UCNPs in cyclohexane. (a) Schematic illustration of the core multi-shell nanostructure and energy transfer processes under the excitations at 976 nm and 808 nm. **(b)** Luminescence photograph of the colloidal sample 1 in cyclohexane (20 mg/mL) excited by 976 and 808 nm lasers (0.5 mW/cm^2) and Upconversion emission spectra of the colloidal sample 1 upon 976 nm (orange) and 808 nm (blue) excitation. (c) HAADF-

STEM image and (d) high-resolution TEM photograph of sample I ($NaYF_4$: 30%Yb^{3+}, 2%Er^{3+}@ $NaYF_4$: 5%Yb^{3+}@ $NaYF_4$:15%Yb^{3+}, 20%Nd^{3+}@$NaYF_4$).

We design four strategies to manage the cascade energy transfer process in the core-multi-shell single nanoparticle and subsequently investigate the optical properties and fine-tune the lifetime fingerprints in a series of unique batches of derivative nanoparticles (Table 4.1, Figure. 4.5b). We synthesized eight arbitrary types of core multi-shell nanoparticles, the summary of morphology and histogram of these core-multi shell UCNPs are shown in Figure. 4.5b, respectively. Based on these STEM and size distribution data, uniform particle size distribution and similar sizes of eight batches of nanoparticles were obtained because of the same synthesis process. Compared with core-shell-shell nanoparticles, an increase in the average diameter of the final core-three layer shell nanoparticles was also observed from 50 nm to 60 nm during the shell coating process.

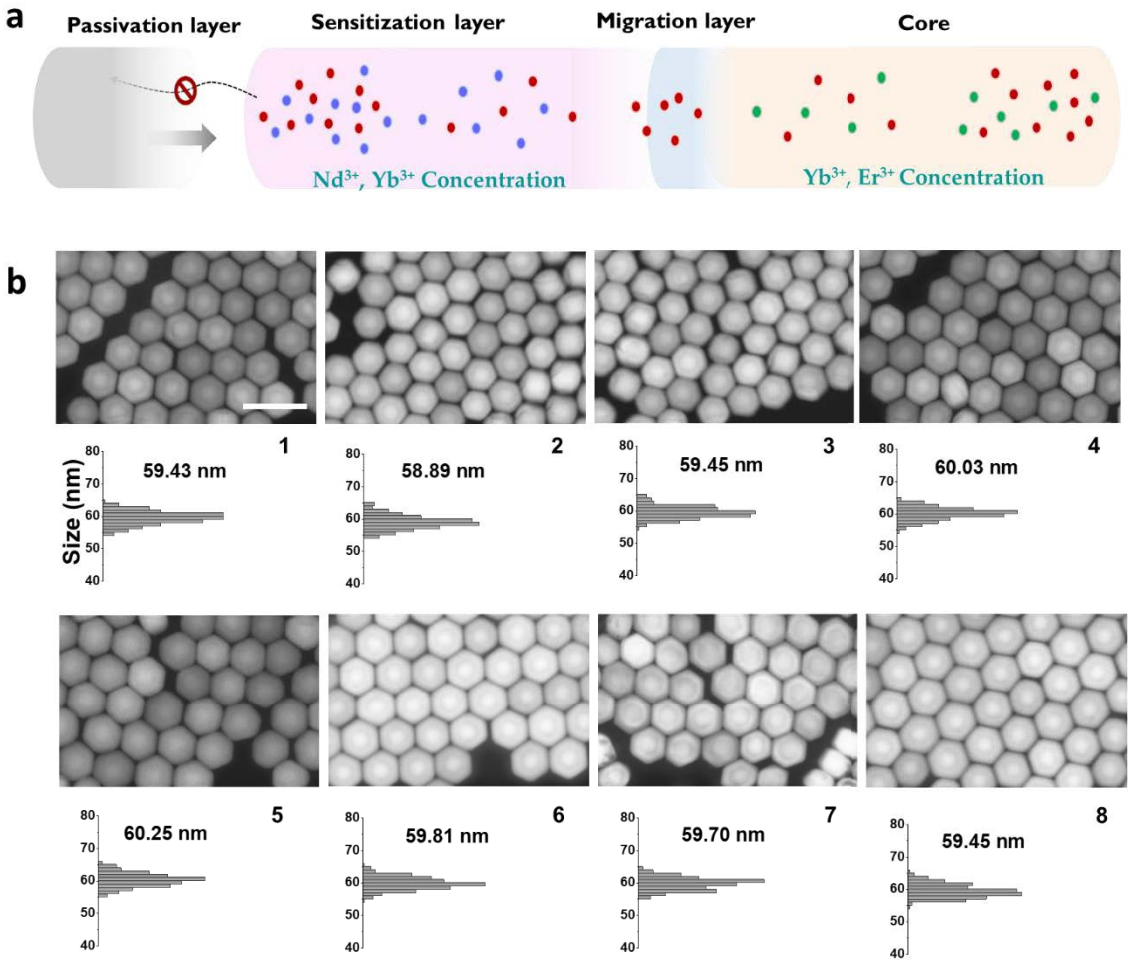

Figure. 4.5 TEM photos and the corresponding size distribution of Yb^{3+}, Nd^{3+}, Er^{3+} core three-layer shell UCNPs. (Sample 1) $NaYF_4$:30%Yb^{3+},2% Er^{3+} @ $NaYF_4$:5%Yb^{3+}@ $NaYF_4$: 15%Yb^{3+}, 20% Nd^{3+}@ $NaYF_4$ nanoparticles. (Sample 2) $NaYF_4$:30%Yb^{3+},8% Er^{3+} @ $NaYF_4$:5%Yb^{3+}@ $NaYF_4$: 15%Yb^{3+}, 20% Nd^{3+}@ $NaYF_4$ nanoparticles. (Sample 3) $NaYF_4$:20%Yb^{3+},2% Er^{3+} @ $NaYF_4$:5%Yb^{3+}@ $NaYF_4$: 15%Yb^{3+}, 20% Nd^{3+}@ $NaYF_4$ nanoparticles. (Sample 4) $NaYF_4$:40%Yb^{3+},2% Er^{3+} @ $NaYF_4$:5%Yb^{3+}@ $NaYF_4$: 15%Yb^{3+}, 20% Nd^{3+}@ $NaYF_4$ nanoparticles. (Sample 5) $NaYF_4$:30%Yb^{3+},2% Er^{3+} @ $NaYF_4$:5%Yb^{3+}@ $NaYF_4$: 15%Yb^{3+}, 20% Nd^{3+}@ $NaYF_4$ nanoparticles. (Sample 6) $NaYF_4$:30%Yb^{3+},2% Er^{3+} @ $NaYF_4$:5%Yb^{3+}@ $NaYF_4$: 30%Yb^{3+}, 20% Nd^{3+}@ $NaYF_4$ nanoparticles. (Sample 7) $NaYF_4$:30%Yb^{3+},2% Er^{3+} @ $NaYF_4$:5%Yb^{3+}@ $NaYF_4$: 15%Yb^{3+}, 40% Nd^{3+}@ $NaYF_4$ nanoparticles. (Sample 8) $NaYF_4$:30%Yb^{3+},2% Er^{3+} @ $NaYF_4$:5%Yb^{3+}@ $NaYF_4$: 15%Yb^{3+}, 60% Nd^{3+}@ $NaYF_4$ nanoparticles. Scale bar: 100 nm

We synthesized a library of Yb^{3+}-Tm^{3+} doped core-inert shell UCNPs by using the same layer by layer synthesis process, which is sensitive to the 976 nm laser activation (Table. 4.2), Yb^{3+} can pass the absorbed energy to Tm^{3+}, followed by multiphoton upconversion process of Tm^{3+}, to produce varied emissions bands located at 455 nm, 475 nm, 650 nm, and 800 nm. Surface passivation through epitaxial growth of optically inert shell of pure $NaYF_4$. To create a set of time-domain optical fingerprints and build a library of different batches of core-shell nanoparticles for optical multiplexing in nanoscale, we further change the Tm^{3+} doped concentration in the core to tailor the excited-state populations of Tm^{3+}, the TEM morphology of core samples are shown in Figure 4.6. These bare cores have relative weaken brightness of single nanoparticles, so an inert shell was coated (Figure 4.7). The thickness of the inert shell can provide different degrees of surface passivation from the surface quenchers and therefore intensify the emission intensity and lengthen the lifetime.

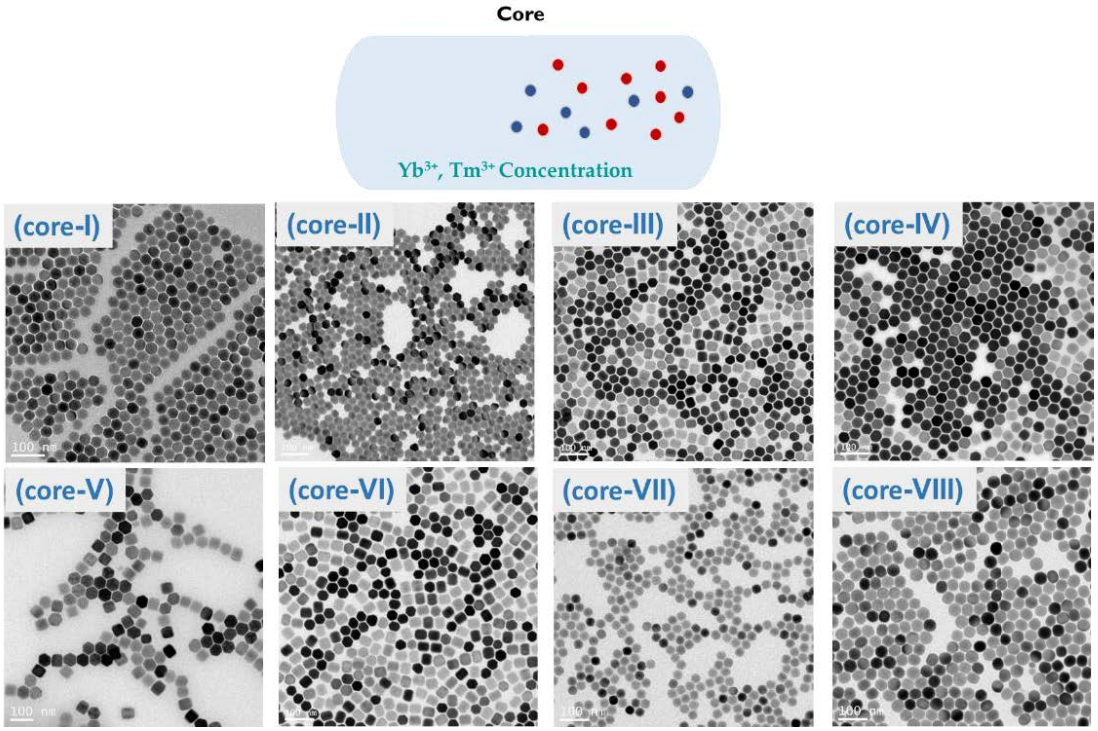

Figure. 4.6 TEM photos of Yb^{3+}-Tm^{3+} doped core UCNPs ~40 nm. (core-I) $NaYF_4$:40%Yb^{3+},0.2% Tm^{3+}. (core-II) $NaYF_4$:40%Yb^{3+},0.5% Tm^{3+}. (core-III) $NaYF_4$:40%Yb^{3+},0.8% Tm^{3+}. (IV) $NaYF_4$:40%Yb^{3+},1% Tm^{3+}. (core-V) $NaYF_4$:40%Yb^{3+},2% Tm^{3+}. (core-VI) $NaYF_4$:40%Yb^{3+},4% Tm^{3+}. (core-VII) $NaYF_4$:40%Yb^{3+},6% Tm^{3+}. (core-VIII) $NaYF_4$:20%Yb^{3+},8% Tm^{3+}. Scale bar: 100 nm.

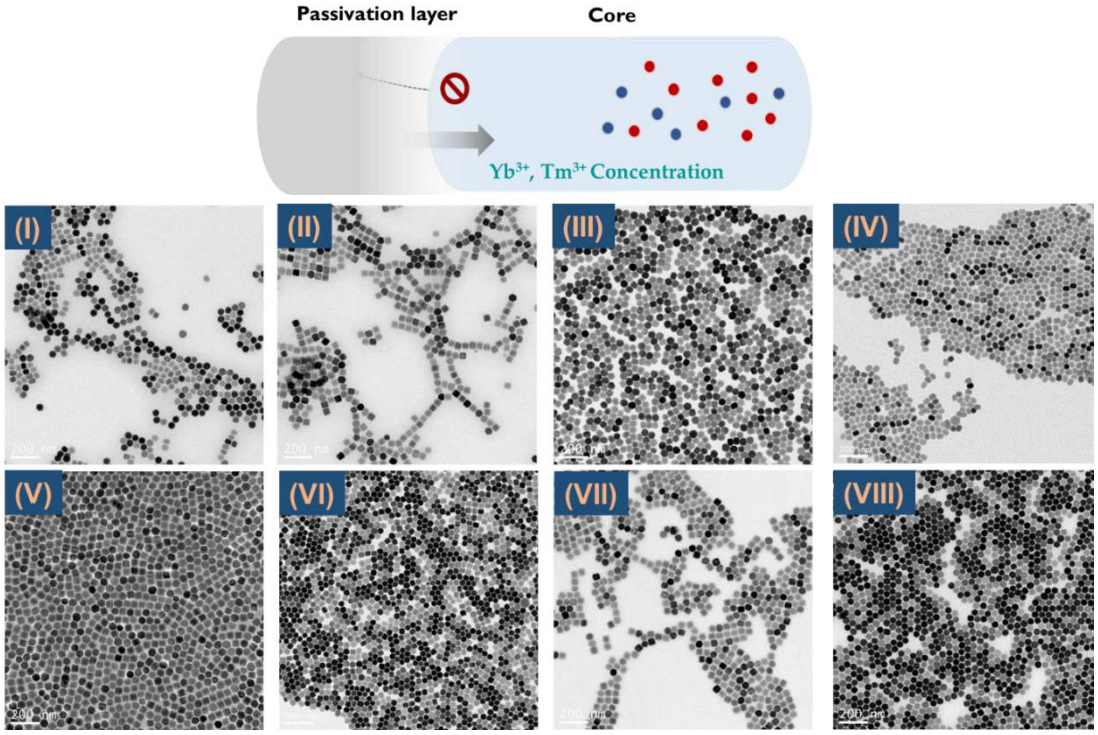

Figure. 4.7 TEM photos of Yb^{3+}-Tm^{3+} doped core-shell $NaYF_4$ samples about 50 nm. (I) $NaYF_4$:40%Yb^{3+},0.2% Tm^{3+}@ $NaYF_4$. (II) $NaYF_4$:40%Yb^{3+},0.5% Tm^{3+}@ $NaYF_4$. (III) $NaYF_4$:40%Yb^{3+},0.8% Tm^{3+}@ $NaYF_4$. (IV) $NaYF_4$:40%Yb^{3+},1% Tm^{3+}@ $NaYF_4$. (V) $NaYF_4$:40%Yb^{3+},2% Tm^{3+}@ $NaYF_4$. (VI) $NaYF_4$:40%Yb^{3+},4% Tm^{3+}@ $NaYF_4$. (VII) $NaYF_4$:40%Yb^{3+},6% Tm^{3+}@ $NaYF_4$. (VIII) $NaYF_4$:20%Yb^{3+},8% Tm^{3+}@ $NaYF_4$. Scale bar: 200 nm.

4.4.2 Optical fingerprints of Yb^{3+}-Nd^{3+}-Er^{3+} doped single nanoparticles under confocal microscope system

Here we systematically investigate the optical properties of Yb^{3+}, Nd^{3+}, Er^{3+} core three-layer shells UCNPs, the intensity, spectrum and lifetime properties at a single nanoparticle level under the confocal microscope system. We bypassed the difficulty of super-capacity optical multiplexing in nanoscale by encoding single UCNPs with time-domain optical fingerprints under the confocal microscope system. As shown in Figure 4.8a and b, We replace tagging the UCNPs nanoparticles on the microbeads with single UCNPs. By obtaining bright UCNPs, the layer-by-layer epitaxial growth method is used to prepare the Yb^{3+}, Nd^{3+}, Er^{3+} core three-layer shell β-$NaYF_4$ UCNPs with a great morphology uniformity, which can arbitrarily control the energy transfer process in the core-shell structure. An inert shell is employed to prevent the energy migration to the surface quenchers[35,36], as well as improving the optical uniformity of single nanoparticles.

The multiple shells can significantly slow down the interfacial energy migration (IEM) process from primary sensitizer Nd^{3+} to the secondary sensitizer Yb^{3+} under the excitation of 808 nm. IEM plays an important role in the slow accumulation of the excited state populations, displayed as a time-delayed up-rising curve of upconversion emissions. To verify this IEM effect, we selectively excite the Yb^{3+} and Nd^{3+} ions using 976 nm and 808 nm lasers in one of the typical Sample 1 and observe the same emission spectra (Figure 4.8c). But from Figure 4.8d, much different lifetime profiles were obtained shows that the rising time for the Er^{3+} excited state populations to reach its plateau can be prolonged from 200 μs to 650 μs when the IEM process is involved. Using a time-resolved confocal microscopy setup, the single nanoparticle optical characterization result (Figure 4.8e) shows high degrees of brightness (e.g.,

81,520 photon counts per second for Sample 1), optical uniformity (CV of 8.1%) and stability of single nanoparticles (Figure 4.8f), ideal for long-term imaging and decoding of the optical fingerprint of any single nanoparticle. As shown in Figure 4.8g, the unique and detectable fingerprint has been successfully assigned to every single Sample 1. More impressively, the characteristic lifetime fingerprints of single nanoparticles, as long as from the same batch of synthesis, are consistently uniform. It means the tunable and prolonged time-domain optical fingerprint is the potential dimension for high-throughput optical multiplexing.

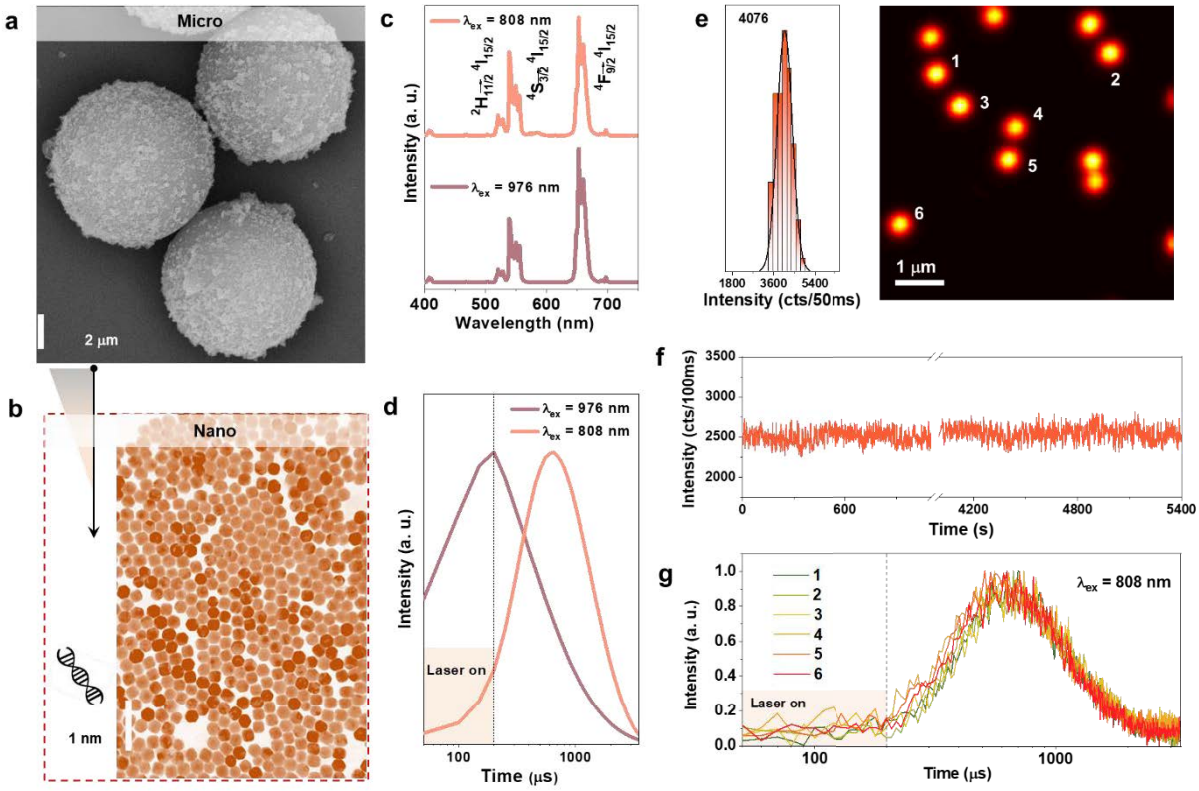

Figure 4.8 Creation of uniform single UCNPs with unique optical signatures. (a) and (b) Encoding information carriers from macroscopic to the nanoscale. **(c) and (d)** Visible region upconversion emission spectra (c) and lifetime curves (d) of powder state Sample 1 under 808 nm excitation and 976 nm excitation. (the confocal microscopy system is shown in Figure 4.1. **(e-g)** Confocal microscopic single nanoparticle imaging and brightness distribution (e), the photostability of a single nanoparticle (f) under 808 nm CW excitation at 5.5×10^6 W/cm^2, and corresponding lifetime curves (g) of single nanoparticles 1-6 in (e) under 808 nm pulse excitation under the confocal microscopy system (by

modulating the CW laser at 5.46 kW/cm^2). An arbitrary batch (Sample 1) of nanoparticles used here was chosen from a library of core three-layer shells nanoparticles synthesized in this work.

To characterize the brightness values of Yb^{3+}, Nd^{3+}, Er^{3+} core three-layer shell single nanoparticles, these eight batches of UCNPs in cyclohexane were drop-cast onto a coverslip for measurement. We measured the brightness of the single UCNPs using a home-built confocal microscope, each of nanoparticle presents a Gaussian spot. The maximum pixel value for the Gaussian spots is used to represent that nanoparticle's brightness, as shown in Figure 4.9. we can see the uniform and stable emission intensity for each single nanoparticle from the same batch, which shows the intensity and monodispersity of each synthesis of single nanocrystals. We quantified the brightness of the eight batches of single nanoparticles using the confocal microscopy approach under 976 nm and 808 nm excitation at 7.6 MW/cm^2 (Figure 4.9a and 4.9b), which show the great intensity uniformity of single nanoparticles from each batch. Quantitative statistics show the peak brightness of sample 1-8 appear at 7197, 11071, 5720, 10543, 8288, 8146, 8187, 7379 counts/50ms under 976 nm excitation and 10720, 11545, 9085,12893, 10932, 12292, 13994, 14223 counts/50ms under 808 nm excitation, respectively. Notably, 808 nm excitation consistently produces stronger brightness for all the samples compared with 976 nm excitation.

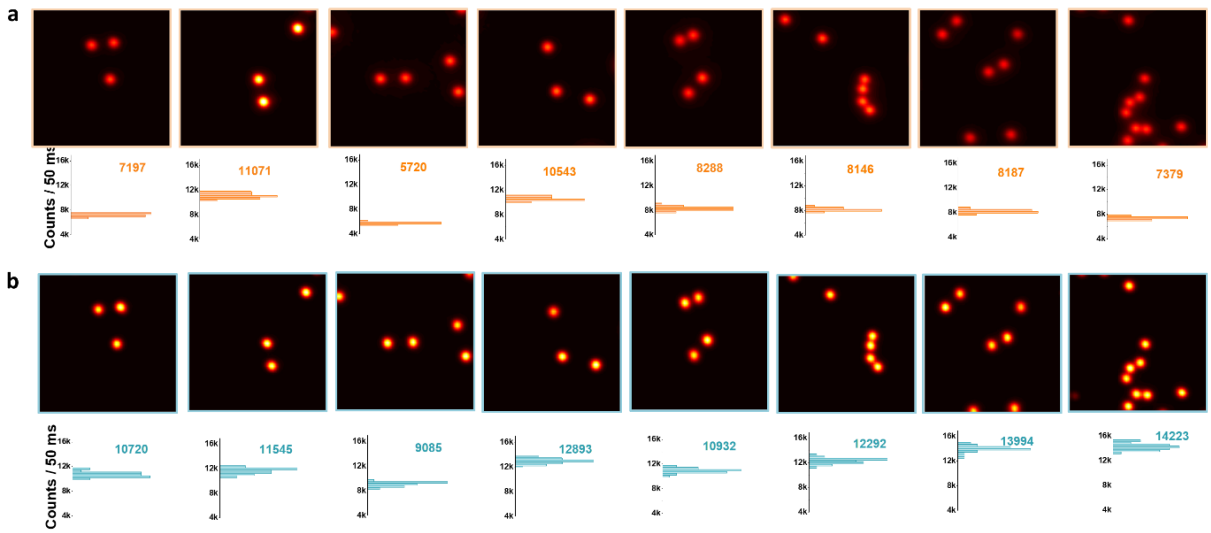

Fig. 4.9 Confocal microscopy images and statistical intensities of Yb^{3+}, Nd^{3+}, Er^{3+}-doped nanoparticles. Confocal microscopy quantitative measurement of whole spectrum luminescence

emission of Yb^{3+}, Nd^{3+}, Er^{3+} core three-layer shells nanoparticles under 976 nm (a) and 808 nm (b) excitation at the power density of 5.5×10^6 W/cm^2. Scale bar: 1 μm.

Figure 4.10 shows the power-dependent brightness values and emission spectra of single nanoparticles (sample 1) at 976 nm and 808 nm excitation wavelengths. Strikingly, according to the power-dependent curves, we observe that the initial brightness under 808 nm excitation is stronger than that under 976 nm excitation. For example, at 1 KW/cm^2, 808 nm excitation produces the brightness of 390 photon counts/50ms, which is ten times stronger compared with 976 nm excitation. When increasing the power to 9 KW/cm^2, the brightness becomes the same. Further increasing the excitation power, brightness inversion occurs two times, which forms the double helix shape relationship. Inserts are the confocal scanning images of single nanoparticles under 808 nm and 976 nm excitation with the power densities of 1 KW/cm^2, 9 KW/cm^2, 490 KW/cm^2, and 7.6 MW/cm^2, respectively.

To understand the helix shape relationship, we measured the emission spectra at different excitation power densities (Figure 4.10b). Both the green ($^2H_{11/2}\rightarrow{}^4I_{15/2}$, $^4S_{3/2}\rightarrow{}^4I_{15/2}$, $^2H_{9/2}\rightarrow{}^4I_{13/2}$) and red ($^4F_{9/2}\rightarrow{}^4I_{15/2}$) emission spectra of Er^{3+} can be collected at 1 KW/cm^2 and 9 KW/cm^2. We find that the electron population pathways for Er^{3+} are different for the 808 nm and 976 nm excitations (as shown in Figure 1a), which indicate the differences in brightness when the power density increases from 1 to 9 KW/cm^2. The $Nd^{3+}\rightarrow Yb^{3+}\rightarrow Er^{3+}$ cascaded energy transfer with Yb^{3+} migration network leads to the brighter Er^{3+} emissions under 808 nm in contrast to the direct $Yb^{3+}\rightarrow Er^{3+}$ energy transfer under 976 nm excitation. The significant role in the energy transfer step of $Nd^{3+}\rightarrow Yb^{3+}$ can be evidenced by the undetectable signal from the $NaYF_4$: Yb, Er core under 808 nm excitation from 1 KW/cm^2 to 9 KW/cm^2. For the emission spectra within the range of 9.0 - 2500 KW/cm^2 (Figure 4.10b), 976 nm excitation favors the three/four-photon upconversion process from higher excited states of Er^{3+} and thereby produces stronger emission intensity in contrast to 808 nm excitation. This is evidenced by the additional emissions at ~469 nm ($^2P_{3/2}\rightarrow{}^4I_{11/2}$), ~504 nm ($^4G_{11/2}\rightarrow{}^4I_{13/2}$), and strong red emission at 654 nm ($^4F_{9/2}\rightarrow{}^4I_{15/2}$) under 976 nm excitation. Further increasing the power to 1

MW/cm^2 and more, the brightness becomes saturated, though the transition probabilities from multiple excited states are different under 976 nm excitation.

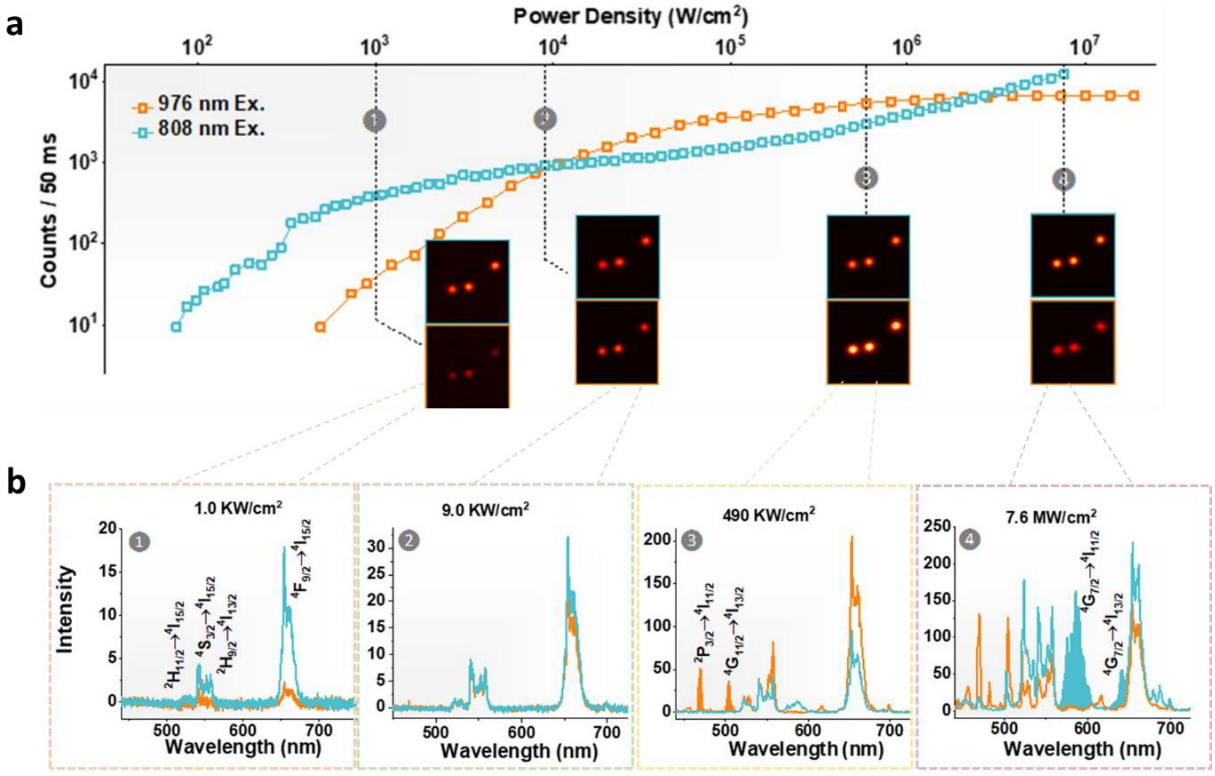

Fig. 4.10 Single nanoparticle optical characterization of sample 1. (a) Single nanoparticle intensity of sample 1 between 400 nm and 742 nm wavelength region as the function of power density under 976 nm and 808 nm excitation. Insets show the corresponding confocal images at four power densities (dotted grey line, 1.0 KW/cm^2, 9.0 KW/cm^2, 490 KW/cm^2, 7.6 MW/cm^2). **(b)** Single nanoparticle emission spectra under the above four power densities upon 976 nm (orange) and 808 nm (blue) excitations.

The power-dependent emission intensity associated with each emission band of Er^{3+} and Nd^{3+} shows in Fig.4.11. The variation tendency of the slope values of n reveals three phases for the excited state populations. Under these two excitation lasers, the two- and three-photon involved upconversion emissions from Er^{3+} are observed. Increasing the power density, the populations for the relevant excited states are approaching saturation and thus the slope values decrease. Under 808 nm excitation in III Phase, the slope values of green and red emission bands of Er^{3+} ions are bigger than that in II phase because of the superposition of emission bands (525 nm:

$^4G_{7/2}\rightarrow{}^4I_{9/2}$, 585 nm: $^4G_{7/2}\rightarrow{}^4I_{11/2}$, 650 nm: $^4G_{7/2}\rightarrow{}^4I_{13/2}$) from direct Nd^{3+} upconverted luminescence. It indicates the competition of excitation energy flux between energy transfer upconversion of $Nd^{3+}\rightarrow Yb^{3+}\rightarrow Er^{3+}$ and direct upconversion from Nd^{3+}.

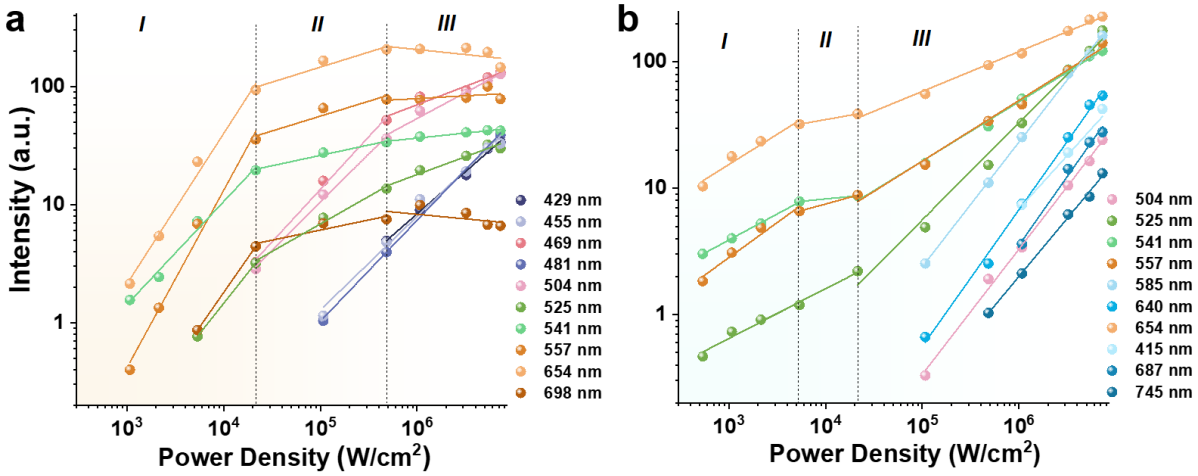

Figure 4.11. Double logarithmic plots of emission intensities as the function of power density. (a) Power density-dependence of upconversion emission intensity of sample I under 976 nm excitation at Er^{3+} emission peaks. (b) Power density-dependent emission intensity changes of sample I under 808 nm excitation at Er^{3+} and Nd^{3+} emission peaks.

Figure 4.12 summarizes the power-dependent evolution curves of the eight types of single Nd^{3+}-Yb^{3+}-Er^{3+} tri-doped UCNPs following the different doping concentrations and the same core multi-shell design pattern. We assigned them into four groups, according to the doping strategy, in which we varied the concentration of Er^{3+} in the core (Figure 4.12a) for sample I (2%Er^{3+}) and II (8%Er^{3+}), the concentration of Yb^{3+} in the core (Figure 4.12b) for sample III (20%Yb^{3+}) and IV(40%Yb^{3+}), the concentration of Yb^{3+} in the sensitization layer (Figure 4.12c) for sample V (5%Yb^{3+}) and VI (30%Yb^{3+}), and the concentration of Nd^{3+} in the sensitization layer (Figure 4.12d) for sample VII (40%Nd^{3+}) and VIII (60%Nd^{3+}). This phenomenon has been universally observed in a series of four-layer core multi-shell Nd^{3+}-Yb^{3+}-Er^{3+} doped UCNPs. The crossing-node is tunable by increasing the Er^{3+} concentration in the core (Figure 4.12a), as the emitter concentration quenching occurs. Increasing the Yb^{3+} concentration in the core (Figure 4.12b) can facilitate the energy transfer from Nd^{3+} to Er^{3+} under 808 nm excitation. Increasing the Yb^{3+} concentration from 5% to 30% in the sensitization layer (Figure 4.12c)

leads to brighter upconversion. We observe the universal double helix shape power-brightness relationship under the 976 nm and 808 nm excitations. We show that the helix shapes (especially at the low power range) and the power density values for the first cross nodes can be tuned. The tunability for the second crossing-node at high power range is limited due to the same electron population behaviors, once the brightness being saturated at 976 nm excitation and direct upconversion emission from Nd^{3+} being generated at 808 nm excitation. The helix shape is highly dependent on the doping concentrations of lanthanides in the heterogeneous core-shell structure of active core, migration layer, sensitization layer and the inert layer of shells, suggesting that the population dynamics of each excited state highly depend on the power-dependent energy transfer pathways under the excitations of 976 nm and 808 nm lasers. It indicates that the power-dependent profile is a possible dimension for optical multiplexing.

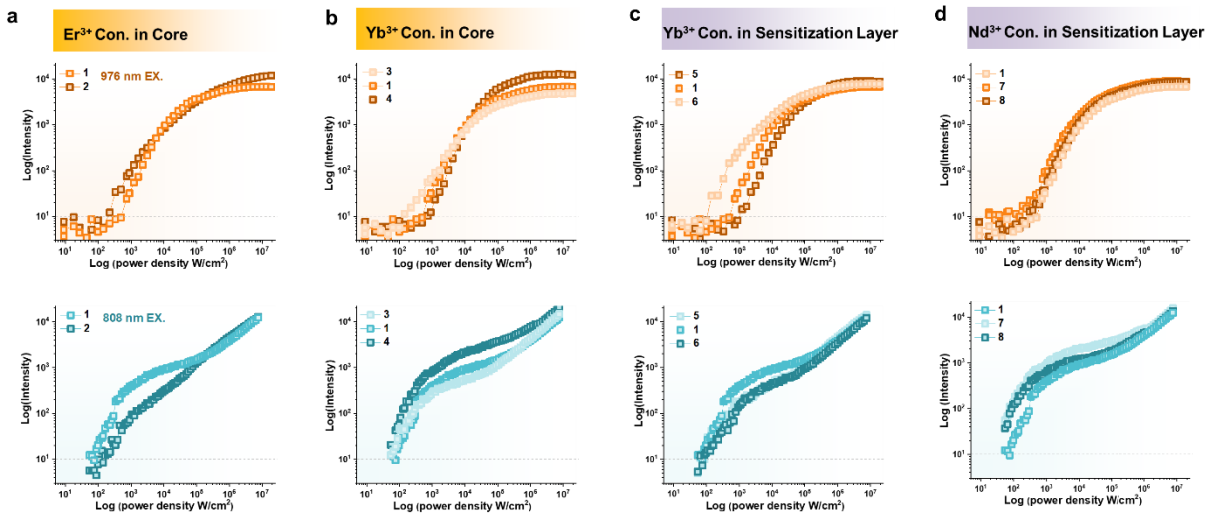

Fig. 4.12. The power-dependent intensity curves of eight different types of single nanoparticles under 976 nm and 808 nm excitations. (a-d) The comparison of the emission intensity as the function of power density under 976 nm and 808 nm excitations for samples 1 and 2 (a), sample 3 and 4 (b), samples 5 and 6 (c), and sample 7 and 8 (d).

The detailed upconversion emission spectra of these eight batches of Yb^{3+}, Nd^{3+}, Er^{3+} core three-layer shell single UCNPs upon 976 nm and 808 nm excitation at 7.6 MW/cm^2 are shown in Fig. 4.13. Because the emission bands of Er^{3+} green (525 nm:$^2H_{11/2}$, 541 nm: $^4S_{3/2}\rightarrow {}^4I_{15/2}$, and 557 nm: $^2H_{9/2}\rightarrow {}^4I_{13/2}$) and red (654/661 nm: $^4F_{9/2} \rightarrow {}^4I_{15/2}$, 698 nm: $^2H_{9/2} \rightarrow {}^4I_{11/2}$) bands

and Nd^{3+} (525 nm: $^4G_{7/2}\rightarrow{}^4I_{9/2}$, 585 nm: $^4G_{7/2}\rightarrow{}^4I_{11/2}$, 650 nm: $^4G_{7/2}\rightarrow{}^4I_{13/2}$) are constant, there is no significant difference in the emission spectrum when changing the doping concentration.

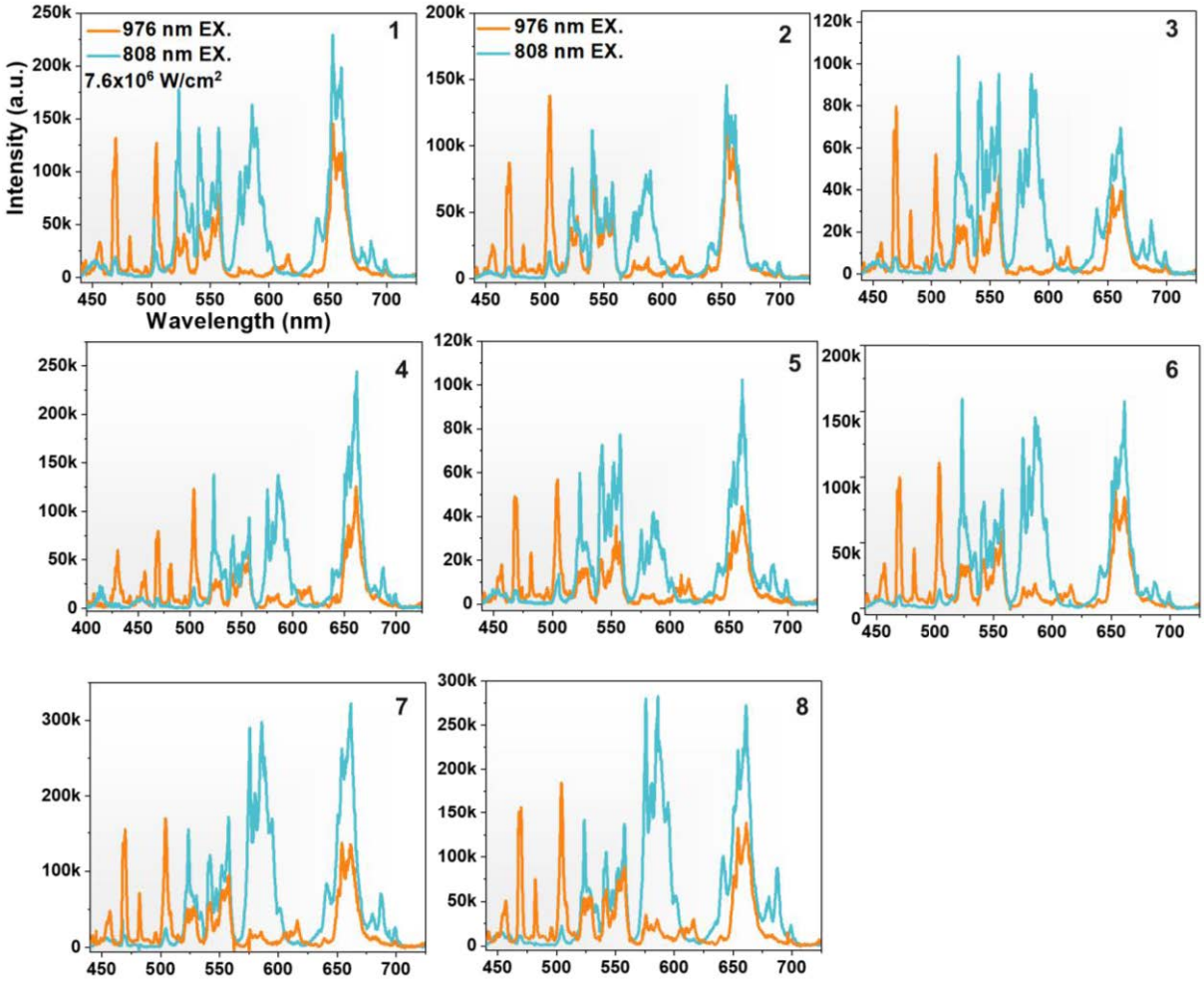

Fig. 4.13 Upconversion emission spectra of sample 2 (a), sample 3 (b), sample 4 (c), sample 5 (d), sample 6 (e), sample 7 (f), sample 8 (g) under 976 nm (orange) and 808 nm (blue) excitation at 7.6 MW/cm^2.

4.4.3 Lifetime property of two groups of single nanoparticles under confocal microscope system

By further investigating the multidimensional optical fingerprints for optical multiplexing, we measure the lifetime curves of Nd^{3+}-Yb^{3+}-Er^{3+} doped and Yb^{3+}-Tm^{3+} doped nanocrystals. It has different population dynamics of Er^{3+} under 976 nm and 808 nm excitation in Nd^{3+}-Yb^{3+}-Er^{3+} core-multi shell UCNPs. The decay slopes of the Er^{3+} emission as the function of power for Yb- and Nd-excitation (976 nm and 808 nm laser) are different, as shown in Figure 4.14a

and b. The decay time values are shown in Figure 4.14c. The time-resolved photon counts located in the wavelength range of 400 nm to 742 nm were collected by the single-photon counting avalanche diode. The time constants are defined as the lifetime value corresponding to the two or one fitting coefficient in the exponential fitting. The high excitation power density induced shorter decay times. This is because the high excitation energy promotes the highly excited states of Er^{3+} (e.g., $^2D_{5/2}$, $^2P_{3/2}$) with a shorter intrinsic lifetime to be populated and long lifetime intermediate excited states of Er^{3+} (e.g., $^4S_{3/2}$, $^2H_{9/2}$, $^4F_{9/2}$) to be depopulated [16,37,38]. At each power density, prolonged rising and decay time appear in the 808 nm excitation relative to 976 nm excitation, indicating the energy reservoir effect of Yb^{3+} through Nd^{3+} pumping. The randomly walking nature of the multi-step excitation migration under 808 nm excitation in Nd^{3+}-Yb^{3+}-Er^{3+} doped UCNPs can cause the accumulative effect in the core-multi shell UCNPs that could cause the occurrence of rising time peak and prolonging lifetime at 808 nm excitation. Comparing to 976 nm excitation, the rising time peaks occur after turning off the 808 nm laser and the rising peak position is prolonged when decreasing the power density because of the energy reservoir effect and multistep energy transfer processes in the core-shell structure of Yb^{3+} through Nd^{3+} pumping.

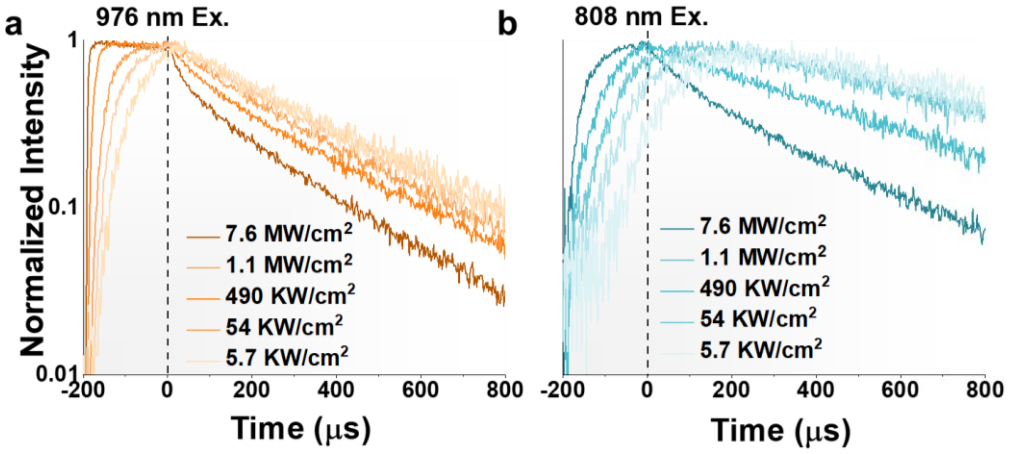

c

Power density	976 nm Excitation	808 nm Excitation
5.7 KW/cm²	337.62 μs	1018.8 μs
54 KW/cm²	107.55 μs	753.17 μs
490 KW/cm²	59.28 μs	353.30 μs
1.1 MW/cm²	52.18 μs	181.41 μs
7.6 MW/cm²	31.13 μs	81.36 μs

Fig. 4.14 The power-dependence lifetime of sample 1 from all wavelengths between 400 nm and 742 nm at 976 nm (a) and 808 nm (b) excitation with 200μs pulse width. (c) The table of the decay time of sample 1 under different laser power density was tuned.

Figure. 4.15 presents the decay profiles of the Er^{3+} green emission ($^4S_{3/2} \rightarrow {}^4I_{15/2}$) and red emission ($^4F_{9/2} \rightarrow {}^4I_{15/2}$) under different power density upon 976 nm (Figure. 4.15 a and b) and 808 nm (Figure. 4.15 c and d) excitations, respectively. For NIR excitation, the decay trends of green and red emission band as the function of power density are similar to the whole emission region, the lifetimes of the green and red emission are matched closely. It also shows a significantly slower luminescence decay for both green and red emissions when the power density decrease from 7.6 MW/cm^2 to 5.7 KW/cm^2, revealing the influence of excitation power density (Figure. 4.15e). Comparing with under 976 nm excitation, the prolonged lifetime of the green and red emission bands appear in the 808 nm excitation at different power density. It indicates the multistep energy reservoir effect of Yb^{3+} through Nd^{3+} pumping can simultaneously affect the emission bands from the different excited energy levels. From Fig.4.15, It also indicates that prolonging the lifetime and large tuning scope can be achieved under a relatively low power density of excitation. It's the potential capacity to expand much more channel lifetime multiplexing by using different emission bands. Our core-shell synthesis procedure also allows us to tune the lifetimes of the different emission bands (green and red emission of Er^{3+} emitters) by continuously tune the doped concentration/size, which could be exploited for lifetime multiplexing.

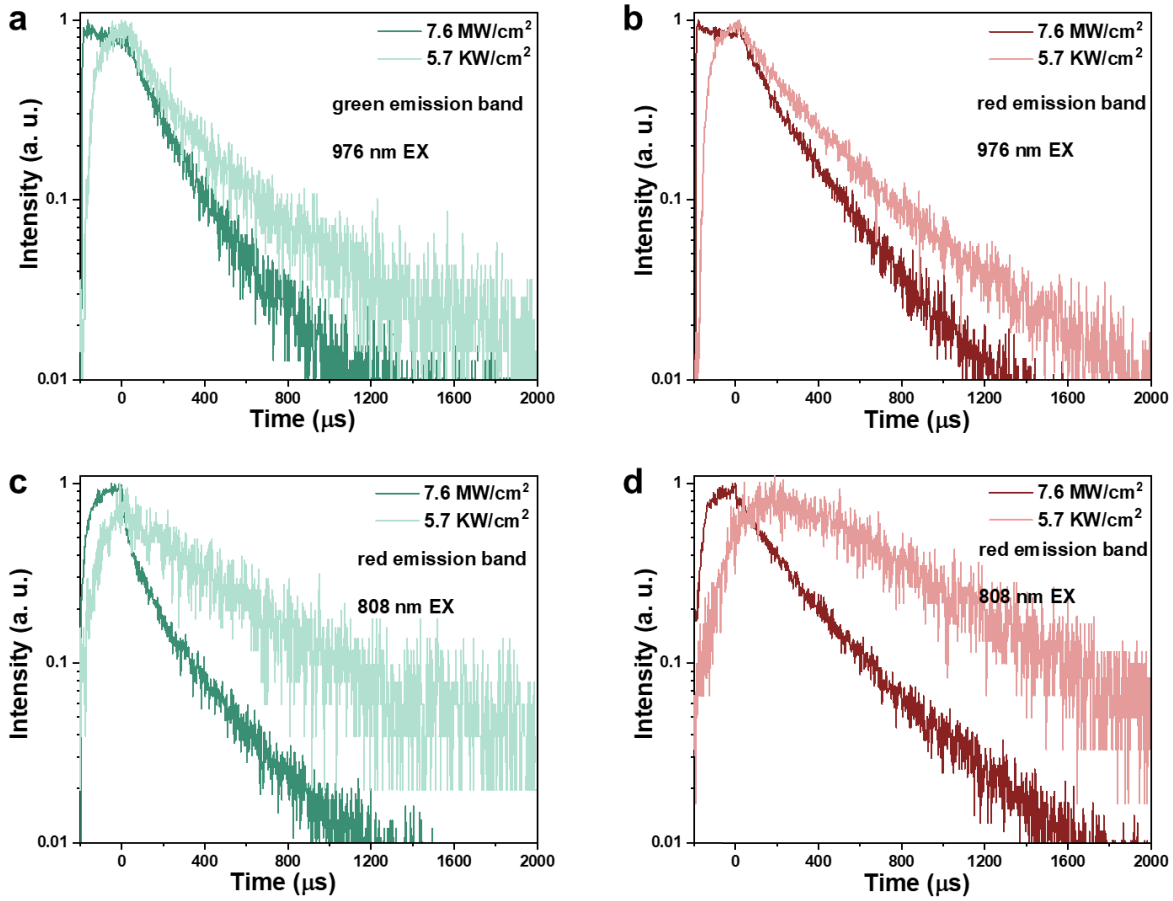

e

Power density	976 nm Ex. (green)	808 nm Ex. (green)	976 nm Ex. (red)	808 nm Ex. (red)
5.7 KW/cm^2	237.46 μs	492.11 μs	288.54 μs	794.48 μs
7.6 MW/cm^2	171.04 μs	188.99 μs	200.49 μs	271.69 μs

Fig. 4.15 Lifetime profiles of single emission band of Nd^{3+}-Yb^{3+}-Er^{3+} doped UCNPs under confocal system: the green (a) and red (b) emission band lifetimes of a kind of nanoparticles under 7.6 MW/cm^2 and 5.7 KW/cm^2 power density upon 976 nm excitation. The green (c) and red (d) emission band lifetimes of a kind of nanoparticles under 7.6 MW/cm^2 and 5.7 KW/cm^2 power density upon 808 nm excitation. (e) The table of the decay time of green and red emission bands of the above sample under different laser power density.

By measuring the lifetime profiles of Yb^{3+}, Nd^{3+}, Er^{3+} core three-layer shell single UCNPs with different doping concentration under the pulsed 976 nm and 808 nm excitation (pulse width of 200 μs) (Figure 4.16), the transient dynamics of the electron populations further reveals the

energy reservoir effect of Yb^{3+} through Nd^{3+} pumping[39], as the rising and decay lifetime curves response a lot of slower under 808 nm excitation compared with under 976 nm excitation. Figure 4.16 shows the decay time of eight batches of Nd^{3+}-Yb^{3+}-Er^{3+} doped UCNPs as the function of power density under 808 nm (dark blue) and 976nm (dark yellow) excitation sources. We observe that lifetime value increases with decreasing pump intensity for Nd^{3+}-Yb^{3+}-Er^{3+} doped core-multi shell nanoparticles. The higher excitation energy fluences can increase the spatial density of populated Er^{3+} intermediate excited states with longer lifetimes (such as $^2H_{9/2}$), which increases rates of energy transfer upconversion and cross-relaxation out of these states. This leads to shorter lifetimes for states that emit visible photons at these two excitation wavelengths. Moreover, compared with under 976 nm laser excitation, the lifetimes are prolonged under 808 nm excitation. It has a wider scope of modification of decay time as the function of power density under 808 nm excitation. These nanoparticles emit luminescence in the microsecond range under 808 nm excitation when the power density decrease to 5.7 KW/cm^2, about three orders of magnitude longer than the background autofluorescence (less than 10 ns), which can be easily suppressed through time-resolved measurements. It indicates that prolonging the duration time for the excited state populations of upconversion emissions following the pulsed excitation, the Nd^{3+}-Yb^{3+}-Er^{3+} doped core three-layer shell UCNPs are potential for optical multiplexing in lifetime domain under 808 nm excitation. Moreover, the luminescence decay lifetimes of Er^{3+} emission are found to diminish as the number of energy distributors increases (increasing the concentration of Yb^{3+} and Er^{3+}), especially under 808 nm excitation. For example, the lifetime of sample 2 (30%Yb, 8% Er) under 808 nm laser with 7.6 MW/cm^2, 54 KW/cm^2 and 5.7 KW/cm^2 are shorter than the lifetime of sample 3 (20%Yb, 2% Er). The results suggest that the vast combinations of different strategies (such as concentration, the excitation light and power density) enable precise depletion of the excited states of activators of Yb^{3+} ions, which allows the emission lifetime of the nanoparticles to be controlled within a wide range. These strategies could be utilized in generating distinct time-domain codes that can be exploited for lifetime multiplexing and encoding.

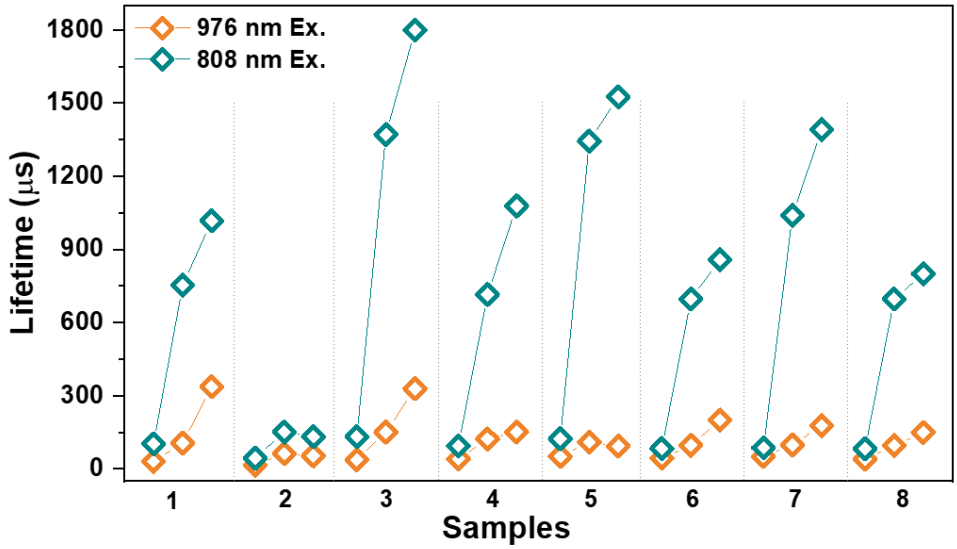

Figure. 4.16 The power-dependence lifetime of eight batches of Nd^{3+}-Yb^{3+}-Er^{3+} doped single nanoparticles under the confocal microscope system. (d) The power density-dependent lifetime curves of single nanoparticles under 976 nm (dark yellow) and 808 nm (dark blue) excitation with 200 μs pulse width, which correlates to the emission signal from the wavelengths between 400 nm and 742 nm. For each kind of UCNPs, the power densities decreased from left to right in the figure are 7.6 MW/cm^2, 54 KW/cm^2 and 5.7 KW/cm^2.

Our lifetime multiplexing concept based on the tunability of lifetimes further been implemented following a simple scheme of co-doping Yb^{3+}-Tm^{3+} core-inert shell UCNPs at stepwise varied concentrations into the $NaYF_4$ nanocrystals. In this case, energy transfer from the Yb^{3+} to the Tm^{3+} ions at varying sensitizer-emitter distances provides lifetime tunability under 976 nm pulse excitation. Because of the advantages of photostability and background-free of time-resolved detection, we achieved a sufficiently high signal-to-background ratio for lifetime measurement of a single nanocrystal's emission at varied emission bands under the time-resolved confocal scanning system (Figure 4.17). Here, we detect the lifetime curves of Tm^{3+} in four emission bands under different power density, the 445 nm ($^1D_2 \rightarrow {}^3F_4$), 475 nm ($^1G_4 \rightarrow {}^3H_6$), 650 nm ($^1G_4 \rightarrow {}^3F_4$), 800 nm ($^3H_4 \rightarrow {}^3H_6$). With the increase of the Tm^{3+} doped concentration, the lifetime values come from all emission bands are decrease. For example, the lifetimes of sample I (0.2% Tm^{3+}) in 650 nm emission band are about 600μs, while the lifetimes are about 60μs when increasing the Tm^{3+} to 8%. The trend is similar to Yb^{3+}, Nd^{3+}, Er^{3+} doped

samples under 808 nm excitation. By changing the doping concentration of Tm^{3+}, the Yb^{3+}-Tm^{3+} core-inert shell UCNPs as a series of nanocarriers carrying unique lifetime identities.

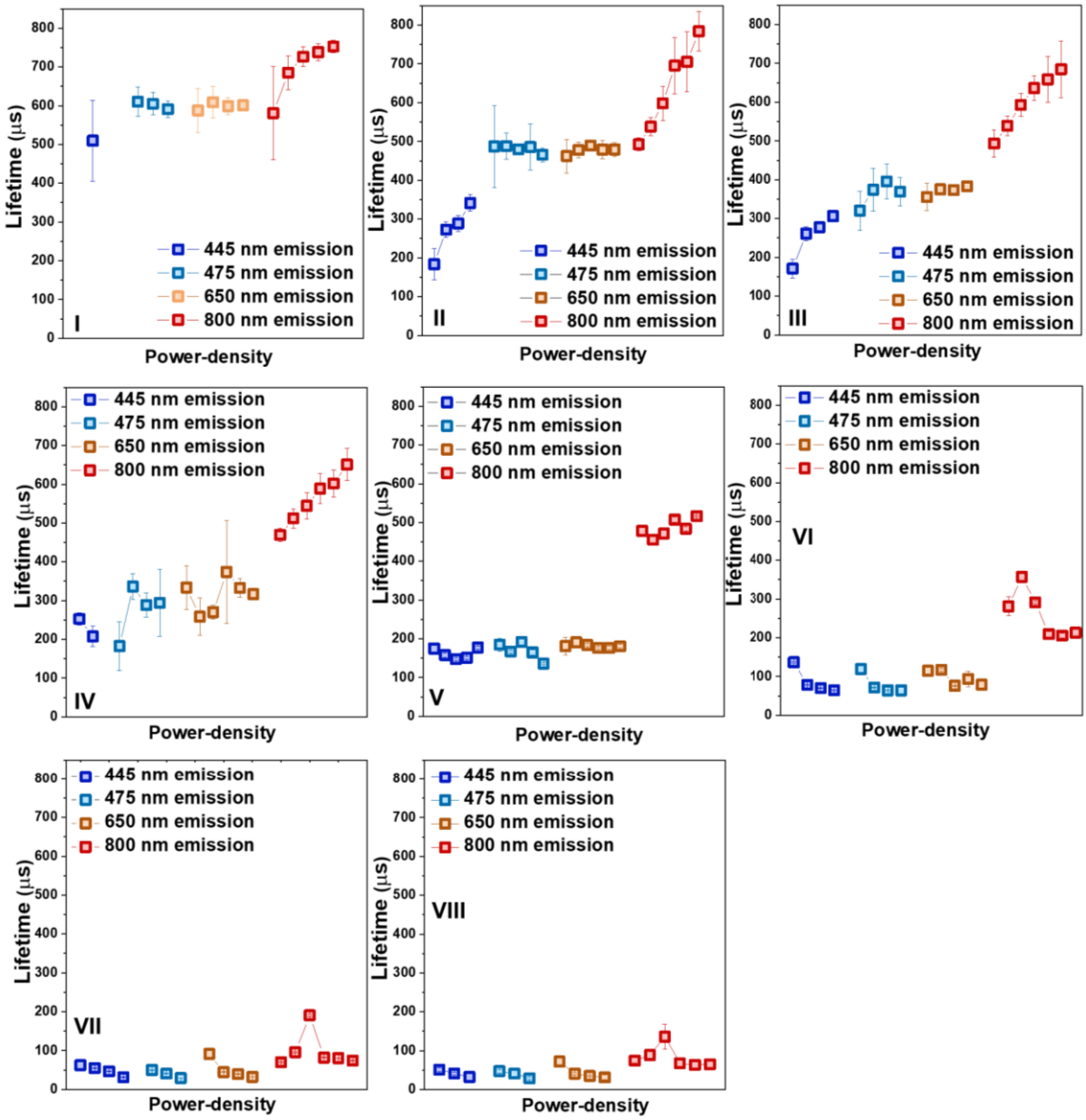

Fig. 4.17 Lifetime tuning in different emission bands for eight batches of $NaYF_4$: Yb, Tm core-shell upconversion nanocrystals. The lifetime curves of Tm^{3+} in four emission bands (445 nm from $^1D_2 \rightarrow {}^3F_4$, 475 nm from $^1G_4 \rightarrow {}^3H_6$, 650 nm from $^1G_4 \rightarrow {}^3F_4$, 800 nm from $^3H_4 \rightarrow {}^3H_6$) were detected under different power densities. For each emission band, the power densities decreased from left to right.

4.5 Conclusion

In summary, we synthesize two groups of UCNPs, Yb^{3+}, Nd^{3+}, Er^{3+} core three-layer shell and Yb^{3+}-Tm^{3+} core-inert shell UCNPs. The core-shell design and controlled synthesis of bright and optically uniform single nanoparticles provide an opportunity for super-capacity optical multiplexing. Strategies to control the energy migration process and to arbitrarily tune the rising time, decay time, and plateau moment can assign each type of nanoparticles with a unique time-domain optical fingerprint. To encoding information carriers from the macroscopic level to the nanoscale, the optical properties of single nanoparticles were investigated under the confocal microscope system. The two groups of bright and uniform Er^{3+} and Tm^{3+} doped UCNPs can form a spectral and lifetime orthogonal multiplexing under 808 nm and 976 nm excitation at the single nanoparticle level through the confocal microscope system, respectively. Moreover, we confirm that the universal helix shape phenomena commonly exist in a set of eight batches of core-shell nanoparticles regardless of the doping concentrations of Nd^{3+}, Yb^{3+} and Er^{3+} ions in the sensitization shell, migration shell, and active core. We systemically analyze the power-dependent emission intensity/spectra and lifetimes of single upconversion nanoparticles, which reveal that the dynamic roles of Nd^{3+} ions in the tri-doped nanosystem with the underlining electron population pathways are power dependent. This study emphasizes the important role of power-dependent properties in both improving the upconversion emission efficiency and the design of non-linear responsive probes for imaging and sensing. This work further suggests the potential of UCNPs for optical multiplexing with diverse and tunable optical signatures in multiple optical dimensions.

4.6 Reference

(1) Liu, D.; Xu, X.; Du, Y.; Qin, X.; Zhang, Y.; Ma, C.; Wen, S.; Ren, W.; Goldys, E. M.; Piper, J. A.; et al. Three-Dimensional Controlled Growth of Monodisperse Sub-50 nm Heterogeneous Nanocrystals. *Nat. Commun.* **2016**, *7* (1), 10254.

(2) Liao, J.; Jin, D.; Chen, C.; Li, Y.; Zhou, J. Helix Shape Power-Dependent Properties of Single Upconversion Nanoparticles. *J. Phys. Chem. Lett.* **2020**. https://doi.org/10.1021/acs.jpclett.9b03838

(3) Zhao, J.; Jin, D.; Schartner, E. P.; Lu, Y.; Liu, Y.; Zvyagin, A. V; Zhang, L.; Dawes, J.

M.; Xi, P.; Piper, J. A.; et al. Single-Nanocrystal Sensitivity Achieved by Enhanced Upconversion Luminescence. *Nat. Nanotechnol.* **2013**, *8* (10), 729–734.

(4) Brouzes, E.; Medkova, M.; Savenelli, N.; Marran, D.; Twardowski, M.; Hutchison, J. B.; Rothberg, J. M.; Link, D. R.; Perrimon, N.; Samuels, M. L. Droplet Microfluidic Technology for Single-Cell High-Throughput Screening. *Proc. Natl. Acad. Sci.* **2009**, *106* (34), 14195–14200.

(5) Cheng, Y. Y.; Khoury, T.; Clady, R. G. C. R.; Tayebjee, M. J. Y.; Ekins-Daukes, N. J.; Crossley, M. J.; Schmidt, T. W. On the Efficiency Limit of Triplet-Triplet Annihilation for Photochemical Upconversion. *Phys. Chem. Chem. Phys.* **2010**, *12* (1), 66–71.

(6) Soukka, T.; Kuningas, K.; Rantanen, T.; Haaslahti, V.; Lövgren, T. Photochemical Characterization of Up-Converting Inorganic Lanthanide Phosphors as Potential Labels. *J. Fluoresc.* **2005**, *15* (4), 513–528.

(7) Wang, M.; Chen, Z.; Zheng, W.; Zhu, H.; Lu, S.; Ma, E.; Tu, D.; Zhou, S.; Huang, M.; Chen, X. Lanthanide-Doped Upconversion Nanoparticles Electrostatically Coupled with Photosensitizers for near-Infrared-Triggered Photodynamic Therapy. *Nanoscale* **2014**, *6* (14), 8274–8282.

(8) Mader, H. S.; Kele, P.; Saleh, S. M.; Wolfbeis, O. S. Upconverting Luminescent Nanoparticles for Use in Bioconjugation and Bioimaging. *Curr. Opin. Chem. Biol.* **2010**, *14* (5), 582–596.

(9) Lin, X.; Wang, Y.; Chen, X.; Yang, R.; Wang, Z.; Feng, J.; Wang, H.; Lai, K. W. C.; He, J.; Wang, F.; et al. Multiplexed Optogenetic Stimulation of Neurons with Spectrum-Selective Upconversion Nanoparticles. *Adv. Healthc. Mater.* **2017**, *6* (17), 1700446.

(10) Dong, H.; Sun, L. D.; Yan, C. H. Energy Transfer in Lanthanide Upconversion Studies for Extended Optical Applications. *Chem. Soc. Rev.* **2015**, *44* (6), 1608–1634.

(11) Lin, G.; Baker, M. A. B.; Hong, M.; Jin, D. The Quest for Optical Multiplexing in Bio-Discoveries. *Chem* **2018**, *4* (5), 997–1021.

(12) Deng, R.; Qin, F.; Chen, R.; Huang, W.; Hong, M.; Liu, X. Temporal Full-Colour Tuning through Non-Steady-State Upconversion. *Nat. Nanotechnol.* **2015**, *10* (3), 237–242.

(13) Lu, Y.; Zhao, J.; Zhang, R.; Liu, Y.; Liu, D.; Goldys, E. M.; Yang, X.; Xi, P.; Sunna, A.; Lu, J.; et al. Tunable Lifetime Multiplexing Using Luminescent Nanocrystals. *Nat. Photonics* **2014**, *8* (1), 32–36.

(14) Zhao, J.; Jin, D.; Schartner, E. P.; Lu, Y.; Liu, Y.; Zvyagin, A. V.; Zhang, L.; Dawes, J. M.; Xi, P.; Piper, J. A.; et al. Single-Nanocrystal Sensitivity Achieved by Enhanced Upconversion Luminescence. *Nat. Nanotechnol.* **2013**, *8* (10), 729–734.

(15) Liu, Q.; Zhang, Y.; Peng, C. S.; Yang, T.; Joubert, L. M.; Chu, S. Single Upconversion Nanoparticle Imaging at Sub-10 W cm^{-2} Irradiance. *Nat. Photonics* **2018**, *12* (9), 548–553.

(16) Gargas, D. J.; Chan, E. M.; Ostrowski, A. D.; Aloni, S.; Altoe, M. V. P.; Barnard, E.

S.; Sanii, B.; Urban, J. J.; Milliron, D. J.; Cohen, B. E.; et al. Engineering Bright Sub-10-nm Upconverting Nanocrystals for Single-Molecule Imaging. *Nat. Nanotechnol.* **2014**, *9* (4), 300–305.

(17) Chen, C.; Wang, F.; Wen, S.; Su, Q. P.; Wu, M. C. L.; Liu, Y.; Wang, B.; Li, D.; Shan, X.; Kianinia, M.; et al. Multi-Photon near-Infrared Emission Saturation Nanoscopy Using Upconversion Nanoparticles. *Nat. Commun.* **2018**, *9* (1), 1–6.

(18) Zhan, Q.; Liu, H.; Wang, B.; Wu, Q.; Pu, R.; Zhou, C.; Huang, B.; Peng, X.; Ågren, H.; He, S. Achieving High-Efficiency Emission Depletion Nanoscopy by Employing Cross Relaxation in Upconversion Nanoparticles. *Nat. Commun.* **2017**, *8* (1), 1–11.

(19) Liu, Y.; Lu, Y.; Yang, X.; Zheng, X.; Wen, S.; Wang, F.; Vidal, X.; Zhao, J.; Liu, D.; Zhou, Z.; et al. Amplified Stimulated Emission in Upconversion Nanoparticles for Super-Resolution Nanoscopy. *Nature* **2017**, *543* (7644), 229–233.

(20) Lu, Y.; Lu, J.; Zhao, J.; Cusido, J.; Raymo, F. M.; Yuan, J.; Yang, S.; Leif, R. C.; Huo, Y.; Piper, J. A.; et al. On-the-Fly Decoding Luminescence Lifetimes in the Microsecond Region for Lanthanide-Encoded Suspension Arrays. *Nat. Commun.* **2014**, *5* (1), 3741.

(21) Jin, D.; Xi, P.; Wang, B.; Zhang, L.; Enderlein, J.; van Oijen, A. M. Nanoparticles for Super-Resolution Microscopy and Single-Molecule Tracking. *Nat. Methods* **2018**, *15* (6), 415–423.

(22) Mickert, M. J.; Soukka, T.; Lahtinen, S.; Tallgren, T.; Gorris, H. H. Large-Scale Purification of Photon-Upconversion Nanoparticles by Gel Electrophoresis for Analogue and Digital Bioassays. *Anal. Chem.* **2019**, *91* (2), 1241–1246.

(23) He, H.; Liu, B.; Wen, S.; Liao, J.; Lin, G.; Zhou, J.; Jin, D. Quantitative Lateral Flow Strip Sensor Using Highly Doped Upconversion Nanoparticles. *Anal. Chem.* **2018**, *90* (21), 12356–12360.

(24) Farka, Z.; Mickert, M. J.; Hlaváček, A.; Skládal, P.; Gorris, H. H. Single Molecule Upconversion-Linked Immunosorbent Assay with Extended Dynamic Range for the Sensitive Detection of Diagnostic Biomarkers. *Anal. Chem.* **2017**, *89* (21), 11825–11830.

(25) Zijlstra, P.; Chon, J. W. M.; Gu, M. Five-Dimensional Optical Recording Mediated by Surface Plasmons in Gold Nanorods. *Nature* **2009**, *459* (7245), 410–413.

(26) Zhang, Q.; Xia, Z.; Cheng, Y. B.; Gu, M. High-Capacity Optical Long Data Memory Based on Enhanced Young's Modulus in Nanoplasmonic Hybrid Glass Composites. *Nat. Commun.* **2018**, *9* (1), 1–6.

(27) Zhou, J.; Wen, S.; Liao, J.; Clarke, C.; Tawfik, S. A.; Ren, W.; Mi, C.; Wang, F.; Jin, D. Activation of the Surface Dark-Layer to Enhance Upconversion in a Thermal Field. *Nat. Photonics* **2018**, *12* (3), 154.

(28) Zhou, J.; Leaño, J. L.; Liu, Z.; Jin, D.; Wong, K. L.; Liu, R. S.; Bünzli, J. C. G. Impact of Lanthanide Nanomaterials on Photonic Devices and Smart Applications. *Small* **2018**, *14* (40), 1–29.

(29) Zhang, X.; Yang, S.; Zhou, H.; Liang, J.; Liu, H.; Xia, H.; Zhu, X.; Jiang, Y.; Zhang, Q.; Hu, W.; et al. Perovskite–erbium Silicate Nanosheet Hybrid Waveguide Photodetectors at the Near-Infrared Telecommunication Band. *Adv. Mater.* **2017**, *29* (21), 1604431.

(30) Brouzes, E.; Medkova, M.; Savenelli, N.; Marran, D.; Twardowski, M.; Hutchison, J. B.; Rothberg, J. M.; Link, D. R.; Perrimon, N.; Samuels, M. L. Droplet Microfluidic Technology for Single-Cell High-Throughput Screening. *Proc. Natl. Acad. Sci.* **2009**, *106* (34), 14195–14200.

(31) Birtwell, S. W.; Morgan, H. Microparticle Encoding Technologies for High-Throughput Multiplexed Suspension Assays. *IFMBE Proceedings*, 2010, 27 (5), 316–319.

(32) Wang, P.; Fan, Y.; Lu, L.; Liu, L.; Fan, L.; Zhao, M.; Xie, Y.; Xu, C.; Zhang, F. NIR-II Nanoprobes in-Vivo Assembly to Improve Image-Guided Surgery for Metastatic Ovarian Cancer. *Nat. Commun.* **2018**, *9* (1), 1–10.

(33) Wilson, R.; Cossins, A. R.; Spiller, D. G. Encoded Microcarriers for High-Throughput Multiplexed Detection. *Angew. Chemie - Int. Ed.* **2006**, *45* (37), 6104–6117.

(34) Li, Y.; Cu, Y. T. H.; Luo, D. Multiplexed Detection of Pathogen DNA with DNA-Based Fluorescence Nanobarcodes. *Nat. Biotechnol.* **2005**, *23* (7), 885–889.

(35) Fischer, S.; Bronstein, N. D.; Swabeck, J. K.; Chan, E. M.; Alivisatos, A. P. Precise Tuning of Surface Quenching for Luminescence Enhancement in Core–shell Lanthanide-Doped Nanocrystals. *Nano Lett.* **2016**, *16* (11), 7241–7247.

(36) Wang, F.; Wang, J.; Liu, X. Direct Evidence of a Surface Quenching Effect on Size-dependent Luminescence of Upconversion Nanoparticles. *Angew. Chemie Int. Ed.* **2010**, *49* (41), 7456–7460.

(37) Alyatkin, S.; Asharchuk, I.; Khaydukov, K.; Nechaev, A.; Lebedev, O.; Vainer, Y.; Semchishen, V.; Khaydukov, E. The Influence of Energy Migration on Luminescence Kinetics Parameters in Upconversion Nanoparticles. *Nanotechnology* **2017**, *28* (3), 035401.

(38) Sun, T.; Li, Y.; Ho, W. L.; Zhu, Q.; Chen, X.; Jin, L.; Zhu, H.; Huang, B.; Lin, J.; Little, B. E.; et al. Integrating Temporal and Spatial Control of Electronic Transitions for Bright Multiphoton Upconversion. *Nat. Commun.* **2019**, *10* (1), 1–7.

(39) Zuo, J.; Sun, D.; Tu, L.; Wu, Y.; Cao, Y.; Xue, B.; Zhang, Y.; Chang, Y.; Liu, X.; Kong, X.; et al. Precisely Tailoring Upconversion Dynamics via Energy Migration in Core-Shell Nanostructures. *Angew. Chemie* **2018**, *130* (12), 3108–3112.

Chapter 5 Optical Fingerprints of Single Nanoparticles for Deep Learning Aided Super-Capacity Optical Multiplexing

5.1 Preamble

Super-capacity optical multiplexing challenges our ability to create multiplexed codes in orthogonal dimensions and to assign them to the macroscopic level and nanoscale carriers. The emerging optical multiplexing within the nanoscale shows super-capacity in encoding information by using the time-domain fingerprints from uniform nanoparticles. However, the upconversion emission efficiency limits compromise the decoding of the high-throughput and accuracy of the nanoparticles during wide-field imaging and the confocal system of different excitation power densities (Fig. 5.1). In turn, this challenges the quality and brightness of nanoparticles to afford the modified excitation condition, and further retain the multiplexed optical fingerprints for the multiplexing digital assay. Here, two sets of conventional Yb^{3+}-Tm^{3+} core-inert shell and Yb^{3+}-Nd^{3+}-Er^{3+} core three-layer shell UCNPs-doped $NaYF_4$ nanoparticles with different doped concentrations were prepared. We demonstrate the nanoparticles show a unique lifetime signature under wide-field systems upon 976-nm (blue emission of the Yb^{3+}-Tm^{3+} system) and 808-nm (green and red emission of the Yb^{3+}-Nd^{3+}-Er^{3+} system) excitation. We report that a single nanoparticle's emission profile of both rising and decay times can be tuned arbitrarily, which creates the diversity of optical signatures in the time domain—that is, to encode nanoparticles by a set of lifetime profiles (τ^2). To achieve high-throughput multiplexing, lifetime profiles are detected under a wide-field microscope system. We demonstrate that the core-multi-shell design can be used to manage the cascade energy transfer process within a single nanoparticle and to subsequently fine-tune the lifetime fingerprints in producing a series of unique batches of derivative τ^2-Dots. We further implement a deep-learning algorithm to coordinate with wide-field images for the more accurate decoding of the lifetime fingerprints of τ^2-Dots. By training the machine with 14 batches of τ^2-Dots types, deep learning can intelligently define a territory for each type of τ^2-

Dot, where the wide-field imaging-based optical multiplexing of 14 channels with decoding accuracies larger than 90% for each channel can be achieved. Our created orthogonal spectral and lifetime dimension multiplexing opens up a new horizon towards handling the growing amount of information content, disease source, and security risks in modern society, as well as providing a new channel for multiplexing digital assays.

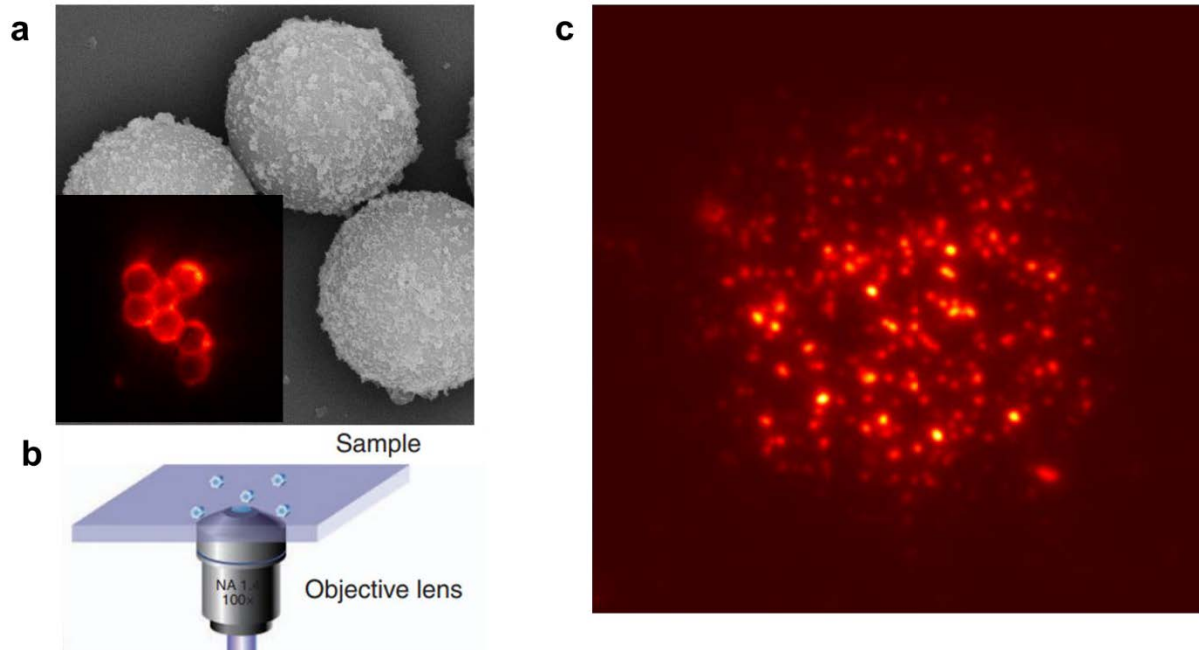

Figure 5.1 (a) SEM photos and corresponding luminescence imaging of 5 μm polystyrene microbeads after tagged with UCNPs. (b) Schematics of the confocal microscope by pixel by pixel scanning. (c) Wide-field microscopic imaging of one typical UCNPs under NIR-infrared excitation.

5.2 Introduction

With the use of optical multiplexing, it is easy to implement a solution that combines many signals onto an assemblage of optical microcarriers for information transmission[1–4], data storage[5–8], security[9–11] and high-throughput digital assays[12–16]. The relatively mature technique of wavelength or colour-division multiplexing is widely used. The major feature of spectrum encoding is the uniqueness of the emission spectra profile of the fluorescent labeling element. It is well-known that both organic (fluorescent dyes)[17–19] and inorganic fluorophores (quantum dots,[20–23] and upconversion nanoparticles[24–27]) as main encoding elements have been used widely in the fabrication of fluorescence-encoded strategies due to their extensive

applications in multiplexed assays. However, this has demonstrated limitations because of the requirement of multi-lasers for excitation and spectral cross-talk for emission bands in most cases. The recently developed time-domain optical carriers have fundamentally resolved the spectral cross-talk issue under single-laser excitation and have subsequently enabled super-capacity multiplexing at the nanoscale level[28]. However, the sub-60 nm nanocarriers have not been able to fully exert their advantages due to the restriction of the brightness limit during imaging, as the amount of signals from a nanoscale object drops exponentially. This reduces the high throughput and signal to noise ratio in applications. In particular, the emission intensity further hampers single nanocarriers for future digital assays in detecting low concentration analytes. In further developing time-domain super-capacity multiplexing method, the quality of nanoprobes is technically challenged, where they have to be bright, stable and have a long lifetime under pulsed-laser excitation.

This unmet expectation has posed significant challenges for the material sciences to pursue high-throughput fabrication strategies and precise control in producing uniform nanoscopic carriers. It has also motivated the photonics community to maximize the amount of signals and to explore the diversity of optical information which can be produced in multiple orthogonal dimensions, such as emission colours (spectrum)[29], lifetime[28], polarization[30,31], and angular momentum[6,22]. The goal is to arbitrarily ensemble more codes within a shared space of the nanoscale medium, such as a single nanoparticle.

In the search for a potential probe candidate, most of the nanoparticles (e.g., quantum dots, carbon dots[32], and organic dyes) show a short lifetime in nanoseconds, limiting the channels for time-domain multiplexing. Lanthanide-doped UCNPs are currently one kind of best candidates. The UCNPs achieve upconversion emissions from isolated lanthanide ions in a crystal field, in which the forbidden partially-allowed f-f transitions show stable signals and the excited-state lifetime of lanthanides could range from microseconds to milliseconds. Moreover, the lifetime of a typical excited state can be arbitrarily tuned through the microlocal environment control within a nanocrystal, not to mention the diversity from diverse ions and

excited states. However, a big concern is the brightness of UCNPs, especially for the single nanoparticles under the excitation condition of pulse mode wide-field microscopy.

Here, we demonstrate a library of Yb^{3+}-Tm^{3+} core-inert shell and Yb^{3+}-Nd^{3+}-Er^{3+} core three-layer UCNPs with tailored lifetime profiles show sufficient brightness and long-term photostability for imaging. The spectral and lifetime encoding ability from single nanoparticles can significantly broaden the scope of luminescent materials for optical multiplexing studies. A machine learning algorithm is further developed to reduce lifetime cross-talk and improve classification accuracies. By taking advantage of such UCNPs, we demonstrate wide-field imaging for the high-throughput multiplexing of 14 kinds of UCNPs, with high decoding accuracies of up to 90% with the assistance of deep learning. To demonstrate the potential of nanoparticles, we also outline the transfer of the nanoparticles from hydrophobic to hydrophilic via surface modification. The OA-nanoparticles were transferred into an aqueous environment via a ligand-exchange and carboxyl-functionalization by the polymer. Next, the carboxyl-nanoparticles were conjugated with probe DNA through specific binding. The lifetime property of nanoparticles provides a significant opportunity for the multiplexing assay of DNA.

5.3 Experimental section

5.3.1 Synthesis of $NaYF_4$: Yb^{3+}, Tm^{3+}/ Er^{3+} core nanoparticles

The $NaYF_4$:20%Yb, 0.2%Tm core nanoparticles were synthesized using a coprecipitation method. 1 mmol $RECl_3$ (RE=Y, Yb, Tm) with 0.798 mmol $YCl_3 \cdot 6H_2O$, 0.2 mmol $YbCl_3 \cdot 6H_2O$, and 0.002 mmol $TmCl_3 \cdot 6H_2O$ together with 6 mL oleic acid and 15 mL 1-octadecene were added to a 50 ml three-neck round-bottom flask under vigorous stirring. The resulting mixture was heated at 150 ^oC for 40 mins to form lanthanide oleate complexes. The solution was cooled down to room temperature. Subsequently, a methanol solution containing 2.5 mmol NaOH and 4 mmol NH_4F was added and stirred for 40 mins, and then the mixture was slowly heated to 150 °C and kept for 40 mins under argon flow to remove methanol and residual water. Next, the solution was quickly heated at 300 ^oC under argon flow for 1.5 h before cooling down to room temperature. The resulting core nanoparticles were precipitated by the addition of ethanol,

collected by centrifugation at 9000 rpm for 5 min, the final $NaYF_4$: Yb, Tm nanocrystals were redispersed in cyclohexane after washing with cyclohexane/ethanol/methanol several times.

We synthesized another nine kinds of core nanoparticles for similar size with different doping concentrations ($NaYF_4$:20%Yb, 0.2%Tm, $NaYF_4$:20%Yb, 0.5%Tm, $NaYF_4$:20%Yb, 1%Tm, $NaYF_4$:20%Yb, 1.5%Tm, $NaYF_4$:20%Yb, 2%Tm, $NaYF_4$:20%Yb, 3%Tm, $NaYF_4$:40%Yb, 1%Tm, $NaYF_4$:40%Yb, 4%Tm, $NaYF_4$:40%Yb, 8%Tm) using the same above method.

We synthesized another four kinds of core nanoparticles for similar size with different doping concentrations ($NaYF_4$:20%Yb, 1.5%Er, $NaYF_4$:20%Yb, 2%Er, $NaYF_4$:30%Yb, 2%Er, $NaYF_4$:30%Yb, 8%Er) using the same above method.

The pure $NaYF_4$ precursors were prepared as the above procedure until the step where the reaction solution was slowly heated to 150 °C after adding NaOH/NH_4F solution and kept for 40 min. Instead of further heating to 300 °C to trigger nanocrystal growth, the solution was cooled down to room temperature to yield the shell precursors.

5.3.2 Synthesis of core-shell nanoparticles

The core@$NaYF_4$ and core@ $NaYbF_4$:5%Yb core-shell nanoparticles were prepared by layer by layer epitaxial growth method. The pre-synthesized $NaYF_4$: Yb, Tm core nanoparticles were used as seeds for shell modification. 0.2 mmol as-prepared core nanocrystals were added to a 50 ml flask containing 3 ml OA and 8 ml ODE. The mixture was heated to 160 °C under argon for 30 min, and then further heated to 300 °C. Next, a certain amount of as-prepared shell precursors were injected into the reaction mixture and ripened at 300 °C for 2 min, followed by the same injection and ripening cycles for approximately several times to get around 3 nm thickness shell. Finally, the slurry was cooled down to room temperature and the formed core-shell nanocrystals were washed dispersed in cyclohexane for next step epitaxial growth.

Table 5.1. Summary of composition and size of nine kinds of Yb^{3+}-Tm^{3+} doped $NaYF_4$ core-shell samples.

Core	Passivation layer (6 nm)	Sample
40Yb^{3+}/8 Tm^{3+} (53 nm)	Y^{3+} (6 nm)	1
40Yb^{3+}/4 Tm^{3+} (53 nm)	Y^{3+} (6 nm)	2
20Yb^{3+}/3Tm^{3+} (52 nm)	Y^{3+} (6 nm)	3
20Yb^{3+}/1.5Tm^{3+} (42 nm)	Y^{3+} (6 nm)	4
40Yb^{3+}/1Tm^{3+} (43 nm)	Y^{3+} (6 nm)	5
20Yb^{3+}/2 Tm^{3+} (42 nm)	Y^{3+} (6 nm)	6
20Yb^{3+}/1Tm^{3+} (42 nm)	Y^{3+} (6 nm)	7
20Yb^{3+}/0.5Tm^{3+} (44 nm)	Y^{3+} (6 nm)	8
20Yb^{3+}/0.2Tm^{3+} (45 nm)	Y^{3+} (6 nm)	9

The core@$NaYF_4$:5%Yb@$NaYF_4$:x%Yb, 20%Nd (x=5, 15, 30) core-shell-shell nanoparticles were also prepared by the epitaxial growth method described above and the core-shell samples were used as the seeds.

The core@$NaYF_4$:5%Yb@$NaYF_4$:x%Yb,20%Nd@$NaYF_4$ (x=5, 15, 30) core-shell-shell-shell nanoparticles were also prepared by epitaxial growth method described above and the core-shell-shell samples were used as the seeds.

Table 5.2. Summary of the composition of Nd^{3+}-Yb^{3+}-Er^{3+} tri-doped core-three layer shells UCNPs used in this chapter.

Sample	core	Migration Layer	Sensitization Layer	Inert Layer
10	30Yb^{3+}/8Er^{3+}	5Yb^{3+}	15Yb^{3+}/20Nd^{3+}	Y^{3+}
11	20Yb^{3+}/1.5Er^{3+}	5Yb^{3+}	15Yb^{3+}/20Nd^{3+}	Y^{3+}
12	20Yb^{3+}/2Er^{3+}	5Yb^{3+}	15Yb^{3+}/20Nd^{3+}	Y^{3+}
13	30Yb^{3+}/2Er^{3+}	5Yb^{3+}	5Yb^{3+}/20Nd^{3+}	Y^{3+}
14	20Yb^{3+}/2Er^{3+}	5Yb^{3+}	5Yb^{3+}/20Nd^{3+}	Y^{3+}

5.4 Results and Discussion

5.4.1 Optical system setup and material characterization of single nanoparticles

We built a widefield fluorescence microscope to acquire the fluorescence lifetime imaging sequences of Yb^{3+}-Nd^{3+}-Er^{3+} core-multi shell single nanoparticles as shown in Fig. 5.2a. By

taking advantage of bright core-shell UCNPs, we develop a wide-field imaging method for high-throughput multiplexing under 980 and 808 nm laser excitation. We acquired the lifetime imaging sequences of 75 frames from 0 μs to 3750 μs with a time gate of 50 μs by using the time-resolved sCMOS camera under the 200 μs pulse laser excitation (Fig. 5.2b). Moreover, the orthogonal encoding technique combining spectral and lifetime dimensions allows for a marked increase in the coding capacity compared with conventional luminescence encoding strategies.

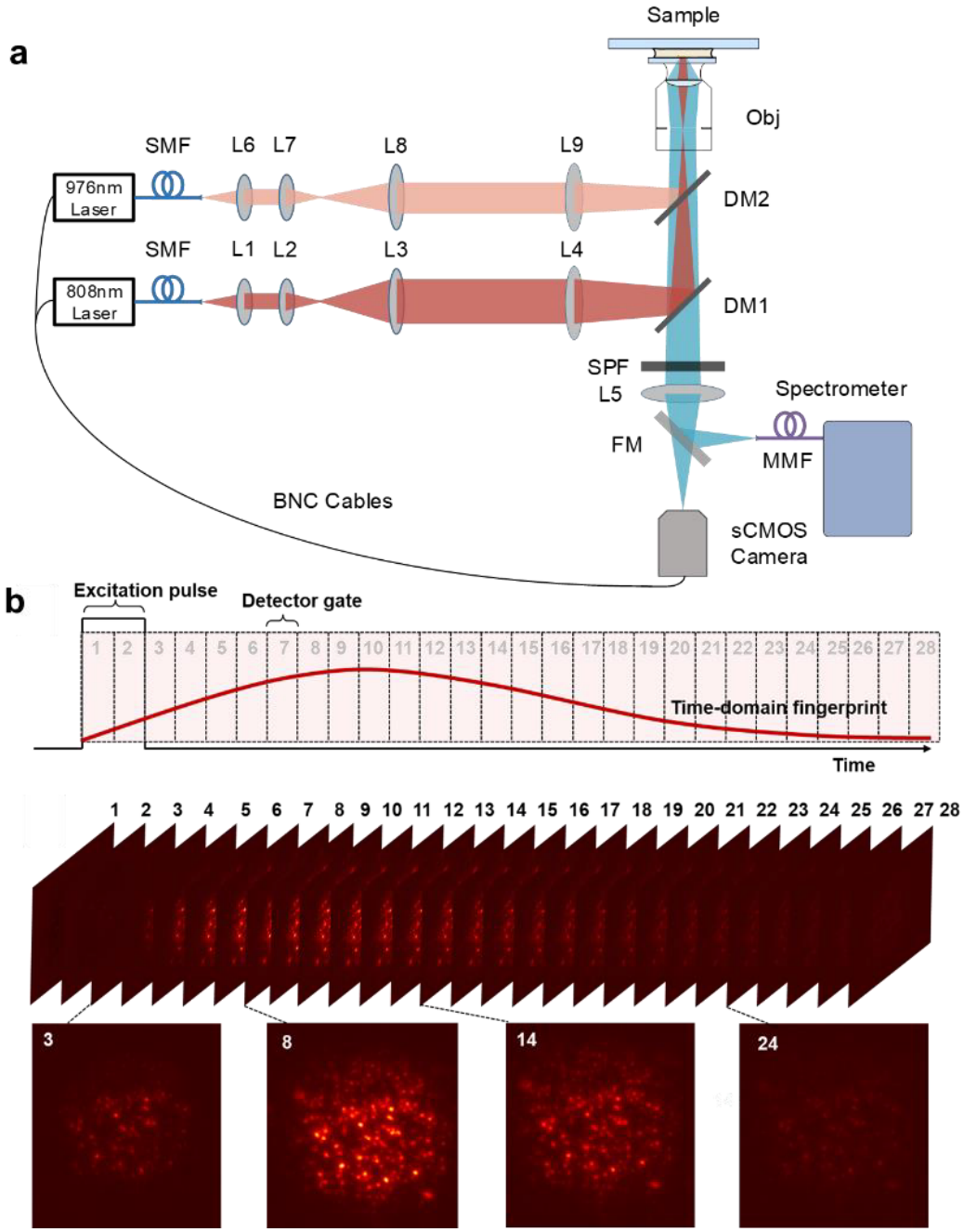

Figure 5.2 (a) Schematic view of the widefield fluorescence imaging setup. (b) Illustration of the time-resolved fluorescence lifetime imaging in the widefield microscope system.

The TEM image in Figure 5.3a shows a typical Yb^{3+}-Tm^{3+} core-inert shell nanocrystal with morphology uniformity. The inset illustration shows the design of the nanoparticles, the core is co-doped by Yb^{3+} sensitizer and Tm^{3+} emitter, the outer layer of pure $NaYF_4$ as optically inert shell passivates each single nanoparticle from surface quenchers. Following our previous work in chapter 4, we excite the Yb^{3+} ions using 976 nm lasers and observe optical signatures, such as spectra and lifetime. The emission spectra and lifetime profiles of sample 1 in Figure 5.3b and c come from the wavelength between 400 and 740 nm of Tm^{3+}. As shown in Figure 5.3d, the wet chemistry approach[33], using a slow injection of precursors, allows layer-by-layer epitaxial growth of core-multi-shell β-$NaYF_4$: Nd^{3+}-Yb^{3+}-Er^{3+} UCNPs. As shown in Figure 5.3e, the rather sophisticated design of core-multi-shell UCNPs permit an arbitrary control in the energy transfer process within a single nanoparticle[34]: the shell co-doped with Nd^{3+}/Yb^{3+} ions sensitizes 808 nm excitation, the energy migration shell containing a small percentage of Yb^{3+} ions is responsible for passing on the exited photon energy to the conventional Yb^{3+}/Er^{3+} co-doped core that emits up-converted emissions at green and red bands (see Figure 5.3f). Doping strategies to achieve lifetime tunability in plateau moment, rising time and decay time (see Figure 5.3g), following our previous work in chapter 4. It shows that the rising time for the Er^{3+} excited state populations to reach its plateau can be prolonged from 200 μs to 650 μs when the interfacial energy migration (IEM) process is involved. The significantly prolonged rising time, together with their exceptionally long decay time, make the nanoparticles display a unique optical fingerprint for each different batch of controlled synthesis, because of the rather sophisticated multi-component lifetime behaviors, namely τ^2-dots.

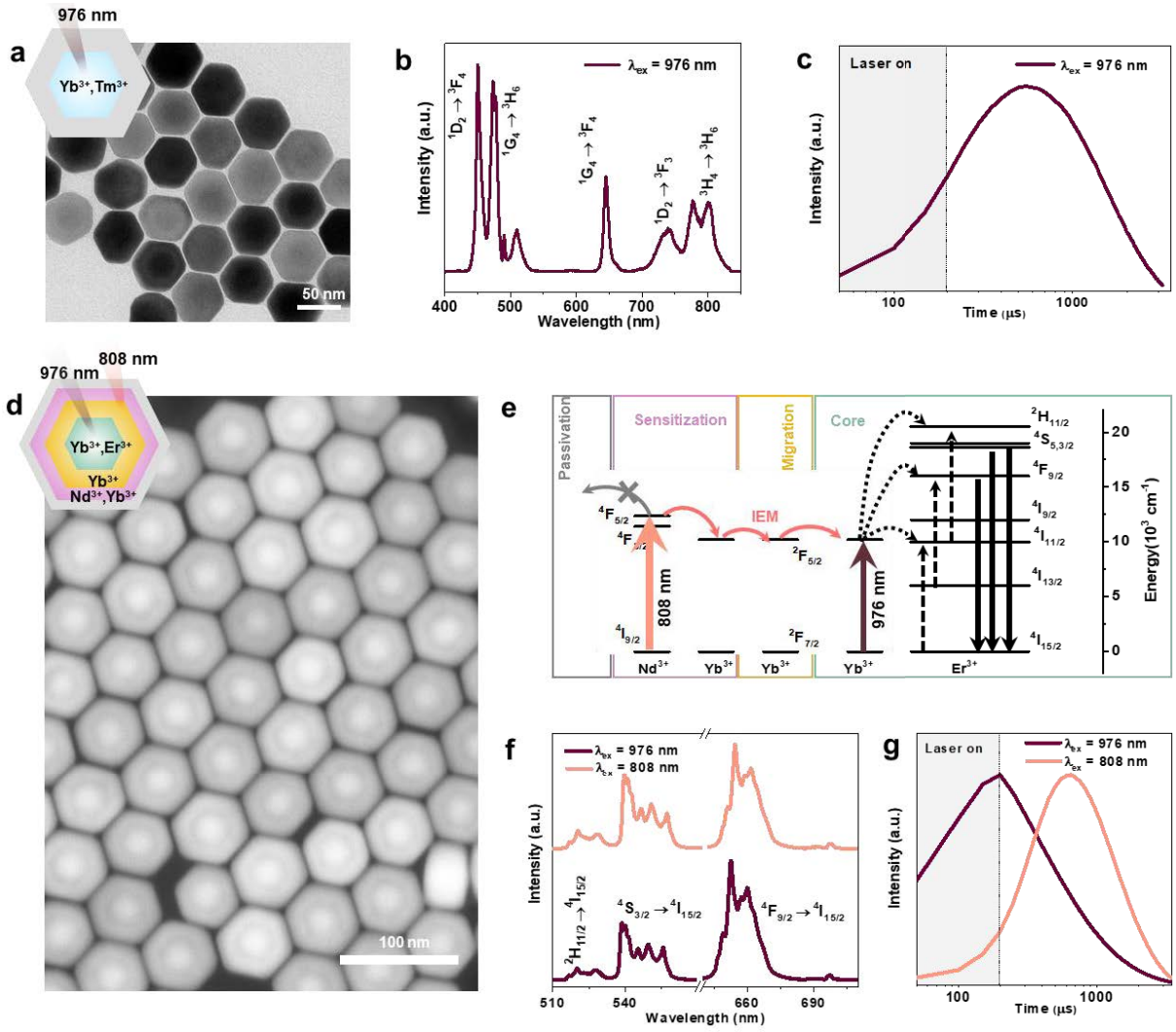

Figure 5.3 Creation of uniform dots with τ^2-like optical signatures of Yb^{3+}-Tm^{3+} core-inert shell UCNPs and Yb^{3+}, Nd^{3+}, Er^{3+} core three-layer shells UCNPs. (a)(d) TEM characterization of a kind of typical Yb^{3+}-Tm^{3+} core-inert shell and Yb^{3+}-Nd^{3+}-Er^{3+} core three-layer UCNPs morphology uniform nanocrystals, respectively. **(b)and (f)** Visible region upconversion emission spectra of Yb^{3+}-Tm^{3+} core-inert shell and Yb^{3+}-Nd^{3+}-Er^{3+} core three-layer UCNPs, respectively. **(c)** lifetime curves of powder state of a kind of typical Yb^{3+}-Tm^{3+} core-inert shell UCNPs under 980 nm excitation **(e)** Schematic illustration of core-multi-shell τ^2-dots using $NaYF_4$ as host nanocrystal.**(g)** lifetime curves of powder state Yb^{3+}-Nd^{3+}-Er^{3+} core three-layer UCNPs under 808 nm excitation and 976 nm excitation.

To create a set of time-domain optical fingerprints and build a library of different batches of τ^2-dots including 14 batches of samples for nanoscale super-capacity optical multiplexing. We change the Yb^{3+} and Tm^{3+} doped concentration to tailor lifetime curves of nine batches of Yb^{3+}-

Tm^{3+} core-inert shell nanocrystal (Table 5.1), the TEM morphology of core-shell samples are shown in Figure 5.4. We further implemented IEM process in the core-shell structure to tailor the excited-state populations of 5 batches of Nd^{3+}-Yb^{3+}-Er^{3+} tri-doped nanoparticles (Table 5.2), which are shown in Figure 5.5.

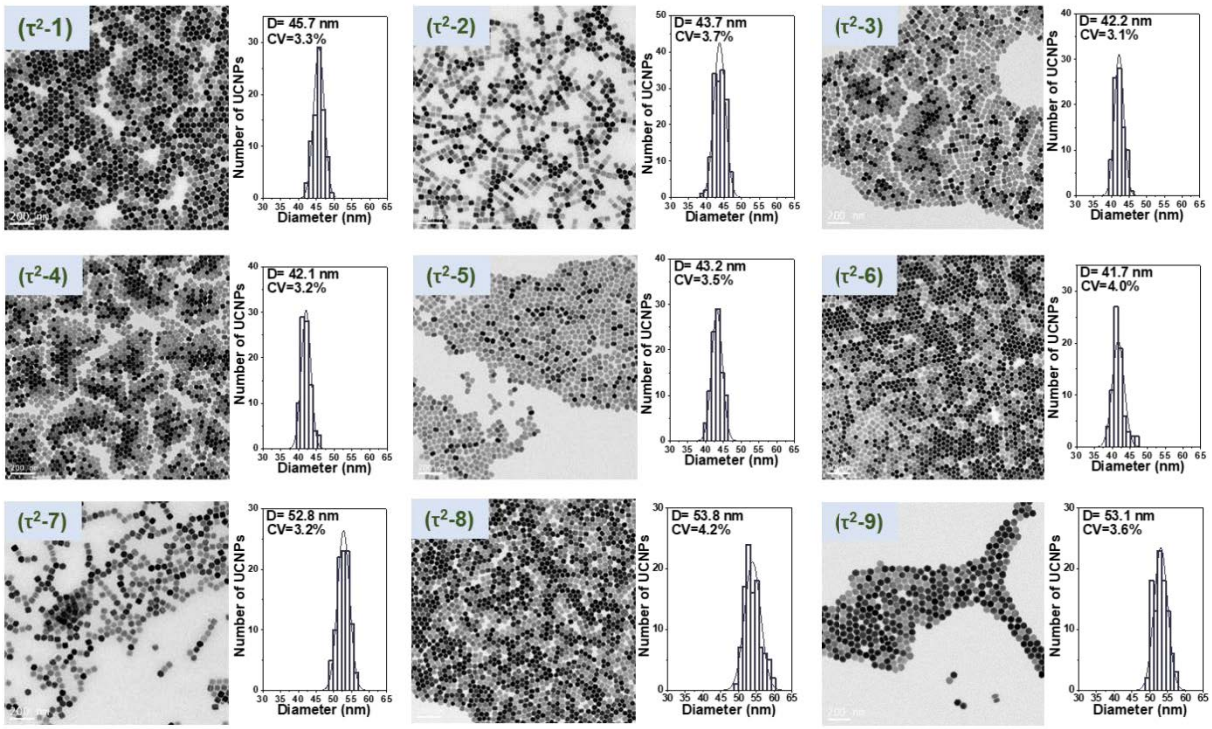

Figure. 5.4 TEM photos of Yb^{3+}-Tm^{3+} core-inert shell UCNPs. (1) $NaYF_4$:20%Yb^{3+},0.2% Tm^{3+} @ $NaYF_4$. (2) $NaYF_4$:20%Yb^{3+},0.5% Tm^{3+} @ $NaYF_4$. (3) $NaYF_4$:20%Yb^{3+},1% Tm^{3+} @ $NaYF_4$. (4) $NaYF_4$:20%Yb^{3+},2% Tm^{3+} @ $NaYF_4$. (5) $NaYF_4$:40%Yb^{3+},1% Tm^{3+} @ $NaYF_4$. (6) $NaYF_4$:20%Yb^{3+},1.5% Tm^{3+} @ $NaYF_4$. (7) $NaYF_4$:20%Yb^{3+},3% Tm^{3+} @ $NaYF_4$. (8) $NaYF_4$:40%Yb^{3+},4% Tm^{3+} @ $NaYF_4$. (9) $NaYF_4$:40%Yb^{3+},8% Tm^{3+} @ $NaYF_4$. Scale bar: 100 nm.

Figure 5.5 shows that the controlled synthesis produces uniform core multi-shell nanostructures of 5 batches of Nd^{3+}-Yb^{3+}-Er^{3+} tri-doped UCNPs under transmission electron microscopy. The histograms of their size distribution show that all the four-layer core multi-shell UCNPs have uniform morphology with a size ~60 nm.

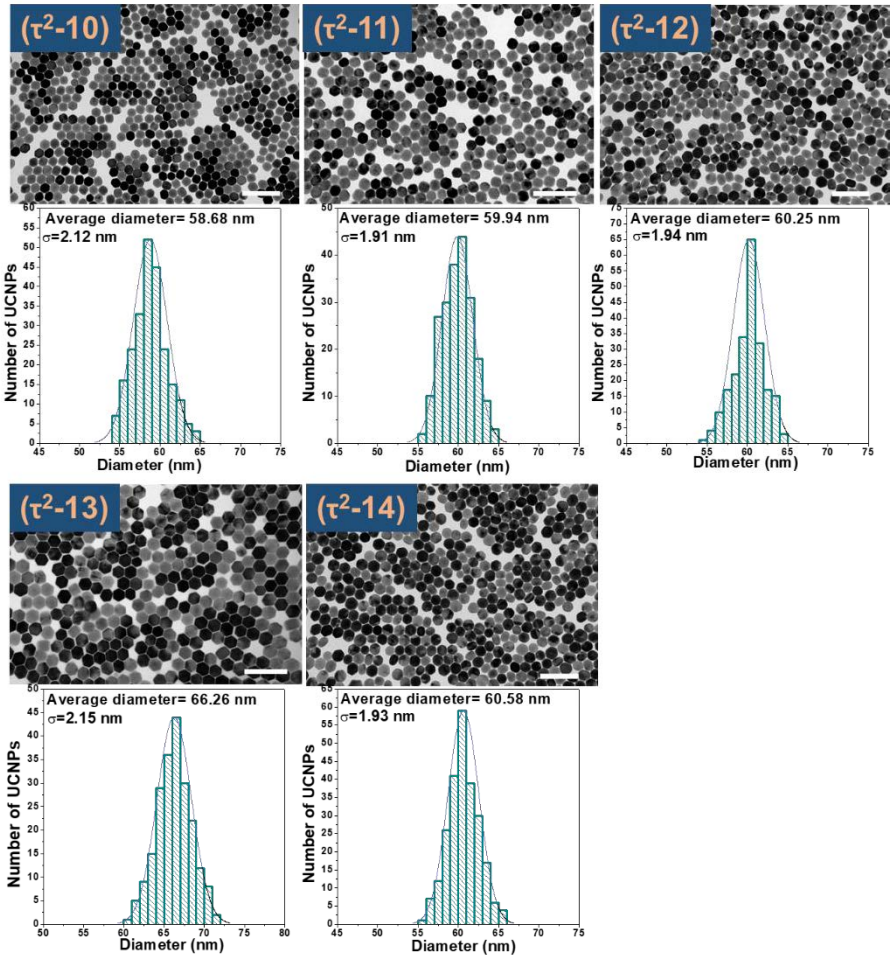

Figure. 5.5 TEM photos and corresponding size distribution of Yb^{3+}-Nd^{3+}-Er^{3+} core three-layer UCNPs. (10) $NaYF_4$:30%Yb^{3+},8% Er^{3+} @ $NaYF_4$:5%Yb^{3+}@ $NaYF_4$: 15%Yb^{3+}, 20% Nd^{3+}@ $NaYF_4$ nanoparticles. (11) $NaYF_4$:20%Yb^{3+},1.5% Er^{3+} @ $NaYF_4$:5%Yb^{3+}@ $NaYF_4$: 15%Yb^{3+}, 20% Nd^{3+}@ $NaYF_4$ nanoparticles. (12) $NaYF_4$:20%Yb^{3+},2% Er^{3+} @ $NaYF_4$:5%Yb^{3+}@ $NaYF_4$: 15%Yb^{3+}, 20% Nd^{3+}@ $NaYF_4$ nanoparticles. (13) $NaYF_4$:30%Yb^{3+},2% Er^{3+} @ $NaYF_4$:5%Yb^{3+}@ $NaYF_4$: 15%Yb^{3+}, 20% Nd^{3+}@ $NaYF_4$ nanoparticles. (14) $NaYF_4$:20%Yb^{3+},2% Er^{3+} @ $NaYF_4$:5%Yb^{3+}@ $NaYF_4$: 5%Yb^{3+}, 20% Nd^{3+}@ $NaYF_4$ nanoparticles. Scale bar: 200 nm

5.4.2 Optical signatures of fourteen kinds of τ^2-dots nanoparticles under the wide-field microscope system

Here we show that the deadlock to super-capacity optical multiplexing in nanoscale can be bypassed by encoding upconversion nanoparticles (UCNPs) with time-domain optical fingerprints under the wide-field microscope system. Figure 5.6a shows an optical image of

the τ^2-10 dots under the wide-field microscopy, which demonstrates the uniform intensity of UCNPs. Within a uniform illumination field of 15×15μm, we observed uniform and bright single UCNPs by detecting the upconversion emissions through the camera (time-resolved sCMOS) under an 808 nm excitation beam. The photostability of long-time traces and peak Gaussian distributions of the single UCNPs are shown in Fig. 5.6b. It shows no photobleaching and blinking behavior for one single nanoparticle in 200 minutes. Keeping the detection time for several hours, the single nanoparticle photostability was consistent intensities with an averaged value of 75,000 cts/200ms. The excellent photostability is more advantages than conventional fluorescent dyes/quantum dots and is highly desired for the long term and continuous recording.

Confocal scanning microscopy typically extracts the time-domain optical fingerprint from one dot to another by scanning across each pixel, which can limit the throughput in the decoding process. The high brightness and optical stability of each τ^2-dot allow moderate excitation power density (5.46 kW/cm^2) to be used in a wide-field microscope with an intensifier coupled CMOS camera for time-resolved imaging (the widefield imaging system is shown in Figure 2.3). As shown in Figure 5.6c, the sequence of time-resolved imaging consists of 75 frames (n=75), each recording the time-gated window period (Δt) of 50 μs.

Compared to the conventional micron-sized beads, optical codes created on nanoscopic sized nanoparticles can significantly increase the capacity of coding information, which takes optical super capacity multiplexing into the region of the optical diffraction limit. To illustrate this opportunity and challenge, we stained 5 μm polystyrene beads with τ^2-5 dots (Figure 5.6) and collected their time-resolved upconversion images under a wide-field microscope. Within an illumination area of 28 μm square, a typical image only contains less than ten micron-sized beads (Figure 5.6d), while in contrast, there are hundreds of single τ^2-5 dots within the same area (Figure 5.6e). Each single micron bead shows a smooth lifetime profile (Figure 5.6f), but the curve from a single τ^2 dot (Figure 5.6g) has some significant level of noise, due to the limited amount of detectable signal within each 50 μs time-gated window.

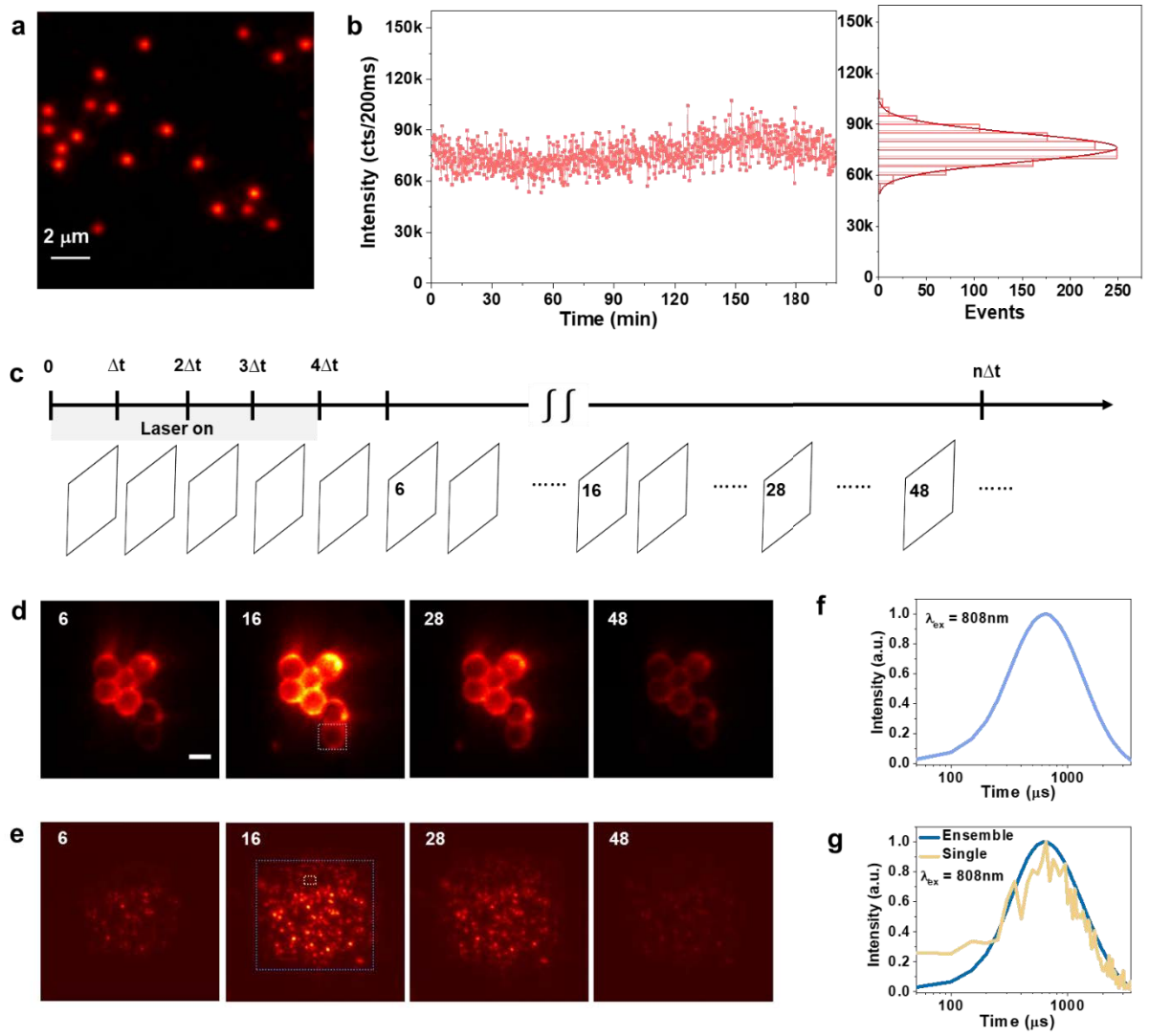

Fig. 5.6 Wide-field time-resolved imaging of τ^2-dots for high-throughput lifetime decoding. **(a)** single nanoparticle imaging of τ^2-10 under wide-field microscopy with 808 nm excitation laser, **(b)** Corresponding photostability and brightness distribution of a single UCNPs under 808 nm excitation under widefield microscopy system. An arbitrary batch of τ^2-dot used here was chosen from a library of core-multi-shell nanoparticles we synthesized in this work. **(c)** Schematic illustration of the transient fluorescence signal detection principle using a time-resolved sCMOS camera. **(d and e)** Typical time-resolved 6^{th}, 16^{th}, 28^{th}, and 48^{th} frames of τ^2-Dots-stained polystyrene beads (d) and single τ^2-Dot (e) within a beam area of 28 μm in diameter. Scale bar is 5 μm. **(f)** Lifetime curve of a single τ^2-Dots-stained bead, which is indicated by a pink dotted square in (d). **(g)** Lifetime curves of a single and ensemble of τ^2-Dots, which are indicated by yellow and purple dotted squares in (e).

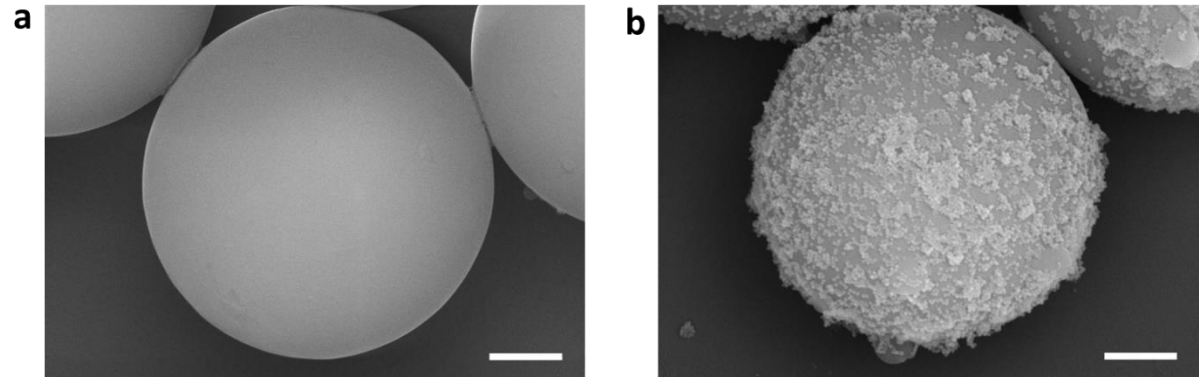

Fig. 5.7 SEM images of microbeads. SEM photos of 5 μm polystyrene beads before (a) and after (b) tagged with τ^2-10 nanoparticles. Scale bar: 1 μm.

The brightness distribution of a single dot (Figure 5.6b) shows that because of properly protected by the passivation layer and IEM process in core-shell structure, all the derivative populations of τ^2-dots provide sufficient photon counts for single-dot based super capacity multiplexing applications. For example, the photon counts of τ^2-10 under confocal microscopy are 300 counts/second under continuous-wave 808 nm laser excitation at 5.5 kW/cm^2, as shown in Fig. 5.8a, which is corresponding to sCMOS readout of 8000 under our testing condition for single-dot based super-capacity multiplexing applications (Fig. 5.8b).

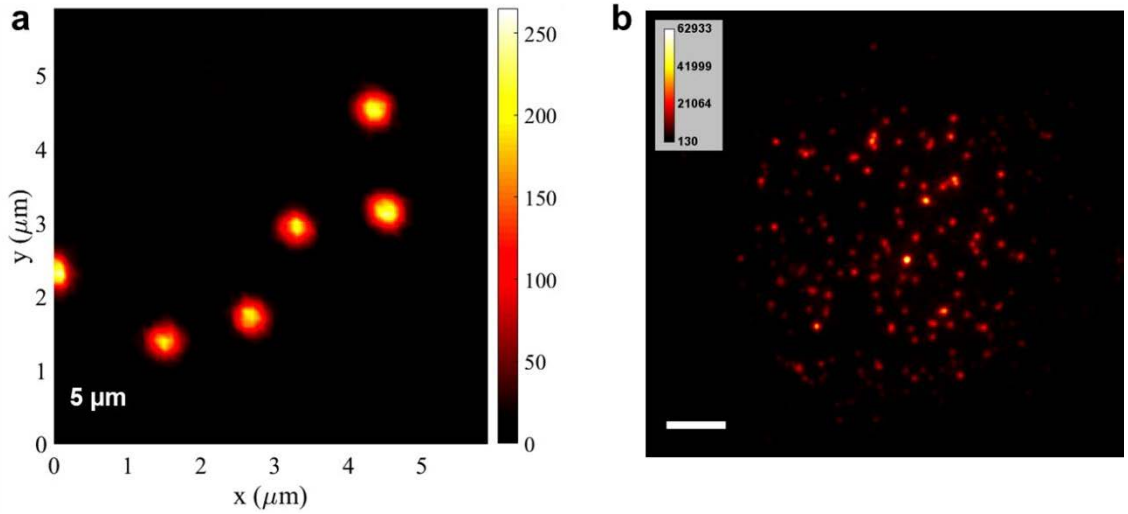

Fig. 5.8 (a) Confocal microscopy measurement and **(b)** widefield intensity readout at sCMOS camera of τ^2-10 under CW 808 nm excitation at 5.46 kW/cm^2.

To characterize the optical properties of single nanoparticles, the UCNPs in cyclohexane were dropped onto a coverslip labeled with the scratch for correlative wide-field fluorescence images and scanning electron microscope (Fig. 5.9). After comparing the wide-field fluorescence images, the diffraction-limited fluorescent spots were carefully registered to corresponding positions on scanning electron micrographs, which is sufficient to resolve and verify the size of the individual nanoparticles.

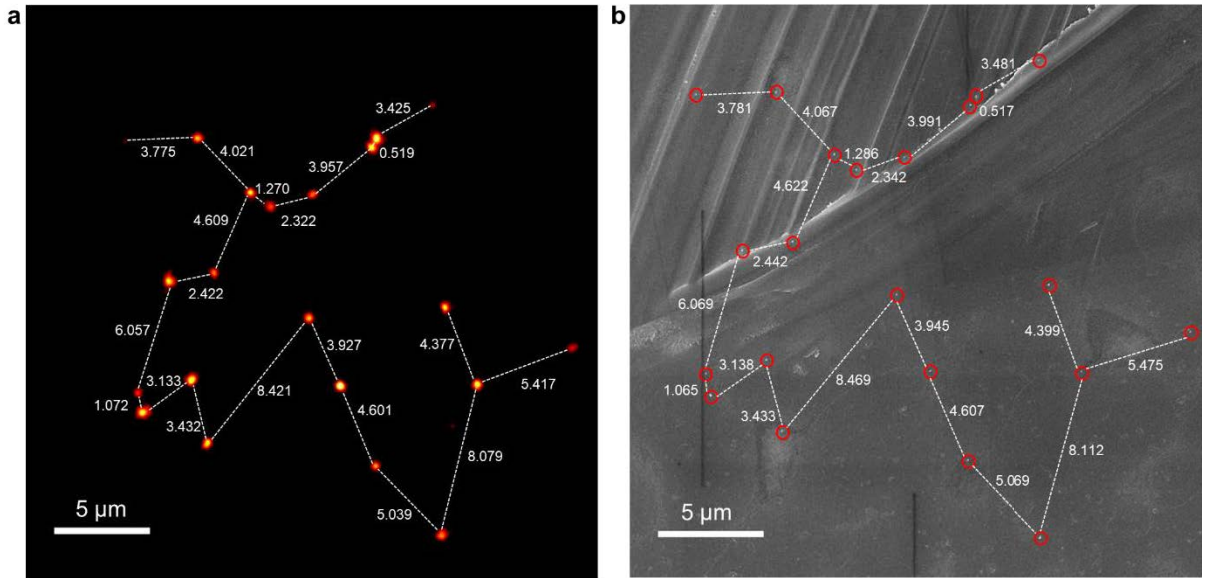

Fig. 5.9 Single nanoparticle detection in wide-field microscopy of single τ^2-10. a) wide-field optical image under 808 nm laser, b) the corresponding SEM image of the same area.

To create a set of time-domain optical fingerprints and build a library of different batches of τ^2-dots for nanoscale super-capacity optical multiplexing, we change the doping concentration of Yb^{3+} and Tm^{3+} to tailor the lifetime profiles in Yb^{3+}-Tm^{3+} doped system. The composition of eight batches of Tm^{3+} doped τ^2-dots nanoparticles was summary in Table 5.1. We further implemented the interfacial energy migration strategy to tailor the excited-state populations in the sophisticated core-multi-shell β-$NaYF_4$: Nd^{3+}-Yb^{3+}-Er^{3+} UCNPs through layer-by-layer epitaxial growth method. The composition of five batches of Er^{3+} doped τ^2-dots nanoparticles was summary in Table 5.2. The statistic counting of their brightness is shown in Figure 5.10.

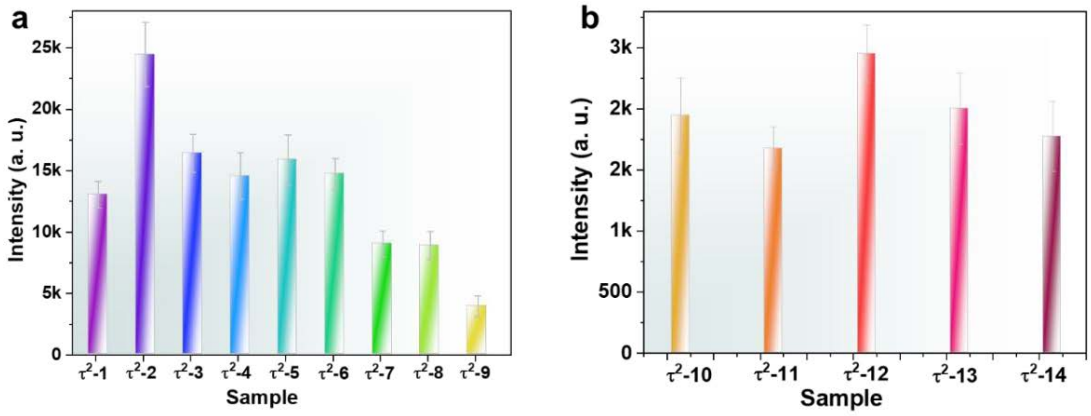

Figure 5.10 Intensity display of averaged single nanoparticle lifetime fingerprints of 14 τ^2-Dots.

The thickness of the inert shell can provide different degrees of surface passivation from the surface quenchers and therefore lengthen the lifetime. Lifetime curve statistics from single τ^2-Dots of these 14 batches of UCNPs are shown in Figure 5.11a. The lifetime curves τ^2-1 to τ^2-9 come from Yb^{3+}-Tm^{3+} doped UCNPs and τ^2-10 to τ^2-14 belong to Nd^{3+}-Yb^{3+}-Er^{3+} doped UCNPs. We have been able to create a new matrix of lifetime-coded single nanoparticles by simply time-domain images under wide-field microscopy. Both the lifetime and the emission colour of individual single nanoparticles could be recorded. As shown in Figure5.11a, the emitter of Tm^{3+} variation within the range 0.2–8 mol% or increasing the Yb^{3+} concentration from 20 to 40 mol% resulted in a remarkably large range of lifetimes. By using this approach we have been able to tune the averaged the plateau moment of τ^2-1 to τ^2-9 (see in Figure 5.11b) from 200 μs to 700 μs. The decay time and rising time statistics are summarised in Figure 5.11c and d, which prolong from 200μs to 1400μs, and 60μs to 210μs, respectively. The averaged lifetime fingerprints of five batches of Nd^{3+}-Yb^{3+}-Er^{3+} doped UCNPs in Figure 5.11e show the plateau moment shifts from 400 μs to 1100 μs. The decay time the and rising time statistics in Figure 5.11f and g prolong from 1200μs to 2200μs, and 140μs to 420μs, respectively. Though some detectable variations of the lifetime curves from dot to dot due to the illumination heterogeneity of wide-field imaging method and subsequently induced intensity variations, the arbitrary tunability is clear. The histogram in Figure 5.11c helped us realize at least six completely separate lifetime channels in the blue band of Tm^{3+} emission, while there are two sets of channels which are almost overlapped, such as τ^2-8 and τ^2-9, which is difficult to

separate them through simply decay time and rising time statistics. The significantly prolonged rising time, together with their exceptionally long decay time, make these τ^2-dots nanoparticles display a unique optical fingerprint for each different batch of controlled synthesis, as shown in Figure 5.11a.

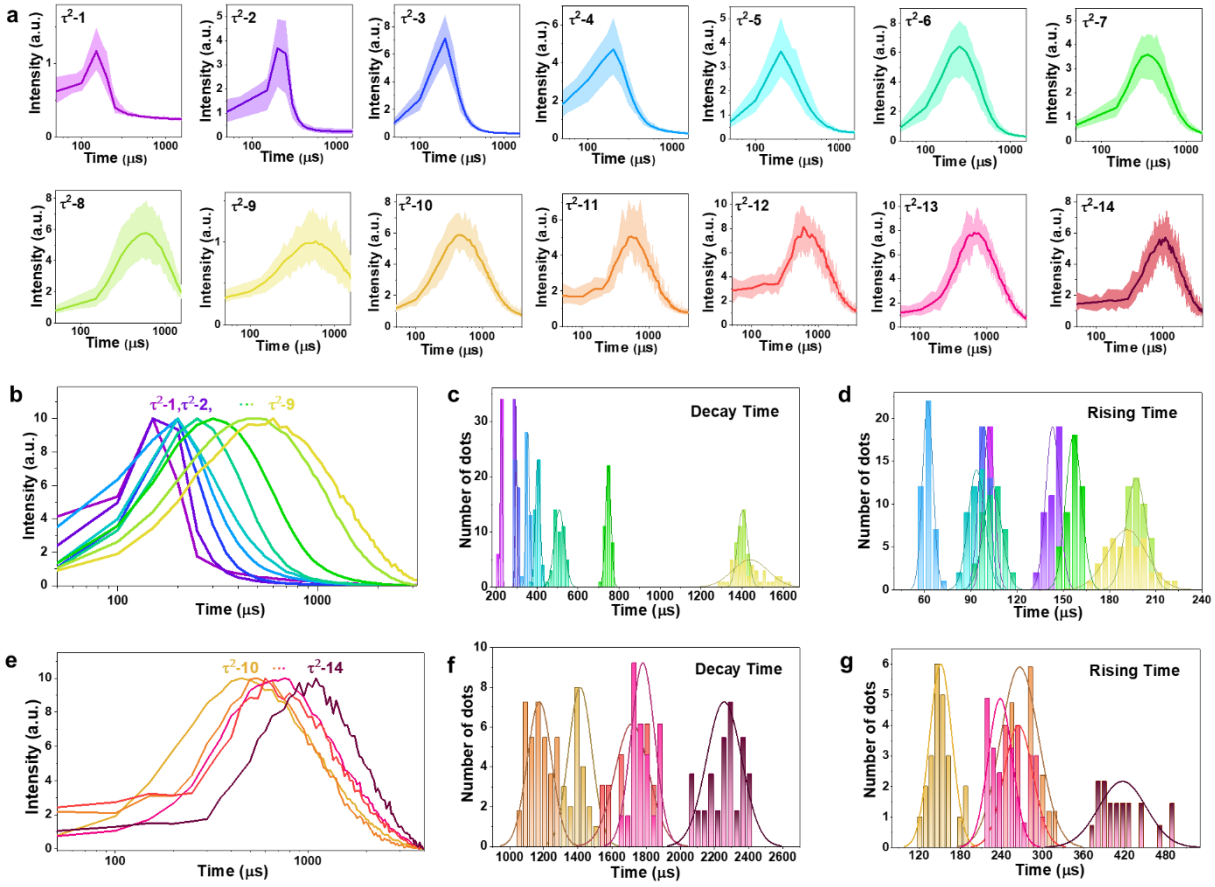

Figure 5.11 Time-domain optical signature control through materials engineering. (a) Lifetime curve statistics from 14 batches of single τ^2-Dots corresponding to Yb^{3+}-Tm^{3+} core-inert shell nanocrystals (τ^2-1 to τ^2-9) and Yb^{3+}, Nd^{3+}, Er^{3+} core three-layer shells UCNPs (τ^2-10 to τ^2-14). Shaded areas cover the lifetime curves from more than 20 single dots for each type of τ^2-Dots. The solid colourful lines represent the averaged lifetime curves for each type of τ^2-Dots. **(b) and (e)** Intensity normalized display of averaged single nanoparticle lifetime fingerprints of τ^2-1 to τ^2-9 and τ^2-10 to τ^2-14, respectively. **(c) and (d)** The decay time and rising time statistics of τ^2-1 to τ^2-9. **(f) and (g)** The decay time and rising time statistics of τ^2-10 to τ^2-14.

Through the distribution statistics (Figure 5.11), we find that most of the τ^2-Dots have their τ_D (Decay indicator) values distributed uniformly with small CV (<10%, Fig.5.12) and a small degree of overlap between each population, which is favourable for the decoding process.

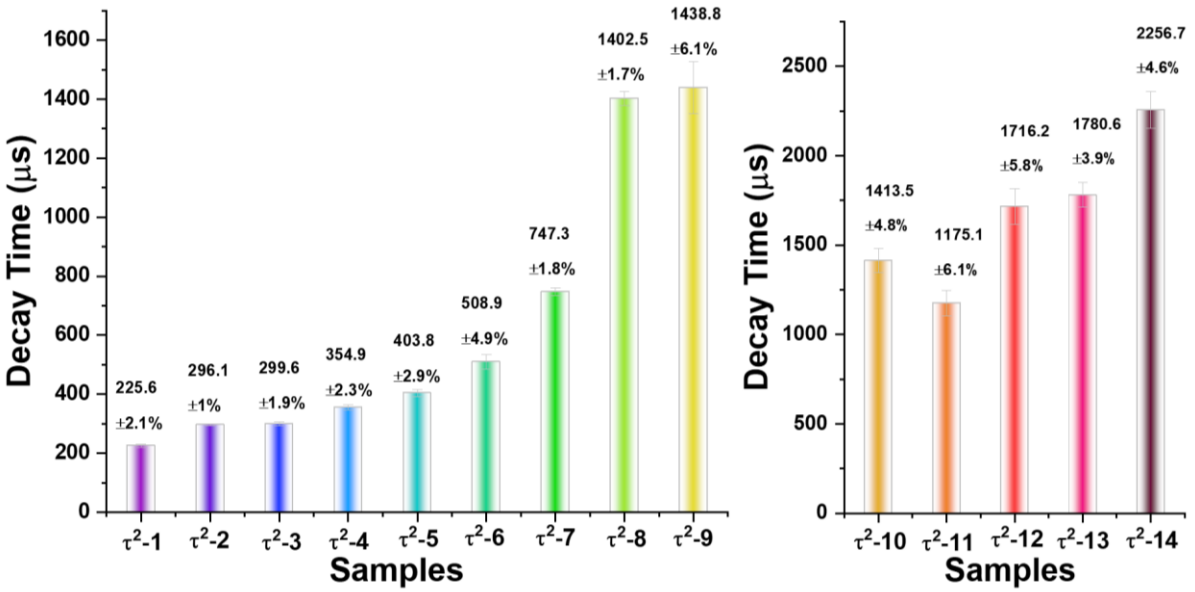

Figure 5.12. The decay time histograms of τ^2-Dots. The numeral beside each histogram is the mean decay time ± decay time CV under wide-field microscopy. The lifetime imaging sequences were acquired under the 808 nm laser excitation pulse of 0-200 μs.

5.4.3 Deep learning aided single nanoparticles classification

Single nanoparticles under a wide-field illumination microscope may only generate a limited amount of photons within each 50 μs time-gated collection window, and their detectable lifetime profiles can be as noisy as the ones displayed in Figure 5.13a. This poses a significant challenge to the decoding approach–optically recognizing the signature of every single dot and within the optical diffraction limit. Here we show an opportunity offered by both the controlled growth of highly optically uniform single nanoparticles and subsequent image analysis to obtain their lifetime fingerprints of single dots, which can generate a large set of high-quality data to train the machine in deep learning. We use the sequences of time-dependent frames of images as the source of input for training, in which we first pre-processing the as-collected images by only selecting the imaging data from single nanoparticles. The typical original

images and selected particles of one set of widefield images of τ^2-10 to τ^2-14 samples are shown in Figure 5.13. After screening the single nanoparticles, deep learning was implemented to define the classification boundaries among these ten batches of τ^2-Dots and decode lifetime fingerprints.

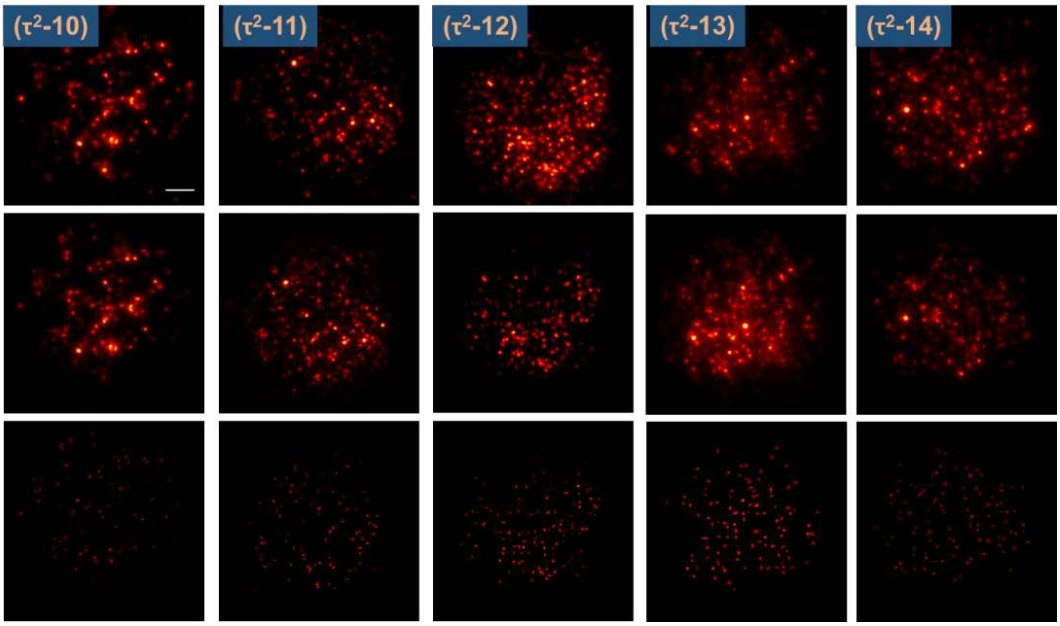

Fig. 5.13 One set of widefield images of τ^2-10 to τ^2-14 samples. a) images under continuous 808 nm laser excitation. b) plateau moment images of time-resolved image sequences of τ^2-dots under the 808 nm laser excitation pulse of 200 μs. c) the corresponding images of b after selecting the single particles. Scale bar: 5 μm.

For each image series, we first select the peak time points frame. Then we find the peak positions of each single nanoparticles. For each peak, a region of interest (ROI) centered on the peak was cropped. In each ROI, the image was segmented with the OTSU threshold and get a binary mask. The watershed segmentation was employed on the binary mask to get the boundaries of each peak. Finally, all the spots were sorted by the peak intensity. After filtering out all the aggregation-induced spots, we obtain the image that only involves single nanoparticles in the images. After that, the imaging sequence is transformed into multiple intensity sequences of single dots in the time-domain (Fig.5.14).

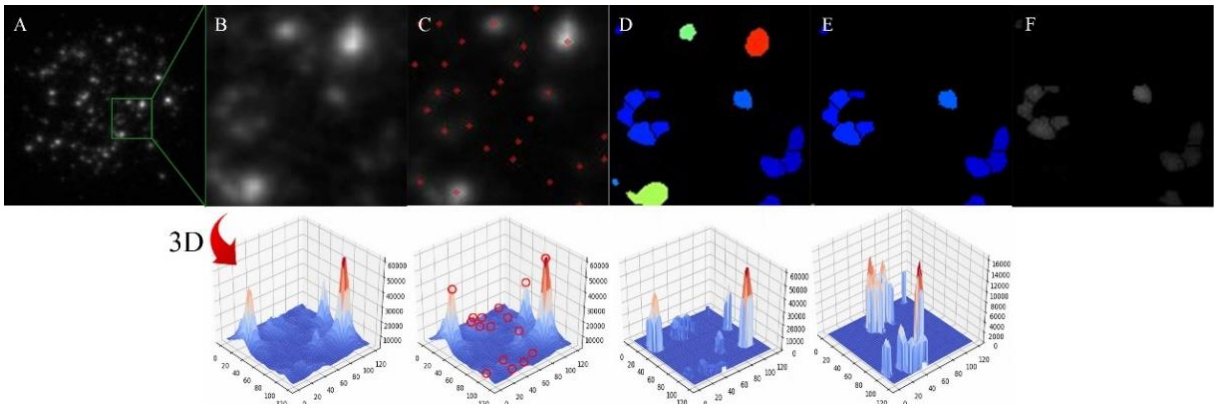

Fig. 5.14 Process of removing overlapped particles from the original image. A. The brightest frame (with maximum mean brightness) in the fluorescence lifetime imaging sequence; B. Local view of image A; C. Image labeled with intensity peaks; D: Segmented mask after local OTSU segmentation and watershed segmentation, the colour of each blob represent peak intensity of nanoparticles; E. Coloured mask after removing blobs whose peaks intensity are outliers. F. Image without overlapped nanoparticles.

To optimize multichannel recognition accuracy, a deep learning algorithm was implemented. the illustration of the flow path of deep learning aided decoding process shown in Figure 5.15. The algorithm is based on an architecture of convolutional neural networks (CNN) including two kinds of networks, the convolutional network and a fully connected network with two layers. We first performed data processing to select the single nanoparticles in the collected images and then apply the wide-field image series of the 14 types of single τ^2-dots with a quantity of about 400 to 800 for training. By taking advantage of the deep learning algorithm, the artificial neural network could extract and recognize the specific fingerprint features of each type of τ^2-dots. Then getting the feedback from recognition accuracies to optimize the CNN and classification boundaries. During training, the output layer neuron whose index corresponds to the input binary number is set to "1" while the other neuron activations are kept at "0". As long as the trained network was built and optimized, we then randomly selected a set of untrained image sequences containing UCNPs to test and obtain their classification accuracies.

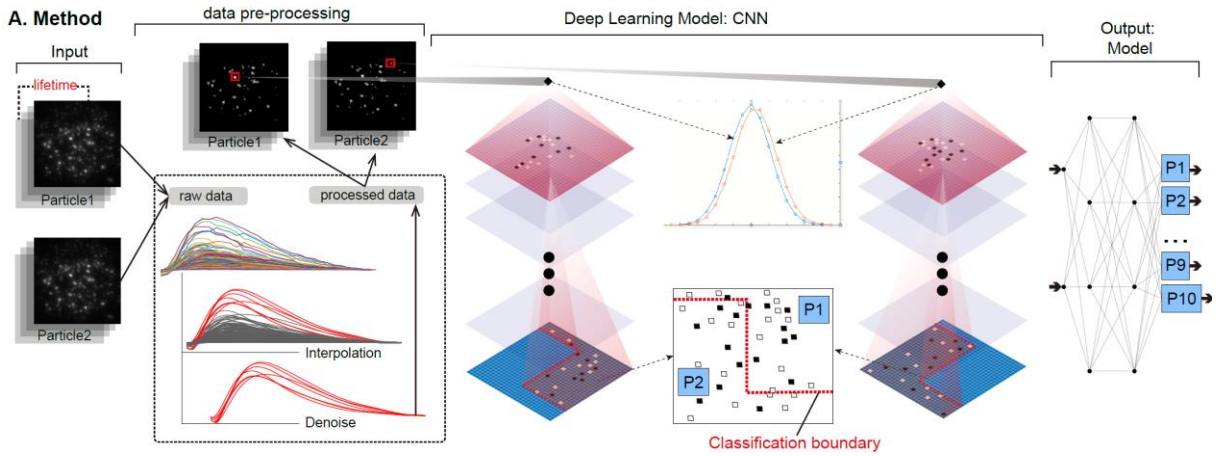

Figure 5.15 Illustration of the flow diagram of the deep learning method aided the decoding process. The time-resolved image sequences of 14 types of single τ^2-dots are inputted to convolutional neural networks (CNN) to extract the optical feature for each type of τ^2-dots to obtain the classification boundaries. Another randomly untrained/unknown seven sets of images for the classification and recognition with acquired boundaries.

As shown in Figure 5.16a, we employed a convolutional network and a fully connected network with two layers (FC1 and FC2) to define the feature coverage and the classification boundaries for each batch of τ^2-dots. The two 1D convolutional layers use the element-wise function $ReLU6(x) = \min(\max(0, x), 6)$. A variant of the stochastic gradient descent (SGD) algorithm ("Adam") is applied to train the parameters in the network through a randomly shuffled batch of size 200. Pytorch deep learning platform was used to train the image series, validate and test the neural network. Before training, the nanoparticles' numbers of each τ^2-dot were counted and the minimum nanoparticle numbers were computed. During training, we randomly pick out a batch of nanoparticles of each τ^2-dot as the training set by the size equaling to 90% of the minimum nanoparticle number. The rest nanoparticles are used as a validation set to adjust CNN architecture. By comparing the recognition accuracy validation set, the two fully connected networks contain two layers with 150 (FC1) neurons in the first layer and 100 (FC1) neurons in the second layer and the element-wise function was employed in each layer. We apply a dropout regularization scheme with 80% keep probability for the fully connected part. The data processing and networks for deep learning were introduced in section 2.7 of chapter 2.

A typical set of visualized results for each τ^2-dot sample was displayed in Figure 5.16b (τ^2-1 to τ^2-9) and Figure 5.16d (τ^2-10 to τ^2-14), in which a small amount of mottled dots represent the error recognition. We then run this experiment of training and validation for another 50 times, each time randomly choose one set of data as the validation target and the other six sets to train the neural networks, which resulted in the statistical distributions of classification accuracy with error bars, displayed in Figure 5.16c and d. We achieved the mean classification accuracies for each τ^2-dot sample with a value large than 90%.

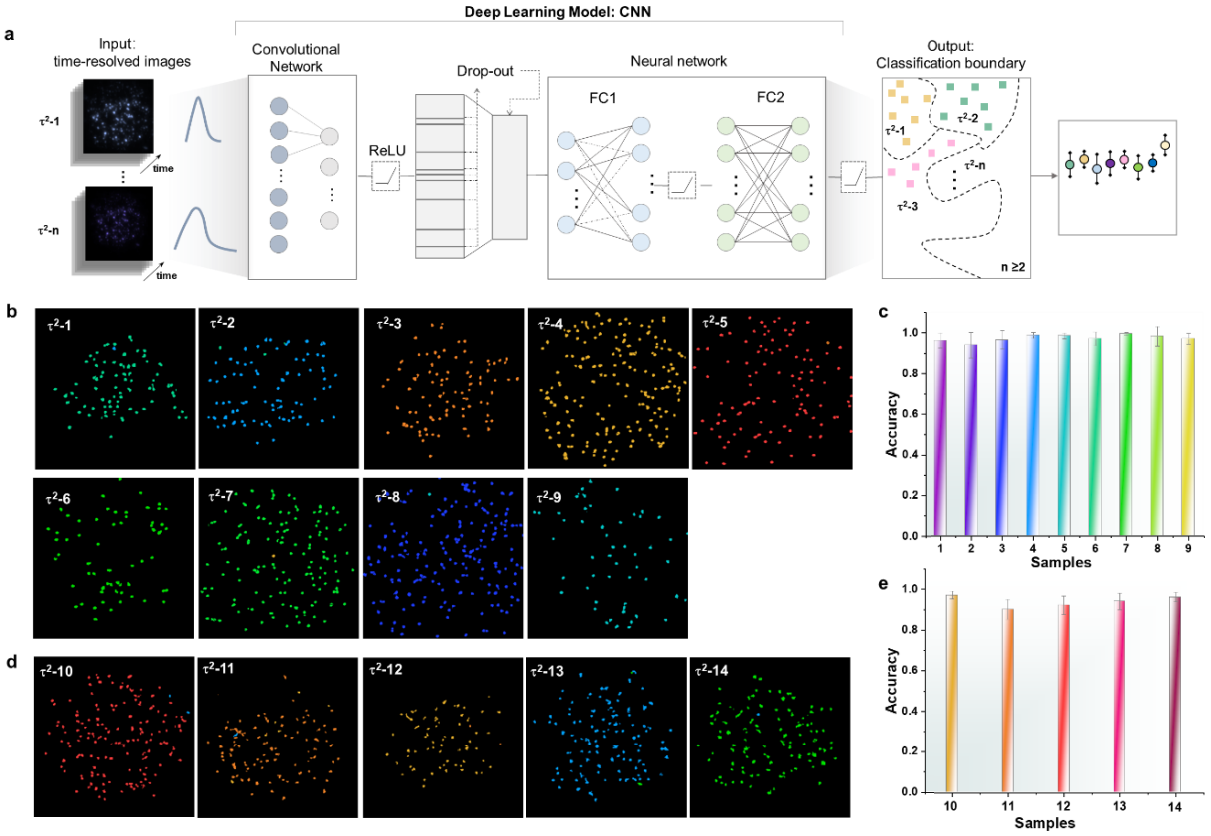

Figure 5.16 Deep learning aided decoding of the fingerprints of single τ^2-Dots. (a) Illustration of the neural network used for the classification task. **(b)** and **(d)** Classification result for the well-trained CNN to recognize the arbitrary seven sets of 'unknown' τ^2-dots, (b) the 9 sets of τ^2-dots of Yb^{3+}-Tm^{3+} core-inert shell nanocrystals (τ^2-1 to τ^2-9) and (d) 5 sets of τ^2-dots of Yb^{3+}, Nd^{3+}, Er^{3+} core three-layer shells UCNPs, respectively. Scale bar: 5 μm. (for visualization purpose, pseudocolour is used to represent each type of single dots) **(c) and (e)** Mean classification accuracy obtained through cross-validation with the database of 6 training sets and 1 validation set for each type of dots. Recognition

accuracies are obtained by comparing recognition results and true categories of tested dots, based on 50 times a random validation test of one set of seven types of dots.

A small amount of mottled dots (e.g., in images of τ^2-2 and τ^2-11) represent the error recognition, which is mainly caused by the samples with similar lifetime curve features (Fig. 5.17). We then run the experiment of training and validation for another 50 times, each time randomly chose one set of data as the validation target and the other six sets to train the neural networks, which resulted in the statistical distributions of classification accuracy with error bars, displayed in Figure 5.16c and 5.16e.

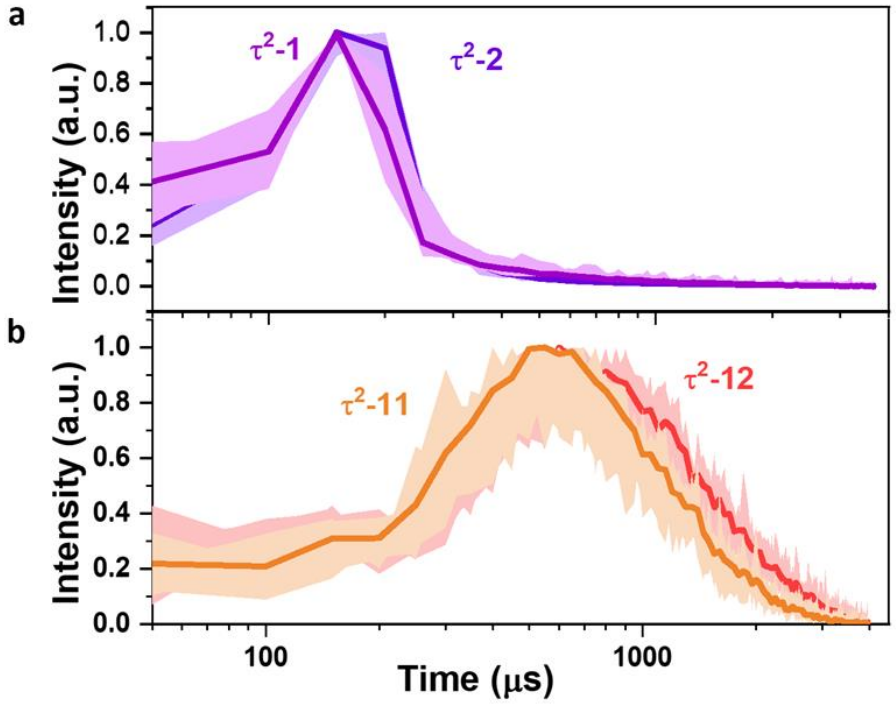

Figure 5.17. τ^2 profile similarity of different samples. (a) Lifetime curves of τ^2-1 and τ^2-2 and **(b)** Lifetime curves of τ^2-11 and τ^2-12, showing the lifetime fingerprints highly overlap with each other.

We achieved the mean classification accuracies for each τ^2-Dot sample, with all the values approaching the unity. The capacity of nanoscale multiplexing can be significantly determined by the brightness of single nanoparticles and the noise background, which explains the relatively broad distributions of τ^2-Dot profiles for the batches of τ^2-Dot samples with relatively low brightness, and therefore less accurate recognition results can be achieved by the machine

intelligence (Fig. 5.18). Nevertheless, this experiment confirms the great potentials for the lifetime profiles of each τ^2-Dot to be used for nanoscale super-capacity optical multiplexing, assisted by deep learning.

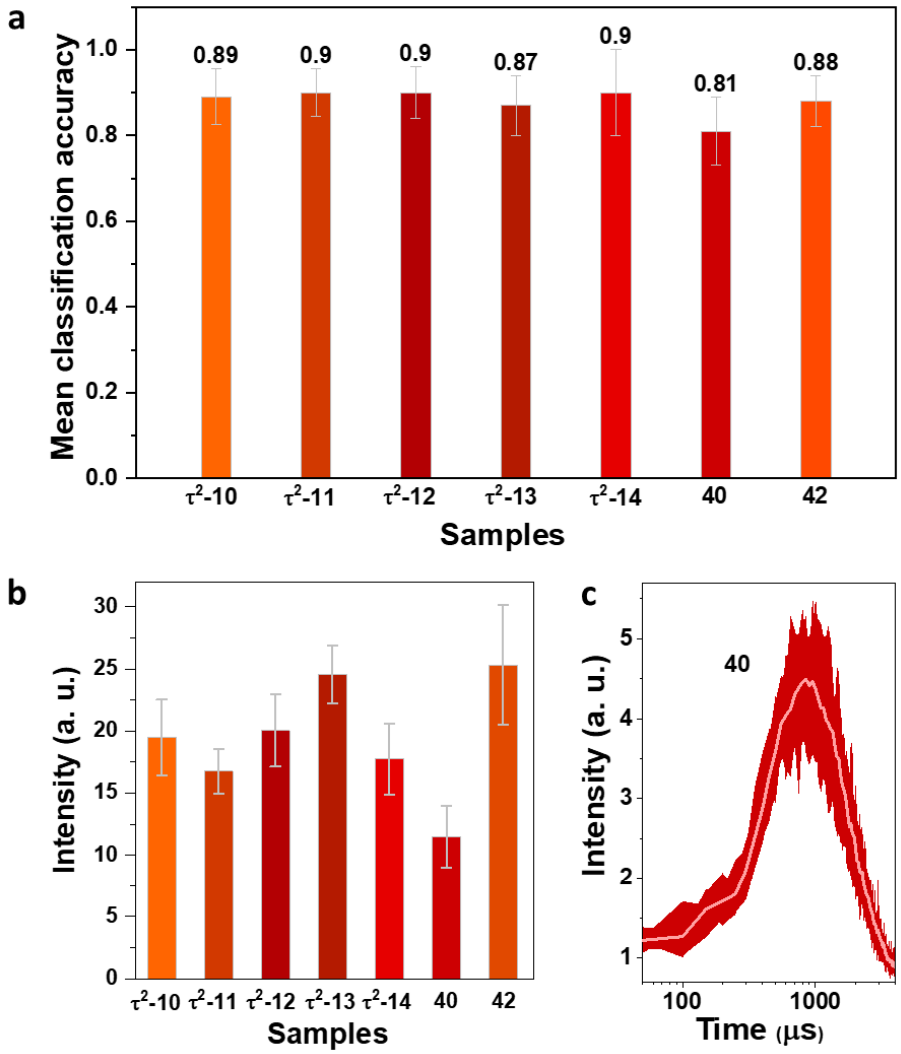

Figure 5.18. (a) Mean classification accuracies of 7 batches of Yb-Nd-Er τ^2-Dots samples after 50 times randomly cross-validation. **(b)** Single nanoparticle intensities under the wide-field microscopy with the same imaging condition of above 7 τ^2-Dots. The averaged brightness was achieved based on counting more than 100 nanoparticles. **(c)** Lifetime curve statistics from more than 20 single nanoparticles of sample 40. When training 7 batches of UCNPs by adding the sample 40 that has relatively weak emission intensity, the classification accuracies of these 7 samples are around 90%. Meanwhile, the classification accuracy of sample 40 is the lowest.

By taking advantage of the τ^2-dots in brightness, photostability, and fine-tuning lifetime, we further demonstrated the super-resolution capacity of τ^2-dots in time-domain through the wide-field super-resolution imaging, i.e.structured illumination microscopy (TR-SIM). By breaking the diffraction-limit restriction to resolve the aggregated particles, the TR-SIM shows advantages to future super-capacity optical multiplexing in decoding throughput and accuracy. Figure 5.19a shows the time-domain dependent intensity evolution of τ^2-dots, which can be detected and integrated to form the lifetime profile of τ^2-dots in the image. The sinusoidal patterns of the laser beam were generated, so the beam loses almost half of the excitation power compared to the conventional Gauss beam, which will challenge the brightness of the τ^2-dots. The pattern angle and phase angle were tuned 9 times' excitation (Figure 5.19b). The partial information outside the diffraction limitation is available under the patterned excitation by optical transfer from the spatial domain to the Fourier domain, as shown in Figure 5.19b. The high-frequency super-resolution information under sinusoidal illumination patterns can be shifted into the diffraction-limited detection passband. So super-resolution images can be reconstructed by shifting and merging the extended frequency spectrum. The TR-SIM image is generated based on the corresponding nine frames, including 3 phase angles in each pattern angle. Figure 5.19c shows the typical TR-SIM and corresponding area imaged by wide-field microscopy in the peak time frame of one kind of τ^2-dot. It shows a higher spatial resolution of SIM and can resolve the aggregated two particles in the wide-field image. Figure 5.19d shows the profile curves from the red selected area in Figure 5.19c, the full width at half maximum (FWHM) reaches about 186 nm under the 808 nm excitation. Then three kinds of τ^2-dots were mixed to demonstrate the potential advantages of TR-SIM for optical multiplexing (Figure 5.19e). The machine learning method also was used to compare the recognition possibility of time-resolved wide-field and TR-SIM imaging. By the deep learning algorithm to identify these three kinds of dots, we can see that the random aggregation of different kinds of τ^2-dots can affect the recognition in wide-field mode. By resolving the particles with the improved lateral resolution, The aggregation-induced bias can be alleviated by TR-SIM.

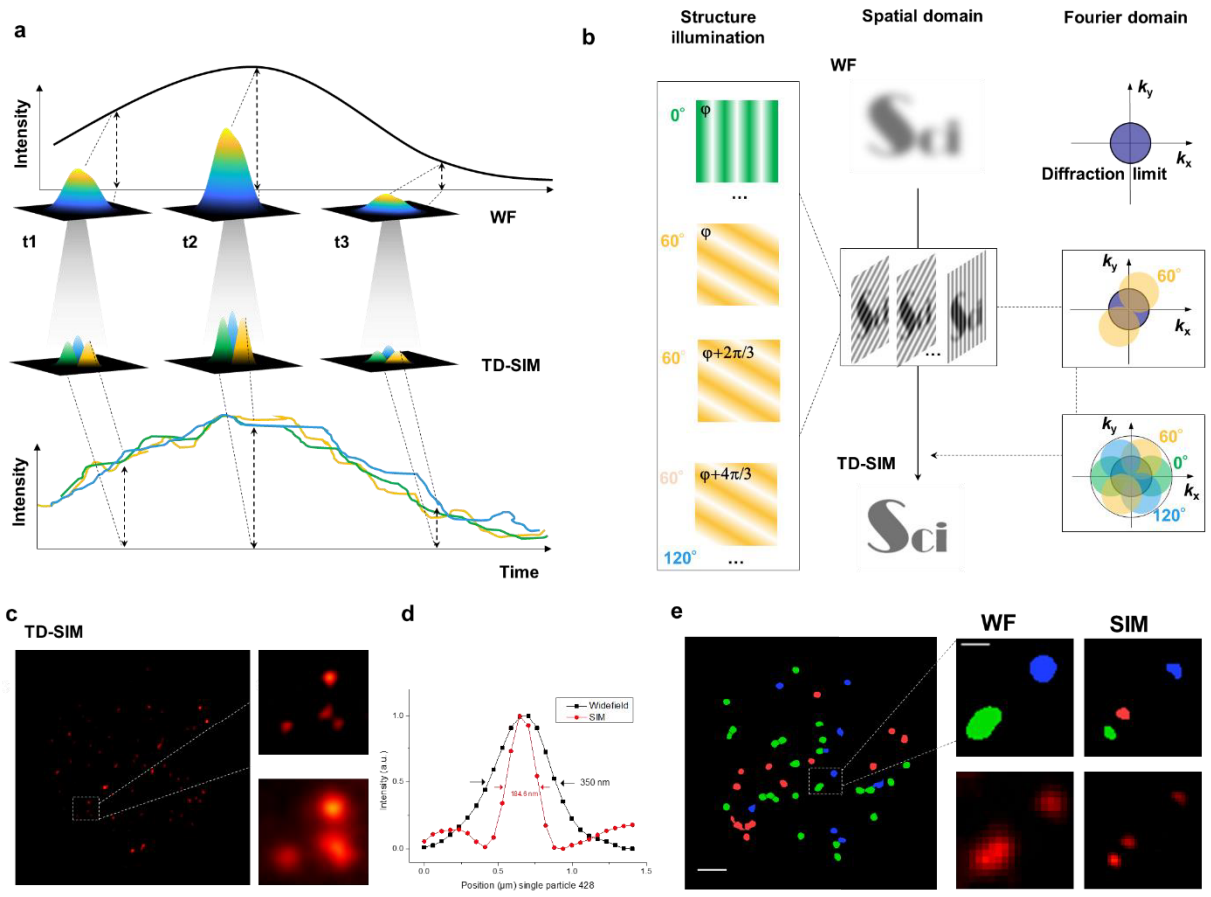

Figure 5.19. Illustration of time-resolved structured illumination microscopy (TR-SIM) for sub-diffraction imaging of τ^2-dots. (a) The schematic diagram of fluorescence lifetime imaging in widefield mode (up) and SIM mode (below). (b) Illustration of the structured illumination microscopy method. 9 kinds of sinusoidal excitation beam patterns with differences in the orientations ($\theta1 = 0°$, $\theta2 = 60°$ and $\theta3 = 120°$) and three different phase shifts ($\varphi1 = 0°$, $\varphi2 = 120°$ and $\varphi3 = 240°$) are used. (c) The typical TR-SIM and conventional wide-field images in the peak time frame of one kind of τ^2-dot. (d) Intensity curves of the red selected area in (c). (d) The typical recognition result of three kinds of τ^2-dots mixtures. Scale bar: 2μm. Recognition image (up) and wide-field/TR-SIM imaging (below) shows the selected small area. Scale bar: 500nm.

Through a wide-field microscope, and compared with the control groups, we concluded that each τ^2-dot were highly specific. Moreover, as shown in Figure 5.20, we demonstrate that the wide-field images of τ^2-dots with different lifetime profiles can be super-resolved using our latest development of upconversion structure-illumination microscopy with a resolution of 184.8 nm.

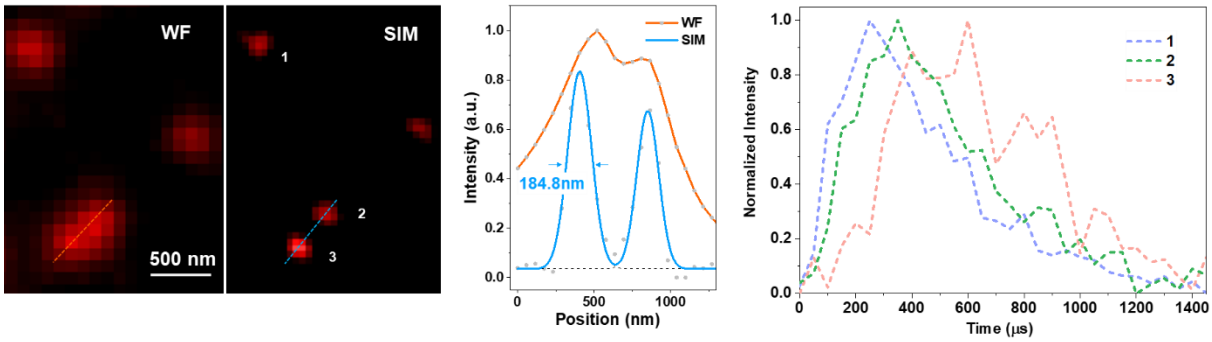

Figure 5.20. Three types Yb-Nd-Er series of UCNPs resolved by upconversion structure illumination microscopy.

5.4.4 DNA conjugation with Yb^{3+}-Tm^{3+} doped single nanoparticles

Low-abundant specific DNA molecules detection is increasingly important to enable in-depth studies and medical diagnosis of genetic diseases. Optical biosensors for DNA detection, such as fluorescent colour and intensity ratio have been widely used. However, detection sensitivity is still limited due to the background noise and emission band overlap. Creating a new dimension is an emerged way for DNA molecules detection. In this chapter, we demonstrated the potential DNA detection by these Yb^{3+}-Tm^{3+} doped core-shell nanoparticles. Five kinds of selected UCNPs were conjugated with five specific DNA molecules respectively and show good specific binding effect. Firstly, surface modification of Yb^{3+}-Tm^{3+} doped core-shell UCNPs to transfer to hydrophilic and biocompatible was performed via ligand exchange with the block copolymer (Figure 5.21a).

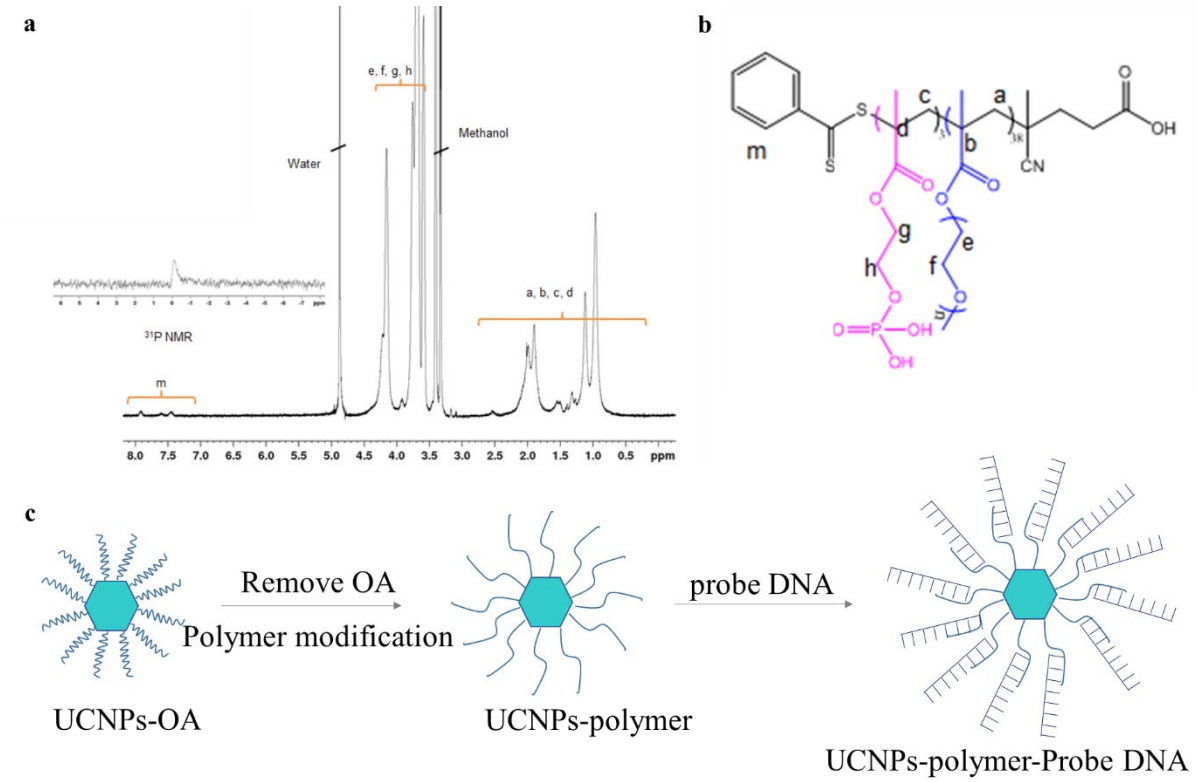

Figure 5.21 (a) ^{1}H NMR and ^{31}P spectra and (b) structure of purified $PEGMEMA_{38}$-b-$EGMP_3$ (c) The illustration of surface modification of Yb^{3+}-Tm^{3+} doped core-shell UCNPS by ligand exchange

Generally, there are two necessary groups including in the ligand, reacting groups (phosphate groups) and the functional groups (carboxyl group), as shown in Figure 5.22b. The binding strength of the reacting groups is the key element for the replacement of the OA molecules on the surface. Moreover, functional groups on the surface of UCNPs are also needed for further bioconjugation with DNA. The general surface modification approach process is illustrated in Figure 5.21c. After obtaining polymer-coated UCNPs with carboxy group, conjugation of five kinds of probe DNAs onto five batches of carboxyl-UCNPs was performed according to the protocol of carbodiimide chemistry to obtain Probe-DNA-UCNPs. Then five kinds of specific capture DNA sequences were conjugated on to the surface of five corresponding carboxyl-UCNPs in 96 plate wells, shown in Figure 5.22 (see section 2.6 of chapter 2).

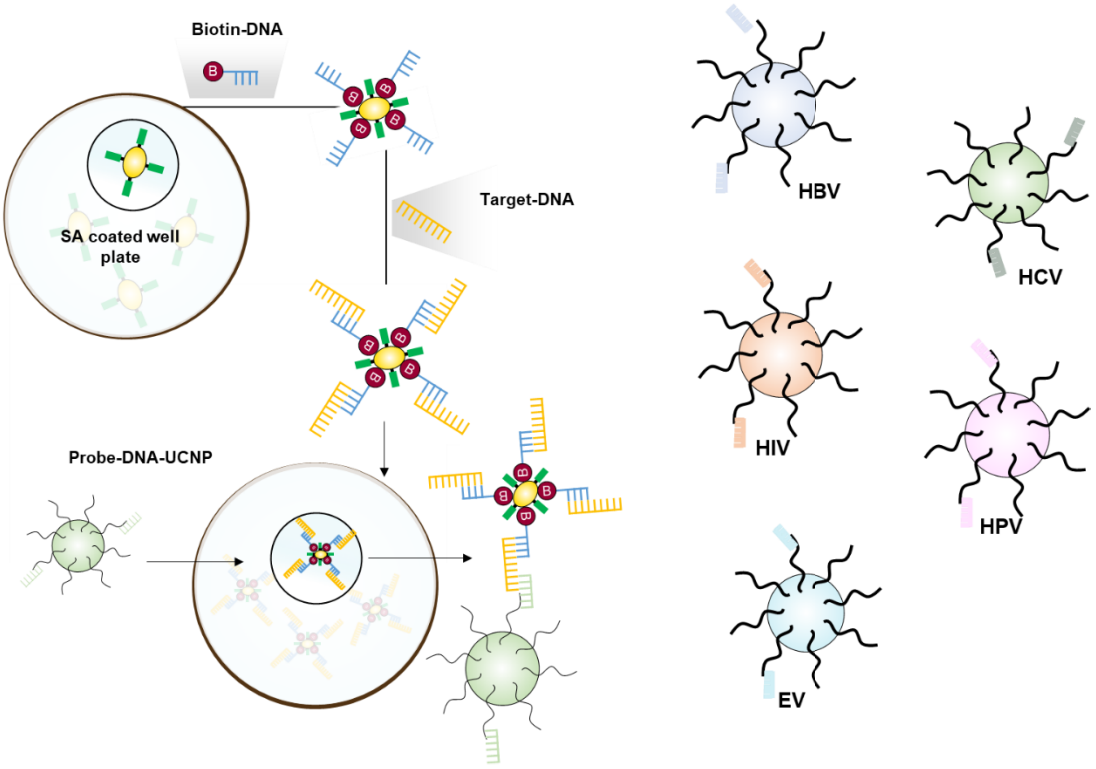

Figure 5.22 The flow diagram of DNA molecules assay based on single upconversion nanoparticles.

We design two sets of experiments for each kind of DNA assay (Figure 5.23), the up group refers to the experimental group in the presence of target DNA and the below group refers to the control group in the absence of target DNA. This is done to ensure the Yb^{3+}-Tm^{3+} doped core-shell UCNPS was conjugated with capture NDA through the specific binding effect. We use the 976 nm laser to excite the nanoparticles conjugated on the surface of plate wells. There are few particles in the control wells, which means the reaction in the absence of target DNAs was nearly blank and no non-specific binding. Comparing with the control experiment, the experimental group when adding the target DNA shows well specific binding effect. The results displayed in Figure 5.23 suggest its potential for low-abundant DNA assay by these ten sets of Yb^{3+}-Tm^{3+} doped core-shell nanoparticles.

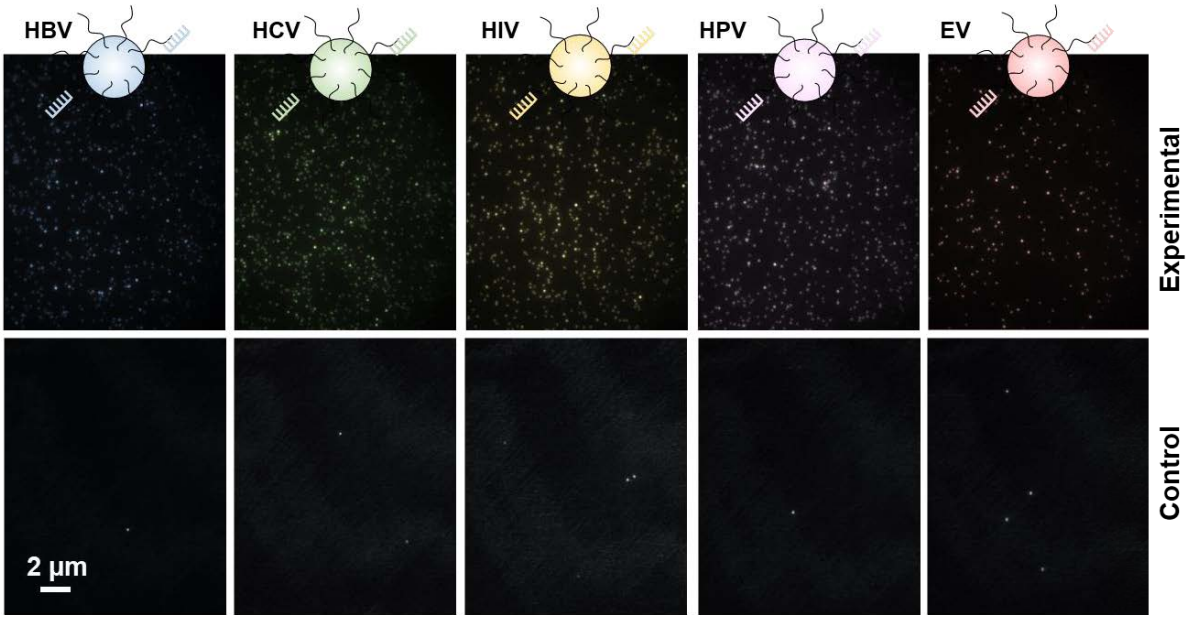

Figure 5.23 Specificity of five types of Yb^{3+}-Tm^{3+} doped core-shell nanoparticles conjugated with DNA molecules. Below group refers to the control group in the absence of target DNA and up group refers to the experimental group in the presence of target DNA.

5.5 Conclusion

In summary, we prepared 14 batches of UCNPs including Yb^{3+}-Tm^{3+} doped and Yb^{3+}, Nd^{3+}, Er^{3+} doped UCNPs. The core-shell design and controlled synthesis of bright and optically uniform single nanoparticles provide a significant opportunity for the super-capacity optical multiplexing. We control the energy migration process and arbitrarily tune the rising time, decay time, and plateau moment, which can assign each type of the nanoparticles with a unique time-domain optical fingerprint. Through deep learning, the large amount of optical data from different batches of UCNPs allows the classification of each single UCNP for the untapped opportunity to decode these nanoscale lifetime barcodes. The classification capability of deep learning allows all 14 kinds of UCNPs to achieve accuracies of over 90%. The implementation of optical super-resolution microscopy techniques through the use of time-resolved SIM allows the high-throughput decoding of these nanoscale super-multiplexed dots to be decodable beyond the diffraction limit. Further expanding the dynamic range, e.g., by following recently reported strategies in the infrared region[35], will allow a larger number of lifetime codes to be created. We also demonstrate the potential of single nanoparticles for DNA

assay. This work further suggests the future synthesis of other types of uniform nanoparticles with diverse and tunable optical signatures in multiple optical dimensions, e.g. spectrum, lifetime, and intensity, to expand super-capacity optical multiplexing. Assignments of these highly uniform and bright luminescent carriers with unique and distinguishable optical signatures will enable high-throughput biomolecular discoveries and data storage.

5.6 Reference

(1) Gupta, R. K. Linear and Nonlinear Frequency-Division Multiplexing. *IEEE Trans. Inf. Theory* **2019**, *66* (1), 478–495.

(2) Gong, L.; Zhao, Q.; Zhang, H.; Hu, X. Y.; Huang, K.; Yang, J. M.; Li, Y. M. Optical Orbital-Angular-Momentum-Multiplexed Data Transmission under High Scattering. *Light Sci. Appl.* **2019**, *8* (1), 27.

(3) Zhou, J.; Leaño, J. L.; Liu, Z.; Jin, D.; Wong, K. L.; Liu, R. S.; Bünzli, J. C. G. Impact of Lanthanide Nanomaterials on Photonic Devices and Smart Applications. *Small* **2018**, *14* (40), 1–29.

(4) Zhang, X.; Yang, S.; Zhou, H.; Liang, J.; Liu, H.; Xia, H.; Zhu, X.; Jiang, Y.; Zhang, Q.; Hu, W.; et al. Perovskite–Erbium Silicate Nanosheet Hybrid Waveguide Photodetectors at the Near-Infrared Telecommunication Band. *Adv. Mater.* **2017**, *29* (21), 1604431.

(5) Ma, M.; Li, Z.; Liu, W.; Tang, C.; Li, Z.; Cheng, H.; Li, J.; Chen, S.; Tian, J. Optical Information Multiplexing with Nonlinear Coding Metasurfaces. *Laser Photonics Rev.* **2019**, *13* (7), 1–9.

(6) Ren, H.; Li, X.; Zhang, Q.; Gu, M. On-Chip Noninterference Angular Momentum Multiplexing of Broadband Light. *Science.* **2016**, *352* (6287), 805–809.

(7) Yang, T. S.; Zhou, Z. Q.; Hua, Y. L.; Liu, X.; Li, Z. F.; Li, P. Y.; Ma, Y.; Liu, C.; Liang, P. J.; Li, X.; et al. Multiplexed Storage and Real-Time Manipulation Based on a Multiple Degree-of-Freedom Quantum Memory. *Nat. Commun.* **2018**, *9* (1), 3407.

(8) Zhang, Q.; Xia, Z.; Cheng, Y. B.; Gu, M. High-Capacity Optical Long Data Memory Based on Enhanced Young's Modulus in Nanoplasmonic Hybrid Glass Composites. *Nat. Commun.* **2018**, *9* (1), 1–6.

(9) Zhou, J.; Wen, S.; Liao, J.; Clarke, C.; Tawfik, S. A.; Ren, W.; Mi, C.; Wang, F.; Jin, D. Activation of the Surface Dark-Layer to Enhance Upconversion in a Thermal Field. *Nat. Photonics* **2018**, *12* (3), 154.

(10) Zhao, J.; Jin, D.; Schartner, E. P.; Lu, Y.; Liu, Y.; Zvyagin, A. V.; Zhang, L.; Dawes, J. M.; Xi, P.; Piper, J. A.; et al. Single-Nanocrystal Sensitivity Achieved by Enhanced Upconversion Luminescence. *Nat. Nanotechnol.* **2013**, *8* (10), 729–734.

(11) Islam, M. N.; Alam, M. S.; Karim, M. A. Optical Security System Employing

Quadrature Multiplexing. *Opt. Eng.* **2008**, *47* (4), 48201.

(12) Liao, Z.; Zhang, Y.; Li, Y.; Miao, Y.; Gao, S.; Lin, F.; Deng, Y.; Geng, L. Microfluidic Chip Coupled with Optical Biosensors for Simultaneous Detection of Multiple Analytes: A Review. *Biosens. Bioelectron.* **2019**, *126*, 697–706.

(13) Li, C.-Y.; Kang, Y.-F.; Qi, C.-B.; Zheng, B.; Zheng, M.-Q.; Song, C.-Y.; Guo, Z.-Z.; Lin, Y.; Pang, D.-W.; Tang, H.-W. Breaking Through Bead-Supported Assay: Integration of Optical Tweezers Assisted Fluorescence Imaging and Luminescence Confined Upconversion Nanoparticles Triggered Luminescent Resonance Energy Transfer (LRET). *Anal. Chem.* **2019**, *91* (12), 7950–7957.

(14) He, H.; Liu, B.; Wen, S.; Liao, J.; Lin, G.; Zhou, J.; Jin, D. Quantitative Lateral Flow Strip Sensor Using Highly Doped Upconversion Nanoparticles. *Anal. Chem.* **2018**, *90* (21), 12356–12360.

(15) Caen, O.; Schütz, S.; Jammalamadaka, M. S. S.; Vrignon, J.; Nizard, P.; Schneider, T. M.; Baret, J. C.; Taly, V. High-Throughput Multiplexed Fluorescence-Activated Droplet Sorting. *Microsystems Nanoeng.* **2018**, *4* (1), 33.

(16) Han, M.; Gao, X.; Su, J. Z.; Nie, S. Quantum-Dot-Tagged Microbeads for Multiplexed Optical Coding of Biomolecules. *Nat. Biotechnol.* **2001**, *19* (7), 631–635.

(17) Um, S. H.; Lee, J. B.; Kwon, S. Y.; Li, Y.; Luo, D. Dendrimer-like DNA-Based Fluorescence Nanobarcodes. *Nat. Protoc.* **2006**, *1* (2), 995–1000.

(18) Li, Y.; Cu, Y. T. H.; Luo, D. Multiplexed Detection of Pathogen DNA with DNA-Based Fluorescence Nanobarcodes. *Nat. Biotechnol.* **2005**, *23* (7), 885–889.

(19) Zhou, W.; Li, D.; Xiong, C.; Yuan, R.; Xiang, Y. Multicolour-Encoded Reconfigurable DNA Nanostructures Enable Multiplexed Sensing of Intracellular MicroRNAs in Living Cells. *ACS Appl. Mater. Interfaces* **2016**, *8* (21), 13303–13308.

(20) Zhao, Y.; Shum, H. C.; Chen, H.; Adams, L. L. A.; Gu, Z.; Weitz, D. A. Microfluidic Generation of Multifunctional Quantum Dot Barcode Particles. *J. Am. Chem. Soc.* **2011**, *133* (23), 8790–8793.

(21) Tian, Z.; Zhang, X.; Li, D.; Zhou, D.; Jing, P.; Shen, D.; Qu, S.; Zboril, R.; Rogach, A. L. Full-Colour Inorganic Carbon Dot Phosphors for White-Light-Emitting Diodes. *Adv. Opt. Mater.* **2017**, *5* (19), 1700416.

(22) Yan, Y.; Xie, G.; Lavery, M. P. J.; Huang, H.; Ahmed, N.; Bao, C.; Ren, Y.; Cao, Y.; Li, L.; Zhao, Z.; et al. High-Capacity Millimetre-Wave Communications with Orbital Angular Momentum Multiplexing. *Nat. Commun.* **2014**, *5*, 1–9.

(23) Yang, J.; Dave, S. R.; Gao, X. Quantum Dot Nanobarcodes: Epitaxial Assembly of Nanoparticle-Polymer Complexes in Homogeneous Solution. *J. Am. Chem. Soc.* **2008**, *130* (15), 5286–5292.

(24) Hu, L.; Fan, Y.; Liu, L.; Li, X.; Zhao, B.; Wang, R.; Wang, P.; El-Toni, A. M.; Zhang, F. Orthogonal Multiplexed Luminescence Encoding with Near-Infrared Rechargeable

Upconverting Persistent Luminescence Composites. *Adv. Opt. Mater.* **2017**, *5* (22), 1–9.

(25) Gorris, H. H.; Wolfbeis, O. S. Photon-upconverting Nanoparticles for Optical Encoding and Multiplexing of Cells, Biomolecules, and Microspheres. *Angew. Chemie Int. Ed.* **2013**, *52* (13), 3584–3600.

(26) Zhang, F.; Shi, Q.; Zhang, Y.; Shi, Y.; Ding, K.; Zhao, D.; Stucky, G. D. Fluorescence Upconversion Microbarcodes for Multiplexed Biological Detection: Nucleic Acid Encoding. *Adv. Mater.* **2011**, *23* (33), 3775–3779.

(27) Shikha, S.; Zheng, X.; Zhang, Y. Upconversion Nanoparticles-Encoded Hydrogel Microbeads-Based Multiplexed Protein Detection. *Nano-Micro Lett.* **2018**, *10* (2), 1–16.

(28) Lu, Y.; Zhao, J.; Zhang, R.; Liu, Y.; Liu, D.; Goldys, E. M.; Yang, X.; Xi, P.; Sunna, A.; Lu, J.; et al. Tunable Lifetime Multiplexing Using Luminescent Nanocrystals. *Nat. Photonics* **2014**, *8* (1), 32–36.

(29) Zhang, Y.; Zhang, L.; Deng, R.; Tian, J.; Zong, Y.; Jin, D.; Liu, X. Multicolour Barcoding in a Single Upconversion Crystal. *J. Am. Chem. Soc.* **2014**, *136* (13), 4893–4896.

(30) Zang, X.; Dong, F.; Yue, F.; Zhang, C.; Xu, L.; Song, Z.; Chen, M.; Chen, P. Y.; Buller, G. S.; Zhu, Y.; et al. Polarization Encoded Colour Image Embedded in a Dielectric Metasurface. *Adv. Mater.* **2018**, *30* (21), 1707499.

(31) Zhou, J.; Chen, G.; Wu, E.; Bi, G.; Wu, B.; Teng, Y.; Zhou, S.; Qiu, J. Ultrasensitive Polarized Up-Conversion of Tm3+-Yb3+ Doped β-NaYF4 Single Nanorod. *Nano Lett.* **2013**, *13* (5), 2241–2246.

(32) Jiang, K.; Sun, S.; Zhang, L.; Lu, Y.; Wu, A.; Cai, C.; Lin, H. Red, Green, and Blue Luminescence by Carbon Dots: Full-colour Emission Tuning and Multicolour Cellular Imaging. *Angew. Chemie Int. Ed.* **2015**, *54* (18), 5360–5363.

(33) Johnson, N. J. J.; Korinek, A.; Dong, C.; Van Veggel, F. C. J. M. Self-Focusing by Ostwald Ripening: A Strategy for Layer-by-Layer Epitaxial Growth on Upconverting Nanocrystals. *J. Am. Chem. Soc.* **2012**, *134* (27), 11068–11071.

(34) Zuo, J.; Sun, D.; Tu, L.; Wu, Y.; Cao, Y.; Xue, B.; Zhang, Y.; Chang, Y.; Liu, X.; Kong, X.; et al. Precisely Tailoring Upconversion Dynamics via Energy Migration in Core-Shell Nanostructures. *Angew. Chemie* **2018**, *130* (12), 3108–3112.

(35) Fan, Y.; Wang, P.; Lu, Y.; Wang, R.; Zhou, L.; Zheng, X.; Li, X.; Piper, J. A.; Zhang, F. Lifetime-Engineered NIR-II Nanoparticles Unlock Multiplexed in Vivo Imaging. *Nat. Nanotechnol.* **2018**, *13* (10), 941–946.

Chapter 6 Conclusion and Perspective

6.1 Conclusion

Various luminescence-based applications of luminescent materials are mostly based on micro-sized information carriers. Such as Luminex xMAP use the fluorescent-dye beads encoded by fluorescent intensity and colour. The fluorescent-dye coded beads are volatile and vulnerable to light. The size of macroscopic beads becomes a limiting factor for certain applications such as quantitative labeling and detection of small amounts of biomolecules.

Despite researchers have developed various strategies for fine-tuning the multicolor luminescence of luminescent materials, there remain several challenges associated with the conventional fluorescent color-coding in biomedical applications, such as limited encoding ability and false decoding because of spectral overlap. Moreover, the spectrum encoding in macroscopic carriers (micro-beads) is unable to meet the requirements of bioanalysis at the nanoscale and in the complicated analytes.

This thesis aims to tackle the challenge for high-throughput detection and quantification of the low concentration of biomarkers, e.g. below 100 copies of viral RNA molecules or cancer biomolecules. Our new UCNPs-based multiplexed digital assays technology, based on a new method to encode and decode the high dimensional fingerprints of the single-molecule probes. In this thesis, I reported on optical fingerprints (especially the lifetime property) of Nd^{3+}-Yb^{3+}-Er^{3+}/Tm^{3+} doped core-multi-shell nanoparticles under 808 nm excitation and Yb^{3+}-Tm^{3+} doped core-shell nanoparticles under 976 nm excitation. I focus on exploring their significant potential for super-capacity optical multiplexing. The development of nanocarriers for multiplexing is very promising for information technologies, high-throughput clinical diagnostics, multichannel bioimaging, etc. I create a set of time-resolved emission profiles over a large dynamic range in nanoscale under the pulse laser excitation. Er^{3+} and Tm^{3+} doped nanocrystals create multiplexed codes in spectral and lifetime orthogonal dimensions to increase encoding capacity. To realize the high-throughput detection of optical signals from single nanoparticles, I explore using different detection instruments, from the confocal microscope to the wide-field microscope system. I further implement a deep-learning algorithm

to coordinate with wide-field images for more accurate decoding lifetime fingerprints of single nanoparticles, which opens new opportunities of nanocarriers in the time domain as a new dimension for display, data storage, anti-counterfeiting, and high-throughput optical multiplexing.

The successful outcomes reported in this thesis are listed next:

(1) I demonstrated the duration for blue upconversion emissions in Nd^{3+}-Yb^{3+}-Tm^{3+} doped core-shell-shell UCNPs. The key to effectively manage the energy transfers was the core-shell-shell design with rational doping of the ions and isolation of surface molecules/defects. By engineering the interfacial energy migration and cascade energy transfer network in the core-shell structure, the peak time of excited-state populations can be fine-tuning and significantly extended from 100 μs to 900 μs after switching off the pulse laser.

(2) A series of Yb^{3+}, Nd^{3+}, Er^{3+}-doped β-$NaYF_4$ UCNPs with the core three-layer shell structure and Yb^{3+}-Tm^{3+} core-inert shell UCNPs were synthesized, which can form a spectral and lifetime orthogonal multiplexing under 808 nm and 976 nm excitation. To encoding information carriers from the macroscopic level to the nanoscale, the optical properties of single nanoparticles were investigated under the confocal microscope system. I demonstrated that a library of these single UCNPs with unique and tailored lifetime profiles show great potential for super-capacity multiplexing.

(3) I further reported that the brightness of Nd^{3+}-Yb^{3+}-Er^{3+} doped nanoparticles displays a pair of unusual double helix shapes as the function of power densities of 976 nm and 808 nm excitations. I systematically investigated the upconversion intensity, spectrum and lifetime properties at a single nanoparticle level under the confocal microscope system, which reveals that the dynamic roles of Nd^{3+} ions in the tri-doped nanosystem with electron population pathways are power dependent.

(4) To further achieve high-throughput multiplexing, the lifetime profiles of single nanoparticles were detected under a wide-field microscope system. I demonstrated that the nanoparticles show a unique lifetime signature under wide-field systems upon 976 nm (blue

emission of Yb^{3+}-Tm^{3+} system) and (green and red emission Yb^{3+}-Nd^{3+}-Er^{3+} system) 808 nm excitation.

(5) I further implemented a deep-learning algorithm to coordinate with wide-field images for more accurate decoding lifetime fingerprints of single nanoparticles. By training the machine with 14 batches of single nanoparticle types, deep learning can intelligently define a territory for each type of single nanoparticles, wide-field imaging-based optical multiplexing of 14 channels with decoding accuracies larger than 90% for each channel. The orthogonal spectral and lifetime dimension multiplexing provides a new channel for multiplexing digital assays, as well as opens a new horizon toward handling the growing amount of information content, disease source, and security risk in modern society.

(6) I demonstrated time-domain wide-field super-resolution imaging based on structured illumination microscopy, which shows benefit to future super-capacity optical multiplexing in decoding throughput and accuracy by breaking the diffraction-limit restriction to resolve the aggregated nanoparticles.

(7) I demonstrated the potential for DNA detection by these Yb^{3+}-Tm^{3+} doped core-shell nanoparticles. Five kinds of selected UCNPs were conjugated with five specific DNA molecules respectively and show good specific binding effect. The lifetime property of nanoparticles provides a new potential way for multiplexing assay of DNA.

It fills the gap by providing remarkable advantages, the technology will be undertaken for solving key technological issues including:

- to arbitrarily tune the τ^2-type lifetime profiles of UCNPs and create a library of high-brightness single nanoparticle-based τ^2-Dots with distinctive optical signatures.
- to functionalize each type of τ^2-Dots to one of the protein-specific antibody molecules or DNA/RNA strands from cancer/virus to form a stable structure with minimal non-specific binding and cross-talks.
- to achieve high-throughput and quantitative detection of low abundance disease biomarkers and different types of protein complexes.

- to engineer the wide-field time-resolved imaging techniques for high-throughput single-particle time-domain optical fingerprint detection.
- to develop the deep-learning algorithm and demonstrate the new way for decoding the super-capacity hidden within the single nanoparticle.

6.2 Perspective

The UCNPs with controlled structure, bright emission, multiple dimensions and tunable optical properties is the first step towards real excellent applications. The confocal microscope and wide-field microscope systems for optical signal detection of single nanoparticles are a preliminary exploration towards the optical multiplexing of nanocarriers. The deep-learning algorithm method for more accurate decoding lifetime fingerprints of single nanoparticles is a new attempt. Under the base of this work, it makes nanoscopic biological applications, super-resolution imaging, and high-throughput optical multiplexing possible.

Nanomaterials: The development of a programmable diversity of nanosystems with the desired functionalities and performance is a great challenge for chemists and materials scientists. The current nano synthesis techniques will continue to advance the development of nanomaterials with specific photophysical properties.[1–3] Efforts are ongoing to realize desirable functionalities in smaller and efficient UCNPs and to integrate them through both heterogeneous and hybrid designs.[4–6] It is challenging to keep high brightness in small UCNPs, which needs proper design and management of efficient energy transfer to achieve high efficiencies in photon sensitization, energy transfer, and upconversion emission. This will boost the development of biomedical and intracellular applications that demand nanoscopic molecular probes and sensors. Moreover, further exploring the distribution and gradient of RE^{3+} ions in UNCPs is useful to optimize their optical properties and precisely control the doping location during synthesis. This can create a library of programmable heterogeneous multilayer doped nanostructures, from heterogeneous to homogeneous and from homo-valence ion to hetero-valence ion doping. For the moment, only the sphere-like core-shell structure was employed to control the energy transfer in UCNPs, we can extend to the emerging heterogenous nanorods and nanoplate structure as well.

Single nanoparticles: Ensemble measurements of nanomaterials obtained by different research groups are affected by different instrumentation settings and measurement environments. Single nanoparticle detection will enable the rapid search for efficient and uniform nanoparticles from various synthesis methods or research groups. The optical characterizations of single nanoparticles play an important role in the discoveries of many unique properties of UCNPs, which all highly dependent on the excitation power density following the sophisticated non-linear process.[7] These nanoparticles can be selected for a variety of potential applications according to their performance in terms of power-dependent intensities, intensity distribution, and saturation in brightness. Except for the optical dimensions of emission spectra and lifetime, the power-dependent intensity curve is a potential non-linear optical signal for multiplexing as well. Moreover, the study of non-linear processes at a single nanoparticle level is important to achieve the rational design for higher upconversion emission efficiency and develop more potential applications, eg., super-resolution imaging regarding the non-linear property, non-linear responsive probes for imaging and sensing.[8–11] The on-demand design of a multifunctional doped nanosystem will enable the multiplexing of the nanoscopy, which is of great importance for bio-applications at the nanoscale such as studying the protein interaction.

High-throughput detection: High-throughput detection of nanoparticles is important in practical application. The wide-field imaging scheme can drastically enhance the detection throughput and speed. It's desirable for the development of next-generation easy-to-use and commercial wide-field technologies to test the optical fingerprints of single UCNPs. Using a commercially available hyperspectral imaging system is a possible way to speedily detect the spectral and lifetime information of single nanoparticles.[12,13] Moreover, the implementation of optical super-resolution microscopy techniques will allow high-throughput decoding these nanoscale super-multiplexed dots decodable beyond the diffraction limit. Super-resolution microscopy, e.g., (stochastic optical reconstruction microscopy) STORM, (photoactivated localization microscopy) PALM, (ground state depletion microscopy) GSD, (stimulated emission depletion) STED and SIM, provides direct insight at scales smaller than light's

diffraction limit. It technically challenges to develop the new generation of time-domain super-resolution imaging method under pulsed laser excitation.

Data analysis: Automation and high efficiency of data analysis are desirable for the implementation of single-particle studies into routine sample analysis. The deep learning method can go beyond the limits of conventional data analysis.[14–16] After building and optimizing the model, the deep learning algorithm has been recently used to analyze single-molecule patterns and reconstruct a super-resolution widefield image.[17,18] This indicates that except for handling a large amount of data and classifying each batch of nanoparticles, the deep learning method maybe predicts the material's characterizations or optical signatures from unknown single nanoparticles.

6.3 Reference

(1) Laramy, C. R.; O'Brien, M. N.; Mirkin, C. A. Crystal Engineering with DNA. *Nat. Rev. Mater.* **2019**, *4* (3), 201–224.

(2) Tan, C.; Chen, J.; Wu, X. J.; Zhang, H. Epitaxial Growth of Hybrid Nanostructures. *Nat. Rev. Mater.* **2018**, *3* (2), 1–13.

(3) Zhou, J.; Chizhik, A. I.; Chu, S.; Jin, D. Single-Particle Spectroscopy for Functional Nanomaterials. *Nature* **2020**, *579* (7797), 41–50.

(4) Zhuo, Z.; Liu, Y.; Liu, D.; Huang, P.; Jiang, F.; Chen, X.; Hong, M. Manipulating Energy Transfer in Lanthanide-Doped Single Nanoparticles for Highly Enhanced Upconverting Luminescence. *Chem. Sci.* **2017**, *8* (7), 5050–5056.

(5) Liu, D.; Xu, X.; Du, Y.; Qin, X.; Zhang, Y.; Ma, C.; Wen, S.; Ren, W.; Goldys, E. M.; Piper, J. A.; et al. Three-Dimensional Controlled Growth of Monodisperse Sub-50 Nm Heterogeneous Nanocrystals. *Nat. Commun.* **2016**, *7*, 10254.

(6) Wen, S.; Zhou, J.; Schuck, P. J.; Suh, Y. D.; Schmidt, T. W.; Jin, D. Future and Challenges for Hybrid Upconversion Nanosystems. *Nat. Photonics* **2019**, *13* (12), 828–838.

(7) Liao, J.; Jin, D.; Chen, C.; Li, Y.; Zhou, J. Helix Shape Power-Dependent Properties of Single Upconversion Nanoparticles. *J. Phys. Chem. Lett.* **2020**. https://doi.org/10.1021/acs.jpclett.9b03838

(8) Jin, D.; Xi, P.; Wang, B.; Zhang, L.; Enderlein, J.; van Oijen, A. M. Nanoparticles for Super-Resolution Microscopy and Single-Molecule Tracking. *Nat. Methods* **2018**, *15* (6), 415–423.

(9) Chen, C.; Wang, F.; Wen, S.; Su, Q. P.; Wu, M. C. L.; Liu, Y.; Wang, B.; Li, D.; Shan, X.; Kianinia, M.; et al. Multi-Photon near-Infrared Emission Saturation Nanoscopy Using Upconversion Nanoparticles. *Nat. Commun.* **2018**, *9* (1), 4–9.

(10) Zhan, Q.; Liu, H.; Wang, B.; Wu, Q.; Pu, R.; Zhou, C.; Huang, B.; Peng, X.; Ågren, H.; He, S. Achieving High-Efficiency Emission Depletion Nanoscopy by Employing Cross Relaxation in Upconversion Nanoparticles. *Nat. Commun.* **2017**, *8* (1), 1–11.

(11) Liu, Y.; Lu, Y.; Yang, X.; Zheng, X.; Wen, S.; Wang, F.; Vidal, X.; Zhao, J.; Liu, D.; Zhou, Z.; et al. Amplified Stimulated Emission in Upconversion Nanoparticles for Super-Resolution Nanoscopy. *Nature* **2017**, *543* (7644), 229–233.

(12) Gonell, F.; Botas, A. M. P.; Brites, C. D. S.; Amorós, P.; Carlos, L. D.; Julián-López, B.; Ferreira, R. A. S. Aggregation-Induced Heterogeneities in the Emission of Upconverting Nanoparticles at the Submicron Scale Unfolded by Hyperspectral Microscopy. *Nanoscale Adv.* **2019**, *1* (7), 2537–2545.

(13) Zhang, Z.; Kenny, S. J.; Hauser, M.; Li, W.; Xu, K. Ultrahigh-Throughput Single-Molecule Spectroscopy and Spectrally Resolved Super-Resolution Microscopy. *Nat. Methods* **2015**, *12* (10), 935–938.

(14) Lecun, Y.; Bengio, Y.; Hinton, G. Deep Learning. *Nature* **2015**, *521* (7553), 436–444.

(15) Butler, K. T.; Davies, D. W.; Cartwright, H.; Isayev, O.; Walsh, A. Machine Learning for Molecular and Materials Science. *Nature* **2018**, *559* (7715), 547–555.

(16) Zhou, J.; Huang, B.; Yan, Z.; Bünzli, J.-C. G. Emerging Role of Machine Learning in Light-Matter Interaction. *Light Sci. Appl.* **2019**, *8* (1), 1–7.

(17) Zhang, P.; Liu, S.; Chaurasia, A.; Ma, D.; Mlodzianoski, M. J.; Culurciello, E.; Huang, F. Analyzing Complex Single-Molecule Emission Patterns with Deep Learning. *Nat. Methods* **2018**, *15* (11), 913–916.

(18) Ouyang, W.; Aristov, A.; Lelek, M.; Hao, X.; Zimmer, C. Deep Learning Massively Accelerates Super-Resolution Localization Microscopy. *Nat. Biotechnol.* **2018**, *36* (5), 460–468.